

AN ABSTRACT OF THE THESIS OF

Jeffrey M. Luitjens for the degree of Doctor of Philosophy in Nuclear Engineering
presented on June 3, 2015.

Title: The Development of a Mechanistic Critical Heat Flux Correlation

Abstract approved: _____

Qiao Wu

A mechanistic based critical heat flux (CHF) correlation has been developed derived from a mass, momentum, and energy balance at a nucleation site for water. The trigger mechanism for the CHF condition is postulated to be related to the maximum boiling frequency on a heated surface. It is observed that dependency of results is directly related to the effective cavity size (surface conditions) and as such the effective cavity size is taken to be the single closure coefficient dependent on the system pressure and mass flux.

The applicable range of the developed model is considered to be with inlet mass fluxes between 128 to 4300 $kg/(m^2 - s)$, pressures between 4.5 to 15.6 MPa , and critical qualities between -0.03 to 1.0. The resulting standard error of the mechanistic CHF model is 12.9% with over 800 experimental data points utilized over these conditions to inform and confirm the development of the model using a bundle geometry.

©Copyright by Jeffrey M. Luitjens
June 3, 2015
All Rights Reserved

The Development of a Mechanistic Critical Heat Flux Correlation

by

Jeffrey M. Luitjens

A THESIS

submitted to

Oregon State University

in partial fulfillment of
the requirements for the
degree of

Doctor of Philosophy

Presented June 3, 2015
Commencement June 2015

Doctor of Philosophy thesis of Jeffrey M. Luitjens presented on June 3, 2015.

APPROVED:

Major Professor, representing Nuclear Engineering

Head of the Department of Nuclear Engineering and Radiation Health Physics

Dean of the Graduate School

I understand that my thesis will become part of the permanent collection of Oregon State University libraries. My signature below authorizes release of my thesis to any reader upon request.

Jeffrey M. Luitjens, Author

ACKNOWLEDGEMENTS

I would like to thank all of my friends and family for the support they have provided. I would especially like to recognize my advisor who has mentored me since the start of my academic studies, none this would have been possible without him, my mother for always encouraging me to push myself further, and my fiancé for all the patience and support while I completed this work.

TABLE OF CONTENTS

	<u>Page</u>
1 Introduction	1
1.1 The Critical Heat Flux	2
1.2 Motivation	5
2 The Boiling Process	7
2.1 Nucleation in a Pure Liquid (Bulk Boiling)	7
2.2 Nucleation at Surfaces	10
2.2.1 Cavity Activation Size	13
2.2.2 Nucleation Site Density	17
2.2.3 Nucleation Waiting Period	23
2.2.4 Bubble Growth Rate	27
2.2.5 Bubble Departure Size	32
2.2.6 Bubble Departure Frequency	33
2.2.7 Bubble Departure Velocity	35
2.3 Heat Transfer Modes	35
2.3.1 Macro-Convective Heat Transfer	36
2.3.2 Bubble Agitation	37
2.3.3 Vapor-liquid Exchange	37
2.3.4 Transient Heat Conduction	38
2.3.5 Microlayer Evaporation	40
2.4 Heat Flux Partitioning for Pool Boiling by Del Valle and Kenning	42
2.4.1 Activation Site Location	44
2.4.2 Maximum Bubble Projected Area	45
2.4.3 Surrounding Area of Influence	45
2.5 Heat Flux Partitioning for Flow Boiling by Chen	46
3 The Critical Heat Flux	53
3.1 Critical Heat Flux Development Domain	53
3.2 Methods to Approach the Critical Heat Flux	55
3.3 Methods to Predict the Onset of Critical Heat Flux	57
3.3.1 Empirical Correlations	57
3.3.2 Look-Up Tables	59
3.3.3 Mechanistic Models	60

TABLE OF CONTENTS (Continued)

	<u>Page</u>
3.4 Fundamental Mechanistic Models	61
3.5 Existing Critical Heat Flux Correlations	65
3.5.1 Kutateladze (1948) [1]	67
3.5.2 Katto (1978) [2]	67
3.5.3 Rogers (1982) [3]	67
3.5.4 Monde (1982) [4]	69
3.5.5 Weisman and Pei (1983) [5]	70
3.5.6 Weisman and Ying (1985) [6]	70
3.5.7 Lee and Mudawwar (1988) [7]	70
3.5.8 Liu et al. (2000) [8]	72
3.5.9 Kureta (2002) [9]	72
3.5.10 Natural Circulation in a Vertical Inclined Tubes (Zhen-hua 2004)	73
4 Parameter Effects on Critical Heat Flux	75
4.1 Surface Tension	75
4.2 Contact Angle	75
4.2.1 Static Contact Angle	76
4.2.2 Dynamic Contact Angle	78
4.3 Wall Thermal Properties	81
4.4 Bulk Subcooling	85
4.5 Mass Flux	85
4.6 Surface Roughness	86
4.7 Wall Superheat	87
4.8 Channel Gap Width	87
4.9 Heated Surface Length	88
4.10 Rectangular Channel Aspect Ratio	89
4.11 Developing Length Effects	90
5 Experimental Data	91
5.1 Bundle Data of the University of Wisconsin [10]	91
5.2 EPRI Experimental Data	95

TABLE OF CONTENTS (Continued)

	<u>Page</u>
6 Proposed Critical Heat Flux Model	103
6.1 Heat Transfer Modes	104
6.2 Bubble Forces Perpendicular to a Vertical Heated Surface	106
6.2.1 Surface Tension (F_{σ})	107
6.2.2 Evaporative Thrust Force (F_{evap})	107
6.2.3 Bubble Shear Lift Force (F_{sL})	112
6.3 Critical Heat Flux Model	115
6.4 Critical Heat Flux Model Constitutive Relations	120
6.4.1 Effective Nucleation Site Cavity Radius	121
6.4.2 Bubble Contact Angle	121
6.4.3 Bubble Contact Radius	122
6.4.4 Wall Superheat	123
6.4.5 Convective Heat Flux Correlation and Boiling Suppression . . .	123
6.4.6 Nucleation Site Density	124
7 Critical Heat Flux Model Results	125
7.1 Model Nodalization	125
7.2 Model Calibration	126
7.3 Applicability Range	128
7.4 University of Wisconsin Database Results	134
7.4.1 Critical Heat Flux Value	134
7.4.2 Critical Heat Flux Location	134
7.5 EPRI Database Results	137
7.5.1 Critical Heat Flux Value for the EPRI Database	137
7.5.2 Critical Heat Flux Location	152
7.5.3 Correlation Bias	154
8 Conclusions	160
Bibliography	161
Appendices	169

LIST OF FIGURES

<u>Figure</u>	<u>Page</u>
1.1 Typical pool boiling boiling curve.	3
2.1 Spherical bubble force balance.	8
2.2 Surface nucleation site.	11
2.3 Bubble parameter variations with heat flux [11].	12
2.4 Bubble height attached to a heated surface.	14
2.5 Possible bubble sizes for a specified wall and saturation temperature at various bulk fluid subcooled temperatures.	16
2.6 Nucleation site density dependence on cavity size [11]	19
2.7 Nucleation site density correlation comparison to experimental data from Basu [12].	22
2.8 Transient temperature profile near a heated wall plotted with a typical bubble superheat as a function of size; taken from [13].	26
2.9 Bubble departure radius by Semeria and Nishikawa.	34
2.10 Microlayer energy balance.	41
2.11 Heat flux partitioned areas.	43
2.12 Area of influence fraction by Del Valle and Kenning [11].	47
3.1 Modes of the critical heat flux.	54
3.2 Boiling curve for transient cooling and transient heating.	56
3.3 Boiling curve for steady state, transient cooling, and transient heating [14].	58
3.4 Vapor and liquid counter-flow in pool boiling.	63
3.5 Model of Lee and Mudawwar (1988) [7].	71
4.1 Surface tension dependence on temperature.	76

LIST OF FIGURES (Continued)

<u>Figure</u>	<u>Page</u>
4.2 Effect of surface roughness on the contact angle [15].	77
4.3 Variation of the normalized departure diameter and departure time with contact angle (fluids: water and PF5060, $\Delta T_w = 8K$, $\Delta T_{sub} = 0K$, $g = 1.0g_e$); taken from Dhir [16].	78
4.4 The variation of heat transfer rates with time for various contact angles from the microlayer (fluids: water, $P = 1.01bar$, $\Delta T_w = 8K$, $\Delta T_{sub} = 0K$, $g = 1.0g_e$); taken from Dhir [16].	79
4.5 The variation of heat transfer rates with time for various contact angles from the macrolayer (fluids: water, $P = 1.01bar$, $\Delta T_w = 8K$, $\Delta T_{sub} = 0K$, $g = 1.0g_e$); taken from Dhir [16].	79
4.6 Depiction of a dynamic and receding contact angle.	80
4.7 Effect of surface temperature on the contact angle for stainless steel with a surface roughness of 0.01 microns [15].	81
4.8 Radial velocity profile for various Grashof numbers for natural circulation loop [17].	83
4.9 Steady-state natural circulation results from Misale [17].	84
4.10 Mass velocity effect on the critical heat flux velocity; from [8].	85
4.11 Mass velocity effect on the critical heat flux velocity[?]; figure from [18].	86
4.12 Surface roughness effects on the CHF value.	87
4.13 Channel gap width effects on the critical heat flux value by Kureta and Akimoto[9].	88
4.14 Heated length effects on the critical heat flux observed by Kureta and Akimoto[9].	89
4.15 Developing length effect on CHF [9].	90
5.1 University of Wisconsin bundle test section[10].	92
5.2 General Electric test section assembly layout for tests 301-318.	98

LIST OF FIGURES (Continued)

<u>Figure</u>		<u>Page</u>
6.1	Continuous boiling frequency near surface.	104
6.2	Boiling heat transfer mechanisms at a heated surface.	105
6.3	Spherical bubble perpendicular force balance on a vertically aligned heated surface.	108
6.4	Evaporative thrust force due to evaporation across a bubble interface (top) similarity to a rocket (bottom).	110
6.5	Correlation algorithm for determining critical heat flux.	119
7.1	Nodalization of critical heat flux model.	126
7.2	Calibration of effective cavity size for EPRI database points.	127
7.3	Calibration of effective cavity size residuals for EPRI database points.	128
7.4	Applicable range of mass flux distribution of EPRI database tests 301-318.	129
7.5	Applicable range of pressure distribution of EPRI database tests 301-318.	130
7.6	Applicable range of inlet temperature distribution of EPRI database tests 301-318.	131
7.7	Applicable range of inlet quality distribution of EPRI database tests 301-318.	132
7.8	Applicable range of critical quality distribution of EPRI database tests 301-318.	133
7.9	CHF model performance against UofW database.	135
7.10	CHF model performance against UofW database.	135
7.11	Predicted CHF location performance against UofW database.	136
7.12	CHF versus axial position for UofW run 2 of 11.	136
7.13	Model CHF performance compared to Full EPRI database tests 301-318.	138
7.14	Model CHF performance compared to Applicable Range of EPRI database tests 301-318.	139

LIST OF FIGURES (Continued)

<u>Figure</u>	<u>Page</u>
7.15 CHF error distribution for model compared to EPRI database tests 301-318.	140
7.16 CHF model results for EPRI test 301.	141
7.17 CHF model results for EPRI test 302.	141
7.18 CHF model results for EPRI test 303.	142
7.19 CHF model results for EPRI test 304.	142
7.20 CHF model results for EPRI test 305.	143
7.21 CHF model results for EPRI test 306.	143
7.22 CHF model results for EPRI test 307.	144
7.23 CHF model results for EPRI test 307.1.	144
7.24 CHF model results for EPRI test 307.2.	145
7.25 CHF model results for EPRI test 308.	145
7.26 CHF model results for EPRI test 309.	146
7.27 CHF model results for EPRI test 310.	146
7.28 CHF model results for EPRI test 311.	147
7.29 CHF model results for EPRI test 312.	147
7.30 CHF model results for EPRI test 313.	148
7.31 CHF model results for EPRI test 314.	148
7.32 CHF model results for EPRI test 315.	149
7.33 CHF model results for EPRI test 316.	149
7.34 CHF model results for EPRI test 316.1.	150
7.35 CHF model results for EPRI test 317.	150
7.36 CHF model results for EPRI test 318.	151

LIST OF FIGURES (Continued)

<u>Figure</u>	<u>Page</u>
7.37 CHF versus axial position for EPRI test 301 run 17.	153
7.38 CHF versus axial position for EPRI test 303 run 24.	153
7.39 Correlation bias on mass flux for EPRI database tests 301-318.	155
7.40 Correlation bias on system pressure for EPRI database tests 301-318. . .	156
7.41 Correlation bias on inlet temperature for EPRI database tests 301-318. .	157
7.42 Correlation bias on inlet quality for EPRI database tests 301-318. . . .	158
7.43 Correlation bias on critical quality for EPRI database tests 301-318. . .	159

LIST OF TABLES

<u>Table</u>	<u>Page</u>
3.1 Typical operating conditions for pressurized water reactors.	55
3.2 Subset of critical heat flux models and applicability range overview. . .	66
3.3 Constants for CHF correlation by Rogers et al. [3].	68
3.4 Applicability of Rogers et al. CHF correlation [3].	68
3.5 Applicability of Kureta and Akimoto CHF correlation for subcooled forced flow in narrow channels[9].	73
5.1 Experimental bundle data of the University of Wisconsin	92
5.2 Thermocouple elevation placement from bottom of heated length for the University of Wisconsin CHF tests	93
5.3 Experimental bundle results of University of Wisconsin [10].	94
5.4 EPRI CHF database organized by sponsor.	95
5.5 EPRI CHF datasets used for analysis; 'in' refers to the CHF occurring on the inner rods of the assembly, 'out' refers to CHF occurring on the outer rods of the assembly as depicted in Figure 5.2.	96
5.6 General Electric test geometry from EPRI CHF database.	97
5.7 General Electric radial peaking for EPRI test section 301.	99
5.8 General Electric radial peaking for EPRI test section 302.	99
5.9 General Electric radial peaking for EPRI test section 303.	99
5.10 General Electric radial peaking for EPRI test section 304.	99
5.11 General Electric radial peaking for EPRI test section 305.	99
5.12 General Electric radial peaking for EPRI test section 306.	99
5.13 General Electric radial peaking for EPRI test section 307.	100
5.14 General Electric radial peaking for EPRI test section 307.1.	100
5.15 General Electric radial peaking for EPRI test section 307.2.	100

LIST OF TABLES (Continued)

<u>Table</u>	<u>Page</u>
5.16 General Electric radial peaking for EPRI test section 308.	100
5.17 General Electric radial peaking for EPRI test section 309.	100
5.18 General Electric radial peaking for EPRI test section 310.	100
5.19 General Electric radial peaking for EPRI test section 311.	101
5.20 General Electric radial peaking for EPRI test section 312.	101
5.21 General Electric radial peaking for EPRI test section 313.	101
5.22 General Electric radial peaking for EPRI test section 314.	101
5.23 General Electric radial peaking for EPRI test section 315.	101
5.24 General Electric radial peaking for EPRI test section 316.	101
5.25 General Electric radial peaking for EPRI test section 316.1.	102
5.26 General Electric radial peaking for EPRI test section 317.	102
5.27 General Electric radial peaking for EPRI test section 318.	102
G.1 General Electric test data 301 from EPRI CHF database.	199
G.2 General Electric test data 302 from EPRI CHF database.	202
G.3 General Electric test data 303 from EPRI CHF database.	205
G.4 General Electric test data 304 from EPRI CHF database.	207
G.5 General Electric test data 305 from EPRI CHF database.	209
G.6 General Electric test data 306 from EPRI CHF database.	210
G.7 General Electric test data 307 from EPRI CHF database.	213
G.8 General Electric test data 307.1 from EPRI CHF database.	214
G.9 General Electric test data 307.2 from EPRI CHF database.	215
G.10 General Electric test data 308 from EPRI CHF database.	216

LIST OF TABLES (Continued)

<u>Table</u>	<u>Page</u>
G.11 General Electric test data 309 from EPRI CHF database.	218
G.12 General Electric test data 310 from EPRI CHF database.	221
G.13 General Electric test data 311 from EPRI CHF database.	223
G.14 General Electric test data 312 from EPRI CHF database.	227
G.15 General Electric test data 313 from EPRI CHF database.	230
G.16 General Electric test data 314 from EPRI CHF database.	234
G.17 General Electric test data 315 from EPRI CHF database.	236
G.18 General Electric test data 316 from EPRI CHF database.	240
G.19 General Electric test data 316.1 from EPRI CHF database.	244
G.20 General Electric test data 317 from EPRI CHF database.	247
G.21 General Electric test data 318 from EPRI CHF database.	252

LIST OF APPENDICES

<u>Appendix</u>	<u>Page</u>
A Clausius-Clapeyron Derivation	170
B MATLAB Script for Test Call Function	174
C MATLAB Script for Calibration Call Function	180
D MATLAB Script for CHF Function	187
E MATLAB Script for Heat Flux Distribution Function	194
F MATLAB Script for Units Conversion Function	196
G EPRI Data for Tests 301-318	199

Nomenclature

α	thermal diffusivity
\bar{A}'_b	bubble projected top-down surface area
\bar{q}''	average heat flux
δ	thermal boundary layer thickness
Δh_{fg}	latent heat of vaporization
ΔH_{in}	inlet enthalpy subcooling
ΔT_e	effective wall superheat; $S(T_w - T_{sat})$
ΔT_w	wall superheat; $T_w - T_{sat}$
ΔT_{sub}	subcooled temperature; $T_{sat} - T_b$
\dot{m}	mass flow rate
\dot{q}_{pin}	pin power
η	non-dimensional distance
λ	Moody friction coefficient
μ	dynamic viscosity
ν	kinematic viscosity
ν_f	liquid specific volume
ν_g	vapor specific volume

v_{fg}	$v_g - v_f$
ρ_v	vapor density
ρ_f	liquid density
σ	surface tension
τ_w	wall shear stress
θ	contact angle
θ_a	advancing contact angle
θ_d	dynamic contact angle
θ_r	receding contact angle
θ_s	static contact angle
ξ	non-dimensional temperature
A	area
a	radius of vapor-solid contact area
A_b	bubble surface area
A_h	heated area
C_f	Fanning friction coefficient
C_L	lift coefficient
$C_{p,l}$	specific heat of liquid
D	diameter
D_b	bubble diameter

D_c	cavity diameter
D_d	departure diameter
D_m	maximum bubble diameter
D_{df}	Fritz diameter
F	flow boiling single-phase enhancement factor
f_d	bubble departure frequency
F_v	vapor pressure force
f_{boil}	fractional boiling area
f_{conv}	fractional non-boiling area
F_{evap}	evaporative thrust force
F_l	liquid pressure force
F_{sigma}	surface tension force
F_{SL}	shear lift force
G	mass flux
g	gravity
Gr	Grashof number
H_b	bubble height
h_{conv}	convective heat transfer coefficient
h_{mac}	macro-convective heat transfer coefficient
h_{mic}	micro-convective heat transfer coefficient

Ja	Jakob number
k_l	liquid conductivity
L	heated length
m_b	bubble mass
$meas$	measured
$N_{a,n}$	nucleation site density
Nu	Nusselt number
P	pressure
P_h	heated perimeter
P_w	wetted perimeter
P_v	vapor pressure
P_l	liquid pressure
Pr	Prandtl number; $\frac{\mu C_{p,l}}{k_l}$
$pred$	predicted
q''	heat flux
$q''_{1\phi}$	single phase convective heat flux
q''_{CHF}	critical heat flux
q''_I	bubble evaporation (interface) heat flux
q''_{slide}	bubble sliding heat flux
q''_{trans}	transient conduction heat flux

R	ideal gas constant
R_a	surface roughness
r_b	bubble radius
r_c	cavity radius
r_d	departure radius
R_m	maximum bubble radius
Re	Reynolds number; $\frac{\rho u D}{\mu}$
Re_b	bubble Reynolds number
S	flow boiling two-phase suppression factor
s	nucleation site spacing
T	temperature
t	time
T_b, T_∞	bulk temperature
t_c	bubble collapse time
t_d	bubble departure time
T_f	film temperature
T_l	liquid temperature
t_L	bubble lifetime
T_w	wall temperature
t_w	bubble waiting time

T_{in}	channel inlet temperature
T_{sat}	saturation temperature
u	velocity
U_l	bulk liquid velocity
V_b	bubble volume
v_b	bubble departure velocity
$v_{b,i}$	bubble interface velocity
x	quality
x, y	distance from wall
x_{CHF}	critical quality; quality at CHF location
y'	bubble center of mass distance from wall
z	axial length along channel

Chapter 1: Introduction

In industry the understanding of the limits of the boiling heat transfer mode is crucial to modeling the thermal hydraulic processes that occur to ensure the safe operation of industrial plants while enhancing a system's effectiveness. This is especially true in nuclear power plants which are characterized by relatively high heat fluxes. At high heat fluxes there is a potential to reach a critical point where the heat removal mechanisms are not sufficient enough to remove energy from the surface. This heat flux is referred to as the critical heat flux (CHF). When the CHF point is reached the surface temperature rises due to the inability to remove energy from the surface. This results in temperature increases often greater than the melting temperature of the heated surface. Understanding the heat transfer processes and the transitions involved is needed to appropriately model the mechanisms of the heat transfer modes to predict the onset of the CHF condition to prevent such scenarios.

Currently, the mechanisms of the onset of the CHF condition are not well understood and rely heavily on empirical correlations and lookup tables. This results in correlations that are often very specific to the scope of the developmental application resulting from the lack of modeling of the mechanistic behaviors. Modeling of the mechanistic processes can result in a broader applicability of a developed model. Focus here will be given to the development of a mechanist based CHF correlation derived from a mass, momentum, and energy conservation equations.

The ability to develop a mechanistic based model allows for more confidence in the conceptual design phase of facilities that utilize high heat flux conditions since the physical mechanisms are captured in the model itself. This has a significant effect on design, testing, and operational costs of high heat flux operating facilities. For example, operating capital can be increased because one better understands the margin/uncertainty of

the design with a more mature mechanistic CHF correlation. A better understanding of one's limits with higher confidence allows for reduction in the potentially unnecessary margin that is used to account for any uncertainties in the utilized correlation. This reduction in margin allows for facilities to operate at a higher capacity increasing capital.

1.1 The Critical Heat Flux

In flat plate or flow boiling and forced or natural circulation driven flow, a boiling curve is used to describe the boiling regime. Figure 1.1 shows a typical boiling curve with heat flux on the y-axis and the wall superheat temperature on the x-axis represented as the wall temperature minus the working fluid saturation temperature at the system pressure ($T_w - T_{sat}$).

The pool boiling curve is broken up into four distinct regions that are phenomenon based. The lines (solid and dotted) outline the transition paths between the regions as shown in Figure 1.1. A flow boiling curve will have similar trends except the curve will be more peaked and shifted to the right when compared to the pool boiling curve due to the enhanced convective heat transfer. The transition paths of a pool boiling curve are described here using Figure 1.1.

- Points I-II: Although this region may be characterized with a wall temperature above the saturation temperature no boiling takes place in this region. The heat transfer in this region is governed by local natural convective forces near the wall. The heat transfer slightly increases with increasing wall superheat as represented by the slope from point I to II.
- Points II-III: The heat removal in this region is enhanced by a phase change process of the working fluid. Point II is the point where nucleate boiling begins. The slope of this curve is greater than that from points I-II depicting a greater enhancement in the heat transfer process from boiling with increasing wall superheat. As the wall superheat increases so does the heat flux. This occurs only up to a criti-

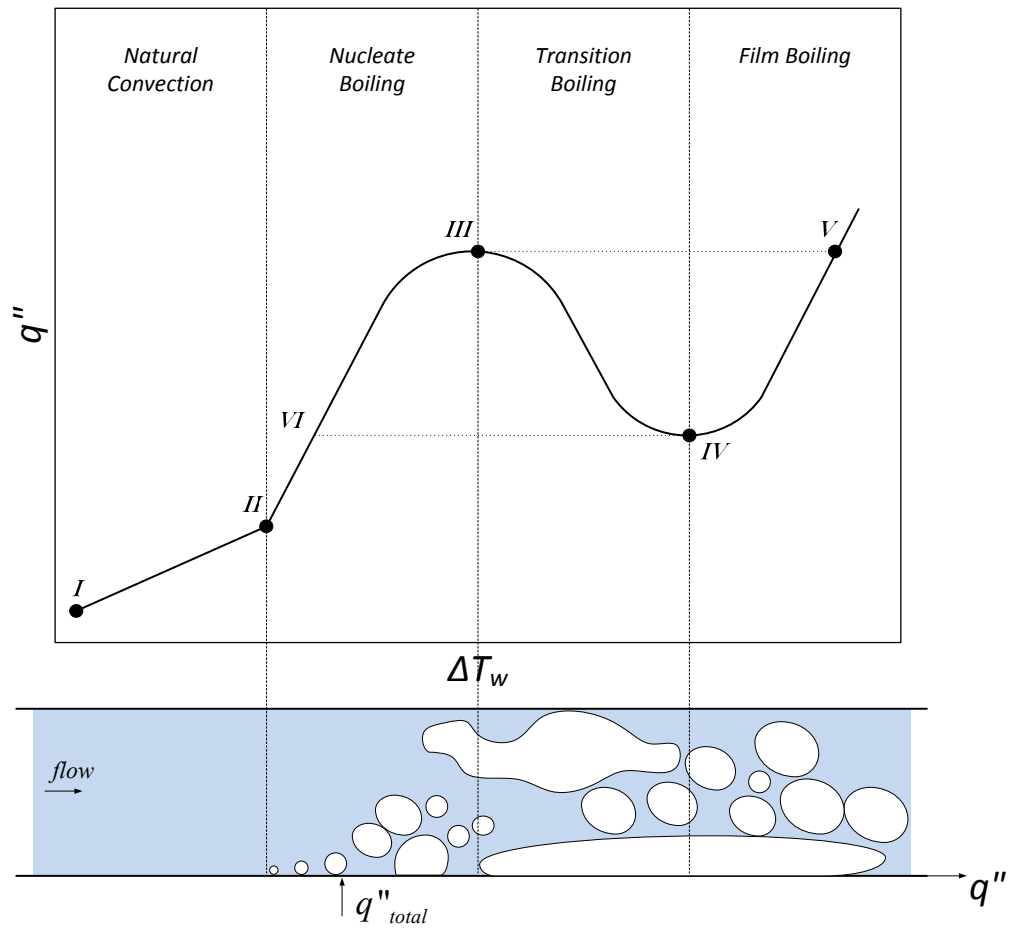


Figure 1.1: Typical pool boiling boiling curve.

cal point (point III) where the heat transfer mechanisms are unable to remove the energy from the surface. This point is referred to as the CHF point.

- Points III-V (for a heat flux controlled surface): At point III where CHF occurs, an unstable vapor film has developed preventing liquid from coming in contact with the heating surface. Noting that the vapor film increases the thermal resistance. In a heat flux controlled system once the heat flux increases above the CHF point, the temperature immediately spikes following the dotted line to point V in the film boiling regime. This phenomenon can be simply described by a simple heat transfer equation:

$$q'' = h(T_w - T_f) \quad (1.1)$$

For a given heat flux, once CHF is reached a vapor film develops. The vapor film has a much smaller heat transfer coefficient than that of the liquid. Thus $(T_w - T_f)$ must dramatically increase to keep the same heat flux. The required temperatures often cause mechanical failure of the heat transfer surface.

- Points III-IV (for a temperature controlled surface): At point III where CHF occurs, an unstable vapor film has developed preventing liquid from coming in contact with the heating surface. The vapor film increases the thermal resistance. As temperature is increased in a temperature controlled system the heat flux drops following the solid curve to point IV within the film transition boiling regime. This is due to the increased void fraction near the wall which is accompanied by a smaller vapor heat transfer coefficient. This curve is followed during the heating and cooling process.
- Points IV-V (temperature controlled surface): Point IV is referred to as the Leidenfrost point. The Leidenfrost point corresponds to the development of a stable vapor film between the surface and cooling working fluid. It is the point of minimum heat transfer post CHF. Further increase in temperature beyond point IV results in an increase in heat flux due to the increase in ΔT through the vapor film. This curve is followed during the heating and cooling process.

- Points V-IV (for a heat flux controlled surface): Once CHF has been reached in the heat flux controlled system and stable film boiling as been developed a decrease in heat flux will result in a temperature decrease that will follow the solid curve from point V to point IV, the Leidenfrost point. Once this point is reached the vapor film begins to break down.
- Points IV-VI (for a heat flux controlled surface): Upon break down of the vapor film at the Leidenfrost point the working fluid begins to wet the surface. The wetting of the surface results in a drastic increase in the heat transfer coefficient causing a dramatic drop in the wall temperature that is represented by the dotted line moving from point IV to point VI.

1.2 Motivation

Many methods exist in literature that aim to predict the onset of the critical heat flux. Many of which are developed for specific geometric and fluid conditions. Hall and Mudawwar [19, 20] compiled an assessment of CHF databases and about 100 CHF correlations. When correlations were assessed against their applicable range root mean square(RMS)values from 6.4% to 662% were obtained with the total mean RMS error of 46%. When assessed outside their applicable range the average RMS error of the tested correlations was >500%. This expresses the limits and lack of potential broad applicability of many developed models forcing one to express great caution when applying relations to a new design with differing geometry and operating conditions. It is strongly believed that the development of a mechanistic based critical heat correlation will mitigate this issue and be more suited to allow for the development of a more broadly applicable correlation by means of modeling the surface phenomena through conventional mass, momentum, and energy balance equations.

The ability to develop a widely applicable model allows for more confidence in the conceptual design phase of facilities that utilize high heat flux conditions. This has a significant effect on the operating costs of high heat flux operating facilities in terms of

margin management. A better understanding of one's limits with a higher confidence allows for a reduction in the potentially unnecessary margin that is used to account for any uncertainties in the utilized correlation. This reduction in margin allows for facilities to operate at a higher capacity increasing capital.

The objectives of the research performed here can be summarized as follows:

- Obtain an understanding of the boiling process.
- Obtain an understanding of the current state of flow based critical heat flux correlations.
- Obtain a set of physical parameters that are believed to have an impact on the critical heat flux based on numerical and experimental observations.
- Obtain and analyze experimental critical heat flux data for a wide range of conditions; including the low-flow conditions.
- Develop a mechanistic critical heat flux correlation for low to high flow and low to high pressures based on governing equations of mass, momentum, and energy balance.
- Compare developed model to experimental data and identify any deficiencies.
- Provide recommendations for future work

Chapter 2: The Boiling Process

Before proceeding to analyze the CHF condition for vertical flow in confined channels, a basic understanding of the pool boiling mechanisms and modeling approaches are introduced. Nucleation theory is at the core of understanding the boiling process. Nucleation involves having a site, whether surface or molecular based, that acts as a promoter for the boiling process.

2.1 Nucleation in a Pure Liquid (Bulk Boiling)

When nucleation in a pure liquid is observed the molecular spacing of the working fluid acts as the nucleation site. This process is often referred to as bulk boiling. This process is typically not the dominant mechanism when boiling is present due to the high superheats that are necessary unless a rapid depressurization of the volume is occurring. The high superheats needed for bulk fluid boiling can be explained by performing a force balance on an assumed spherical bubble as shown in Figure 2.1. Performing a force balance accounting for the vapor pressure, liquid pressure, and surface tension forces on the bubble surface results in the following:

$$F_v - F_l = F_\sigma$$
$$P_v - P_l = \frac{4\sigma}{D} \quad (2.1)$$

Equation 2.1 represents the equilibrium bubble size for a given internal bubble pressure and external liquid pressure. Relating the required superheat needed create this

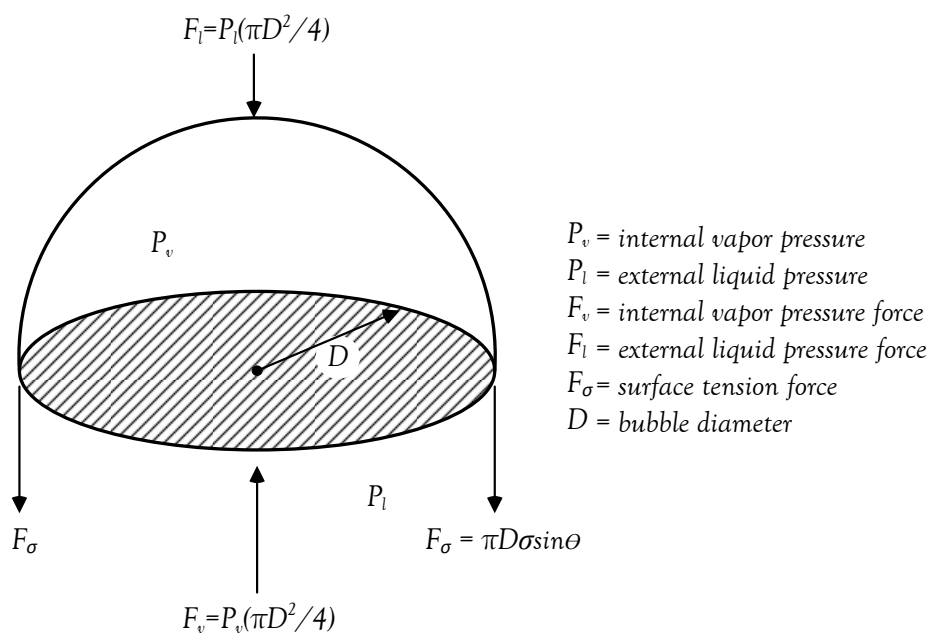


Figure 2.1: Spherical bubble force balance.

equilibrium bubble can be found by using the Clausius-Clapeyron relation.

$$\frac{dP}{dT} = \frac{\Delta h_{fg}}{v_{fg}T} \quad (2.2)$$

The derivation of the Clausius-Clapeyron relation is provided in Appendix A. Representing Equation 2.2 in finite difference form and assuming that $v_v \gg v_l$:

$$P_v - P_l = (T_v - T_{sat}) \frac{\Delta h_{fg}}{T_{sat}} \rho_v. \quad (2.3)$$

Combining Equation 2.1 and Equation 2.3 results in Equation 2.4 which describes the relationship between the equilibrium bubble size and fluid properties.

$$D = \frac{4\sigma T_{sat}}{(T_v - T_{sat}) \Delta h_{fg} \rho_v} \quad (2.4)$$

This represents the required superheat needed to sustain bubble with a given diameter (D). A few things to note are:

1. a larger superheat allows for smaller diameter bubbles to exist.
2. a diameter smaller than this critical diameter at a given superheat will collapse.
3. a diameter bigger than the critical size will grow until a balance is obtained between the pressure and surface tension forces.

To demonstrate the larger superheats required for homogeneous boiling, consider the case of a 3.2 Angstrom diameter bubble (about the molecular spacing of water molecules), where the pool pressure is $14MPa$. This yields the following properties: $T_{sat} = 336^\circ C$, $\rho_v = 87.04kg/m^3$, $\Delta h_{fg} = 1,067.21kJ/kg$, $\sigma = 0.00644N/m$. The resulting superheat required for bubble formation is then:

$$(T_v - T_l) = \frac{4(0.00644Nm) 336^\circ C}{(3.2 \times 10^{-10}m)(1,067.21kJ/kg)(87.04kg/m^3)} = 290^\circ C. \quad (2.5)$$

This is a relatively high superheat as will be seen when compared to nucleation requirements at a surface. The focus of this work will consider only nucleation that takes place on surfaces since this is what is prevalent in typical heat transfer systems. Typically, the onset of nucleation on a surface occurs well before nucleation in a homogeneous fluid due to the required superheats of the latter.

2.2 Nucleation at Surfaces

When nucleation takes place at surface the superheat temperatures required are not as great when compared to the homogeneous boiling case. This is due to pockets of vapor being trapped in cavities with diameters on the order micrometers. Figure 2.2 represents a general case for bubble growth at a surface nucleation site. The thermal boundary is represented by δ and varies from the wall temperature to the bulk fluid temperature. Figure 2.3 produced by Del Valle and Kenning [11] provides much insight on the effect of heat flux, up to 90% of the CHF point ($4.92 MW/m^2$), on key bubble parameters observed with a high speed camera at a frame rate of $104 fps$. The following major conclusions can be drawn from Figure 2.3:

- Maximum bubble diameter (D_m) is independent of heat flux.
- Nucleation site density (n) linearly increases with increasing heat flux.
- Nucleation site spacing (s) linearly decreases with increasing heat flux.
- Bubble life time (t_L) is nearly independent with heat flux with a slight decrease in lifetime with increasing heat flux.
- The waiting period (t_w) for the next nucleation event drastically drops as the CHF point is reached.

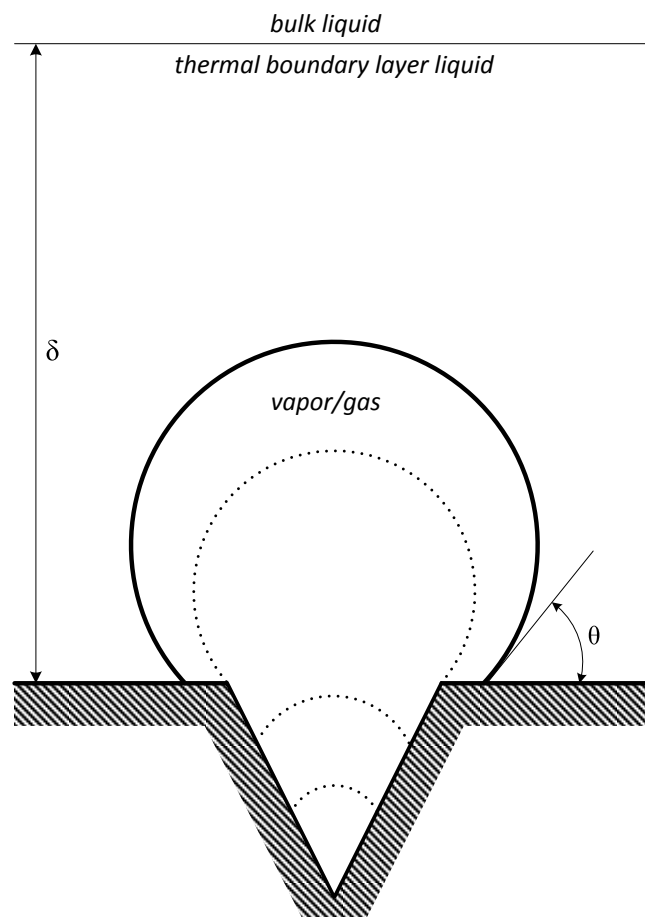


Figure 2.2: Surface nucleation site.

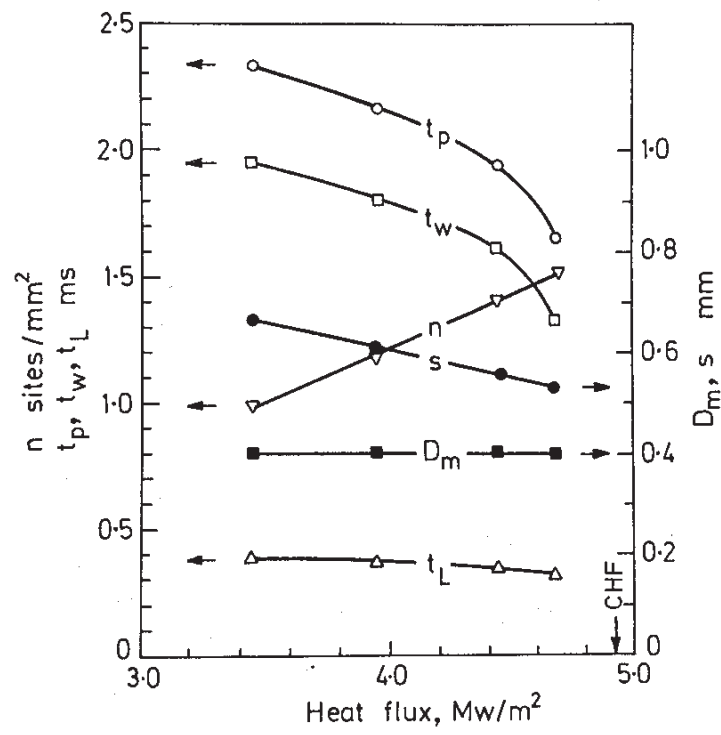


Figure 2.3: Bubble parameter variations with heat flux [11].

2.2.1 Cavity Activation Size

The superheat required to initiate nucleation can be determined by use of Equation 2.4 but it has been investigated by Hsu [21] who observed that the theoretical results do not agree with experimental data. It was concluded that Equation 2.4 is not valid when only the heated surface is hot and that the thermal boundary layer has a contributing effect on the critical bubble size. He concluded that since the bubble is at the equilibrium bubble pressure, resulting in a higher temperature than the exterior liquid, the bubble would have to be surrounded by a warmer superheated liquid layer relative the bubble interior temperature. If the bubble were not surrounded by a superheated liquid, collapse of the bubble would occur due to heat removal from the bubble (condensation at the bubble interface).

Based on this, Hsu [21] developed the maximum bubble size allowed using the criterion that the bubble vapor temperature must be less than or equal to the superheated liquid layer near the wall. This was determined by using a linear temperature profile from the heated wall out to the bulk liquid temperature through the thermal boundary layer thickness (δ). This requires knowing the bubble height (H_b) to determine how far into the thermal layer the bubble has protruded. Figure 2.4 depicts the height of a cap bubble in contact with the heated surface. The height of the bubble is found from the addition of H' and the bubble radius (r_b):

$$H_b = r_b + H'. \quad (2.6)$$

Using the following geometric relations,

$$a = r_b \sin(\theta) \quad (2.7)$$

$$H' = r_b \cos(\theta) \quad (2.8)$$

and substituting Equation 2.8 into Equation 2.6 and using Equation 2.7, an expression for the bubble height based on the cavity radius and contact angle can be expressed by

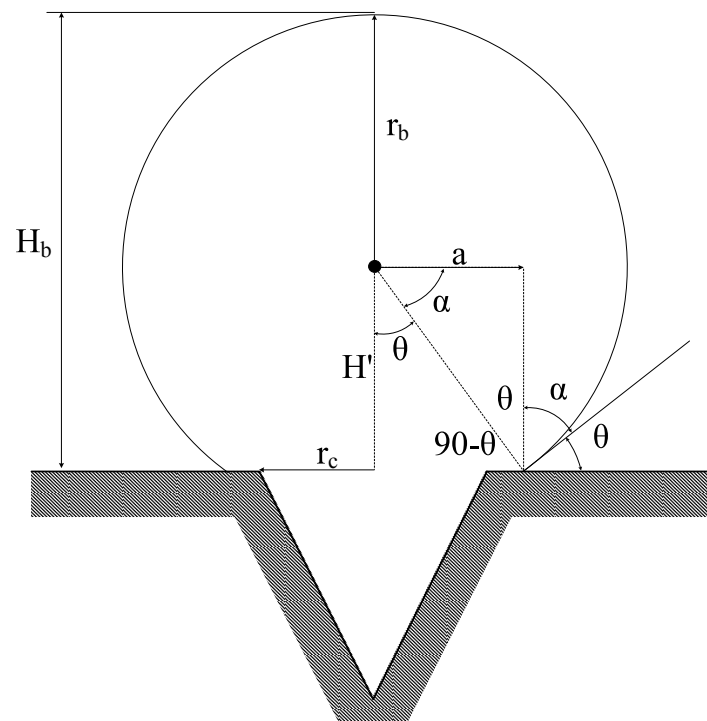


Figure 2.4: Bubble height attached to a heated surface.

Equation 2.9.

$$H_b = (1 + \cos(\theta)) \frac{a}{\sin(\theta)} \quad (2.9)$$

The bubble temperature in terms of the cavity radius and contact angle can be determined by inserting Equation 2.7 into Equation 2.4,

$$T_v = T_{sat} + \frac{2\sigma T_{sat} \sin(\theta)}{a\Delta h_{fg}\rho_v}. \quad (2.10)$$

The bubble will grow as long as the temperature at the bubble cap ($y = H_b$) is less than the boundary layer temperature at a distance y from the heated wall. The temperature in the boundary layer is often assumed linear with the following temperature profile varying from 1 at the wall to 0 at $y = \delta$,

$$\frac{T_y - T_\infty}{T_w - T_\infty} = \frac{\delta - y}{\delta} \quad (2.11)$$

Setting the boundary layer temperature (T_y) at a position $y = H_b$ equal to the bubble temperature (T_b) allows for the finding of the maximum bubble size when solved with Equation 2.10.

$$\frac{T_v - T_\infty}{T_w - T_\infty} = \frac{\delta - H_b}{\delta} \quad (2.12)$$

Or in terms of bubble radius and contact angle this becomes:

$$\frac{T_v - T_\infty}{T_w - T_\infty} = \frac{\delta - (1 + \cos \theta) a \sin^{-1} \theta}{\delta} \quad (2.13)$$

A set of solutions are plotted in Figure 2.5 for Equation 2.10 and Equation 2.13 for a pressure of 14 MPa, a wall temperature of 337°C, thermal boundary layer thickness of 1 micron, a contact angle of 50°, and for bulk fluid temperatures of 2°C, 4°C, and 6°C subcooled. As can be seen from Figure 2.5 by the intersections of the bubble and boundary layer temperatures, there exists a region of possible bubble sizes. The region to the left of the boundary layer temperature curve represents those bubble sizes which are possible. The smaller bubble sizes are limited due to the required superheat needed to

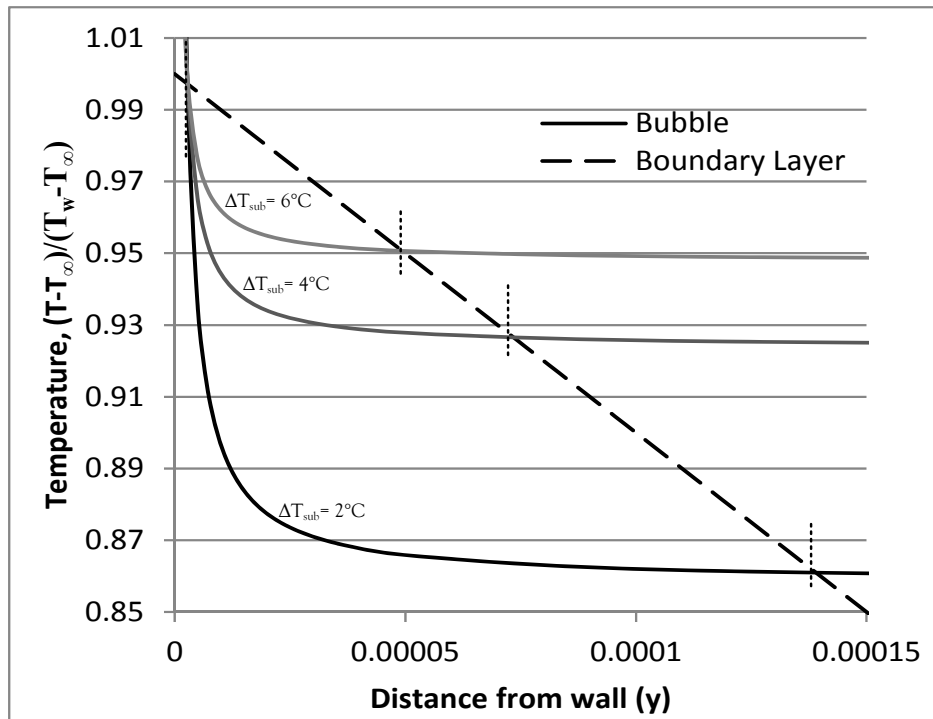


Figure 2.5: Possible bubble sizes for a specified wall and saturation temperature at various bulk fluid subcooled temperatures.

support such a small bubble size. The larger bubbles are limited due to the temperature in the boundary layer dropping below that of the local bubble temperature. An interesting thing to note from this curve is the effect of the bulk fluid subcooling. The effect of higher subcooling values is to create bubbles with smaller diameters. This is due to the suppression of the boundary layer. The critical cavity radius was analytically solved by Hsu and Graham [13] in Equation 2.14 with the use of Equation 2.10 and Equation 2.13. Equation 2.14 provides the minimum and maximum possible bubble sizes that can be supported within a thermal boundary layer.

$$r_c = \frac{\delta (T_w - T_{sat})}{2 (T_w - T_\infty)} \frac{\sin(\theta)}{1 + \cos(\theta)} \left[1 \pm \sqrt{1 - 8(1 + \cos \theta) \frac{(T_w - T_\infty) T_{sat} \sigma}{(T_w - T_\infty)^2 \delta \rho_v \Delta h_{fg}}} \right] \quad (2.14)$$

The boundary layer thickness (δ) was used as a calibration parameter by Hsu and Graham [13]. It was estimated at one set of conditions and assumed to be constant at a given channel velocity.

2.2.2 Nucleation Site Density

Zuber [22] notes that at low heat fluxes an increase in heat flux results in the increase of the nucleation site density. This is consistent to the conclusions drawn by Figure 2.3. Whereas at high heat fluxes, an increase in the heat flux results in an increase in the bubble frequency and not an increase in the nucleation site density. This is consistent in terms of the boiling frequency increasing as demonstrated by a decrease in the waiting time with increasing heat flux by Figure 2.3. This however is not consistent with Figure 2.3 which shows the nucleation site density always linear increases no matter the magnitude of the heat flux. When attempting to partition the energy removed from boiling versus from other modes of heat removal it is essential to understand the fractional effective boiling area which can be calculated by knowing the nucleation site density.

The nucleation site density was thoroughly studied by Del Valle and Kenning [11] through a sudden depressurization of a system with a surfaces immersed in water satu-

rated with nitrogen. As can be seen from Figure 2.6, a decrease in the effective cavity size results in an increase in the nucleation site density. This is due the fact that smaller bubbles have a smaller area of influence imparting less turbulent forces locally which work to deactivate neighboring nucleation sites; this is discussed in more detail in Section 2.4. The surface thickness (δ) is observed to have a minimal effect on the nucleation site density.

Listed here are a subset of nucleation site density correlations that have been developed by various researchers. As will be seen later this will be a crucial closure relation for the proposed CHF correlation.

Gaertner and Westwater [23] developed a relation for nucleation site density as a function of wall heat flux as:

$$Na \sim q''^{2.1}. \quad (2.15)$$

Mikic and Rohsenow [24] developed a relation of nucleation site density to active cavity sizes and available cavity sizes of commercial surfaces:

$$Na \sim \left(\frac{D_s}{D_c}\right)^m$$

$$m = 6.5 \text{ (empirical constant)}$$

$$D_s = \text{cavity size available on surface} \quad (2.16)$$

$$D_c = \text{active cavity size}$$

where the active cavity size is expressed by the Clausius-Clapeyron relation:

$$D_c = \frac{4\sigma T_{sat}}{\rho_v \Delta h_{fg} \Delta T_w}. \quad (2.17)$$

Cornwell and Brown [25] developed a relation on nucleation site density to the wall superheat:

$$Na \sim \Delta T_w^{4.5} \quad (2.18)$$

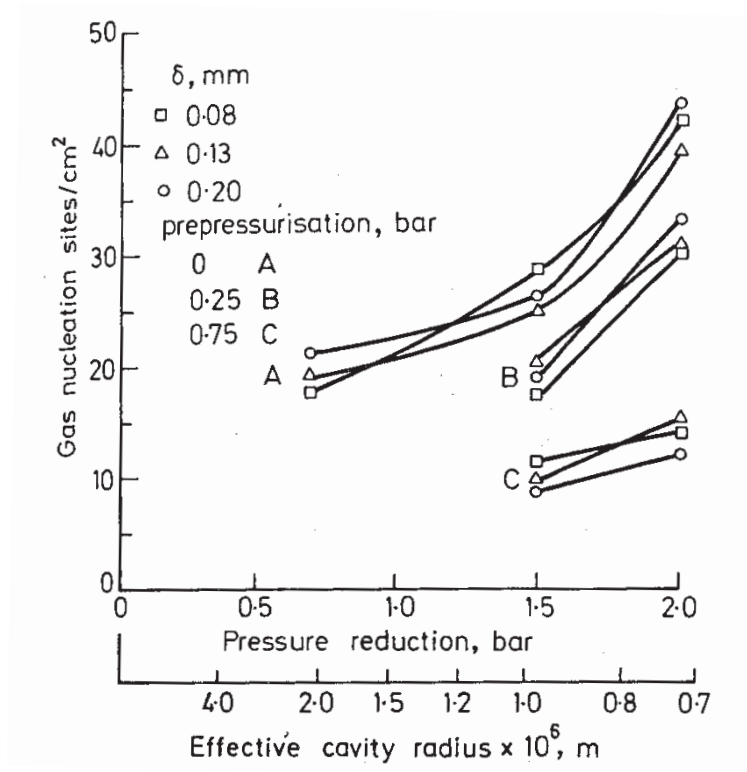


Figure 2.6: Nucleation site density dependence on cavity size [11].

Kocamustafaogullari and Ishii [26] developed an analytical relation for the nucleation site density for flow boiling as a function of pressure (through the use of a non-dimensional density difference (ρ^*)) and a critical radius (R_c). This is presented in Equation 2.19. Also, instead of using the standard definition of wall superheat (ΔT_w) [26] recommends the use of an effective wall superheat (ΔT_e). The effect is to relate the dependence of the boundary layer thickness to the bulk mass flow rate. The boundary layer thickness effects the temperature gradient near the wall and thus the bubble temperature. The effective wall superheat is defined with the use of the Suppression factor as defined by Chen. The same approach of applying the effect wall superheat will be used in the proposed CHF model of this work.

$$\begin{aligned}
 N_a^* &= f(\rho^*) R_c^{*m} \\
 m &= -4.4 \\
 N_a^* &= N_a D_d^2 \\
 R_c^* &= \frac{2r_c}{D_d} \\
 \rho^* &= \frac{\Delta\rho_{fg}}{\rho_v} = \frac{\rho_l - \rho_v}{\rho_v} \\
 r_c &= \frac{2\sigma T_{sat}}{\rho_v \Delta h_{fg} \Delta T_e} \\
 D_d &= 0.0012 D_{dF} \left(\frac{\Delta\rho}{\rho_v} \right)^{0.9} \\
 f(\rho^*) &= 2.157 \times 10^{-7} (\rho^*)^{-3.12} (1 + 0.0049 \rho^*)^{4.13}
 \end{aligned} \tag{2.19}$$

where D_{dF} is the Fritz diameter,

$$D_{dF} = 0.208\theta \sqrt{\frac{\sigma}{g(\rho_l - \rho_v)}}. \tag{2.20}$$

It was recommended by [26] that instead of the simplified approximate relation of the critical bubble size (as defined by Equation 2.4) that a more exact solution for the critical bubble radius be used utilizing the ideal gas law as shown by Equation 2.21 and derived

in Appendix A.

$$r_c = \frac{2\sigma}{\rho_l} \left(1 + \frac{\rho_v}{\rho_l} \right) \frac{1}{\exp \left[\frac{(T_v - T_{sat})\Delta h_{fg}}{RT_v T_{sat}} \right] - 1} \quad (2.21)$$

Caution was expressed by the authors with the use of the simplified equation for the critical radius that is prevalent in literature due to errors at extreme pressures. This is noted as an area of improvement for the proposed model since the traditional simplified form is used.

Wang and Dhir [27] developed a relation of nucleation site density to wall heat flux with the use of a prepared copper surfaces controlling the oxidation levels of the surface. The actually cavity (D_c) size was corrected by a factor, $f_d = 0.89$, for surfaces with contact angle of $18^\circ < \theta < 90^\circ$ for cavities less than $5.8 \mu m$ they propose Equation 2.22.

$$\begin{aligned} Na \left[sites/cm^2 \right] &= 5.0 \times 10^5 (1 - \cos\theta) f_d D_c^{-6.0} \\ D_c \left[\mu m \right] &= \frac{4\sigma T_{sat}}{\rho_v \Delta h_{fg} \Delta T_w} \\ f_d &= 0.89 \end{aligned} \quad (2.22)$$

For cavities greater than $5.8 \mu m$ they propose Equation 2.23.

$$Na \left[sites/cm^2 \right] = 9.0 \times 10^3 f_d D_c^{-2.0} \quad (2.23)$$

The nucleation site density as a function of wall superheat was fit by Basu [12] based on experimental data. Most data was correlated to within $\pm 40\%$ as shown by Figure 2.7. The correlation that describes Figure 2.7 is given by Equation 2.24. This relation is used in the current proposed CHF model due to its simplicity to incorporate and the ability to

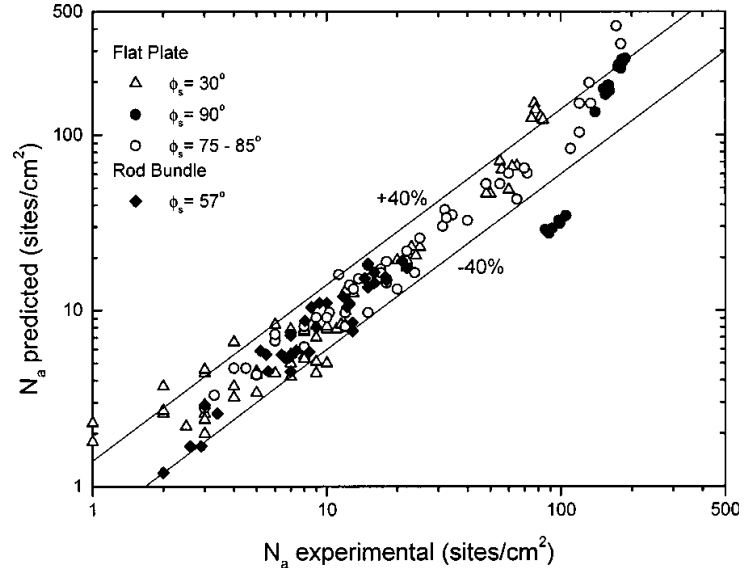


Figure 2.7: Nucleation site density correlation comparison to experimental data from Basu [12].

capture both the contact angle and wall superheat.

$$\begin{aligned}
 N_a &= 0.34 (1 - \cos(\theta_s)) \Delta T_w^{2.0}, & \Delta T_w < 15^\circ \\
 N_a &= 3.4 \times 10^{-5} (1 - \cos(\theta_s)) \Delta T_w^{5.3}, & \Delta T_w \geq 15^\circ
 \end{aligned}$$

where,

$$N_a = \text{nucleation site density [sites/cm}^2\text{]}$$

$$\theta_s = \text{static contact angle [degrees]}$$

$$\Delta T_w = \text{wall superheat temperature [}^\circ\text{C]}$$

(2.24)

2.2.2.1 Nucleation Site Density by Hibiki and Ishii [28]

Hibiki and Ishii [28] developed a relation for nucleation site density derived primarily from the works of Yang and Kim [29]. A major addition to the newly developed model was the inclusion of pressure effects (through the use of a non-dimensional density difference (ρ^*)) similar to that of [26].

$$\begin{aligned}
 Na &= \overline{Na} \left[1 - \exp\left(-\frac{\theta^2}{8\mu'^2}\right) \right] \left[\exp\left(f(\rho^+) \frac{\lambda}{r_c}\right) - 1 \right] \\
 \overline{Na} &= 4.72 \times 10^5 \frac{\text{sites}}{\text{m}^2} \\
 \mu' &= 0.722 \text{ radians} \\
 \lambda &= 2.50 \times 10^{-6} \text{ m} \\
 f(\rho^+) &= -0.01064 + 0.48246\rho^+ - 0.22712\rho^{+2} + 0.05468\rho^{+3} \\
 \rho^+ &= \log \rho^* \\
 \rho^* &= \frac{\rho_l - \rho_v}{\rho_v} \\
 r_c &= \frac{2\sigma(1 + \rho_v/\rho_l)/P_f}{\exp[\Delta h_{fg}(T_v - T_{sat})(RT_v T_{sat})] - 1}
 \end{aligned} \tag{2.25}$$

2.2.3 Nucleation Waiting Period

The discussion of what is called the ebullition cycle begins here with the waiting period for a nucleation site to become active. The ebullition cycle involves the birth, growth, and possible collapse of the bubble from a nucleation site.

There exists a waiting period between the time of departure of one bubble to the onset of nucleation for the next bubble. During this time frame the thermal boundary layer that has been disturbed by the release of the previous bubble is being re-established back to the steady-state linear temperature profile as depicted in Figure 2.5.

As an estimate to the waiting period, Jakob [30] proposed that the bubble growth period was equal to the bubble waiting period. This results in a bubble frequency of

$$f = \frac{1}{t_w + t_d} \quad (2.26)$$

where t_w is the waiting time from bubble departure to the onset of nucleation and t_d is the time from onset of nucleation to bubble departure. This was found to be inaccurate and Hsu and Graham [21] proposed the following model where the following processes take place:

1. An active nucleation site with a radius of r_c that has produced a bubble has just departed from the heated surface.
2. At departure, the volume originally occupied by bubble is filled by relatively cooled liquid from the bulk region outside the thermal boundary layer.
3. The trapped vapor/gas in the cavity that remains after bubble departure serves as a nucleation site for the next bubble.
4. The heating of the liquid results in a temperature rise of the vapor at the nucleation site. However, the bubble will not be activated until the surrounding liquid is hotter than the bubble interior. This is represented by Equation 2.10.
5. The heating of the bulk liquid that has moved into the thermal boundary is approximated by transient conduction into a slab of thickness δ ,

$$\frac{\partial^2 T}{\partial y^2} = \frac{1}{\alpha} \frac{\partial T}{\partial t} \quad (2.27)$$

with boundary conditions,

$$\begin{aligned}
 T &= T_{\infty} \text{ at } t = 0 \\
 T &= T_w \text{ at } y = 0 \\
 T &= T_{\infty} \text{ at } y = \delta
 \end{aligned}
 \tag{2.28}$$

This assumes a constant wall temperature at $y = 0$ and a constant bulk temperature at $y = \delta$. The non-dimensional temperature to solution to Equation 2.27 and Equation 2.28 in series form is given by Hsu and Graham [13] as,

$$\xi = \frac{T - T_{\infty}}{T_w - T_{\infty}} = \frac{y}{\delta} + \frac{2}{\pi} \sum_{n=1}^{\infty} \frac{\cos(n\pi)}{n} \sin\left(n\pi \frac{y}{\delta}\right) \exp\left(-\frac{n^2 \pi^2 \alpha t}{\delta^2}\right)
 \tag{2.29}$$

6. The intersection of Equation 2.29 and the bubble superheat temperature given by Equation 2.10 gives a range cavity sizes at various wall temperatures for varying transient times in which nucleation is possible. This is shown in Figure 2.8 by Hsu and Graham [13] where $\xi(\eta, \tau)$ and $\xi_b(\eta_b, \tau)$ are the wall dimensionless temperature for an η distance from the wall for time τ and the bubble dimensionless superheat at a cavity size η_b and for time τ respectively.

As can be seen by Figure 2.8, a limiting case exists for the minimum bubble size for nucleate boiling similar to that presented by Figure 2.5. The equivalent of Figure 2.5 is obtained for the non-dimensional time τ approaching infinity.

Soon after Hsu and Graham [21] proposed their model for waiting time, Han and Griffith [31] in the same year presented a simplified solution to obtain an explicit form as expressed by Equation 2.30.

$$t_w = \frac{\delta^2}{\pi\alpha} = \frac{9}{4\pi\alpha} \left[\frac{(T_w - T_{\infty}) r_c}{T_w - T_{sat} \left(1 - 2\sigma / (r_c \rho_v \Delta h_{fg})\right)} \right]^2
 \tag{2.30}$$

Four years later Hatton and Hall [32] proposed model for the waiting time that included

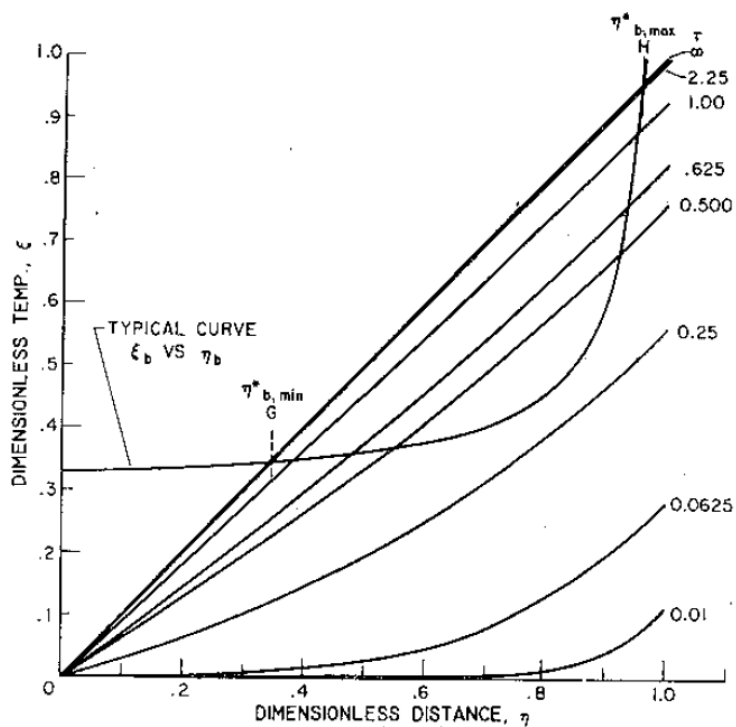


Figure 2.8: Transient temperature profile near a heated wall plotted with a typical bubble superheat as a function of size; taken from [13].

the heat capacity of the surface as shown in Equation 2.31.

$$t_w = \frac{\rho_w C_w \delta_w \delta_l}{k_l} \ln \left[1 - \frac{k_l (T_{sat} - T_\infty) + 2\sigma T_{sat} / (r_c \rho_v \Delta h_{fg})}{(H \delta_w \delta_l / k_l) [1 - (1 + \cos(\theta)) r_c / (\sin(\theta) \delta_l)]} \right]^{-1} \quad (2.31)$$

where C_w , ρ_w , and δ_w are the wall specific heat, density, and wall thickness.

2.2.4 Bubble Growth Rate

The following subsections describe the bubble growth rate and its dependence on the local conditions. The most general models include heat transfer through the bubble base and the bubble interface within the thermal boundary layer.

2.2.4.1 Griffith Bubble Growth Rate Model

The growth rate of a bubble at a heated surface was first approximated by Griffith [33] by assuming hemispherical bubble that was being provided energy through evaporation at the bubble interface from a superheated thermal boundary layer with a thickness δ . He gave an initial temperature profile similar to that of Hsu [21] (Equation 2.13):

$$T = (T_w - T_b) \left(1 - \frac{r}{\delta} \cos \phi \right) + T_b$$

$$T = T_v \text{ for } y = r \cos \phi > \delta \quad (2.32)$$

Here the angle ϕ is measured from the vertical axis from $0 - \pi/2$. With the temperature profile from Equation 2.32 the heat equation can be solved numerically with appropriate boundary conditions,

$$\frac{\partial T}{\partial t} + \bar{u} \cdot \nabla T = \frac{k_l}{\rho_l C_{p,l}} \nabla^2 T$$

$$\begin{aligned}
T &= T_{sat} \quad \text{at} \quad r = R \\
T &= T_w \quad \text{at} \quad \phi = \frac{\pi}{2}
\end{aligned} \tag{2.33}$$

Rewriting Equation 2.33 as Equation 2.34.

$$\rho_v \Delta h_{fg} \frac{dR}{dt} + k_l \int_0^{\pi/2} \left. \frac{\partial T}{\partial r} \right|_R \sin \phi d\phi = 0 \tag{2.34}$$

Here the left hand side of Equation 2.34 represents the vaporization energy for the evaporation of a mass of fluid encompassed by the bubble size change ($\frac{dR}{dt}$) and the right term represents the heat conducted through the bubble surface from the surrounding liquid to the bubble. Integrating Equation 2.34 yields the transient bubble size. The graphical solution to Equation 2.34 plotted with data experimental data from Ellion [34] showed good agreement.

Major conclusions from Griffith's work [33] are as follows:

1. The average bubble growth rate decreases with maximum bubble size.
2. The average bubble growth rate decreases with increasing system pressure.
3. The maximum bubble size at high pressure was found to be primarily dependent on the thermal layer thickness.

2.2.4.2 Zuber Bubble Growth Rate Model

Zuber's [35] bubble growth rate model approximates the bubble as being spherical and growing uniformly in a superheated liquid with a thermal layer thickness much like that of Equation 2.34 as presented by Equation 2.35 with the transient conduction term derived in Section 2.3.4. Here $\sqrt{\pi\alpha t}$ represents the thermal boundary layer thickness(δ).

$$\rho_v \Delta h_{fg} \frac{dR}{dt} = k_l \frac{T_w - T_{sat}}{\sqrt{\pi\alpha t}} \tag{2.35}$$

Zuber added a modification that includes a convective term, q''_{conv} , representing the heat flux from the surface to the bulk layer. After Zuber's modification Equation 2.35 then takes the form of Equation 2.36. This model assumes two parallel processes for heat transfer; latent heat transfer to the bubble and sensible heat transfer to the bulk layer.

$$\rho_v \Delta h_{fg} \frac{dR}{dt} = A' \left[k_l \frac{T_w - T_{sat}}{\sqrt{\pi \alpha t}} - q''_{conv} \right] \quad (2.36)$$

The term A' is a geometric correction that takes on a range 1.0 for a slab and $\sqrt{3}$ for a sphere. Integrating Equation 2.36 yields the transient bubble size. The maximum bubble size can be found by setting $\frac{dR}{dt} = 0$ at $t = t_m$, where t_m is the time of occurrence of the maximum bubble size. Zuber also proposed that $q''_{conv} = ct^n$ with c and n being empirical constants. He stated that if a bubble grows and then begins collapsing in a subcooled liquid, i.e. when $\frac{dR}{dt} = 0$ at $t = t_m$, and $R = 0$ at the end of collapse requires the following relationship between the bubble growth time and collapse time (t_c),

$$t_c = t_m [2(n+1)]^{2/[2n+1]} \quad (2.37)$$

It was then concluded that these are parameters of subcooling and data from Nishikawa et al. [36] agreed with this conclusion.

2.2.4.3 Hsu and Graham Bubble Growth Rate Model

Hsu and Graham [37] developed their model based on the assumption that the heat of evaporation for bubble growth is supplied from a bubble base and from the superheated thermal layer. This is represented by Equation 2.38.

$$A_{surf} \frac{dR}{dt} \Delta h_{fg} \rho_v = q''_{base} A_{base} + q''_{liq} A_{surf} \quad (2.38)$$

For a constant heat flux system q_{base} is equal to the wall heat flux. The heat flux from the superheat liquid is time dependent and in earlier stages is equivalent to Zuber's

expression from Equation 2.35 where

$$q''_{liq} = k_l \frac{T_w - T_{sat}}{\sqrt{\alpha \pi t}}. \quad (2.39)$$

However, in the later stages, heat transfer to the bubble can become negative when the thermal layer loses its heat and can become negative if the bubble grows beyond the thermal layer into the bulk. The base area (A_b) and the bubble-thermal layer contact area (A_s) are dependent on the bubble shape and contact angle. Small bubbles ($R < 0.1\text{cm}$) have been shown by experiment to be approximated by a hemisphere and large bubbles ($R > 0.1\text{cm}$) a truncated sphere with a contact angle equal 75° . This results in the following area fractions for large and small bubbles are expressed by Equation 2.40.

$$\begin{aligned} A_{base}/A_s &= 0.25 \quad \text{for } R > 0.1 \text{ cm} \\ A_{base}/A_s &= 0.50 \quad \text{for } R < 0.1 \text{ cm} \end{aligned} \quad (2.40)$$

This results in two separate equations as shown by Equation 2.41.

for $R < R^* \approx 0.1 \text{ cm}$

$$R - b = \frac{C}{\rho_v \Delta h_{fg}} \left\{ \begin{aligned} &\left(\frac{0.5q_{base}}{C} - \frac{k_l(T_w - T_{sat})}{\delta} \right) t \\ &+ 2 \left(q_{base} - \frac{k_l(T_w - T_{sat})}{\delta} \right) \frac{\delta^2}{\alpha \pi^2} \left[\frac{\pi^2}{6} - \sum_{n=1}^{\infty} \frac{\exp\left(-\frac{\alpha n^2 t}{\delta^2}\right)}{n^2} \right] \end{aligned} \right\} \quad (2.41)$$

for $R > R^* \approx 0.1 \text{ cm}$

$$R - R^* = \frac{C}{\rho_v \Delta h_{fg}} \left\{ \begin{aligned} &\left(\frac{0.25q_{base}}{C} - \frac{k_l(T_w - T_{sat})}{\delta} \right) (t - t^*) \\ &+ 2 \left(q_{base} - \frac{k_l(T_w - T_{sat})}{\delta} \right) \frac{\delta^2}{\alpha \pi^2} \sum_{n=1}^{\infty} \frac{1}{n^2} \left[\begin{aligned} &\exp\left(-\frac{\alpha \pi^2 n^2 t^*}{\delta^2}\right) \\ &- \exp\left(-\frac{\alpha \pi^2 n^2 t}{\delta^2}\right) \end{aligned} \right] \end{aligned} \right\}$$

Here δ represents the limiting thermal boundary thickness, t^* is the time that the bubble radius reaches R^* , and C is constant to account for geometry with $C = 1$ for flat surface

and $C = \pi/2$ for a spherical surface.

Hsu and Graham neglect the hydrodynamic effect here which is valid in earlier bubble growth stages. In later stages however buoyancy and inertial effects may play a role and bubble deformation may occur and a simplified bubble geometry may no longer be valid.

2.2.4.4 Han and Griffith Bubble Growth Rate Model

Han and Griffith [31] provide the most general form for the bubble growth rate at a heated surface for an initially non-uniform superheated liquid where the effects of contact angle, waiting period, surface temperature, and sub-cooling are all considered as summarized by Hsu and Graham [13].

$$\begin{aligned} \phi_v \Delta h_{fg} \rho_v \left(4\pi R^2 \frac{dR}{dt} \right) &= \phi_c \phi_s \left(4\pi R^2 \right) k_l C_{p,l} \rho_l \left. \frac{d(T - T_{sat})}{dx} \right|_{x=0} \\ &+ \phi_{base} \left(4\pi R^2 \right) \tilde{h}_v (T_w - T_{sat}) \end{aligned} \quad (2.42)$$

where,

$$\begin{aligned} \phi_c &= \text{curvature factor to account for 3D geometry, } 1 < \phi_c < \sqrt{3} \\ \phi_s &= \text{surface factor} = \frac{1 + \cos \theta}{2} \\ \phi_{base} &= \text{base factor} = \frac{\sin^2 \theta}{4} \\ \phi_v &= \text{volume factor} = \frac{1}{4} \left[2 + \cos \theta \left(2 + \sin^2 \theta \right) \right] \\ \theta &= \text{contact angle} \\ \tilde{h}_v &= \text{heat transfer coefficient from heating surface vapor} \\ \left. \frac{d(T - T_{sat})}{dx} \right|_{x=0} &= \frac{(T_w - T_{sat})}{\sqrt{\pi \alpha t}} - \frac{(T_w - T_\infty)}{\delta} \operatorname{erf} \left(\frac{\delta}{\sqrt{\pi \alpha t}} \right) \\ \delta &= \sqrt{\pi \alpha t_w} \\ t_w &= \text{waiting period} \end{aligned} \quad (2.43)$$

2.2.5 Bubble Departure Size

To determine the bubble size at departure from a heated surface one must consider the following forces:

- surface forces,
- buoyancy forces,
- liquid inertia from bubble growth,
- viscous forces,
- liquid convective forces around the bubble, and
- evaporative force.

For a horizontal surface Fritz [38] proposed a simple balance of buoyancy and surface tension forces for hydrogen and water vapor in water:

$$D_d = 0.0208\theta \sqrt{\frac{2\sigma}{g(\rho_l - \rho_v)}} \quad (2.44)$$

where θ is the contact angle in degrees. The Fritz diameter (D_d) is used by many to provide a closure to various models.

Staniszewski [39] performed studies of bubble departure size for water and alcohol for various pressures and proposed a modified form of Equation 2.44 to include the bubble growth rate:

$$D_d = 0.0071\theta \sqrt{\frac{2\sigma}{g(\rho_l - \rho_v)}} \left(1 + 0.435 \frac{dD}{dt} [\text{inches/sec}] \right). \quad (2.45)$$

He found that the diameter is linearly proportional to the bubble growth rate in the later stages of bubble growth. His form reduces to Fritz's as the bubble reaches the maximum

size where the growth rate approaches zero. Cole and Shulman [40] proposed a similar form to Staniszewski based on six fluids:

$$D_d = 0.0208\theta \sqrt{\frac{2\sigma}{g(\rho_l - \rho_v)}} \left(1 + 0.0025 \left(\frac{dD}{dt} [\text{mm/sec}] \right)^{3/2} \right). \quad (2.46)$$

Semeria [41] and Nishikawa [42] each proposed similar empirical expressions to describe the bubble departure radius. Their expressions are shown in Equation 2.47 and Equation 2.48 and plotted in Figure 2.9.

$$r_d = 0.242P^{-0.5}$$

$$r_d = \text{departure diameter [inches]} \quad (2.47)$$

$$P = \text{pressure [psia]}$$

$$r_d = 0.672P^{-0.575}$$

$$r_d = \text{departure diameter [inches]} \quad (2.48)$$

$$P = \text{pressure [psia]}$$

Bubble size generally increases with a decrease in subcooling and pressure as has been consistently observed by many researchers.

2.2.6 Bubble Departure Frequency

Bubble departure from a surface will occur after a departure time, t_d . Following departure of a bubble, the bulk liquid will rush in to come into contact with the surface. At which time a contact time or waiting period, t_w , is required for nucleation to begin. Thus the frequency of the bubble cycle can be generally characterized by Equation 2.26.

Departure frequency increases for increasing heat fluxes due to the reduction in both the

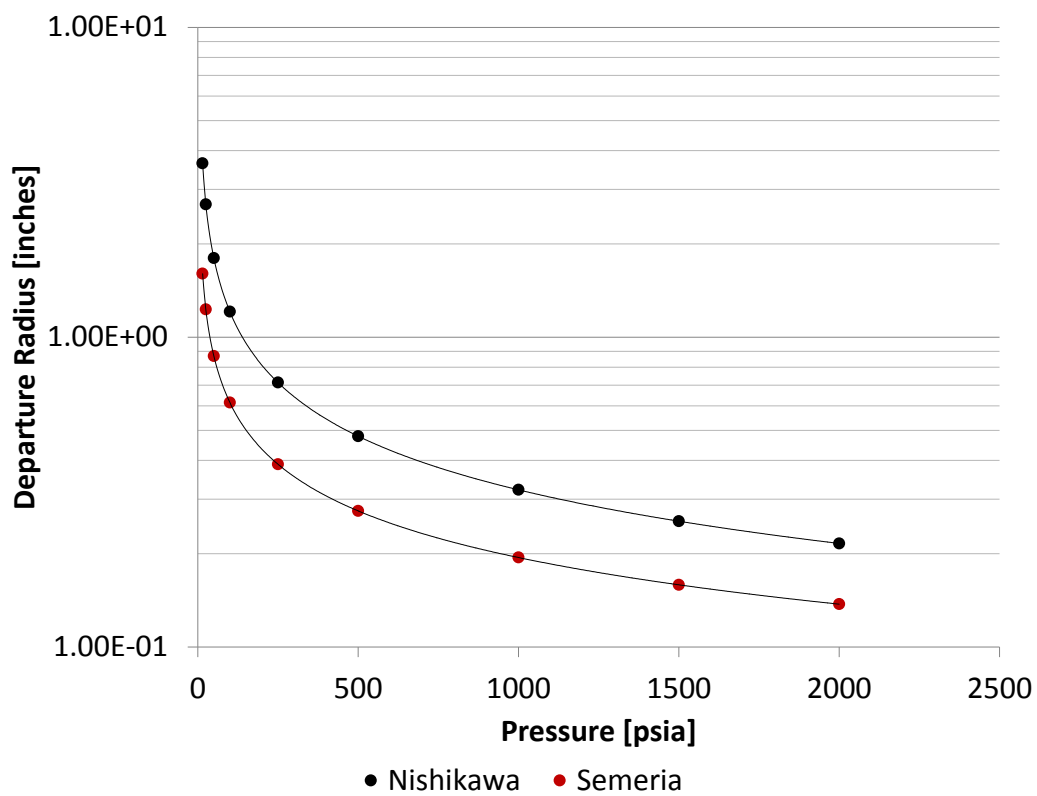


Figure 2.9: Bubble departure radius by Semeria and Nishikawa.

waiting time and departure time as shown by Figure 2.3. At high heat fluxes the bubble grows rapidly and the high evaporative forces help detach the bubble from the surface, reducing the departure time, and causing the bubble radius at departure to be smaller. An increase in pressure reduces the bubble size since at higher pressures the saturation temperature increases resulting in a higher needed wall superheat and a lower surface tension.

2.2.7 Bubble Departure Velocity

Peebles [43] observed the bubble rise velocity in a gravitational field as:

$$v_b = 1.18 \left[\frac{\sigma g (\rho_L - \rho_v)}{\rho_L^2} \right]^{1/4} \quad (2.49)$$

Jakob and Linke [44] observed that the bubble rise velocity could be represented by the following:

$$v_b = D_d f_d \frac{t_w + t_d}{t_d} \quad (2.50)$$

Using Equation 2.49 and Equation 2.50 and assuming the waiting time (t_w) is equal to the departure time (t_d):

$$D_d f_d = \frac{1.18}{2} \left[\frac{\sigma g (\rho_L - \rho_v)}{\rho_L^2} \right]^{1/4} \quad (2.51)$$

Hsu and Graham [37] point out that the waiting time and departure time are not necessarily equal for all heat fluxes.

2.3 Heat Transfer Modes

Before discussing the partitioning mechanisms of the total heat flux the various modes of heat transfer first need to be understood. This will provide insight into the classification of the partitioned mechanisms. There are two basic fundamental modes for heat transfer.

The first is that by the transfer of sensible heat and the second by latent heat. These two modes make up the total heat transfer from the heated surface:

$$q''_{total} = q''_{sensible} + q''_{latent}. \quad (2.52)$$

The sensible heat can be described by four mechanisms: macro- convective heat transfer, bubble agitation, vapor-liquid exchange, and transient conduction as shown in Equation 2.53.

$$q''_{sensible} = q''_{macro-conv} + q''_{agitation} + q''_{exchange} + q''_{trans} \quad (2.53)$$

The latent heat transfer mechanisms consists of evaporation at the curved bubble interface and evaporation in the bubble micro-layer residing between the heated wall and the lower bubble surface described by Equation 2.54.

$$q''_{latent} = q''_{curved} + q''_{micro} \quad (2.54)$$

An investigation of the magnitude of the various mechanisms postulated for the total heat transfer was performed by Graham and Hendricks [45]. Their conclusion is that no one mechanism contributes dominantly to the total heat flux in the general nucleate boiling process for heat fluxes below 20% of the critical value. Above 20% of the critical heat flux value however it is expressed that the evaporation is the chief mechanism. This is a key point for the model developed by this work.

A comprehensive review on the mechanisms are provided by [45] and summarized here.

2.3.1 Macro-Convective Heat Transfer

The macro convective heat transfer mechanism describes the heat transfer due to the single phase turbulent motion of the bulk flow (often expressed as a function of Reynolds number). This mode is typically modeled by the Dittus-Boelter relation as presented by

Equation 2.55.

$$h_{mac} = 0.023\text{Re}^{0.8}\text{Pr}^{0.4} \left(\frac{k_l}{D} \right) \quad (2.55)$$

2.3.2 Bubble Agitation

The bubble agitation mechanism is used to describe the heat transfer enhancement due to the added micro-convective turbulent forces from the bubble motion and departure from the surface as studied by Hsu and Graham [37] and Gaertner and Westwater [23]. The effect of bubble agitation has been observed to influence distances as far as twice the bubble radius. This area has been termed the surrounding area of influence and is described in Section 2.4.3.

Doubts are raised however on the magnitude of this mechanism due to the required local agitation velocities required to dominate any evaporative process that occurs.

2.3.3 Vapor-liquid Exchange

The Vapor-liquid exchange mechanism proposed by Forster and Greif [46] has a similar effect to that of the random motion of the bubble agitation mechanism. The difference is that the vapor-liquid exchange mechanism attributes the enhancement of the near surface heat transfer to the organized pumping action of hot fluid away from the surface which is replaced by cooler bulk fluid. However, rather than relating the enhancement to the added micro-turbulence forces, it is related to the heat carrying capacity of the slug that is pumped away from the surface. The importance of this mechanism is typically characterized by the Jakob number. The Jakob number (Ja) is the ratio of the sensible heat removal by liquid to latent heat removal of a bubble of the same volume.

$$Ja = \frac{m_L C_{p,l} (T_w - T_b)}{m_v h_{f_g}} = \frac{C_{p,l} \rho_L (T_w - T_b)}{\rho_g h_{f_g}} \quad (2.56)$$

Questions have been raised as to the quantification and magnitude of the departing vapor and the incoming liquid slug mass and energy and the assumed temperature of the incoming liquid slug; however, it has been demonstrated that the process is physical and does a play a role in the boiling process.

2.3.4 Transient Heat Conduction

The transient heat conduction mechanism is identical to that of transient conduction studied in solids. When a vapor bubble is removed from a surface it is replaced by cooler single-phase liquid. Once this liquid is in contact with the superheated surface sensible heat is conducted away from the surface until the ebullition cycle of the bubble begins again.

The semi-infinite transient heat conduction equation is solved to determine the heat transfer after bubble release/collapse when bulk liquid from the mainstream fills volume once occupied by the bubble. Starting with the one-dimensional heat equation with appropriate boundary conditions:

$$\begin{aligned} \frac{1}{\alpha} \frac{\partial T}{\partial t} &= \frac{d^2 T}{dy^2} \\ T(y, t = 0) &= T_i \\ T(y = \infty, t) &= T_i \\ T(y = 0, t = 0) &= T_w. \end{aligned} \tag{2.57}$$

Using a similarity variable (η) with appropriate derivatives:

$$\begin{aligned}
 T &= T(\eta) \\
 \eta &= \frac{y}{\sqrt{4\alpha t}} \\
 \frac{dT}{dt} &= \frac{d\eta}{dt} \frac{dT}{d\eta} = -\frac{y}{2t\sqrt{4\alpha t}} \frac{dT}{d\eta} \\
 \frac{dT}{dy} &= \frac{d\eta}{dy} \frac{dT}{d\eta} = \frac{1}{\sqrt{4\alpha t}} \frac{dT}{d\eta} \\
 \frac{d^2T}{dy^2} &= \frac{d\eta}{dy} \frac{d^2T}{d\eta^2} = \frac{1}{4\alpha t} \frac{d^2T}{d\eta^2} \\
 \frac{d^2\eta}{dy^2} &= 0.
 \end{aligned} \tag{2.58}$$

Rewriting Equation 2.57 in terms of the similarity variable (η):

$$\frac{1}{\alpha} \frac{\partial T}{\partial \eta} \frac{\partial \eta}{\partial t} = \left(\frac{\partial \eta}{\partial y} \right)^2 \frac{\partial^2 T}{\partial \eta^2}. \tag{2.59}$$

The following equation is solved with the newly transformed boundary conditions:

$$\frac{dT}{d\eta} = -2\eta \frac{\partial^2 T}{\partial \eta^2} \tag{2.60}$$

$$T(\eta = 0) = T_w \tag{2.61}$$

$$T(\eta = \infty) = T_i.$$

The general solution to the second order equation is:

$$\frac{T - T_w}{T_i - T_w} = \frac{2}{\sqrt{\pi}} \int_0^\eta e^{-u^2} du = 1 - \operatorname{erfc}(\eta). \tag{2.62}$$

Of interest though is the transient heat flux at the wall. This is described by Equation 2.63 with $y = 0$ ($\eta = 0$).

$$q'' = -k \left. \frac{dT}{dy} \right|_{y=0} = -k \left. \frac{d\eta}{dy} \frac{dT}{d\eta} \right|_{\eta=0} = \frac{k}{\sqrt{4\alpha t}} \frac{2(T_i - T_w)}{\sqrt{\pi}} e^{-\eta^2} \Big|_{\eta=0} \tag{2.63}$$

$$q'' = \frac{k(T_i - T_w)}{\sqrt{\pi\alpha t}} \quad (2.64)$$

This form is used to determine the heat flux during the transient conduction (quenching) phase and is expressed by Equation 2.65.

$$q'' = \frac{k(T_i - T_w)}{\sqrt{\pi\alpha t_{qnch}}} = \frac{k(\Delta T_{sat} - \Delta T_{sub})}{\sqrt{\pi\alpha t_{qnch}}}. \quad (2.65)$$

2.3.5 Microlayer Evaporation

The microlayer evaporation mechanism attributes the enhancement in boiling heat transfer to the evaporation of the microlayer. This region resides between the heated wall and the underside of a growing bubble.

DelValle and Kenning [11] approximated the time dependent growth of a bubble from their experimental data as:

$$R = 4R_m \left(\frac{t}{t_L} \right) \left(1 - \frac{t}{t_L} \right). \quad (2.66)$$

From the analysis of Cooper [47] the initial microlayer thickness is taken be:

$$\delta_o = 0.8 (\nu_l t_o)^{1/2}. \quad (2.67)$$

Here the microlayer is initially at the wall temperature and the bubble interface is at the saturation temperature. The heat transfer from the wall is thus approximated as

$$q'' = -k_l (\Delta T_w) / \delta_{micro}. \quad (2.68)$$

Performing an energy balance on an arbitrary block of fluid, as represented by Figure 2.10, that rests on a heated wall with heat flux q'' one can obtain the rate of change of the microlayer thickness. The rate of change of the microlayer thickness is derived

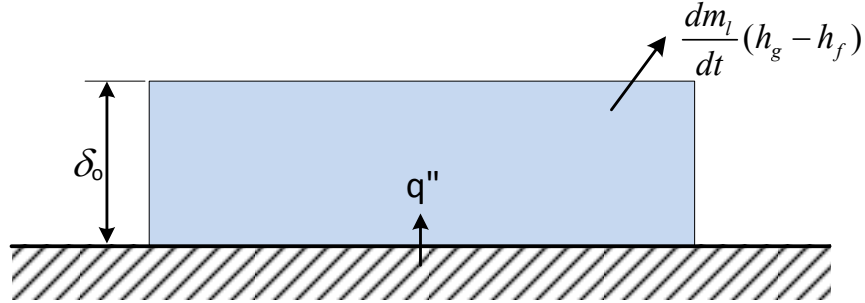


Figure 2.10: Microlayer energy balance.

with the use of Equation 2.69.

$$-k_l(\Delta T_w)A/\delta_{micro} = \frac{dm_l}{dt}(\Delta h_{fg}) \quad (2.69)$$

Here A is the bubble base area. Noting that dm_l/dt can be expressed as $\rho_l A d\delta_{micro}/dt$ the rate of change of the microlayer thickness is expressed as

$$\frac{d\delta_{micro}}{dt} = \frac{-k_l(\Delta T_w)}{\rho_l(\Delta h_{fg})\delta_{micro}} \quad (2.70)$$

The microlayer thickness can then be solved as a function of time,

$$\int_0^t \delta_{micro} d\delta_{micro} = \int_0^t \frac{-k_l(\Delta T_w)}{\rho_l(\Delta h_{fg})} dt \quad (2.71)$$

$$\delta_{micro} = \sqrt{\delta_o^2 - \frac{2k_l(\Delta T_w)}{\rho_l(\Delta h_{fg})}t} \quad (2.72)$$

The time to the microlayer evaporation can be found by setting $\delta_{micro} = 0$ and solving

for t resulting in Equation 2.73.

$$t_{evap} = \frac{\delta_o^2 \rho_l (\Delta h_{fg})}{2k_l (\Delta T_w)} \quad (2.73)$$

Equation 2.68 and Equation 2.72 are used to calculate the microlayer evaporation heat flux over the time interval of $0 < t < t_{evap}$:

$$q'' = \frac{-k_l (\Delta T_w)}{\sqrt{\delta_o^2 - \frac{2k_l (\Delta T_w)}{\rho_l (\Delta h_{fg})} t}} \quad (2.74)$$

2.4 Heat Flux Partitioning for Pool Boiling by Del Valle and Kenning

The total wall heat flux is partitioned into various mechanisms. It's important to understand the different mechanisms in order to determine which modes are crucial to the heat transfer rate near the CHF point. Del Valle and Kenning [11] developed a sub-cooled boiling model which considered the bubble dynamics at the heated wall. They assumed the heat flux could be partitioned into the four regions identical to that of Hsu and Graham [13]. These four regions are depicted by Figure 2.11 and listed here along with their effective modes of heat transfer:

1. Maximum bubble projected area - microlayer evaporation and transient conduction
2. Surrounding area of influence - transient conduction
3. Overlapping areas of influence - enhanced transient conduction
4. Non-boiling area - single phase forced convection

Discussion is provided here on activation site location, projected bubble area, and area of influence.

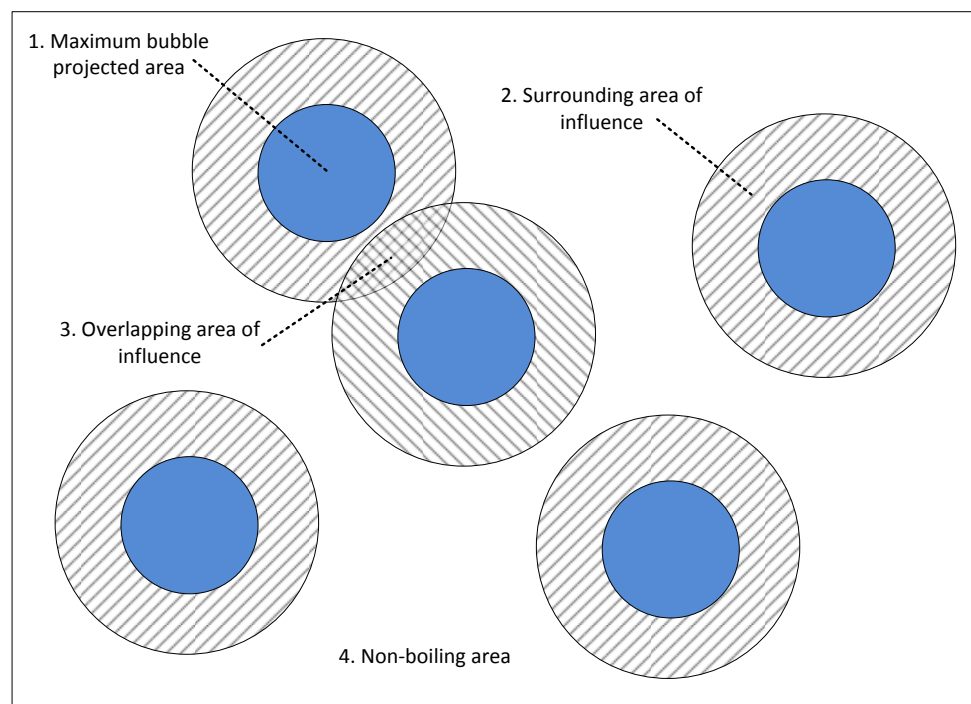


Figure 2.11: Heat flux partitioned areas.

2.4.1 Activation Site Location

Activation sites are not present in any regular manner. It is observed that for the flow boiling case many sites at lower heat fluxes become deactivated at higher heat fluxes with some again becoming active at even higher heat fluxes. Of the total 256 recorded sites by Del Valle and Kenning only 152 were active at the highest heat flux. This shows that there is not a simple addition of new activation sites to the already existing activation sites. Rather, activation sites move (activate and deactivate) with a changing heat flux. Some explanations of this phenomenon are hypothesized as being a result of the process of activation itself inhibiting further activations by refilling the activation site completely with liquid or leaving the site in a state requiring a higher heat flux. Unfavorable conditions created by adjacent activation sites also may affect the activation site density such that the result is a decrease in wall superheat due to the lateral energy transfer within the heated surface. The magnitude of this effect is dependent on the material properties of the heated surface.

Del Valle and Kenning show that an active nucleation site influence area of 2.0 – 2.5 times the bubble maximum radius exists and that nucleation sites can't be sustained within 1.5 – 2 times the bubble maximum radius. They express that failure to account for the interference of other active nucleation sites will over predict the population of active nucleation sites at large wall superheats. This implies that there exists a maximum boiling fraction that can be present on a surface for a given effective bubble size. Using a factor of 2.0 as the sustained influence area, the maximum boiling fraction is then 25% as determined by Equation 2.75.

$$f_{max} = \frac{\pi r_b^2}{\pi (2.0r_b)^2} = 25\% \quad (2.75)$$

2.4.2 Maximum Bubble Projected Area

The maximum projected bubble area ($A_{b,m}$) in Figure 2.11 (shaded blue) represents the projected area of the bubble at its maximum radius (R_m) and is represented by:

$$A_{b,m} = \pi R_m^2. \quad (2.76)$$

The total fraction of the maximum bubble projected area over a heated surface with a nucleation site density (N_a) is:

$$F = N_a \pi R_m^2. \quad (2.77)$$

R_m here is assumed constant for all sites, overlapping of projected areas is discounted due to the minimum spacing of $2R_m$ as discussed earlier, and all bubbles are assumed to grow and collapse as hemispheres. It is noted that N_a was not correlated in Del Valle and Kenning [11] but was tabulated as a function of wall superheat. Dependence of N_a was also taken to be a function of wall superheat by Basu [12] and used in the proposed model of this work (Section 6.4.6).

2.4.3 Surrounding Area of Influence

The second area is the surrounding area of influence. The parameter ($K > 1$) was introduced by Del Valle and Kenning [11] to account for the added heat removal from the area of influence represented as:

$$K = \frac{\text{Area of influence}}{\text{Maximum bubble projected area}}. \quad (2.78)$$

Letting the radius of the area of influence (R_{AI}) be twice as large as the maximum bubble radius, as described above, a value of K can be determined:

$$\begin{aligned}
 K\pi R_m^2 &= \pi R_{AI}^2 \\
 2R_m &= R_{AI} \\
 K\pi R_m^2 &= \pi 4R_m^2 \\
 K &= 4.
 \end{aligned}
 \tag{2.79}$$

The effective boiling area fraction then becomes FK and the non-boiling fraction $1 - FK$. The area of influence is then $(K - 1)F$. There exists however an overlapping of some areas of influence that is yet unaccounted for. This is accounted for by introducing another factor, X , which was found to be dependent primarily on F and not so much K as shown by Figure 2.12.

Applying these factors, as presented by Del Valle and Kenning [11], results in a non-boiling fraction area of $1 - FKX$, a non-overlapping area of influence of $(2X-1)KF-F$, and an overlapping area of influence fraction of $(1 - X)FK$.

2.5 Heat Flux Partitioning for Flow Boiling by Chen

After Chen's review of the available boiling heat transfer correlations in 1966 [48] he noted the incapability of any correlation to be used for general use for the flow boiling case. This conclusion was reached by the capability of the developed correlations to model the data in which they were derived and by the correlations incapability to model or predict the behavior of other experimenter's work. Chen aimed to develop a correlation that could be used in the general sense. Chen believed that it is 'unprofitable' to obtain averaged heat transfer coefficients and sought to achieve general local heat transfer coefficients. He also noted the importance of the effect of the flow regimes. Chen's correlation considered the the following development domain:

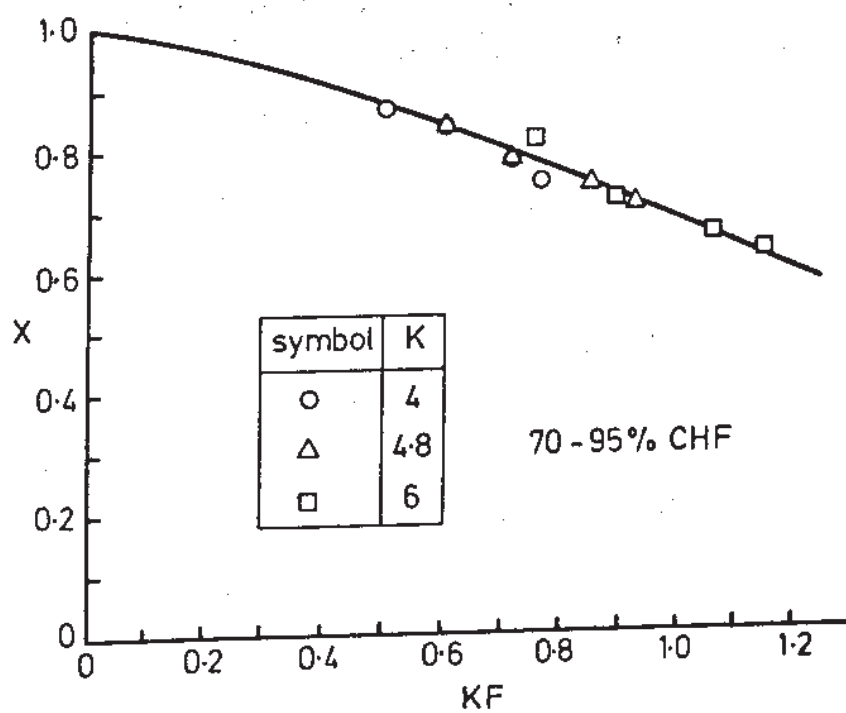


Figure 2.12: Area of influence fraction by Del Valle and Kenning [11].

- Saturated two-phase convective flow
- Vertical axial flow
- Steady-state flow
- No slug flow
- Low void fractions
- Heat fluxes less than the critical heat flux

Chen hypothesized that two mechanisms exist in the heat transfer process for boiling convective flow: the macro-convective and micro-convective processes. The macro-convective explains the heat transfer that is typical of a moving fluid through a channel while the micro-convective explains the heat transfer due to bubble nucleation and growth covering the modes discussed in Section 2.3. A key assumption by Chen is that these two mechanisms are directly additive.

Chen began with using the Dittus-Boelter equation Equation 2.55 to define the effective macro-convective heat transfer coefficient.

Where the Reynolds number, the Prandtl number, and the thermal conductivity represent the two-phase flow effective values. The single phase liquid parameters are introduced by taking ratios of the effective values to the liquid values:

$$\begin{aligned}
 \beta &= \text{Pr}/\text{Pr}_l \\
 \gamma &= k/k_l \\
 F &= (\text{Re}/\text{Re}_l)^{0.8} = \left(\text{Re} \frac{\mu_l}{DG}\right)^{0.8}
 \end{aligned}
 \tag{2.80}$$

Here G represents the mass flux and is constant for a given flow rate. It is argued here that for ordinary liquids, including water which is of interest here, that the Prandtl number for the liquid and vapor phase are of the same magnitude and thus the effective (two-phase fluid) should be the same order of magnitude as the liquid phase and

near unity. Also, since heat transfer in the two-phase flow is dominated by the liquid properties due to adherence of the liquid to the heated wall, the ratio of the effective to liquid thermal conductivity is near unity. A modified Dittus-Boelter correlation is then expressed by Equation 2.81 leaving F as the only unknown which is dependent on the liquid fraction.

$$h_{mac} = 0.023\text{Re}_l^{0.8}\text{Pr}_l^{0.4} (k_l/D) F \quad (2.81)$$

For the development of the micro-convective heat transfer coefficient Chen used the work from Forster and Zuber [49] who derived a Nusselt number for the pool boiling case expressed as by Equation 2.82.

$$Nu_b = 0.0015\text{Re}_b^{0.62}\text{Pr}_l^{0.33} = (h_b r_b)/k_l$$

$$r_b = \frac{\Delta T_w}{\Delta h_{fg}\rho_v} \left(\frac{2\pi k_l \rho_l C_{p,l} \sigma}{\Delta P} \right)^{0.5} \left(\frac{\rho_l}{g\Delta P} \right)^{0.25} \quad (2.82)$$

Forster and Zuber show that for a specific superheat the product of the bubble growth rate and the bubble radius is a constant:

$$\frac{dr_b}{dt} r_b = \frac{\pi k_l \rho_l C_{p,l}}{(\Delta h_{fg}\rho_v)^2} \Delta T_w^2$$

$$r_b = 2 \sqrt{\frac{\pi}{2}} \text{Ja} \sqrt{\alpha_l t}$$

$$\frac{dr_b}{dt} = \sqrt{\frac{\pi}{2}} \text{Ja} \sqrt{\frac{\alpha_l}{t}}$$

$$\frac{dr_b}{dt} r_b = \pi \alpha_l \text{Ja}^2 \quad (2.83)$$

For a given wall superheat, the temperature gradient moving away from the heated surface for the convective boiling case is steeper than that of the pool boiling case due to suppression of the boundary layer (δ). Thus an effective superheat is needed to account for this. The bubble Reynolds number is expressed by Equation 2.84 with the use of

Equation 2.83.

$$\text{Re}_b = \frac{dr_b}{dt} r_b \rho_l \left| \mu_l \right.$$

$$\text{Re}_b = \left(\frac{\pi k_l C_{p,l} \sigma}{\mu_l} \right) \left(\frac{\Delta T_w \rho_l}{\Delta h_{fg} \rho_v} \right)^2 \quad (2.84)$$

Inserting this into Equation 2.82 an expression for the micro- convective heat transfer coefficient is obtained using effective two-phase flow parameters:

$$h_{mic} = 0.0122 \left(\frac{k_l^{0.79} C_{p,l}^{0.45} \rho_l^{0.49} g^{0.25}}{\sigma^{0.5} \mu_l^{0.29} \Delta h_{fg}^{0.24} \rho_v^{0.24}} \right) \Delta T_e^{0.24} \Delta P_e^{0.75} \quad (2.85)$$

Defining a suppression factor (S) to express in terms of the total wall superheat an effective wall superheat where the power of 0.99 has been arbitrarily chosen by Chen such that S is to the first power in the final form:

$$S = (\Delta T_e / \Delta T_w)^{0.99} \quad (2.86)$$

Using the Clausius-Clapeyron relation expressed in Equation 2.2 and writing in terms of total and effective superheat and taking both sides to the 0.75 power and multiplying by $\Delta T^{0.24}$:

$$\Delta T_e^{0.99} = \left(\frac{T_e}{\Delta h_{fg} \rho_v} \right)_{T_e}^{0.75} \Delta T_e^{0.24} \Delta P_e^{0.75}$$

$$\Delta T_w^{0.99} = \left(\frac{T_w}{\Delta h_{fg} \rho_v} \right)_{T_w}^{0.75} \Delta T_w^{0.24} \Delta P_w^{0.75} . \quad (2.87)$$

Assuming a constant slope along the saturation curve of a phase change diagram:

$$\left(\frac{T_e}{\Delta h_{fg} \rho_v} \right)_{T_e} \cong \left(\frac{T_w}{\Delta h_{fg} \rho_v} \right)_{T_w} . \quad (2.88)$$

Using Equation 2.87 and Equation 2.88 in Equation 2.86 gives:

$$S = (\Delta T_e / \Delta T_w)^{0.24} (\Delta P_e / \Delta P)^{0.75} . \quad (2.89)$$

The final form for the micro-convective heat transfer coefficient is then expressed using total superheats by Equation 2.90.

$$h_{mic} = 0.0122 \left(\frac{k_l^{0.79} C_{p,l}^{0.45} \rho_l^{0.49} g^{0.25}}{\sigma^{0.5} \mu_l^{0.29} \Delta h_{fg}^{0.24} \rho_v^{0.24}} \right) \Delta T_w^{0.24} \Delta P^{0.75} S. \quad (2.90)$$

The suppression factor (S) takes into account the pool to flow boiling transition. At high flow rates the suppression factor approaches zero representing the suppression of the boiling phenomenon due to the increased convective heat removal. At low flow rates the suppression factor approaches unity signifying an increase in the boiling mechanism (micro-convective forces) relative to the convective term (macro-convective forces).

The total heat transfer coefficient is found by the summation of the macro- and micro-convective heat transfer coefficients:

$$h = h_{mac} + h_{mic} \quad (2.91)$$

The solution steps to Chen's correlation are as follows:

1. A first estimate of F from Equation 2.81 is made by taking the experimental heat transfer coefficient and dividing by the liquid macro-convective heat transfer coefficient.
2. The first estimate of F is used to solve for Equation 2.81 to obtain h_{mac} .
3. Next Equation 2.91 is used to solve for h_{mic} .
4. Knowing h_{mic} Equation 2.90 is solved to determine the suppression factor S .
5. This was repeated until convergence of F and S were obtained.

Chen has also shown it is possible to determine F from a heat-momentum analogy. Chen's correlation resulted in the data analyzed to fall onto one curve with minimal variability in the results. The maximum error reported was 15.4%.

A simplification to Chen's method has widely been used as presented by [?, ?, 18, 13] for determination of the F and S factors. Where the F factor is a function of the Martinelli parameter (χ_{tt}) as demonstrated by Equation 2.92.

$$F = 2.35 (\chi_{tt}^{-1}) \quad (2.92)$$

$$\chi_{tt}^{-1} = \left(\frac{G_g}{G_f}\right)^{0.9} \left(\frac{\rho_l}{\rho_v}\right)^{0.5} \left(\frac{\mu_g}{\mu_f}\right)^{0.1} \quad (2.93)$$

The suppression factor is a function of the two-phase Reynolds number as expressed by Equation 2.94.

$$S = \begin{cases} (1 + 0.12Re_{tp}^{1.14})^{-1} & Re_{tp} < 32.5 \\ (1 + 0.42Re_{tp}^{0.78})^{-1} & 32.5 < Re_{tp} < 70 \\ 0.0797 & Re_{tp} > 70 \end{cases} \quad (2.94)$$

An approximate single expression can also be used as shown by Equation 2.95.

$$S = (1 + 0.14Re_{tp})^{-1} \quad (2.95)$$

Here the two-phase Reynolds is defined by Equation 2.96.

$$Re_{tp} = \frac{G(1-x)D}{\mu_f F^{1.25}} \times 10^{-5} \quad (2.96)$$

Chapter 3: The Critical Heat Flux

A literature survey is performed to investigate the current state of understanding of the onset of the critical heat flux condition and the developed prediction techniques and models. It was quickly apparent that a tremendous amount of work has been completed since the 1950's. However, there has been little success for a single broadly applicable correlation. Presented in Section 3.1 are the desired development ranges for a critical heat flux correlation based on the current and future nuclear operating plants. Provided in Section 3.2 is a high level description of how the CHF condition can be approached from the standpoint of cooling versus a heating approach and transient versus steady state CHF. In Section 3.3 the approaches employed by various researchers to calculate the CHF condition is summarized. Section 3.4 addresses the basis for many mechanistic models with a small subset of correlations summarized in Section 3.5.

3.1 Critical Heat Flux Development Domain

Two main modes of critical heat flux are typically defined; the departure from nucleate boiling (DNB) type and the dryout type. The modes and branching mechanistic based models are depicted in Figure 3.1. A discussion of the branching mechanistic based models is provided in Section 3.4.

The DNB mode is traditionally characterized under conditions of low local/exit bulk quality where the critical heat flux is based on the limitations of the nucleate boiling process itself. This mode is traditionally prevalent for pressurized water reactors. The dryout type is typically characterized under conditions where the bulk fluid is at saturation conditions where an annular flow regime exists. The breakdown of the annular film is the condition of onset for CHF in the dryout case. This mode is standard of boiling

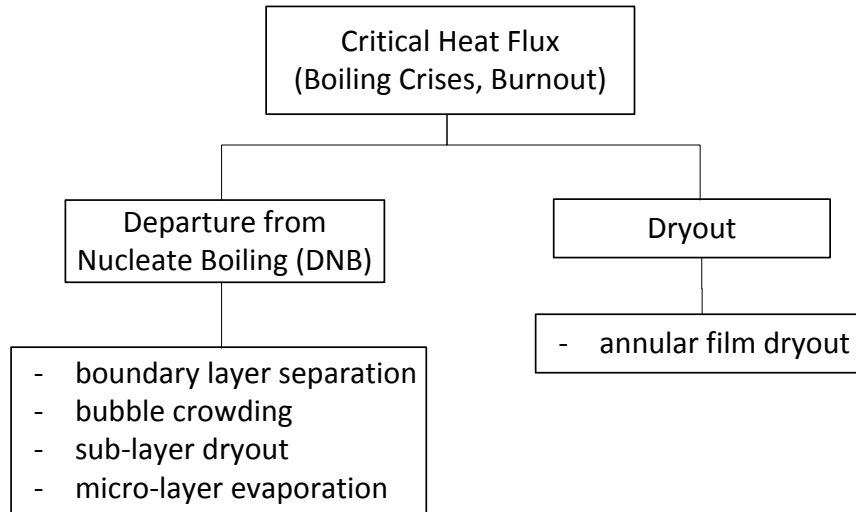


Figure 3.1: Modes of the critical heat flux.

water reactors.

Legacy nuclear reactor designs operate under a forced circulation mode (relying on reactor coolant pumps) to move coolant through the primary loop and transport energy from the core to the steam generator. A new paradigm shift is underway for the development and construction of small modular reactors (SMRs) which rely on natural circulation to transport mass and energy through the primary loop. These designs do not rely on pumps during normal and off-normal operating modes. The main operating characteristics do differ between the legacy and recent designs in a few critical areas in terms of studying the critical heat flux. Recent modular designs operate under much lower operating mass fluxes and under lower linear heat rates (power per length of fuel). Most relational developments for the prediction of the critical heat flux onset have been developed for the legacy reactor designs leaving a void for investigations in the more recent modular designs. One goal of this work is to not only develop a mechanistic model for the legacy domain of plants but also to fill this gap of the new innovative designs breaching the market. One current light water SMR design leading the development

Table 3.1: Typical operating conditions for pressurized water reactors.

Parameter	Range	
	Typical Legacy PWRs ¹	Modern SMR ²
Operating Power [MW_{th}]	3400	160
Pressure [MPa]	15.51	12.75
Mass Flux [$kg/(m^2 - s)$]	3390.6	-
Core Inlet Temperature [K]	552.6	-
Core Outlet Temperature [K]	598	-
Average Heat Flux [kW/m^2]	629	277
Maximum Heat Flux [kW/m^2]	1634.7	-
Average Linear Power [kW/m]	18.77	8.27
Maximum Linear Power [kW/m]	48.88	-

within the nuclear market is NuScale Power LLC. A comparison between the legacy and modern SMR designs is provided in Table 3.1 with publicly available data. Not all data is publicly available and thus gaps may exist in Table 3.1.

3.2 Methods to Approach the Critical Heat Flux

The critical heat flux point can be reached by two methods. The first is to approach the CHF point from the film or transition boiling regimes of Figure 3.2 (from right to left) or from the nucleate boiling regime (from left to right). Normal heating systems such as nuclear reactors approach CHF by the latter.

Another characteristic to understand is transient CHF versus steady state CHF. Traditionally experiments are performed under quasi-steady state conditions to develop correlations that are then applied to the transient case. Steady state data is obtained by

¹Values taken from Westinghouse design certification document for the AP1000 [50].

²Values taken and derived from NuScale submitted technical report [51].

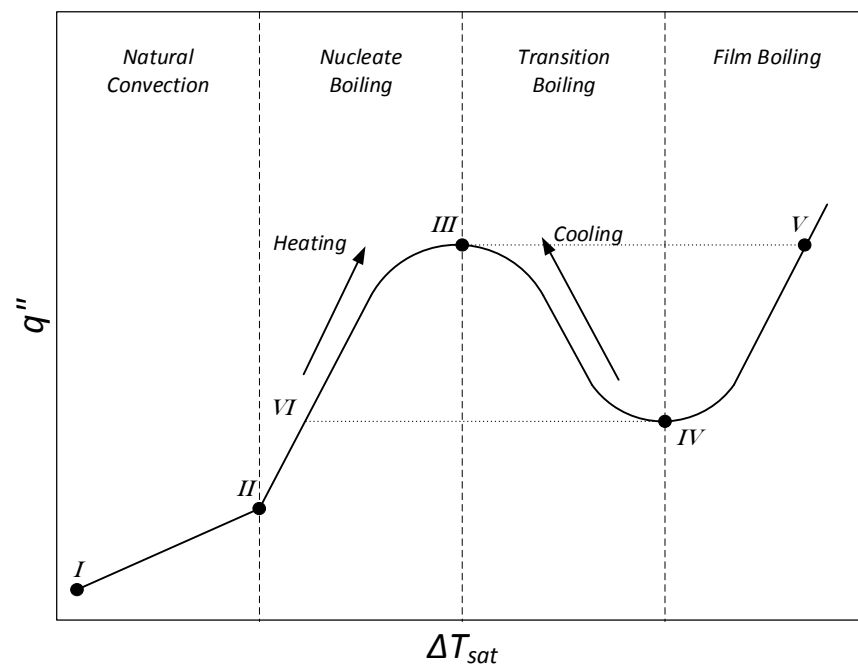


Figure 3.2: Boiling curve for transient cooling and transient heating.

a gradual increase in power in incremental steps while maintaining the specified test boundary conditions (e.g. flow, inlet subcooling, and pressure). During the incremental power steps the fluid and heated surface conditions are allowed stabilize until a critical point is reached where stabilized conditions do not exist. This unstable condition is observed by an uncontrollable rise in the heated surface temperature for a given set of boundary conditions. Figure 3.3 from Liaw and Dhir [14] describes the subtle differences between the transient and steady CHF tests along with cooling and heating CHF tests. As can be seen good agreement exists between the actual transient experiments and steady state tests. Thus, it is deemed appropriate to use steady state data to describe the transient case. Key observations drawn from Figure 3.3 are as follows:

- transient heating (black squares) provides a higher CHF value than that of transient cooling (black triangles) showing a hysteresis effect and
- steady state (white squares and circles) and transient heating (black squares and circles) are continuous near the CHF point showing that no matter the method of approach (steady or transient) the CHF value itself should be the same.

The heating case is considered for the modeled within this work.

3.3 Methods to Predict the Onset of Critical Heat Flux

Various approaches have been employed in effort to correlate data to a prediction method for predicting the onset of the critical heat flux. The following subsections will discuss these approaches and provide some advantages and disadvantages for each method.

3.3.1 Empirical Correlations

Empirical correlations have historically been the focus of development of critical heat flux models due to the lack of understanding of the physical mechanisms that occur dur-

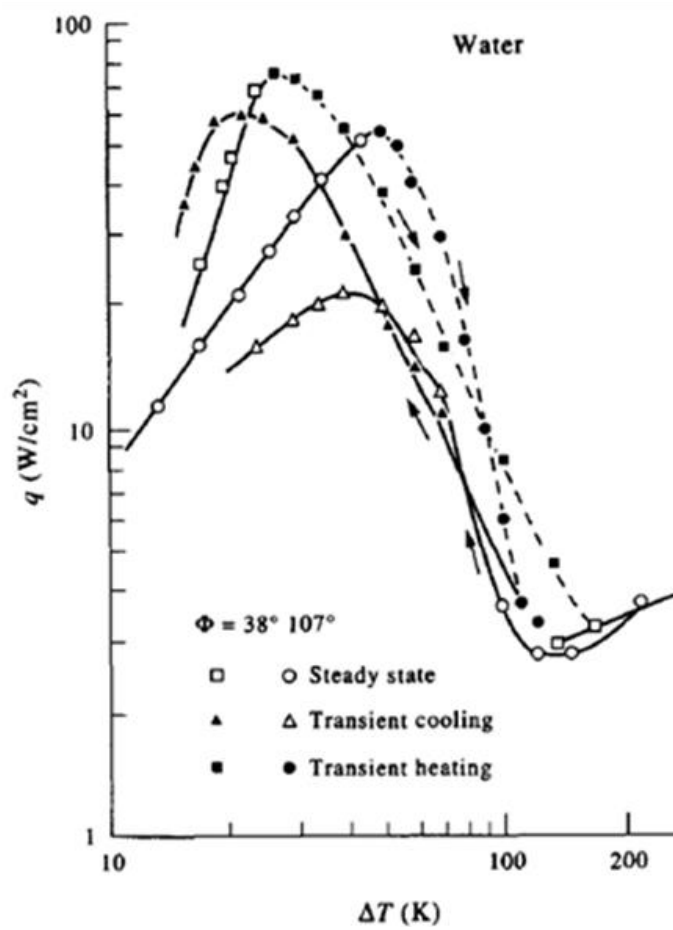


Figure 3.3: Boiling curve for steady state, transient cooling, and transient heating [14].

ing the boiling process. These models are developed relating a few key parameters to the CHF conditions by determining a set of fitted coefficients with the use of experimental data.

Empirical correlations are developed often with disregard to the physical processes that are actually occurring. An example of this type of correlation is that developed by the Electric Power Research Institute (EPRI) which utilizes over 11,000 data points [52, 53, 54, 55] with the following form of Equation 3.1.

$$q''_{CHF} = \frac{A' + 0.25GD\Delta H_{in}}{C' + L} \quad (3.1)$$

Another example is that developed by Tong [56] and used as the basis for the W3 CHF correlation applied in the analysis of the Westinghouse AP600 and AP1000 nuclear reactor designs. Correlations like this are acceptable for their final application when they are developed and applied to a specified geometry and operating conditions.

The drawback to such relations is the lack of the incorporation of the model's response to physically sound mechanisms which often results in a correlation that is only valid for the specific geometry and conditions for which the coefficients were developed. The lack of the broad applicability of such models limits the usefulness of the correlation itself especially when attempting to apply the correlations to other system configurations.

3.3.2 Look-Up Tables

Lookup tables provide the critical heat flux value in terms of a few determined key parameters in a tabular format. The parameters often are pressure, mass flux, and quality. The values presented are normalized to a single geometric configuration. Once the CHF value for the normalized condition is obtained correction factors are then applied for the specific geometry and flow conditions. Conditions that lie between table values are determined through interpolation methods. Development of these tables requires

a massive data base of experimental values in an attempt to cover a wide variety of fluid conditions. The most common lookup tables developed are those by Groeneveld [57, 58, 59] which consists of >7,000 points. These tables are indeed very powerful and utilized in many thermal-hydraulic system codes such as RELAP5, RELAP5-3D, and TRACE. They offer solutions that are not computationally expensive and appear to provide the widest operating range coverage. They can provide an analyst with general trends at the cost of confidence in the actual magnitude of the CHF value. The resulting form of the final CHF value for Groeneveld [57, 58, 59] is represented by Equation 3.2 with variation of the exponent of the diameter (D_{exp} depending on the version of the table utilized).

$$q''_{CHF}(D_{exp}, P_{exp}, G_{exp}, x_{exp}) = q''_{CHF}(D = 8 \text{ mm}, P_{exp}, G_{exp}, x_{exp}) \left(\frac{D_{exp}}{8} \right)^{-1/2} \quad (3.2)$$

The applicability of look-tables however, like empirical correlations, must be scrutinized carefully for the intended application. The lookup tables of Groeneveld for example can have as many as seven correction factors applied to account for various geometric and flow conditions. Lookup tables do not provide responses to actual physical mechanisms and thus trends may be skewed or even missed when applied to conditions not represented exactly by the conditions under which the table was developed.

3.3.3 Mechanistic Models

Mechanistic based critical heat flux correlations are developed by first postulating a trigger mechanism for the CHF condition and identifying the phenomena that occur during this process. Balance equations are then formulated to capture the process of the trigger mechanism. The advantage of such a method is that the potential applicability of the model is greatly expanded than that for a simply tested subset of experimental data. These types of correlations can be considered (with caution) to be applicable outside there tested parameters if similar phenomena are present in the desired application the correlation is to be applied. The key to this effort is to capture the fundamental processes

of a phenomenon in a general sense.

The drawback however to such models historically, has been the dependence on information needed for closure of a model that is not well understood or hasn't been investigated. Also, the solution methods have often been computationally too expensive to perform large or many analyses in the production environment of industry. Advances in separate effects experimental facilities with regards to visualization tools that provide multidimensional data and measuring techniques have begun to provide insight to help understand what are classified as the meso-/micro-phenomena allowing for understanding of the fundamental processes occurring and for the development of closure relations. However, even these closure relations can often be empirical in nature making it impossible to develop a purely mechanistic based model. For the sake of argument of discussion here, the model developed and proposed in this work will be referred to as being mechanistic even though, like other claimed mechanistic models, requires dependency on non-mechanistic based closure relations. However, a justification for why the form and dependence of the chosen closure relation is provided in this work based on a physical argument. It is the author's belief that trends observed in empirical relations should at least physically be explainable and make sense.

3.4 Fundamental Mechanistic Models

Since the focus of this work is on the development of a mechanistic based CHF model, discussion from this point forward with regard to methods will heavily focused to literature work discussing these type of models.

In general there are two fundamental approaches that have been taken in developing a mechanistic based CHF model as summarized by Katto [60]. The first is referred to as the hydrodynamic models and the second the macro-layer dryout models. The hydrodynamic models postulates that a stability limit is reached with the ejection of vapor from the surface and the incoming re-flood of liquid. With these types of models near wall fluid conditions are generally neglected. The macro-layer dryout models postulate that

CHF occurs when the underlying liquid layer below a vapor mass is evaporated away. Described here are the general CHF mechanistic based approaches.

The boundary layer separation model is a hydrodynamic based model that postulates that vapor injection from the wall into the bulk flow field reduces the liquid velocity gradient near the wall causing the liquid to separate from the wall. This 'blow-off' of liquid near the wall results in a transition from nucleate to local film boiling when the vapor flow from the surface reaches the critical velocity. This model was first postulated by Kutateladze [1] and applied by Zuber [61].

As heat flux increase the number of nucleation sites and nucleation frequency is postulated to increase. The increase of the vapor generation has an effect to impede liquid from coming back into contact with the heated surface. This phenomenon was studied by Zuber [61] and is referred to as Helmholtz instability. The general problem setup is depicted in Figure 3.4.

In counter-current flow of two fluids there exists a maximum relative velocity before any disturbance at the interface will grow unbounded. The velocity of propagation, c , of a surface wave of counter-current flow is given by Zuber [61] and Lamb [62] as:

$$c^2 = \left(\frac{n}{m}\right)^2 = \frac{\sigma mg}{\rho_l + \rho_v} - \frac{\rho_l \rho_v}{(\rho_l + \rho_v)^2} (v_v - v_l)^2. \quad (3.3)$$

The wave height is expressed as,

$$\eta = \eta_o e^{-ni} \cos(mx) \quad (3.4)$$

with the following definitions:

$$m = \frac{2\pi}{\lambda}, \quad \text{wave number} \quad (3.5)$$

$$n = \frac{2\pi}{\lambda} c = mc, \quad \text{wave angular velocity.} \quad (3.6)$$

For a stable surface condition to exist a positive and real angular velocity must be present

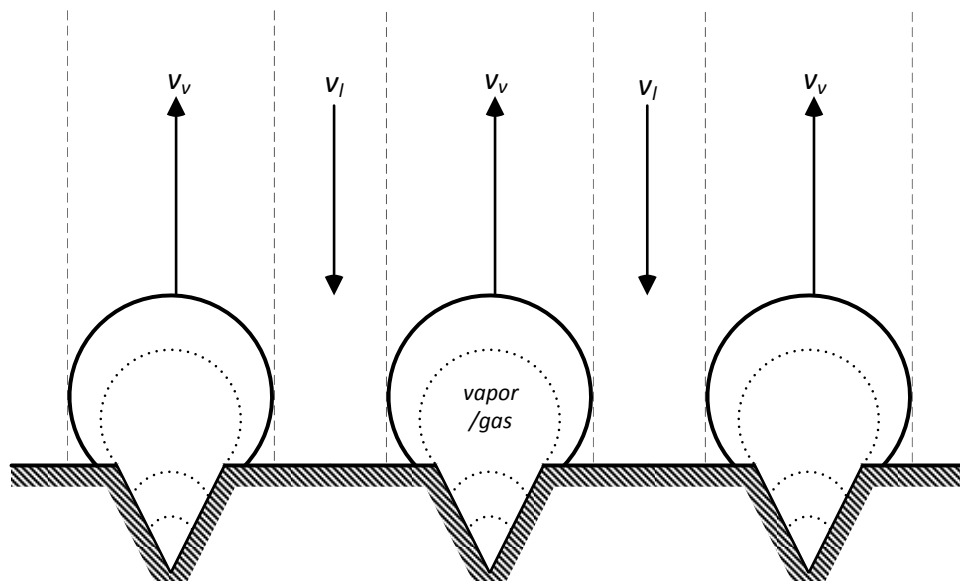


Figure 3.4: Vapor and liquid counter-flow in pool boiling.

requiring that

$$\left(\frac{n}{m}\right)^2 > 0 \quad (3.7)$$

and hence

$$\frac{\sigma mg}{\rho_l + \rho_v} > \frac{\rho_l \rho_v}{(\rho_l + \rho_v)^2} (v_v - v_l)^2 \quad (3.8)$$

For a steady-state flow where the discharging vapor and incoming liquid mass fluxes are equal and hence from continuity

$$v_l = \frac{\rho_v}{\rho_l} v_v. \quad (3.9)$$

Substituting Equation 3.9 into Equation 3.8 gives a criteria for the maximum vapor velocity before the development of instabilities:

$$v_v = \sqrt{\frac{\rho_l \sigma mg}{\rho_v (\rho_l + \rho_v)}}. \quad (3.10)$$

Once this maximum stability velocity is reached the development of unstable waves prevents the escape of vapor away from vapor and the surge of bulk liquid from coming into contact with the heated wall.

The near-wall bubble crowding based models postulate that the turbulent interchange between the bubbly layer and the core is the limiting mechanism for the trigger of the CHF condition. A balance between the outward vapor flow and the inward liquid flow is used to determine the void fraction in the bubbly sublayer. The CHF is then predicted at a critical void fraction in the bubbly sublayer varying between 0.3 and 0.95 depending on the degree of subcooling, mass fluxes, and pressure. This model was proposed by Weisman and Pei [5].

The sublayer dryout models assume that a vapor blanket isolates the heated surface from being cooled from the bulk liquid leaving an isolated thin liquid sublayer near the wall. It then assumes that the CHF trigger occurs when the evaporation rate of the liquid sublayer exceeds the liquid layer replenishment from the core region. This model is based on the improvement of the Weisman and Pei model [5] and was developed by Lee and Mudawwar [7]. The model of Lee and Mudawwar is discussed in Section 3.5.7.

The micro-layer evaporation model postulates that the CHF point is triggered when the layer (micro-layer) between the wall and a bubble attached to the wall evaporates.

3.5 Existing Critical Heat Flux Correlations

With the proposed models and postulated mechanisms outlined in the previous sections, much work has been done in effort derive expressional form to accurately predict the onset of the critical heat flux condition. Table 3.2 provides a small subset of the various CHF relations in literature including mechanistic, empirical, and look-up table CHF relations. In general not many correlations exist for the low mass flux conditions ($< 1000 \text{ kg} - \text{m}^2/\text{s}$) and the intermediate to higher pressure conditions. This demonstrates an area of need for further development. A general discussion of some models are provided in the following subsections. Many other correlations have been developed and attempting to list them all would be futile. A sample of various correlations as shown here in order to become familiar with the proposed forms. Hall and Mudawwar [19, 20] compiled a detailed assessment of CHF databases and about 100 CHF correlations. The reader is referred to the work of Hall and Mudawwar [19, 20] for a detailed assessment of existing CHF correlations.

Table 3.2: Subset of critical heat flux models and applicability range overview.

Model	Mass Flux		Pressure	
	[kg/m ² -s]		[MPa]	
	Low	High	Low	High
Kutateladze (1948) [1]	atmospheric pool boiling			
Zuber (1959) [22]				
Tong (1968) [56]	1356	6781	6.89	13.79
Rogers et al.(1982) [3]	180	1200	0.16	0.16
EPRI (1982) [52, 53, 54, 55]	271	5560	1.38	16.55
Weisman & Pei (1983) [5]	972	13611	2	20.2
Lee & Mudawwar (1988) [7]	1350	5200	6.89	15.76
Weber & Johannsen (1990a) [63]	25	200	0.11	1
Weber & Johannsen (1990b) [64]	10.8	301.4	0.11	1.2
Katto (1992) [65]	350	40,600	0.1	20
Huang et al. (1993) [66]	25	500	0.1	1.2
Oh & Englert (1993) [67]	30	80	0.02	0.085
Liu et al. (2000) [8]	900	90,000	0.1	19.25
Kwon et al. (2001) [68]	1000	18000	3	19
Kureta & Akimoto (2002) [9]	1000	2000	0.101	0.101
Groeneveld (1986) [57]				
Groeneveld (1996) [58]	0	8,000	0.1	20
Groeneveld (2007) [59]				
Chung & No (2007) [69]	atmospheric pool boiling			
Wright et al. (2008) [70]	9.5	39	0.089	1.15

3.5.1 Kutateladze (1948) [1]

Kutateladze [1] developed a correlation using for the pool boiling case where small aspect ratios exist

$$\frac{q''_{CHF} / \Delta h_{fg} \rho_v}{(g \sigma (\rho_L - \rho_v) / \rho_v^2)^{1/4}} = K, \text{ for } l/s \rightarrow 0. \quad (3.11)$$

with K being a constant independent of fluid properties between 0.12 and 0.16. This equation was later analytically derived and confirmed by Zuber [22].

3.5.2 Katto (1978) [2]

Katto [2] developed a functional form of predicting CHF based on the Kutateladze number:

$$\frac{q''_{CHF} / (\Delta h_{fg} \rho_v)}{(g \sigma (\rho_L - \rho_v) / \rho_v^2)^{1/4}} = f(\rho_L / \rho_v, g (\rho_L - \rho_v) s^2, l/s). \quad (3.12)$$

Katto and Kosho [71] finally came to the final form for predicting the onset of CHF within $\pm 15\%$ for a space bounded between two horizontal disks :

$$\frac{q''_{CHF} / \Delta h_{fg} \rho_v}{(g \sigma (\rho_L - \rho_v) / \rho_v^2)^{1/4}} = \frac{0.18}{1 + 0.00918 (\rho_L / \rho_v)^{0.14} [g (\rho_L - \rho_v) d^2 / \sigma]^{0.5} (d/s)} \quad (3.13)$$

3.5.3 Rogers (1982) [3]

An investigation into low natural circulation flow low- pressure CHF was investigated by Rogers et al. [3]. This correlation was developed for a natural circulation pool type reactor. An empirical correlation was derived to minimize the RMS between experi-

mental data and proposed correlation and is shown in Equation 3.14.

$$q''_{CHF} = A_1 - A_2\dot{m} + (C_1\dot{m} - C_2)\frac{\Delta h_i}{\Delta h_v} \quad (3.14)$$

With constants defined in Table 3.3.

Test Section #	L/D_{heated}	A_1	A_2	C_1	C_2
1	20.2	63.61	0.0329	1.781	279.7
2	13.9	74.86	0.0329	2.251	112.5
3	8.5	92.06	0.203	3.894	-6.567

Table 3.3: Constants for CHF correlation by Rogers et al. [3].

A maximum deviation of 11% was reported. The range of applicability is shown in Table 3.4.

Parameter	Applicability
Pressure	160kPa
Heated hydraulic diameter	23.8 – 56.5mm
Ratio of inlet subcooled enthalpy to enthalpy of vaporization	0.06 – 0.175
L/D_{heated}	8.5 – 20.2
Mass flux	180 – 1200
Inlet water temperature	20 – 80°C
Heat flux	15 – 280W/m ²
Critical quality	-0.163 – 0.0099

Table 3.4: Applicability of Rogers et al. CHF correlation [3].

3.5.4 Monde (1982) [4]

Monde [4] carried out CHF experiments for natural convective boiling at atmospheric pressure in vertically oriented rectangular channels with aspect ratios up to 120. Water and ethanol were studied. Using a functional form similar to that developed by Katto [2]:

$$\frac{q''_{CHF} / \Delta h_{fg} \rho_v}{(g\sigma(\rho_L - \rho_v) / \rho_v^2)^{1/4}} = \frac{K}{1 + C(\rho_L / \rho_v)^m [g(\rho_L - \rho_v) d^2 / \sigma]^n (l/s)} \quad (3.15)$$

The following outlines the experimental conditions for the development of the correlation by Monde:

- Vertical flow in rectangular channels
- Natural circulation
- Heat fluxes between $5 \cdot 10^5$ to 10^6 W/m^2
- Heated lengths between 20 to 50 *mm*
- 0 to 30 *K* subcooling
- Rectangular channel widths between 0.45 to 7.0 *mm*
- *l/s* ratios of 2.8 to 111
- Heated width of 10 *mm*

Monde determined that for water, ethanol, Benzene, and R113 with small aspect ratios ($l/s < 10$) that K approaches a constant between 0.12 and 0.17 similar to that predicted by Kutateladze [72] (see Section 3.5.1). Monde used an average value from his experimental data and set $K = 0.16$ and found that $n = 0$, $C = 0.00067$, and $m = 0.6$.

$$\frac{q''_{CHF} / \Delta h_{fg} \rho_v}{(g\sigma(\rho_L - \rho_v) / \rho_v^2)^{1/4}} = \frac{0.16}{1 + 0.00067(\rho_L / \rho_v)^{0.6} (l/s)} \quad (3.16)$$

This correlation matched the experimental data collected within $\pm 20\%$.

3.5.5 Weisman and Pei (1983) [5]

Weisman and Pei [5] proposed a correlation based on the bubble crowding mechanism. A turbulent mass interchange between the core and bubbly layer was used to determine the near wall void fraction. A critical void fraction 0.82 was postulated to be the trigger for the CHF condition.

3.5.6 Weisman and Ying (1985) [6]

Weisman and Ying (1985) [6] extended the work of Weisman and Pei [5] to lower mass fluxes through incorporation of a slip model instead of the homogeneous flow model. This was later extended to rod bundles.

3.5.7 Lee and Mudawwar (1988) [7]

Lee and Mudawwar [7] developed a mechanistic based CHF correlation for vertical sub-cooled flow at a high pressures and mass fluxes ($6.89\text{MPa} < P < 15.76\text{MPa}$; $1350\text{kg}/\text{m}^2 - \text{s} < G < 5300\text{kg}/\text{m}^2 - \text{s}$). Their model is based on the dryout of the sublayer between the heated wall and a vapor blanket. They note that at high mass fluxes, as observed photographically, small bubbles tend to slide along the surface prior to departure and coalesce in the sublayer region not affecting the bulk two-phase flow pattern. The flow pattern considered is shown in Figure 3.5. 560 data points were used to evaluate the three empirical constants of their proposed model. The mean deviation of the model against the 560 data points was 11.94% and against the 89 data points 13.37%. Results for both sets mainly lie within $\pm 30\%$ error.

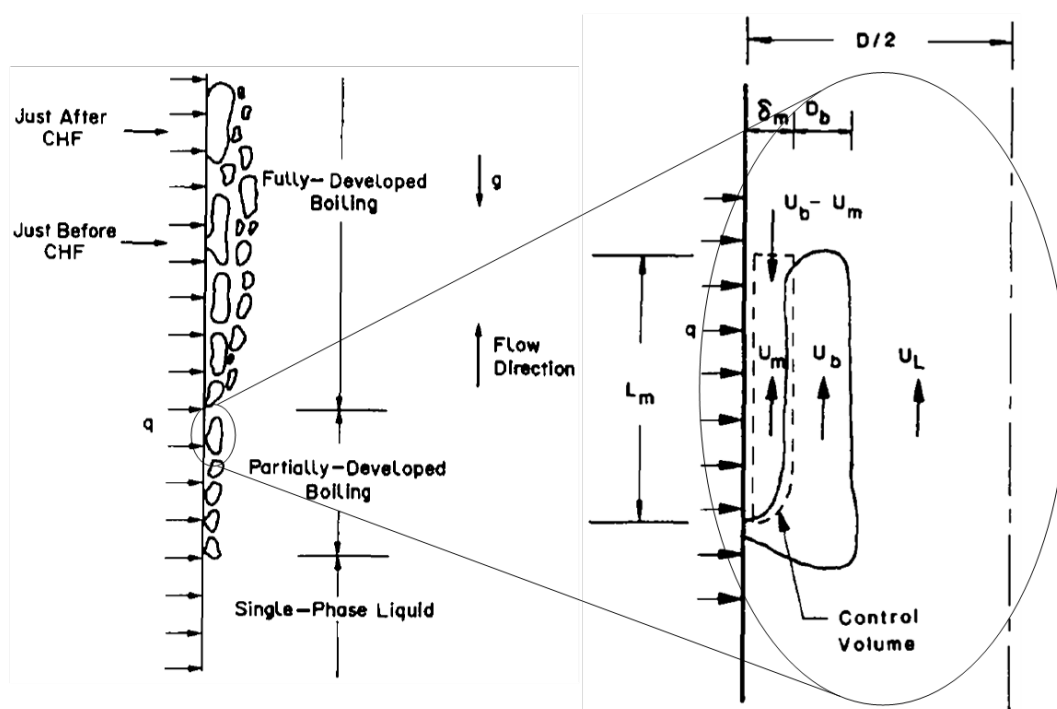


Figure 3.5: Model of Lee and Mudawwar (1988) [7].

3.5.8 Liu et al. (2000) [8]

Liu et al. [8] developed a mechanistic based critical heat correlation derived on the basis of the sub-layer dryout model. This model assumes that the sub-layer of liquid beneath a passing vapor blanket and between the heated surface evaporates during the blanket passage time. The general relation is expressed by Equation 3.17.

$$q''_{CHF} = \frac{\rho_l \delta \Delta h_{fg}}{L_B U_B} \quad (3.17)$$

ρ_l = liquid saturation density

δ = liquid sublayer thickness

Δh_{fg} = latent heat of vaporization

L_B = vapor blanket length

U_B = vapor blanket velocity

This correlation was tested with over 2000 data points obtaining an error within 30% for 89% of the data. The sub-layer thickness is calculated based on the Karman velocity distribution. The vapor blanket length and velocity are calculated based on the Helmholtz critical wave length. The solution is obtained through an iterative process.

3.5.9 Kureta (2002) [9]

Kureta and Akimoto [9] developed a critical heat flux correlation for subcooled force flow through narrow one-sided heated channels. The correlation was then modified to be more general to account for single and double sided heated channels and half and fully

circumferential heated tubes. The developed correlation has accuracy of $\pm 45\%$.

$$\left(\frac{q''_{CHF}}{G\Delta h_{fg}}\right)\left(\frac{Gv}{\sigma}\right)^{0.5} = C_1(x_{CHF} + C_2)$$

where,

$$C_1 = \left[6.9\left(\frac{P_h}{P_w}\right)^2 - 10\left(\frac{P_h}{P_w}\right) + 2\right] \times 10^{-3} \quad (3.18)$$

$$C_2 = -0.75\left(\frac{P_h}{P_w}\right)^2 + 0.9\left(\frac{P_h}{P_w}\right) - 0.28$$

x_{CHF} is the critical quality at the location of CHF

The applicability of the correlation is within the following ranges:

Parameter	Symbol	Applicability
Hydraulic diameter	D_h	1.0 – 7.8mm
Heated perimeter ratio	$\frac{P_h}{P_w}$	0.25 – 1.0
Heated length	L_h	10 – 200mm
Mass flux	G	1,000 – 2,000kg/(m ² s)
Inlet water temperature	T_{in}	5 – 90°C
Critical heat flux	q''_{CHF}	1.0 – 70.0MW/m ²
Critical quality	x_{CHF}	–0.163 – 0.0099

Table 3.5: Applicability of Kureta and Akimoto CHF correlation for subcooled forced flow in narrow channels[9].

3.5.10 Natural Circulation in a Vertical Inclined Tubes (Zhen-hua 2004)

Zhen-hua and Rong-hua [11] used Monde's CHF correlation [4] in developing a semi-theoretical CHF model as a basis for developing their CHF correlation for inclined tubes submerged in a saturated liquid of water and R11. The following outlines the experi-

mental conditions for the development of the correlation by Monde:

- Vertical flow in tubes
- Natural circulation
- Inclination angles between 30° and vertical
- Heat fluxes between $5 \cdot 10^5$ to 10^6 w/m^2
- Heated lengths between 100 to 400 *mm*
- Saturated fluid of water and $R - 11$
- Tube diameters between 0.90 to 8.0 *mm*
- l/D ratios of 12.5 to 440

Chapter 4: Parameter Effects on Critical Heat Flux

Two approaches are used to predict the onset of CHF. The first and most common type are global parameters which involve system pressure, mass flow rate, and channel geometry. These parameters are typically used to develop empirical correlations and involve minimal to no mechanistic modeling efforts. The second involves microscopic/local parameters which use flow velocity near a surface, local void fractions, working fluid properties, and surface conditions. These parameters are used to model principle forces in developing mechanistic based models.

The following subsections describe the parameters which have been observed to affect the CHF value.

4.1 Surface Tension

The surface tension of a fluid interface with the surface curvature describes the interfacial pressure drop. The surface tension directly affects the interfacial force working to maintain a bubble's spherical shape. When a bubble is in contact with a surface, the force holding a bubble to the surface is proportional to the surface tension. A strong dependence of surface tension exists on the local temperature as shown in Figure 4.1.

4.2 Contact Angle

The contact angle is an important variable when analyzing the departure of a bubble from a surface. The contact angle is primarily dependent on the surface roughness as shown by [15] in Figure 4.2. In general an increase in surface roughness causes

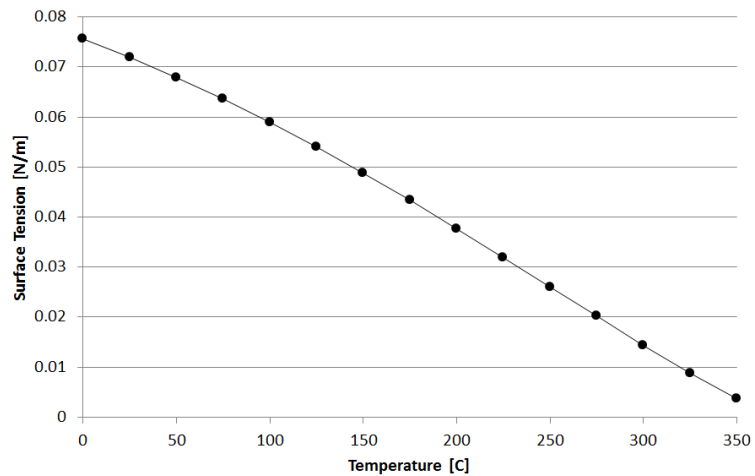


Figure 4.1: Surface tension dependence on temperature.

a decrease in contact angle. However, there is a point at which a further increase in surface roughness results in an increase in the contact angle. It has been postulated that an increase in roughness improves wettability (decrease in contact angle) but when the roughness is too high the wettability is disrupted. Further investigation of this behavior is still needed.

The contact angle can be categorized into two groups; a static contact angle or a dynamic contact angle. The dynamic contact angle is further subdivided into a receding and advancing contact angle. The following subsections describe characteristics of static and dynamic contact angles.

4.2.1 Static Contact Angle

The static (equilibrium) contact angle method assumes a single contact angle which is determined by a placement of a drop on a known surface. Dhir [16] performed a complete numerical simulation investigating the nucleation, growth time, and departure diameter. Considered in the numerical simulation are conservation equations for mass,

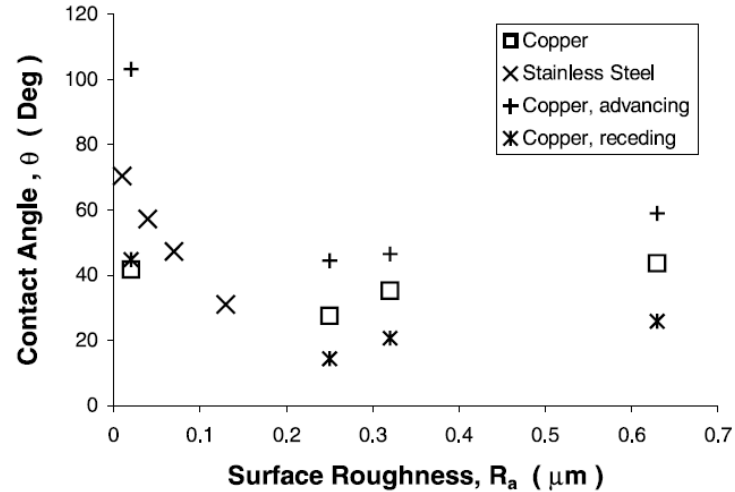


Figure 4.2: Effect of surface roughness on the contact angle [15].

momentum, and energy for both phases. It was observed that an increase in the contact angle linearly increased the bubble departure diameter while the departure time was non-linear below 45° and linear above 45° as shown in Figure 4.3. The bubble departure size being linear with contact angle is consistent with relation developed by Fritz in Equation 2.44 [38].

The larger diameters are due to the increased surface tension and can be described by the surface tension force:

$$F_{\sigma} = 2\sigma\pi a \sin(\theta), \quad (4.1)$$

where a is the bubble surface contact radius. This increased force works to 'hold' the bubble to the surface longer and thus increasing the departure time and size.

Dhir [16] also investigated the effect that the contact angle has on the heat transfer rates across the bubble interface. Since larger bubble sizes are obtainable with higher contact angles there is more bubble interface area available for interfacial heat transfer (evaporation) to allow the bubble to grow at a faster rate. Thus with increasing contact angle the net heat transfer rate should also be increased. This is depicted in Figure 4.4

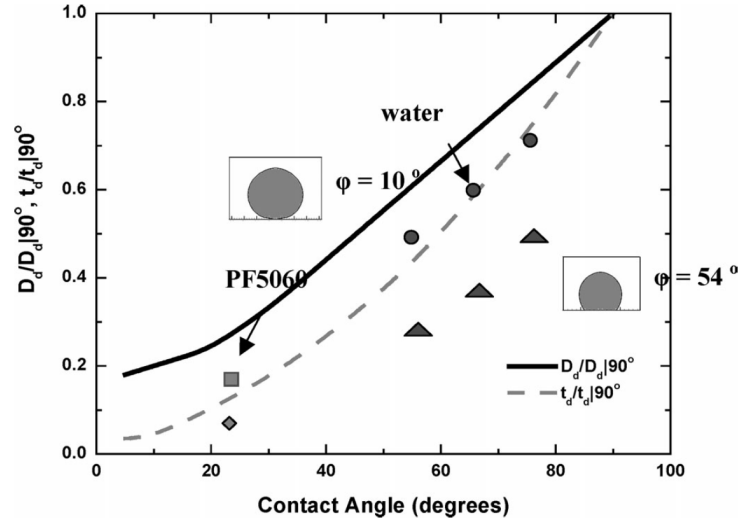


Figure 4.3: Variation of the normalized departure diameter and departure time with contact angle (fluids: water and PF5060, $\Delta T_w = 8K$, $\Delta T_{sub} = 0K$, $g = 1.0g_e$); taken from Dhir [16].

for the microlayer heat transfer and Figure 4.5 for the macrolayer heat transfer.

Based on these numerical results an increase in contact angle causes an increase in the transfer rate. Thus, the maximum capability to remove heat (CHF) should also increase.

4.2.2 Dynamic Contact Angle

The dynamic contact angle results when non-symmetric forces act at the vapor, liquid, and surface interface. Two types of contact angles arise; the advancing and the receding contact angle. The advancing angle refers to the interface region that moves towards (advances) the vapor phase while the receding contact angle refers to the to the interface the moves away (recedes) from the vapor phase. Figure 4.6 depicts both the receding and contact angles.

A detailed investigation of the differences that arise between the equilibrium, advancing,

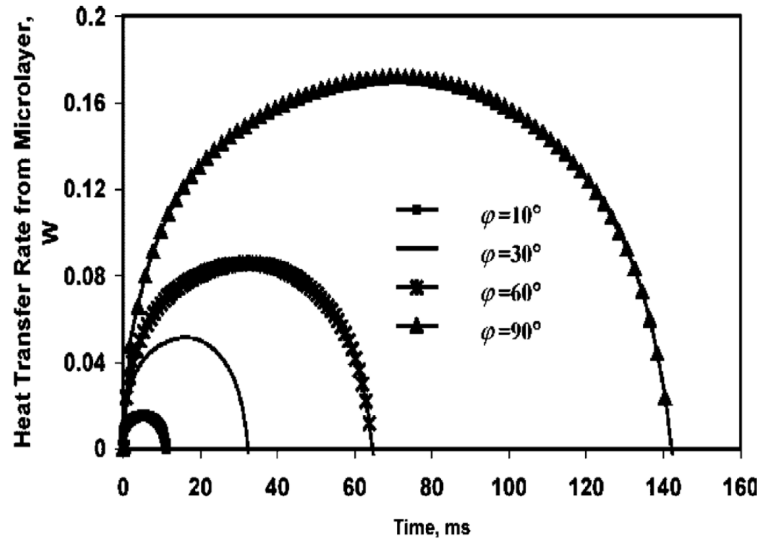


Figure 4.4: The variation of heat transfer rates with time for various contact angles from the microlayer (fluids: water, $P = 1.01\text{bar}$, $\Delta T_w = 8K$, $\Delta T_{sub} = 0K$, $g = 1.0g_e$); taken from Dhir [16].

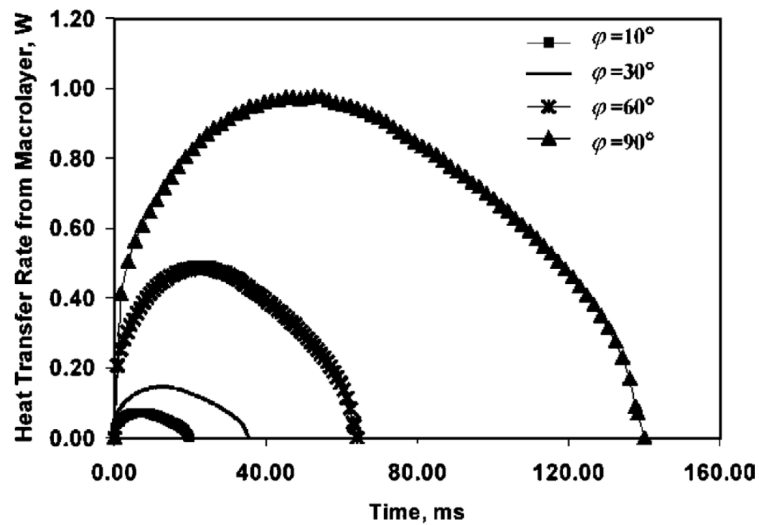


Figure 4.5: The variation of heat transfer rates with time for various contact angles from the macrolayer (fluids: water, $P = 1.01\text{bar}$, $\Delta T_w = 8K$, $\Delta T_{sub} = 0K$, $g = 1.0g_e$); taken from Dhir [16].

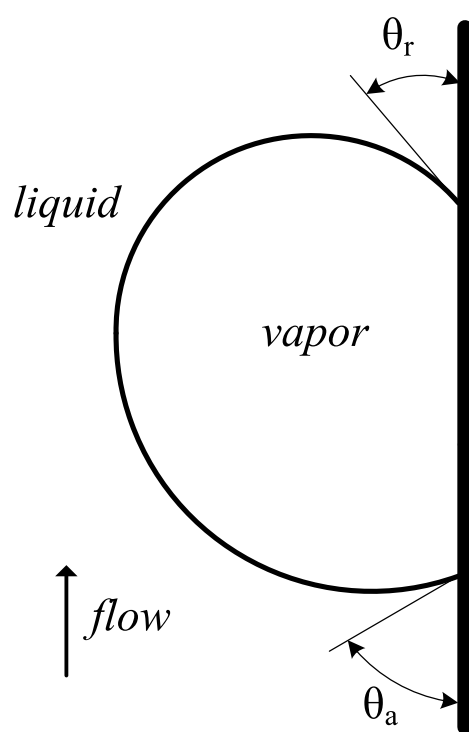


Figure 4.6: Depiction of a dynamic and receding contact angle.

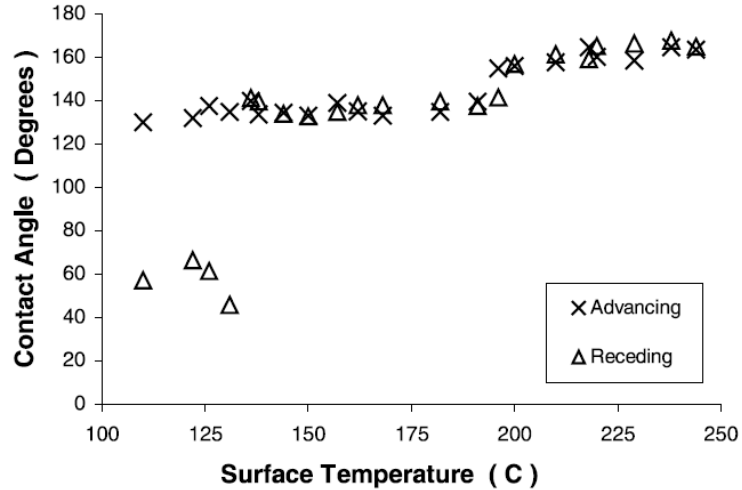


Figure 4.7: Effect of surface temperature on the contact angle for stainless steel with a surface roughness of 0.01 microns [15].

and receding contact angle was performed by Kandlikar [15]. The equilibrium contact angle resides within the limits of the advancing and receding contact angles. The advancing contact angle is always greater than the receding angle until a critical point is reached at which the angles become equal. This is depicted in Figure 4.7. Kandlikar [15] points out that at the point of which the angles become equal is simultaneous of the CHF point (beginning of the transition point). Other than this transition point the actual receding and advancing contact angle appear to be independent of the surface temperature. Based on this a constant static contact angle will be considered for the CHF point.

4.3 Wall Thermal Properties

The importance of the thermal properties of the wall have been described by Wright [70] and Misale [17]. In an effort by Wright [70] to develop a CHF correlation three correlation iterations were developed until a final expression for predicting the onset of CHF

was reached. These correlations, although utilizing an empirical fit method of important non-dimensional parameters, demonstrate the need to capture the thermal effects of the heated wall when trying to model the onset of CHF. The first correlation developed had a $\pm 22\%$ error when compared to experimental data. The second iterated correlation included a term to capture the density differences between the vapor and liquid. This correlation had between -11% to $+19\%$ error. The final correlation included the conductivity, density, and specific heat of the fluid and heated surface. This resulted in an error of $\pm 8.5\%$. This shows that in order to reduce the error of CHF models the properties of the heating surface must be accounted for which effects the transient conduction phase of nucleate boiling. This may provide in part an explanation of why correlations developed for a particular set data perform poorly when applied to another set. Since correlations developed for CHF typically do not account for the heated material, the constants developed may be unique to the thermal characteristics of the heating material and the surface characteristics. When a correlation is applied to another data set these thermal and surface characteristics may be very different and thus even when the correlation is developed for the range of fluid flow characteristics specified, the correlation may give poor results because the surface and material characteristics have not been properly captured.

Misale [17] performed a two-dimensional numerical study on the effects of the wall thermal properties on the resulting flow and temperature distribution in a natural circulation loop. The studied loop included a lower horizontal heated surface with a constant boundary heat flux and an upper horizontal heat sink held at a constant temperature. Figure 4.8 shows the resulting radial velocity profile for varying Grashof numbers.

$$Gr = \frac{g\beta(T_w - T_\infty)L^3}{\nu^2} = \frac{\text{Buoyancy Force}}{\text{Viscous Force}} \quad (4.2)$$

At low Grashof numbers the flow behaves like parabolic laminar flow. Increasing the heater surface power causes the peak velocity to shift from the central pipe axis to the outer regions of the pipe ($r/R_{int} \approx 0.7$). Due to the increased velocity gradient at the

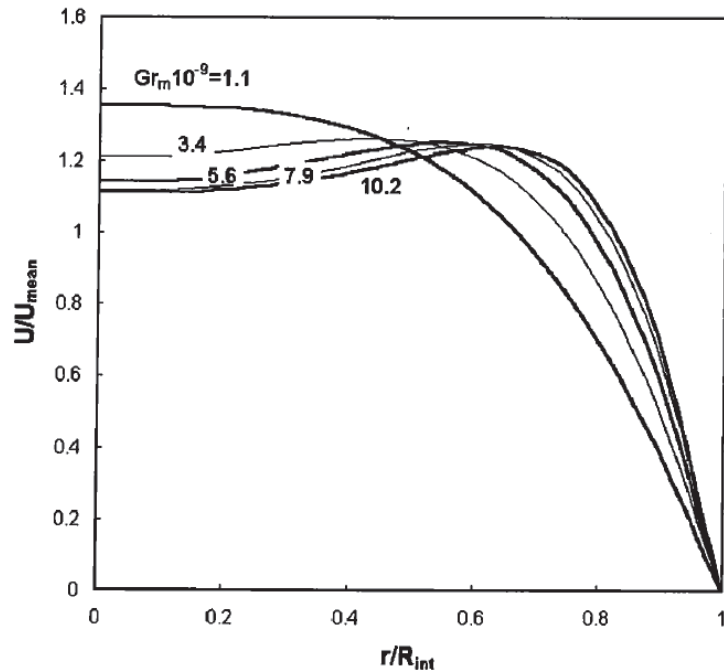


Figure 4.8: Radial velocity profile for various Grashof numbers for natural circulation loop [17].

wall the viscous forces also increase.

Three materials were studied by Misale: copper, steel, and Plexiglas in order to investigate the effect of thermal capacity and conductivity on the Reynolds number. He found that with decreasing thermal capacity and conductivity the Reynolds number increases due to the increased temperature gradient through the heated surface. This can be simply understood by considering the case of a constant heat flux where the result of decreasing the conductivity is to increase the temperature gradient through the wall. The specific heat acts as a resistance to a change in temperature in that for large heat capacities the rate of change of temperature with respect to time will be small. This means for the nucleation process the local surface temperature will have a minimal change for a surface with a large heat capacity than for that of a surface with a relatively small heat capacity.

The two-dimensional results compare well with experimental results while the previous

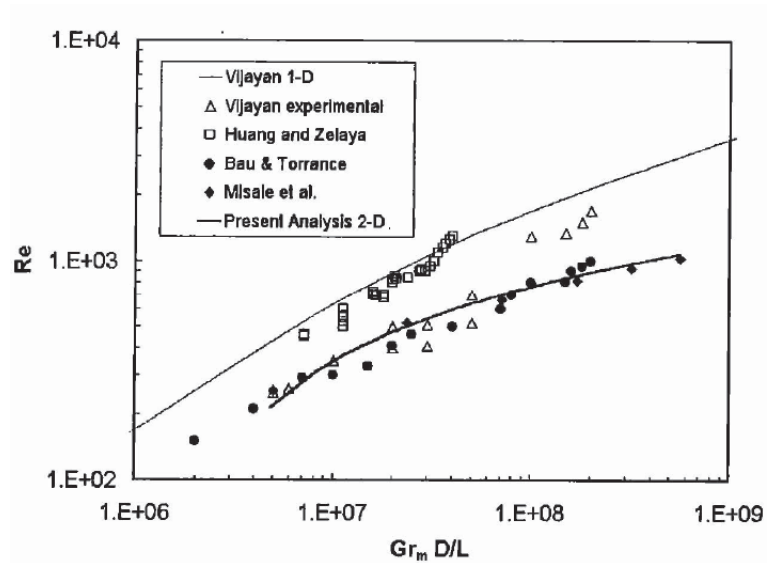


Figure 4.9: Steady-state natural circulation results from Misale [17].

one-dimensional results over predict the Reynolds number (Figure 4.9).

The following general characteristics of the numerical study can be summarized:

- The velocity profile is near parabolic for low Grashof numbers and becomes off-axially centered for higher Grashof numbers due to the increased surface temperatures.
- The Nusselt number increases as linear function of increasing the Grashof number.
- The friction factor increases as linear function of increasing the Grashof number.
- The one-dimensional model over predicts the Reynolds number as a function of the Grashof number. The two-dimensional model does well.
- The one-dimensional models predict higher velocities than two-dimensional model investigated. This higher prediction is due to the neglecting of axial conduction along the loop surface.

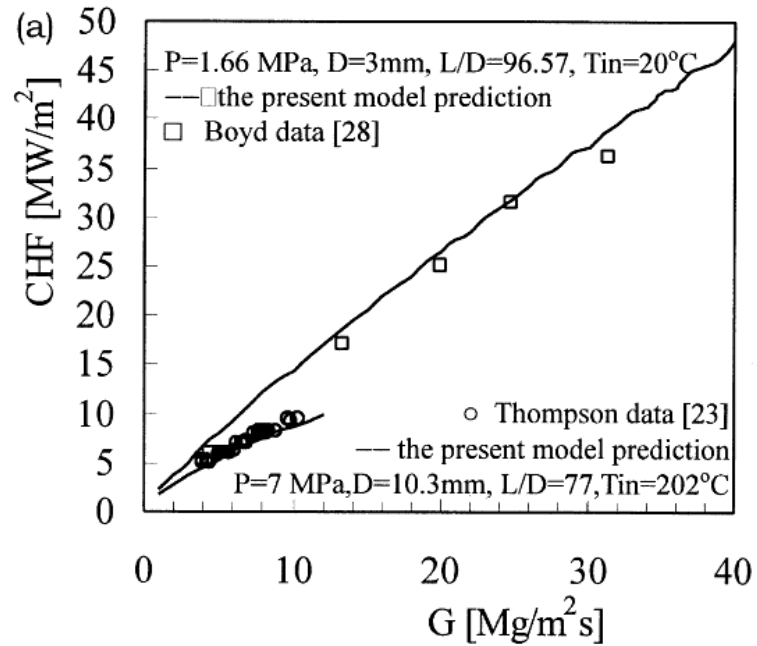


Figure 4.10: Mass velocity effect on the critical heat flux velocity; from [8].

4.4 Bulk Subcooling

The effects of bulk subcooling were studied by Dhir [16] in a numerical simulation and compared to experimental data. Increased subcooling increased the time to bubble departure and decreased the bubble departure size. Bulk subcooling has the effect to increase the temperature gradient across the thermal boundary layer.

4.5 Mass Flux

Liu et al. [8] observed various parameter effects on the CHF value from a collection of CHF databases totaling over 2,000 data points. The parametric effect of changing the mass velocity is observed to have a linear effect on the CHF value. This is shown in Figure 4.10.

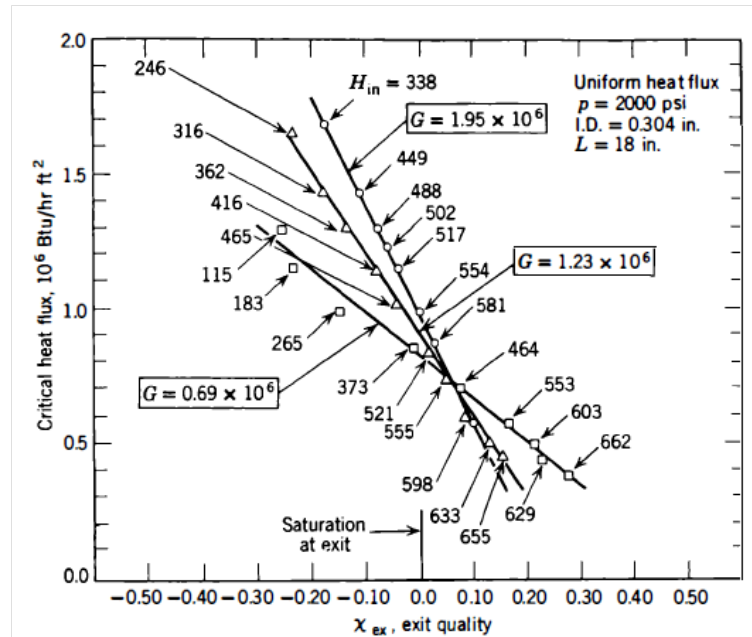


Figure 4.11: Mass velocity effect on the critical heat flux velocity[?]; figure from [18].

An inverse mass flux effect was been observed by Weatherhead [?] as shown in figure Figure 4.11 from [18]. At higher mass fluxes and higher qualities an increase in max flux reduces the CHF. This is due to an increase in the entrainment phenomenon of the film in the annular flow.

4.6 Surface Roughness

Wall roughness plays a similar role as the mass flux effect. In the regimes below the annular mist regime the effect of increasing the surface roughness is to enhance the local convective forces and thus enhance the CHF value. However, a degradation occurs when in the annular mist regime since increasing mass flux increases the entrainment and thus results in a decrease in the CHF value. This is represented in Figure 4.12.

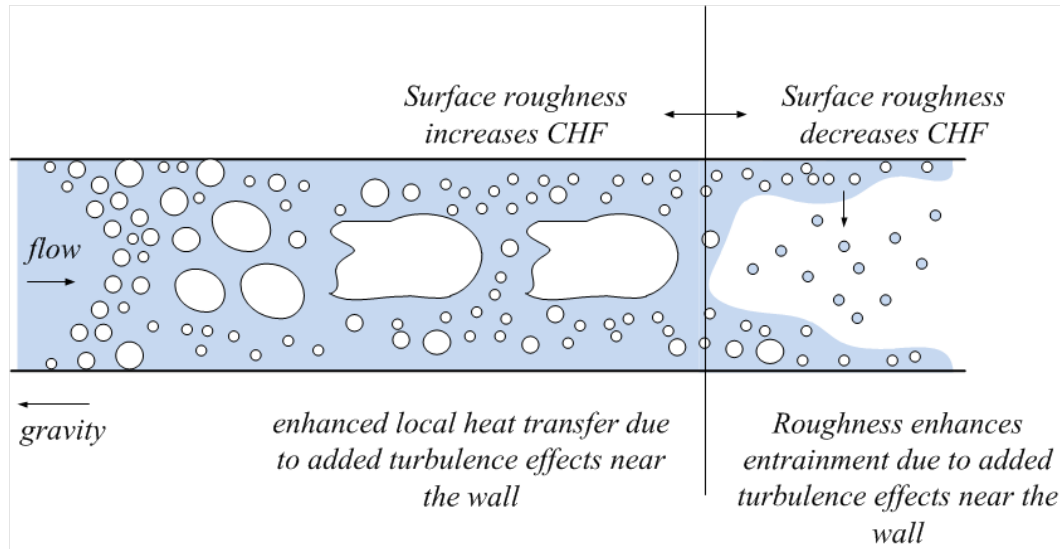


Figure 4.12: Surface roughness effects on the CHF value.

4.7 Wall Superheat

The effects of wall superheat was studied by Dhir [16] in a numerical simulation and compared to experimental data. Increased wall superheat decreases the time to bubble departure and increases the bubble departure size. This is due to the increase in the temperature gradient through the thermal boundary layer, suppression of the boundary layer, and the increase in the the nucleation site activation potential. This dependency is observed in many expressions for the nucleation site density as demonstrated in Section 2.2.2.

4.8 Channel Gap Width

The effect of the flow channel gap width on the critical heat flux was investigated by Kureta and Akimoto [9]. In general there appears to be only a minor sensitivity of the channel gap width on the CHF value as shown in Figure 4.13 . At a given mass flux a decrease in the channel width causes an increase in velocity suppressing the thermal

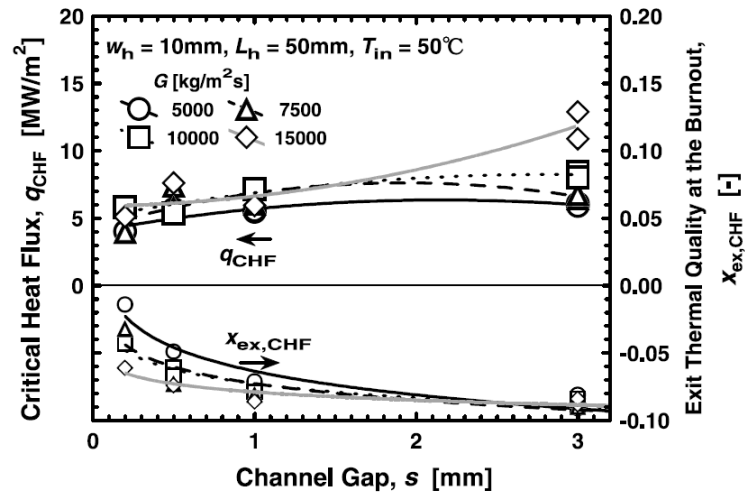


Figure 4.13: Channel gap width effects on the critical heat flux value by Kureta and Akimoto[9].

boundary layer resulting in smaller bubbles. This is a result of the dependency of the bubble size on the thermal boundary layer temperature profile. Bubbles cannot grow beyond a position where the boundary temperature is lower than the required superheat of the bubble. The increase in velocity has the effect of increasing the convective heat removal mechanisms. At larger channel widths lower velocities exist increasing the allowable bubble size at departure but also decreasing the convective mechanisms. The decrease in the convective mechanisms is believed to be counteracted by the increased local turbulence from the larger bubble departure resulting in a net minimal effect.

4.9 Heated Surface Length

Heated length effects were investigated by Kureta and Akimoto [9] in the development on their empirical critical heat flux correlation. It was observed that an increased sensitivity of the heated length on the CHF value exists for higher inlet subcooling values. This dependency vanishes at lower subcooling conditions; this is shown in Figure 4.14. This is a result of the local fluid enthalpy. Considering a hypothetical channel with some

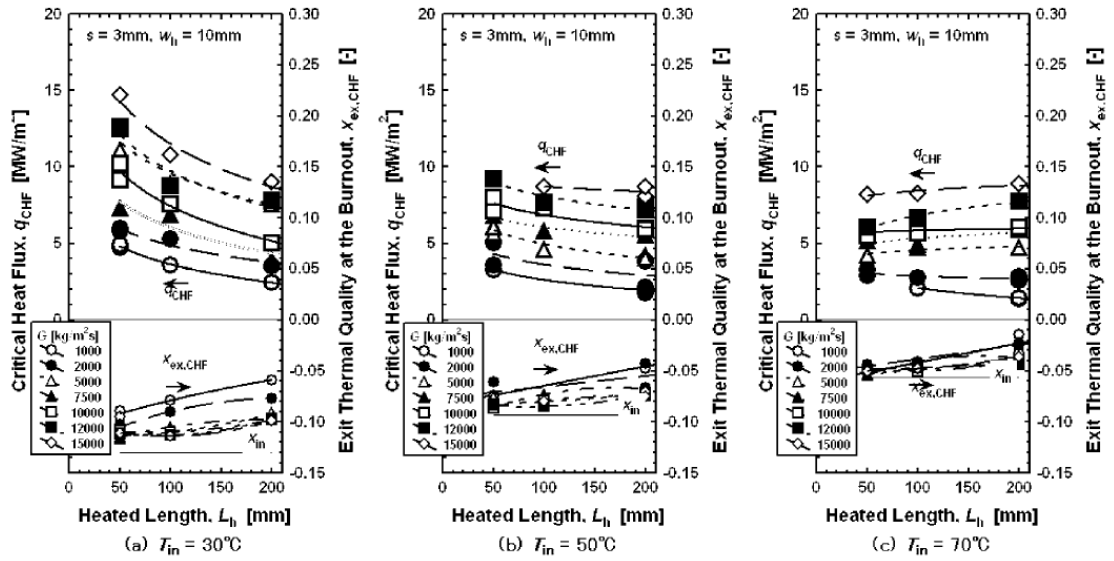


Figure 4.14: Heated length effects on the critical heat flux observed by Kureta and Akimoto[9].

length, at smaller inlet subcooling values the CHF will occur in a shorter channel length whereas at higher subcooling values CHF will occur at larger channel lengths. For higher subcooling values decreasing the heated length will reduce the quality near the channel exit allowing for a higher heat flux to obtain similar critical quality conditions.

4.10 Rectangular Channel Aspect Ratio

Monde [4] carried out CHF experiments for natural convective boiling at atmospheric pressure in vertically oriented rectangular channels. Water and ethanol were studied and the CHF results plotted against the aspect ratio of the channel length divided by the channel width (l/s). He showed that at increasing aspect ratios the CHF decreases hyperbolically. This is most likely due to the observance of a slight decrease in the heat transfer coefficient as the channel width (s) becomes smaller. This is similar to the effect discussed in Section 4.8.

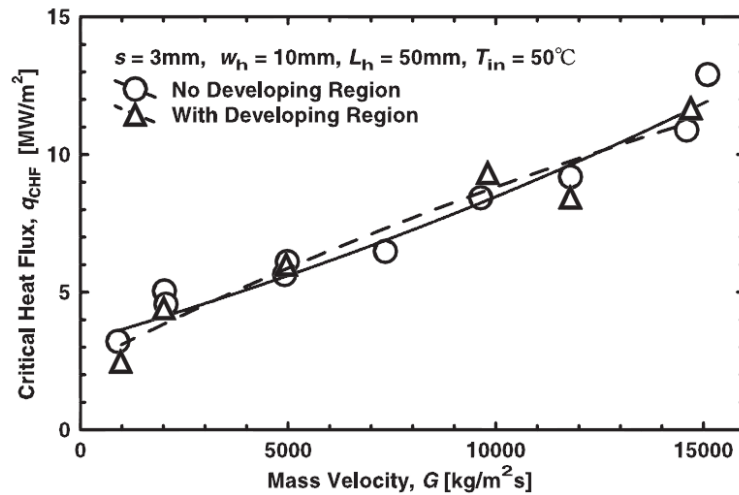


Figure 4.15: Developing length effect on CHF [9].

4.11 Developing Length Effects

Kureta and Akimoto [72] performed studies of the effects of the developing length on the onset of CHF. The developing length tests were performed at $L/D = 46$. They found no appreciable difference in the critical heat flux between having and not having a developing region for various mass fluxes as shown in Figure 4.15.

Chapter 5: Experimental Data

Two experimental configurations are used to verify model performance. The data from the University of Wisconsin are used to confirm the validity and capability to capture the non-uniform heat flux configurations. The second test series utilized is that from Columbia University collected for the EPRI CHF database. Since a large number of data points exists for this test series this set is used to evaluate the statistical performance of the proposed CHF model.

5.1 Bundle Data of the University of Wisconsin [10]

Experimental data from the University of Wisconsin [10] is used as the first data set for the development and testing of a mechanistic based CHF model. A high-pressure forced flow test facility was constructed with a 2x2 bundle configuration. A non-uniform heat flux profile was applied equally to all four rods. The tested conditions for CHF are presented in Table 5.2 with the geometric configuration depicted in Figure 5.1. The non-uniform power profile of the tested rod is given by Equation 5.1. The average heat flux (\bar{q}'') is calculated by Equation 5.2. Thermocouples are placed at various radial and axial locations for each of the four heated rods. The axial location for thermocouple measurements are provided in Table 5.2. These elevations are relative to the lowest elevation of the heated length. The results of the critical heat flux testing is summarized in Table 5.3.

Table 5.1: Experimental bundle data of the University of Wisconsin .

Flow Area	4.3185 cm^2
Heated Pin Length	38.1 cm
Critical Rod Power	39.98 - 55.98 kW
Critical Heat Flux	837.67 - 1077.60 kW/m^2
Mass Flux	0 - 400 $kg/m^2 - s$
Pressure	110 - 200 kPa
Centerline Grid Spacer 1 Location	1.5 [m]
Centerline Grid Spacer 2 Location	1.75 [m]
Centerline Grid Spacer 3 Location	2.01 [m]

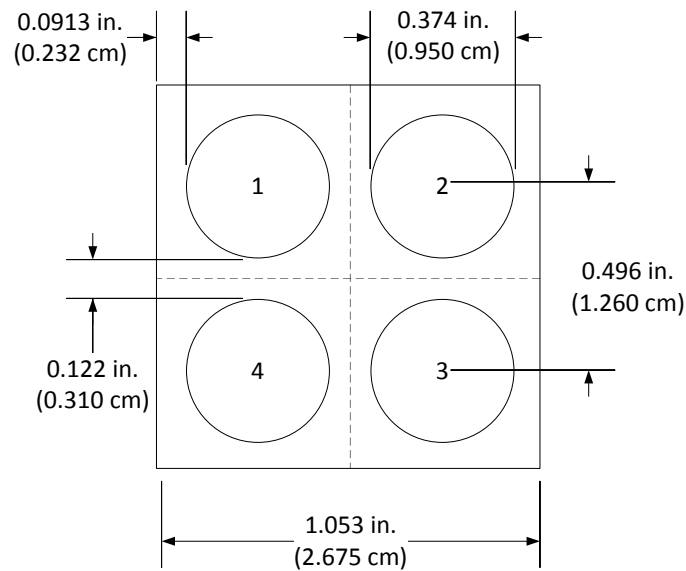


Figure 5.1: University of Wisconsin bundle test section[10].

Table 5.2: Thermocouple elevation placement from bottom of heated length for the University of Wisconsin CHF tests .

Elevation [m]
0.9619
1.0381
1.3335
1.4620
1.5382
1.7780
1.9746

$$\frac{\bar{q}''(z)}{\bar{q}''} = \theta_0 + \theta_1 \cos(2\theta_2 (z/L - 1/2))$$

$$\theta_0 = 0.8187458177$$

$$\theta_1 = 0.6812541823$$

$$\theta_2 = 2.436354311$$

L = total heated length

z = local position

(5.1)

$$\bar{q}'' = \frac{q_{pin}}{A_h} \quad (5.2)$$

Table 5.3: Experimental bundle results of University of Wisconsin [10].

Test	Inlet Temperature [°C]	Pressure [MPa]	Mass Flux [kg/m ² - s]	Average Critical Rod Power [kW]	Critical Heat Flux [kW/m ²]	Normalized CHF Location
1	254.33	12.55	585.68	46.06	856.70	0.731
2	251.19	12.30	740.34	51.03	950.87	0.731
3	250.61	12.37	740.97	52.00	968.44	0.731
4	251.05	12.11	889.43	55.98	1042.03	0.731
5	251.17	12.11	889.61	55.98	1041.97	0.731
6	275.29	13.02	542.19	39.98	861.90	0.667
7	273.41	12.90	547.46	40.67	877.82	0.667
8	271.56	12.47	701.66	45.00	837.67	0.731
9	271.12	12.47	702.05	45.00	969.24	0.667
10	265.52	12.16	860.17	50.01	1077.60	0.667
11	269.14	12.20	852.36	49.00	1056.04	0.667

Table 5.4: EPRI CHF database organized by sponsor.

Test Number	Section	Number of Test Runs	Number of Data Points	Sponsor
1-71		76	4745	Combustion Engineering Inc. (CE)
101-170		73	2485	Westinghouse Electric Co. (WH)
201-207		8	526	Exxon Nuclear Co. (EX)
301-318		21	871	General Electric Co. (GE)
401-411		9	744	Babcock & Wilcox Co. (BW)
501-517		17	517	United Nuclear Corp. (UN)
601-603		13	400	Atomic Energy of Canada Limited (AECL)
701-708		10	644	Idaho National Engineering Laboratories LOFT program (IN)
801-810		9	145	United Kingdom Atomic Energy Authority (UK)
Total		236	11,077	

5.2 EPRI Experimental Data

Columbia University compiled an extensive database of over 11,000 data points for 235 different test section assemblies [52, 53, 54, 55]. An overview of the test campaign is provided in Table 5.4.

The data from the General Electric test series (test sections 301-318 Table 5.4) are used as the focus for the model development here. Characteristics of each of the considered test series are provided in Table 5.5 where a total 871 data points were utilized. All test sections have the same geometry as described in Table 5.6 and depicted in Figure 5.2. All test configurations utilized a uniform power profile with varying radial peaking factors for each set of test runs. Radial peaking factors are identified in Table 5.7 through Table 5.27. All CHF test conditions related to the General Electric test series (test sections 301-318) are provided in Appendix G.

Table 5.5: EPRI CHF datasets used for analysis; 'in' refers to the CHF occurring on the inner rods of the assembly, 'out' refers to CHF occurring on the outer rods of the assembly as depicted in Figure 5.2.

Data Set #	EPRI Section #	Test #	# of Spacers	Grid Loss	Heated Length [m]	CHF Location	Pressure Range [MPa]	Inlet Quality	Critical Quality	Inlet Mass Flux [kg/m ² -s]	# Data Points
1	301	7	0.80	1.83	1.83	out	4.13 - 8.62	0.22 - 0.72	0.22 - 0.72	305.2 - 1745.5	54
2	302	4	1.47	1.83	1.83	out	4.14 - 8.62	0.25 - 0.70	0.25 - 0.70	344.5 - 1730.6	48
3	303	3	1.47	1.83	1.83	out	6.89 - 6.89	0.21 - 0.52	0.21 - 0.52	686.3 - 1798.4	26
4	304	7	0.80	1.83	1.83	in	6.86 - 6.9	0.26 - 0.61	0.26 - 0.61	687.6 - 1745.5	26
5	305	3	1.47	1.83	1.83	in	6.89 - 6.89	0.36 - 0.42	0.36 - 0.42	1032.1 - 1061.9	4
6	306	3	1.47	1.83	1.83	in/out	6.89 - 9.65	0.15 - 0.65	0.15 - 0.65	328.2 - 1696.6	48
7	307	2	1.47	1.22	1.22	in/out	6.89 - 6.89	0.13 - 0.45	0.13 - 0.45	672.7 - 1706.1	17
8	307.1	2	1.47	1.22	1.22	in/out	6.89 - 6.89	0.19 - 0.30	0.19 - 0.30	1323.7 - 1373.9	5
9	307.2	2	1.47	1.22	1.22	out	6.89 - 6.89	0.15 - 0.44	0.15 - 0.44	665.9 - 1542.0	7
10	308	3	1.47	1.83	1.83	out	6.89 - 6.89	0.21 - 1.02	0.21 - 1.02	128.8 - 1704.8	31
11	309	3	1.47	1.83	1.83	in	6.89 - 6.89	0.19 - 0.90	0.19 - 0.90	131.6 - 1717.0	40
12	310	3	1.47	1.83	1.83	out	6.89 - 6.89	0.18 - 1.32	0.18 - 1.32	130.2 - 1715.6	30
13	311	3	1.47	1.83	1.83	out	6.83 - 9.78	0.12 - 0.64	0.12 - 0.64	366.2 - 1668.2	59
14	312	3	1.47	1.83	1.83	out	6.55 - 10.02	0.09 - 0.73	0.09 - 0.73	339.1 - 1668.2	55
15	313	7	0.80	1.83	1.83	out	6.86 - 9.93	0.18 - 0.72	0.18 - 0.72	339.1 - 1668.2	60
16	314	3	1.47	1.83	1.83	out	6.89 - 7.17	0.16 - 0.76	0.16 - 0.76	325.5 - 1708.9	34
17	315	3	1.47	1.83	1.83	out	6.89 - 9.77	0.13 - 0.68	0.13 - 0.68	339.1 - 1722.4	70
18	316	3	1.47	1.83	1.83	out	4.83 - 9.79	0.13 - 0.70	0.13 - 0.70	325.5 - 1695.3	65
19	316.1	3	1.47	1.83	1.83	in/out	6.89 - 9.72	0.18 - 0.71	0.18 - 0.71	325.5 - 1681.7	44
20	317	3	1.47	1.83	1.83	out	6.76 - 15.55	-0.03 - 0.79	-0.03 - 0.79	335.0 - 3573.7	76
21	318	3	1.47	1.83	1.83	in	6.86 - 15.59	0.04 - 0.36	0.04 - 0.36	1297.9 - 4297.9	72
							4.13-15.59	-0.03 - 1.02	-0.03 - 1.02	128.8 - 4297.9	871

Table 5.6: General Electric test geometry from EPRI CHF database.

Number of heated rods	16
Number of unheated rods	0
Rod pitch	0.738 in.
Rod diameter	0.563 in.
Flow area	5.232 in. ²

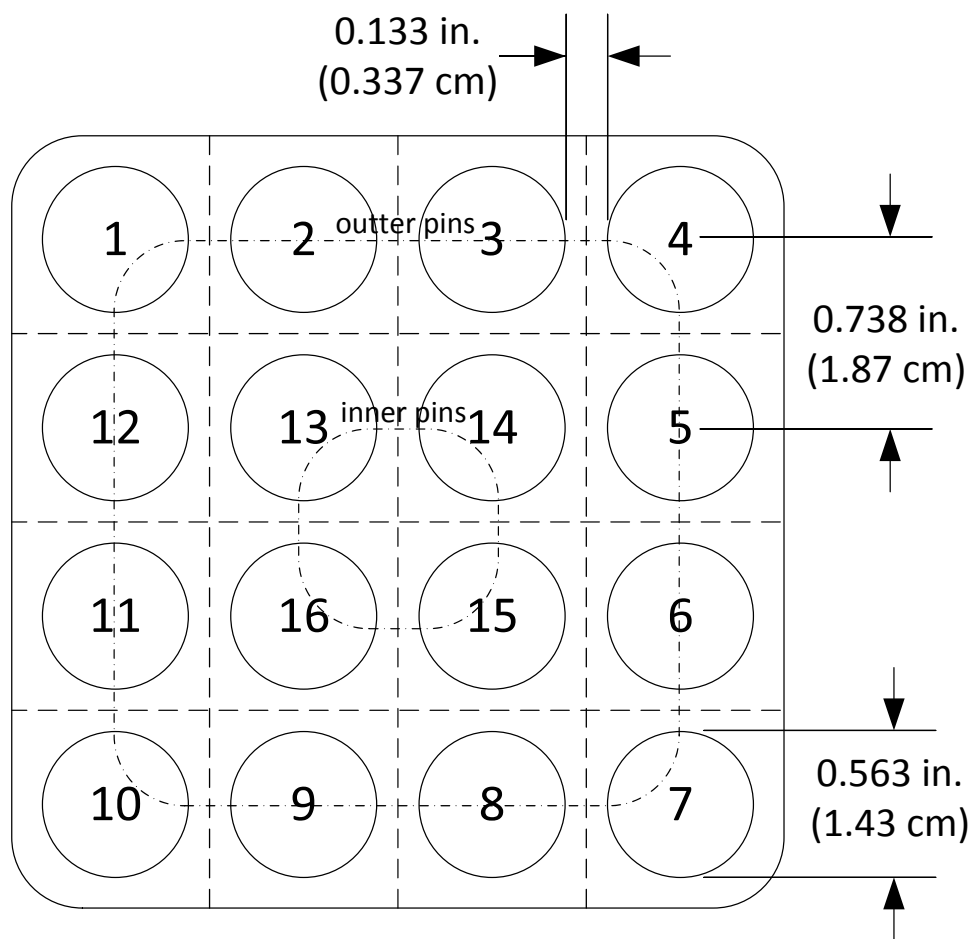


Figure 5.2: General Electric test section assembly layout for tests 301-318.

Table 5.7: General Electric radial peaking for EPRI test section 301.

EPRI test 301.			
1.010	0.995	0.998	0.995
1.002	0.998	1.018	0.997
1.008	1.000	0.995	0.990
1.002	0.997	1.000	1.000

Table 5.8: General Electric radial peaking for EPRI test section 302.

EPRI test 302.			
1.002	0.988	1.004	1.004
0.988	1.004	0.988	1.013
1.006	0.993	1.003	0.996
1.015	0.988	1.003	1.006

Table 5.9: General Electric radial peaking for EPRI test section 303.

EPRI test 303.			
1.002	0.989	1.004	1.004
0.989	1.004	0.989	1.005
1.006	0.994	1.003	0.996
1.016	0.989	1.003	1.006

Table 5.10: General Electric radial peaking for EPRI test section 304.

EPRI test 304.			
0.756	0.991	0.991	0.756
0.991	1.262	1.262	0.991
0.991	1.262	1.262	0.991
0.756	0.991	0.991	0.756

Table 5.11: General Electric radial peaking for EPRI test section 305.

EPRI test 305.			
0.755	0.991	0.991	0.755
0.991	1.263	1.263	0.991
0.991	1.263	1.263	0.991
0.755	0.991	0.991	0.755

Table 5.12: General Electric radial peaking for EPRI test section 306.

EPRI test 306.			
1.000	1.000	1.000	1.000
1.000	1.000	1.000	1.000
1.000	1.000	1.000	1.000
1.000	1.000	1.000	1.000

Table 5.13: General Electric radial peaking for EPRI test section 307.

EPRI test 307.			
1.000	1.000	1.000	1.000
1.000	1.000	1.000	1.000
1.000	1.000	1.000	1.000
1.000	1.000	1.000	1.000

Table 5.16: General Electric radial peaking for EPRI test section 308.

EPRI test 308.			
1.210	1.110	1.110	0.940
1.110	0.940	0.940	0.940
1.110	0.940	0.940	0.930
0.940	0.940	0.940	0.940

Table 5.14: General Electric radial peaking for EPRI test section 307.1.

EPRI test 307.1.			
1.000	1.000	1.000	1.000
1.000	1.000	1.000	1.000
1.000	1.000	1.000	1.000
1.000	1.000	1.000	1.000

Table 5.17: General Electric radial peaking for EPRI test section 309.

EPRI test 309.			
0.940	0.940	1.100	0.940
0.940	1.210	0.940	1.100
1.110	0.950	0.950	0.940
0.940	1.100	0.940	0.940

Table 5.15: General Electric radial peaking for EPRI test section 307.2.

EPRI test 307.2.			
1.000	1.000	1.000	1.000
1.000	1.000	1.000	1.000
1.000	1.000	1.000	1.000
1.000	1.000	1.000	1.000

Table 5.18: General Electric radial peaking for EPRI test section 310.

EPRI test 310.			
1.610	1.610	1.130	0.950
1.610	1.220	0.950	0.660
1.110	0.950	0.660	0.650
0.950	0.660	0.650	0.650

Table 5.19: General Electric radial peaking for EPRI test section 311.

EPRI test 311.			
1.000	1.000	1.000	1.000
1.000	1.000	1.000	1.000
1.000	1.000	1.000	1.000
1.000	1.000	1.000	1.000

Table 5.20: General Electric radial peaking for EPRI test section 312.

EPRI test 312.			
1.271	1.271	1.041	0.897
1.271	1.041	0.897	0.897
1.041	0.897	0.897	0.897
0.897	0.897	0.897	0.897

Table 5.21: General Electric radial peaking for EPRI test section 313.

EPRI test 313.			
0.988	0.993	1.002	1.015
0.990	0.997	1.019	1.002
1.002	1.009	0.998	0.996
0.988	1.005	1.006	0.989

Table 5.22: General Electric radial peaking for EPRI test section 314.

EPRI test 314.			
1.285	1.285	1.085	0.889
1.285	1.085	0.889	0.889
1.085	0.889	0.889	0.889
0.889	0.889	0.889	0.889

Table 5.23: General Electric radial peaking for EPRI test section 315.

EPRI test 315.			
0.992	0.990	0.989	1.018
0.992	1.005	0.993	0.999
1.001	1.014	1.001	0.999
0.990	1.004	1.003	1.008

Table 5.24: General Electric radial peaking for EPRI test section 316.

EPRI test 316.			
0.992	0.990	0.989	1.018
0.992	1.005	0.993	0.999
1.001	1.014	1.001	0.999
0.990	1.004	1.003	1.008

Table 5.25: General Electric radial peaking for EPRI test section 316.1.

EPRI test 316.1.			
0.992	0.990	0.989	1.018
0.992	1.005	0.993	0.999
1.001	1.014	1.001	0.999
0.990	1.004	1.003	1.008

Table 5.27: General Electric radial peaking for EPRI test section 318.

EPRI test 318.			
0.922	0.928	0.932	0.940
0.929	1.232	1.204	0.920
0.922	1.221	1.230	0.929
0.928	0.931	0.915	0.917

Table 5.26: General Electric radial peaking for EPRI test section 317.

EPRI test 317.			
1.204	1.179	1.099	0.901
1.196	1.100	0.918	0.914
1.111	0.921	0.905	0.911
0.902	0.921	0.912	0.908

Chapter 6: Proposed Critical Heat Flux Model

Derived here will be the framework for determining a limiting surface heat flux for flow boiling. This involves determining the separate heat transfer components that make up the total heat flux. Focus here is given to the phenomena that occur very near the surface (scale of the bubble size). This approach is investigated by relating the forces acting on a bubble growing on a heated surface within a flow field. The limiting heat removal point (the critical heat flux) is hypothesized to occur at the highest attainable boiling frequency at a nucleation site given a nucleation site density and size over a heated surface. The highest attainable boiling frequency implies that at the same time a bubble departs from a nucleation site the next bubble immediately begins to grow as qualitatively demonstrated in Figure 6.1. This model does not depend on the coalescence of departed bubbles away from the surface; rather it is postulated that the coalescence is a result of the large vapor generation from the highest attainable boiling frequency.

For heat transfer to occur from the local superheated fluid near the wall to the bubble through the interfacial evaporation process, the bubble internal temperature must be lower than the local fluid superheat temperature (i.e. a non-equilibrium state exists). When the bubble internal vapor temperature equals the local superheat temperature the evaporative heat transfer that promotes bubble growth ceases. This represents the physical limit for boiling heat transfer to occur. The bubble(s) are thus assumed to be at the maximum potential internal vapor temperature dependent on and set equal to the wall superheat temperature.

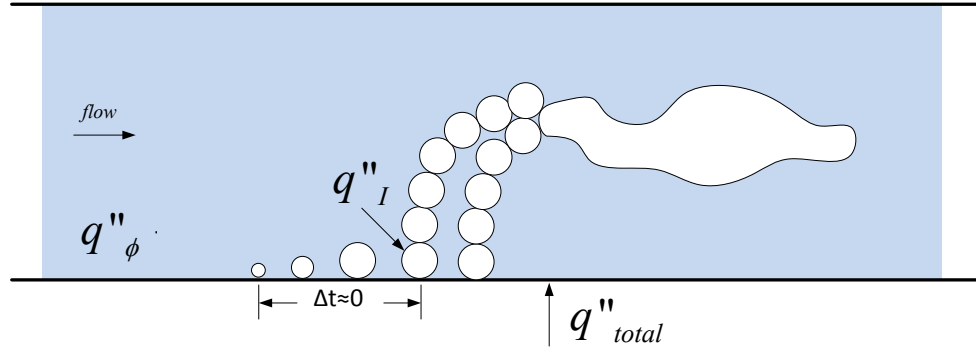


Figure 6.1: Continuous boiling frequency near surface.

6.1 Heat Transfer Modes

The total surface heat flux can be partitioned into the following generalized heat transfer modes as presented in Section 2.3:

- $q''_{1\phi}$ - convective heat flux
- q''_I - evaporation (interface) heat flux
- q''_{trans} - transient conduction heat flux
- q''_{slide} - sliding transient conduction heat flux

The total heat flux is expressed by Equation 6.1 with the mechanisms depicted in Figure 6.2.

$$q''_{total} = q''_{1\phi} + q''_I + q''_{trans} + q''_{slide} \quad (6.1)$$

It is assumed that the heat flux at the surface is high enough (due to the CHF condition) such that the bubble generation rate is continuous at a given nucleation site. This phenomenon was also considered by Zuber [22] where it was observed that as the surface heat flux increases the number of activated sites increases up to a point. Following a

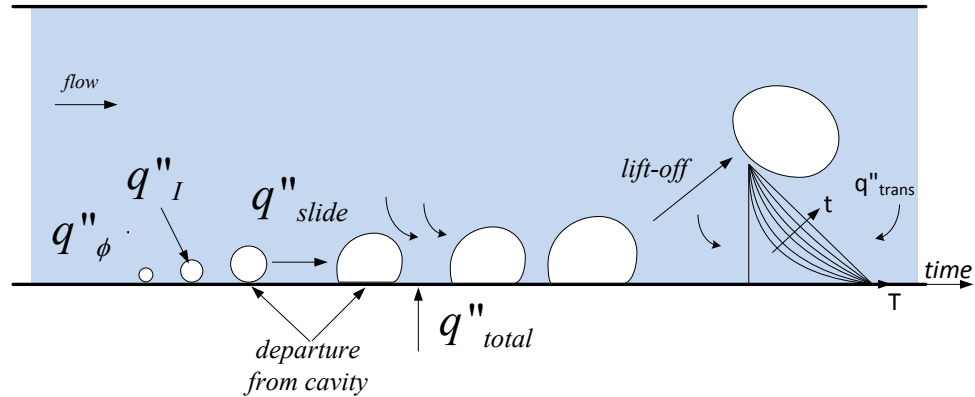


Figure 6.2: Boiling heat transfer mechanisms at a heated surface.

further increase in heat flux, causes an increase in the boiling frequency, not an increase in the number of activated sites. It appears that a limit to the nucleation site density does in fact exist as hypothesized with the use of Equation 2.75. The number of sites only increases once a continuous vapor column is formed. At this condition, the point of the potential limit of the nucleation site to remove energy has been reached. It has been considered by many the behavior of the nucleation site density as a function of heat flux (see Section 2.2.2).

Due to the high heat flux, the bubble departure from a cavity and bubble lift-off from the surface are assumed coincident (i.e. the bubble does not slide on the heated surface). This is assumed due to the initial rapid growth of the bubble causing the bubble to be ejected away from the surface with a such a large force that any lateral drag that results from the flow conditions is overcome to prohibit much sliding of the bubble. The limited sliding was also observed by Del Valle and Kenning [11] in observance of their boiling data near the CHF condition (90%). Sliding is postulated to be more of a contributor to the low heat flux nucleate boiling process where the evaporation force and the lateral drag force are of the same order of magnitude.

With these assumptions, liquid is not allowed to occupy the region of the previously departed bubble nor is there a lateral displacement of liquid along the surface where boiling does not occur due to the prohibition of bubble sliding. Thus, the transient conduction heat flux mechanism at the nucleation site and heat removal from sliding of a bubble along the surface are neglected from Equation 6.1. The two major contributions to the total heat flux is then expressed by Equation 6.2.

$$q''_{total} = q''_{1\phi} + q''_I \quad (6.2)$$

Relations describing the evaporative interfacial energy transfer (q''_I) and the single phase heat transfer ($q''_{1\phi}$) are developed in the following sections.

6.2 Bubble Forces Perpendicular to a Vertical Heated Surface

An extensive review of the forces acting on a growing bubble are provided by Thorncroft [73, 74] for various boiling configurations. A similar force balance as that employed here was performed by Kandlikar [75] in the investigation of orientation effects on the CHF condition. For a vertically aligned flow channel the assumed significant forces acting perpendicular to a heated surface are:

- surface tension force (F_σ)
- evaporative thrust force (F_{evap})
- bubble shear lift force (F_{SL})

These forces are depicted in Figure 6.3. The forces in action on this volume are described in the following subsections. For this analysis only the forces perpendicular to the surface are assumed to participate in the departure of the bubble. The buoyancy force is neglected since it is assumed to be negligible when compared to the evaporative thrust force. This is due to being near the CHF condition (i.e. large heat fluxes and evaporation

rates). The lateral drag force (in the direction of flow) on a bubble is also neglected here based on the assumption this force is small relative to the assumed forces. Both these forces work to remove the bubble from the surface.

6.2.1 Surface Tension (F_{σ})

The surface tension force describes the force along the bubble interface contact line with the surface. This force works to keep the bubble interface attached to the surface. This force is expressed by Equation 6.3 with variables defined by Figure 6.3.

$$F_{\sigma,y} = 2\pi\sigma a \sin(\theta)$$

(6.3)

σ = surface tension

a = radius of vapor and solid contact area

θ = liquid-vapor-solid interface contact angle

Here the static contact angle will be used (not the receding or advancing contact angle) resulting in an equal and opposite horizontal surface tension force and to the fact of being near the CHF condition since at this condition it is observed that advancing and receding contact angles are equal (Section 4.2).

It is noted that the maximum surface tension force occurs when the contact angle between the bubble and heated surface is 90 degrees. This will yield the highest theoretically required heat flux condition to eject a bubble from a nucleation site.

6.2.2 Evaporative Thrust Force (F_{evap})

The evaporative thrust force derives from the bubble growth rate due to the interfacial mass transfer across the bubble interface. This force is identical to that of the thrust force that results by mass discharge across a nozzle boundary. This force is depicted in

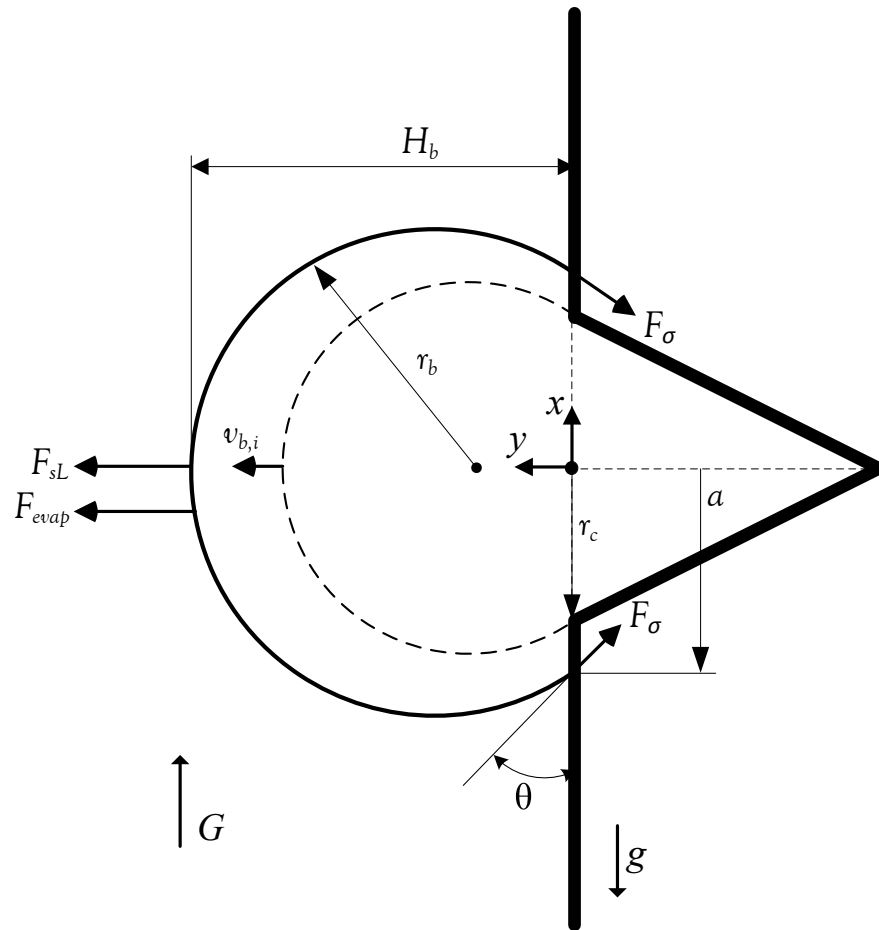


Figure 6.3: Spherical bubble perpendicular force balance on a vertically aligned heated surface.

Figure 6.4. The difference here, when compared to a nozzle which has a constant plane area at which this force acts, is that the area of action (bubble interface area) is dynamic.

This evaporative force will be shown to be proportional to the square of the heat flux and the bubble size (interfacial area). Due to symmetry, the thrust forces in the direction parallel to the heated surface negate each other. In the direction perpendicular to the surface there is a net reaction force (F_{evap}) causing the bubble interface to displace away from the heated surface due to mass exchange and expansion across the bubble interface area. The perpendicular force is defined by Equation 6.4.

$$-F_{thrust} = F_{evap} = \frac{d(m_b v)}{dt} = v \frac{\partial m_b}{\partial t} + m_b \frac{\partial v}{\partial t} \quad (6.4)$$

The interface velocity perpendicular to the plate is determined by an energy balance of the growing bubble. The bubble here is assumed to have a spherical shape as shown in Figure 6.3 . An energy balance of the bubble of Equation 6.5 relates the bubble size to the heat transfer across the bubble interface.

$$\rho_v \Delta h_{fg} \frac{dV_b}{dt} = q''_i A_b \quad (6.5)$$

The terms q''_i and A_b of Equation 6.5 represent the heat transfer rate at the bubble interface and the total bubble interface surface area.

The volume of a spherical shaped bubble is defined by Equation 6.6.

$$V_b = \frac{\pi}{6} H_b (3a^2 + H_b^2) \quad (6.6)$$

Here a is the vapor-solid contact area radius and H_b is the bubble height from the surface to the bubble cap, both of which vary with time as the bubble grows.

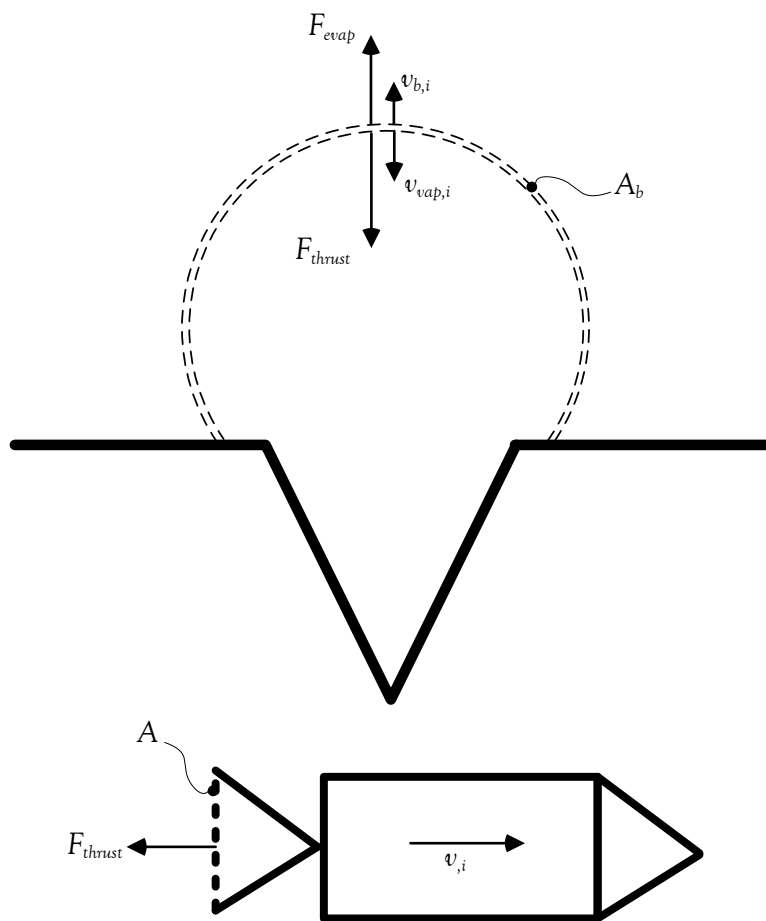


Figure 6.4: Evaporative thrust force due to evaporation across a bubble interface (top) similarity to a rocket (bottom).

The total surface area of a spherical shaped bubble is defined by Equation 6.7.

$$A_b = 2\pi r_b H_b = \pi(a^2 + H_b^2) \quad (6.7)$$

Inserting these geometric relations (Equation 6.6 and Equation 6.7) into Equation 6.5 the bubble interface velocity perpendicular to the heated surface can then be expressed by Equation 6.10. It is noted that the bubble contact radius is taken to be equal to the cavity size and thus the term 3 of Equation 6.9 is zero. This assumption is further discussed in in Section 6.4.3.

$$\frac{\pi}{2}\rho_v\Delta h_{fg}\frac{dH_b}{dt}\left(a^2 + H_b^2 + 2aH_b\frac{da}{dt}\right) = q_I''\pi(a^2 + H_b^2) \quad (6.8)$$

$$\frac{\pi}{2}\rho_v\Delta h_{fg}\frac{dH_b}{dt}(a^2 + H_b^2) = q_I''\pi(a^2 + H_b^2) \quad (6.9)$$

$$v_{b,i} = \frac{dH_b}{dt} = \frac{2q_I''}{\rho_v\Delta h_{fg}} \quad (6.10)$$

It is noted that the interface velocity is independent with time with the assumption that the interfacial heat flux is also constant with time.

Using the defined boundary in Figure 6.3, the mass evaporation rate at the interface is found similarly using the energy balance equation and expressed in Equation 6.12.

$$\Delta h_{fg}\frac{dm_b}{dt} = q_I''A_b, \quad (6.11)$$

$$\dot{m}_b = \frac{dm_b}{dt} = \frac{q_I''\pi(a^2 + H_b^2)}{\Delta h_{fg}}. \quad (6.12)$$

Inserting Equation 6.10 and Equation 6.12 into Equation 6.4 and noting that since the

rate of change of the bubble height is zero the evaporative thrust force is then expressed by Equation 6.13.

$$F_{evap} = v_{b,i} \frac{dm_b}{dt} = \left(\frac{q''_I}{\Delta h_{fg}} \right)^2 \frac{\pi (a^2 + H_b^2)}{\rho_v} \quad (6.13)$$

Equation 6.13 describes the lift force imparted on a bubble due to the interfacial mass/energy exchange occurring at the bubble interface.

6.2.3 Bubble Shear Lift Force (F_{sL})

The bubble shear lift force results from the entrainment phenomena on a bubble from the bulk fluid movement parallel to the surface. The result of such a force is to aid in bubble removal from the surface and will thus result in a decrease in the maximum heat flux required to remove a bubble from the surface. With the increase of this force the evaporative potential will decrease but there will be a counter increase in the convective heat flux.

The lift force as derived by Klausner and Mei [76] is expressed in a general form by Equation 6.14.

$$F_{sL} = \frac{1}{2} C_L \rho_l u_l (y')^2 \pi r_b^2 \quad (6.14)$$

In Equation 6.14 y' is the bubble center of mass distance from the wall approximated here as $y' \approx H_b/2$. The lift coefficient is expressed by Equation 6.15 with G_s defined by Equation 6.16 and the bubble Reynolds number (Re_b) defined by Equation 6.17.

$$C_L = 3.877 G_s^{\frac{1}{2}} \left[Re_b^{-2} + 0.014003 G_s^2 \right]^{\frac{1}{4}} \quad (6.15)$$

$$G_s = \left| \frac{du_l}{dy} \right| \frac{y}{u_l(y)} \quad (6.16)$$

$$Re_b = \frac{r_b u_l(y')}{\nu_l} \quad (6.17)$$

Using the standard turbulence definitions, the non-dimensional velocity and distance from the wall are expressed by Equation 6.18 and Equation 6.19 respectively.

$$u^+ = \frac{u_l}{u^*} = \frac{u_l}{\sqrt{\tau_w/\rho_l}} \quad (6.18)$$

$$y^+ = \frac{y u^*}{\nu_l} = \frac{y \sqrt{\tau_w/\rho_l}}{\nu_l} \quad (6.19)$$

The bubbles are assumed to be of a small size such that the distance from the center of a bubble to the wall is assumed to be small with a $y^+ \leq 5$. This allows for approximating y^+ and u^+ as being equal (Equation 6.20).

$$y^+ = u^+. \quad (6.20)$$

The wall shear stress is determined by Equation 6.21 with the defined fanning friction coefficient of Equation 6.22 and the moody friction coefficient of Equation 6.23. U_l is the volumetric average velocity.

$$\tau_w = C_f \frac{1}{2} \rho_l U_l^2 \quad (6.21)$$

$$C_f = \frac{\lambda}{4} \quad (6.22)$$

$$\lambda = \begin{cases} \frac{64}{Re}, & Re < 2320 \\ \frac{0.3164}{Re^{0.25}}, & 4 \times 10^3 < Re < 10^5 \\ 0.0032 + 0.221Re^{-0.237}, & 10^5 < Re < 2 \times 10^6 \end{cases} \quad (6.23)$$

The differential term of Equation 6.16 is evaluated with Equation 6.18 and Equation 6.19 and expressed by Equation 6.24.

$$\left| \frac{du_l}{dx} \right| = \frac{u^{*2}}{\nu_l} \left| \frac{du^+}{dx^+} \right|. \quad (6.24)$$

Based on the assumption from Equation 6.20 and inserting the definition of the non-dimensional velocity (Equation 6.18) into Equation 6.24, Equation 6.24 is then evaluated as expressed by Equation 6.25.

$$\left| \frac{du_l}{dx} \right| = \frac{u^{*2}}{\nu_l} = \frac{\tau_w}{\mu_l}. \quad (6.25)$$

Equation 6.25 is integrated to yield the expected result of a linear velocity profile as shown in Equation 6.26.

$$u_l(y) = \frac{\tau_w}{\mu_l} y. \quad (6.26)$$

In Equation 6.26 $u_l(y = 0) = 0$ as a result of the no-slip condition at the wall.

For this case of analyzing the critical conditions for bubble lift off, inserting Equation 6.26 and Equation 6.25 into the expression for G_s (Equation 6.16), it is found that G_s simplifies to 1.0 as demonstrated by Equation 6.27.

$$G_s = \left| \frac{du_l}{dx} \right| \frac{y}{u_l(y)} = \frac{\tau_w}{\mu_l} \frac{y}{\frac{\tau_w}{\mu_l} y} = 1.0. \quad (6.27)$$

It is noted that this equation is only valid for distances very near to the wall for $y^+ \leq 5$

(i.e. very small bubble sizes). With the derived relations above, the shear lift force induced on a growing bubble by a flow parallel to the surface can be determined by the general expression given by Equation 6.14.

6.3 Critical Heat Flux Model

The balance equation for the final forces studied here is expressed by Equation 6.28. Substituting the force expressions from the previous sections, the general force balance for a bubble is expressed by Equation 6.28.

$$\frac{dM}{dt} = -F_{\sigma,y} + F_{evap} + F_{sL} \quad (6.28)$$

The end point of bubble growth is then taken to be the time at which the forces are balanced. That is $\frac{dM}{dt} = 0$ with the net force balance shown in Equation 6.29.

$$0 = -2\pi\sigma a \sin(\theta) + \left(\frac{q''_I}{\Delta h_{fg}} \right)^2 \frac{\pi(a^2 + H_b^2)}{\rho_v} + \frac{1}{2} C_L \rho_l u_l |_{H_b/2}^2 \pi r_b^2 \quad (6.29)$$

Solving for the interfacial heat flux (q''_I), the evaporative component of the heat flux is finally expressed by Equation 6.30.

$$q''_I = \left(\frac{2\pi\sigma a \sin(\theta) - \frac{1}{2} C_L \rho_l u_l |_{H_b/2}^2 \pi r_b^2}{\frac{\pi(a^2 + H_b^2)}{\rho_v \Delta h_{fg}^2}} \right)^{1/2} \quad (6.30)$$

This provides the evaporative heat flux component of Equation 6.2.

The fractional boiling area of Equation 6.31 is determined from the nucleation site area density (Na), the average bubble projected bubble area (\bar{A}'_b), and the total heated area

(A_h).

$$f_{boil} = NaA_h \frac{\bar{A}'_b}{A_h} = Na\bar{A}'_b \quad (6.31)$$

The total contribution to the convective heat flux is then the complement of Equation 6.31, as expressed by Equation 6.32.

$$f_{conv} = 1 - f_{boil} \quad (6.32)$$

The Nusselt number for the convective heat transfer coefficient is determined from the standard single phase convective relation by Equation 6.33 with the single-phase convective heat flux determined by Equation 6.34.

$$Nu = \frac{\bar{h}_{conv} L_c}{k_l} \quad (6.33)$$

$$q''_{1\phi} = \bar{h}_{conv} (T_w - T_b) \quad (6.34)$$

With the evaporative and convective heat flux components defined, the total heat transfer is then described by Equation 6.35 as the sum of the boiling and convective contribution.

$$q''_{total} = q''_{CHF} = \bar{h}_{conv} (T_w - T_b) (1 - f_{boil}) + \left(\frac{2\pi\sigma a \sin(\theta) - \frac{1}{2} C_L \rho_l u_l^2 \left[\frac{H_b}{2} \right]^2 \pi r_b^2}{\frac{\pi(a^2 + H_b^2)}{\rho_v \Delta h_{fg}}} \right)^{1/2} f_{boil} \quad (6.35)$$

This equation is used to postulate the maximum potential heat transfer for flow boiling. The step by step process for solving Equation 6.35 is provided here. The algorithm diagram for determining the critical heat flux is provided in Figure 6.5. The theoretically derived critical heat flux value is to be solved axially in a flow channel. This is then compared to experimental data to validate the newly developed mechanistic model that is centered on a mass, momentum, and energy balance of a bubble at a nucleation site.

The solution steps are as follows:

1. Specify specific channel geometry.
 - flow area
 - hydraulic diameter
 - heater diameter
 - heated length
2. Specify fluid boundary conditions.
 - system pressure
 - inlet mass flux
 - inlet temperature/enthalpy
3. Define resolution of axial nodalization to model the channel heated length.
4. Define the heat flux profile shape.
5. With the known heat flux profile shape the one-dimensional energy equation is solved to determine the axially dependent fluid properties.
6. The effective active cavity size is then determined with a calibration curve dependent on heated surface conditions, system pressure and mass flux (Section 7.2).
7. Based on the effective active cavity size the internal vapor bubble pressure is estimated and wall temperature is determined from the Clausius-Clapeyron relation.
8. The boiling suppression (S) and enhancement (F) factors are calculated to determine the effective wall superheat.
9. With the heated surface temperature known the near wall thermal fluid properties are calculated at each axial node.

10. The contact angle is defined based on the fluid and surface.
11. Assuming a spherical bubble shape and with contact angle and effective cavity size defined, the bubble interfacial area is calculated.
12. Based on wall superheat and contact angle the nucleation site density is then determined.
13. The nucleation site density is then used to determine the surface boiling fraction and the convective fraction.
14. The individual terms of the force balance equation are then solved and the maximum boiling heat flux calculated.
15. The single phase convective heat flux is calculated.
16. The boiling and convective heat fluxes are then partitioned based on the available boiling and convective fractional areas. The sum of the partitioned boiling and convective heat flux is then the predicted critical heat flux. This is obtained for each axial node.
17. The critical heat flux value, critical pin power, critical heat flux location are determined for the tested inlet mass flux, pressure, and inlet temperature for given geometric condition.
18. A criterion is tested to determine if the axial heat flux and the axial dependent CHF value are tangent such as that depicted by Figure 7.12. If not the pin power is adjusted and the loop is repeated until this tangency condition is met. This method is known as the heat balance method.

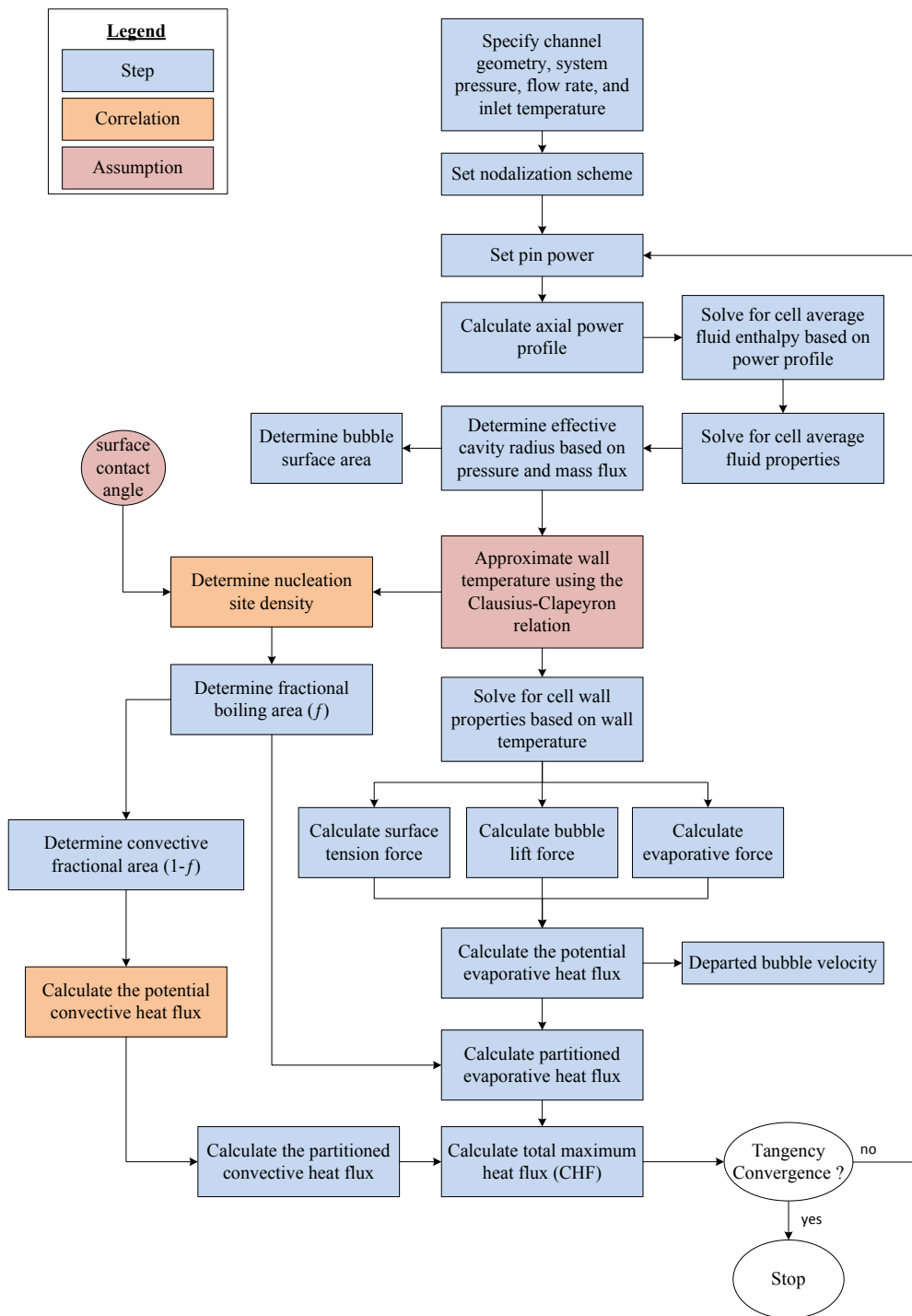


Figure 6.5: Correlation algorithm for determining critical heat flux.

The remaining closure relations to be defined are:

- The effective nucleation site cavity size.
- The bubble-surface contact angle.
- The bubble-surface contact radius.
- Effective wall heat (suppression (S) factor) for nucleate boiling.
- The nucleation site density to partition the convective and boiling heat fluxes.
- A convective heat flux correlation.

The choice and justification for each constitutive relation is described in the following subsections.

6.4 Critical Heat Flux Model Constitutive Relations

This section provides the closure relations used in order to obtain a solution. It is noted that the exactness of the individual closure relations is not critical. What is critical is that the trends and behaviors are captured. The reason for this is due to the fact that a calibration factor is utilized to lump the deviations that may exist from a selected closure relation to capture the surface characteristics. For example, if one were to assume a bubble-surface contact angle, a particular calibration will be developed for that method and assumed parameters. If the assumed contact angle is changed than the underlying calibration needs to be updated for that closure relation set. This allows flexibility in the closure set utilized. Every effort was made here to choose reasonable relations.

6.4.1 Effective Nucleation Site Cavity Radius

This parameter is the calibration coefficient for the model. The effective nucleating cavity size is determined by calibrating a single set of data for a given geometric condition and surface type/finish. Specifically, it found to be dependent on the wall superheat temperature and the boundary layer profile.

The wall superheat represents the range of possible activation sizes and maximum temperature a nucleating bubble can reach before heat transfer ceases. The thermal boundary layer presents another limit for bubble growth. If the bubble grows beyond the point in the thermal boundary where the boundary layer temperature is equal to the bubble internal temperature a secondary path for heat rejection exists. Heat at this point will be transferred from the bubble cap to the bulk. This will limit the bubble growth rate and size. This concept is depicted in Figure 2.5.

To account for these two effects two independent variables are chosen to represent the effective cavity size in a functional form. These parameters are system pressure and inlet mass flow rate. It is noted that mass flow rate could be replaced by velocity, mass flux, Reynolds number, non-dimensional velocity, and etc just as long as velocity is represented.

6.4.2 Bubble Contact Angle

From Figure 4.2 of Section 4.2 a representative static contact angle of 45.0° is assumed. This is applicable for copper and stainless steel surfaces over a broad range of surface roughnesses. It is believed that the lack modeling of the exact value will be captured within the nucleation site size calibration. A more complex relation of contact angle could be employed if desired. The effects of dynamic versus receding contact angles are not taken into account here. This is believed to be more valid for lower flows where the drag in the flow direction on the bubble is minimal as compared to large flow rates (velocities) which can result in asymmetric geometry of a bubble as shown in Figure 4.6.

Furthermore, at the CHF condition it is observed that the advancing and receding contact angles become equal (Section 4.2.2). Thus a constant static contact angle is deemed appropriate.

6.4.3 Bubble Contact Radius

The bubble-surface contact radius (a) as depicted in Figure 6.3 needs yet to be determined for use in Equation 6.35. The contact radius is defined as to obtain the maximum theoretical potential heat flux with the use of Equation 6.30. When the contact area between bubble vapor region and the surface is the smallest the value of the interfacial heat transfer rate is the largest. This can be demonstrated by inserting the geometric relations for a spherical bubble, as presented in Section 2.2.1, into Equation 6.35 which is then re-written in terms of the contact radius as shown in Equation 6.30.

$$\begin{aligned}
 q_I'' &= \left(\frac{2\pi\sigma a \sin(\theta) - \frac{1}{2} C_L \rho_l u_l^2 H_b / 2 \pi r_b^2}{\frac{\pi(a^2 + H_b^2)}{\rho_v \Delta h_{fg}^2}} \right)^{1/2} \\
 &= \left(\frac{2\sigma}{a} - \frac{C_L \rho_l u_l^2 H_b / 2}{2 \sin^2 \theta} \right)^{1/2} \left(\frac{1 + \left(\frac{1 + \cos \theta}{\sin \theta} \right)^2}{\rho_v \Delta h_{fg}^2} \right)^{-1/2}
 \end{aligned} \tag{6.36}$$

As can be seen by Equation 6.36 the smaller the contact radius the larger the interfacial heat flux. It is further assumed that the bubble contact radius can be no smaller than the cavity size. The effective cavity size is thus taken to be the bubble-surface contact radius. This implies that once a bubble completely emerges from a cavity it is ejected from the surface and no longer allowed to grow. This assumption is consistent with the assumed high boiling frequencies and high heat fluxes that exist at/near the CHF condition.

6.4.4 Wall Superheat

The wall superheat is defined as $(T_w - T_{sat})$ and can be approximated by various methods. Two were considered here: (1) based on saturation property limits at an equilibrium condition and (2) that derived from the Clausius-Clapeyron relationship. Both relations are observed to give generally similar results (within 5 degrees).

The first method uses the size of the effective active cavity (Section 6.4.1) and the bubble internal pressure calculated from a force balance across the bubble interface as shown in Equation 2.1. The internal bubble temperature is then determined based on the saturation temperature of the bubble internal pressure. This temperature is then taken to be equal to the wall temperature.

The second method uses the Clausius-Clapeyron equation. It is noted that various versions exist for this relation depending on the assumptions made. The wall superheat for this work uses the Clausius-Clapeyron relationship as defined by Equation 2.4.

6.4.5 Convective Heat Flux Correlation and Boiling Suppression

The convective heat correlation used is the Dittus-Boelter relation as written in Equation 2.55. This is used in Equation 6.33 to determine the convective heat transfer coefficient.

The boiling suppression factor developed by Chen [48] (see Section 2.5) is used to determine the effect wall superheat. The wall superheat determines the near wall fluid properties.

6.4.6 Nucleation Site Density

The nucleation site density as a function of wall superheat was fit by Basu [12] based on experimental data. Most data was correlated to within 40% as shown by Figure 2.7. This relation as expressed in Equation 2.24 and is used in Equation 6.31 to determine the boiling fraction of the entire heated surface area. This also determines the convective heat transfer fraction of the heated surface as defined by Equation 6.32. In order to determine the average boiling area (\bar{A}_b) in Equation 6.31 the average departure diameter is needed. From Figure 2.9 an average constant value 0.5 inches is used as the departure radius. The size distribution of the nucleation site size is noted as a area for future development.

Chapter 7: Critical Heat Flux Model Results

The proposed model and solution algorithm are coded using MATLAB© version 2014b 8.4.0.150421. The following sections will discuss the implementation and results of the model compared to the University of Wisconsin and EPRI experimental data presented in Section 5.1 and Section 5.2 respectively.

Two experimental configurations are used to verify model performance. The data from the University of Wisconsin are used to confirm the validity and capability to capture the non-uniform heat flux configurations. The second test series utilized is that from Columbia University collected for the EPRI CHF database (Section 5.2). Since a large number of data points exists for this test series this set is used to evaluate the statistical performance of the proposed CHF model.

The error of the proposed model is quantified by the the root means square error (RMSE) as calculated by Equation 7.1.

$$RMSE = \sqrt{\frac{1}{N} \sum \left(\frac{q''_{CHF,pred} - q''_{CHF,meas}}{q''_{CHF,meas}} \right)^2} \quad (7.1)$$

7.1 Model Nodalization

A one-dimensional axial nodalization is defined with three sub-regions. The first region is the wall heat source modeled as a heat flux boundary condition. The second is the fluid near the wall with fluid properties determined at the wall temperature. This region is modeled as having zero thickness. The last region is the bulk region where fluid properties are determined by a one-dimensional energy balance in the axial direction of the channel. Figure 7.1 depicts the nodalization scheme and the three sub-regions. All

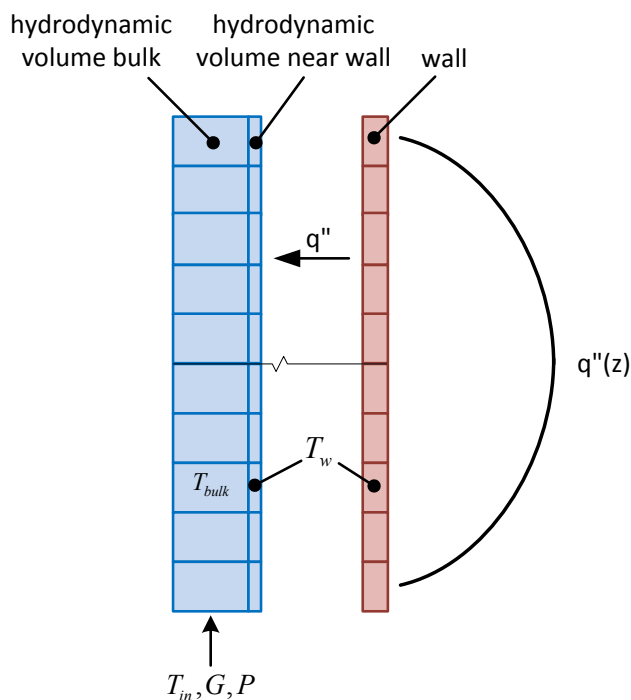


Figure 7.1: Nodalization of critical heat flux model.

analysis is done utilizing 200 axial nodes for all cases considered in this work.

7.2 Model Calibration

Based on the data collected for each test series, a calibration is performed as discussed in Section 6.4.1 to determine the effective active nucleation site cavity size. Dependence is found to be mainly related to the system pressure and mass flux (velocity) as shown in Figure 7.2 for the General Electric EPRI test series. The mass flux dependence follows a power law while pressure a linear relation. The mass flux here has a larger influence on the cavity size. This is postulated to be a result of its more dominate effect on the

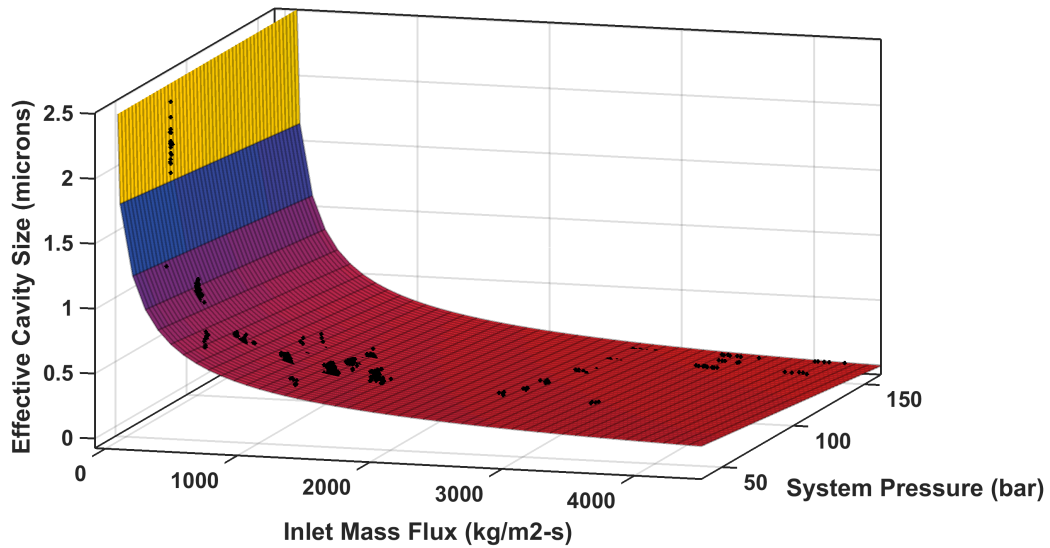


Figure 7.2: Calibration of effective cavity size for EPRI database points.

thermal boundary layer thickness. Equation 7.2 expresses the form developed to relate the effective nucleation cavity size (r_c) in μm to the system pressure (P_{sys}) in bar and inlet mass flux (G) in $\text{kg}/(\text{m}^2 - \text{s})$ for the EPRI test sets.

$$\begin{aligned}
 r_c [\text{microns}] &= a_1 G^{a_2} + a_3 P_{sys} \\
 a_1 &= 26.55 \\
 a_2 &= -0.5631 \\
 a_3 &= -0.001472
 \end{aligned}
 \tag{7.2}$$

The calibration curve developed for the University of Wisconsin data is provided by

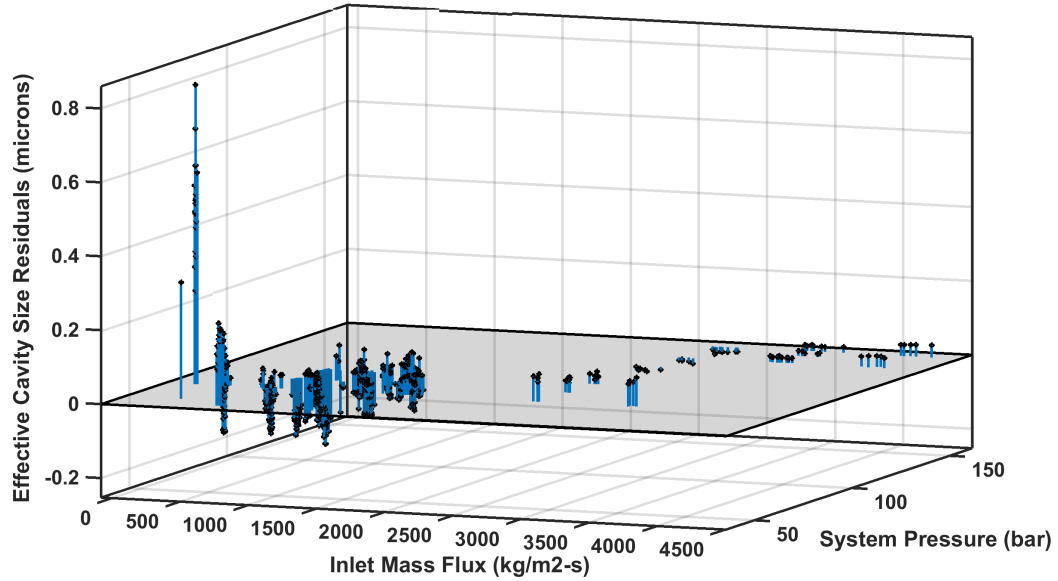


Figure 7.3: Calibration of effective cavity size residuals for EPR database points.

Equation 7.3.

$$\begin{aligned}
 r_c [\text{microns}] &= a_1 G^{a_2} + a_3 P_{sys} \\
 a_1 &= 2.151 \\
 a_2 &= -0.09458 \\
 a_3 &= -0.005594
 \end{aligned}
 \tag{7.3}$$

7.3 Applicability Range

The range of the proposed model is based on the larger data set of the EPR database as summarized in Section 5.2 with the valid range considered to be with inlet mass fluxes between 200 to 4000 $kg/(m^2 - s)$, pressures between 4.0 to 15.6 MPa , and critical qualities between -0.03 to 1.0. The tested distribution based on the EPR CHF data set presented in Section 5.2 for the applicable mass fluxes, pressures, inlet temperatures, inlet qualities, and critical qualities depicted in Figure 7.4, Figure 7.5, Figure 7.6,

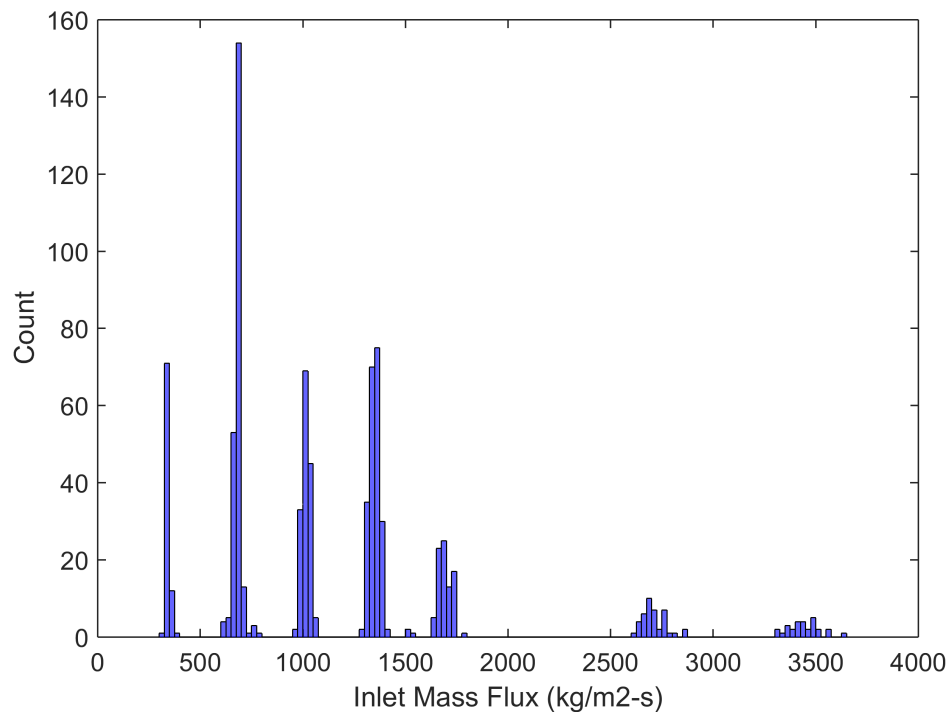


Figure 7.4: Applicable range of mass flux distribution of EPRI database tests 301-318.

and Figure 7.8 respectively. It is noted that a superheated test condition does exist at the channel outlet for a single data point from the test conditions. This data point is questionable, but left here as is.

It is determined that wide coverage in the tested conditions exists to provide broad testing of the proposed CHF model.

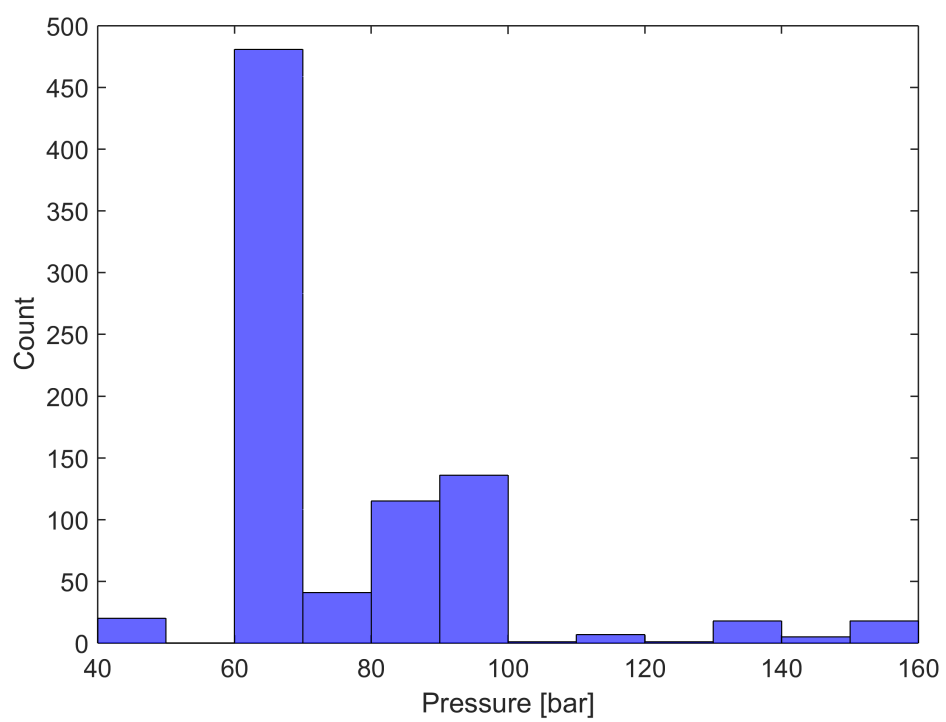


Figure 7.5: Applicable range of pressure distribution of EPRI database tests 301-318.

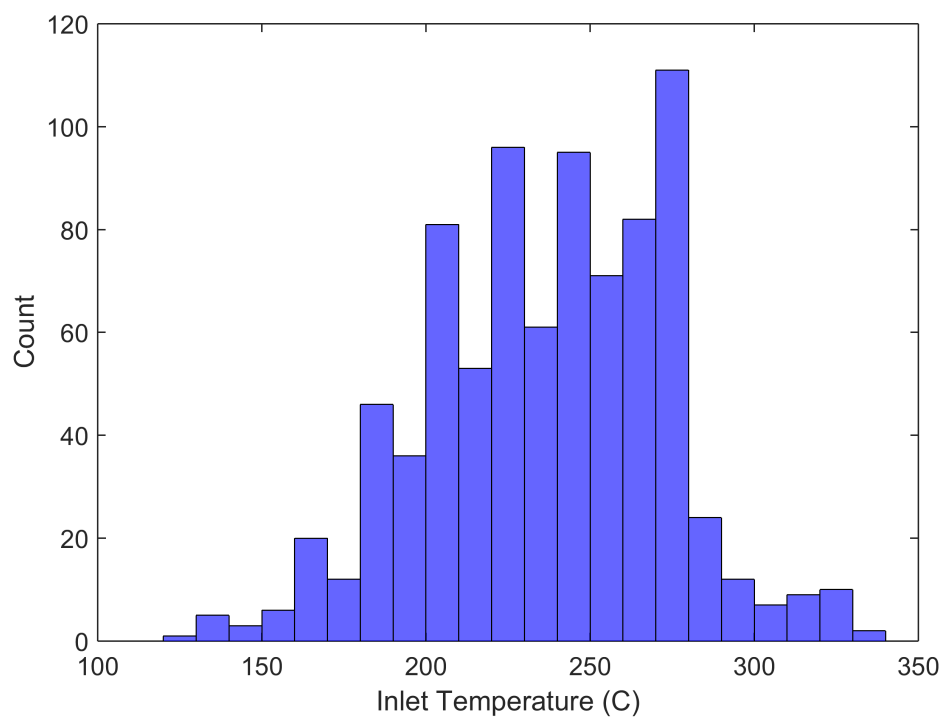


Figure 7.6: Applicable range of inlet temperature distribution of EPRI database tests 301-318.

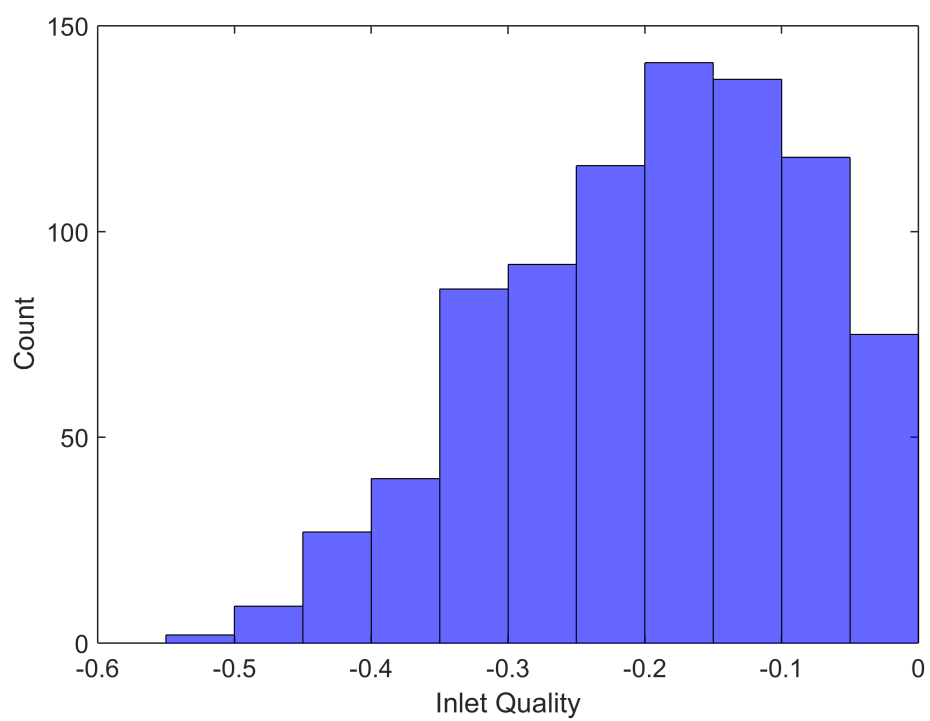


Figure 7.7: Applicable range of inlet quality distribution of EPR database tests 301-318.

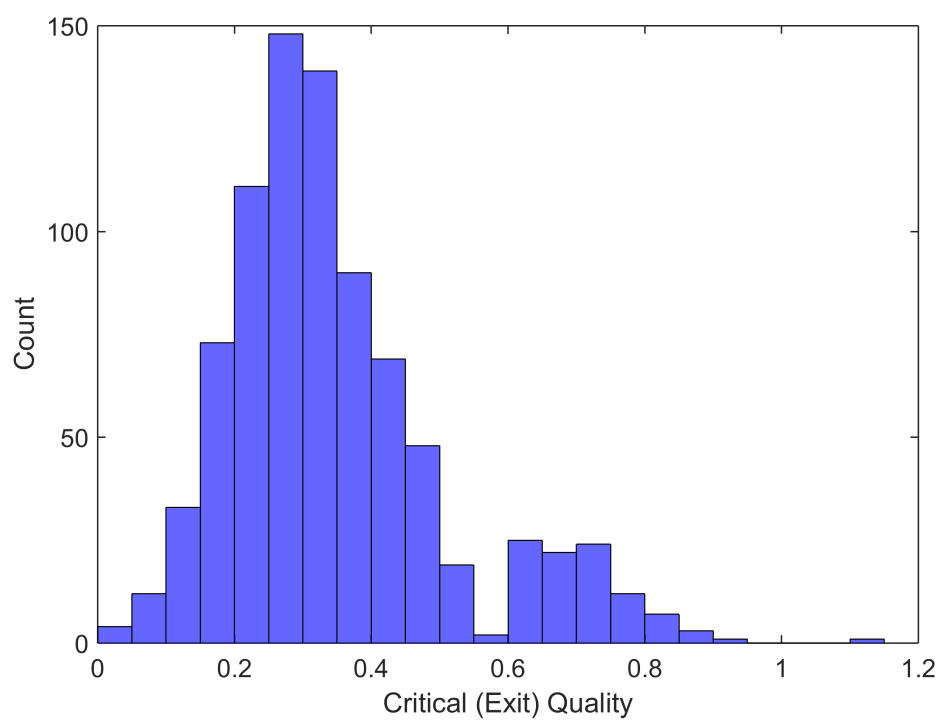


Figure 7.8: Applicable range of critical quality distribution of EPRI database tests 301-318.

7.4 University of Wisconsin Database Results

The University of Wisconsin database is used to confirm the model's capability capture the CHF condition for non-uniform power profiles. Due to the small number of test data points it is not used to determine the statistical performance of the proposed model. This is left to the EPRI database.

7.4.1 Critical Heat Flux Value

Results of the performance of the model to predict the CHF value for the University of Wisconsin test series is shown in Figure 7.9. As can be observed excellent agreement is obtained with prediction of the CHF value with a RMSE of 5.51%. Figure 7.10 presents the results relative to the critical pin power with excellent agreement obtained with a RMSE 0.53%.

7.4.2 Critical Heat Flux Location

The critical heat flux prediction location is critical to get correct since this influences the CHF value. The results of the measured and predicted CHF location are presented in Figure 7.11. As is demonstrated excellent agreement is obtained for the predicted CHF location with a RMSE of 4.12%. The axial behavior of the CHF value is presented in Figure 7.12. The tangency location of the two curves is taken as the model CHF value and location. This demonstrates the model's capability to capture the axially dependent trends of the CHF value. The hook in Figure 7.12 is due to the transition from laminar to turbulent flow.

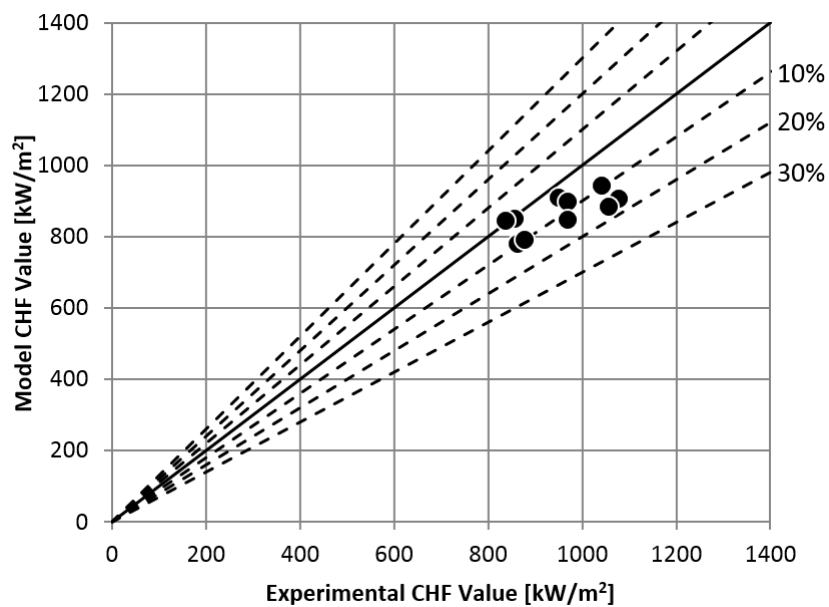


Figure 7.9: CHF model performance against UofW database.

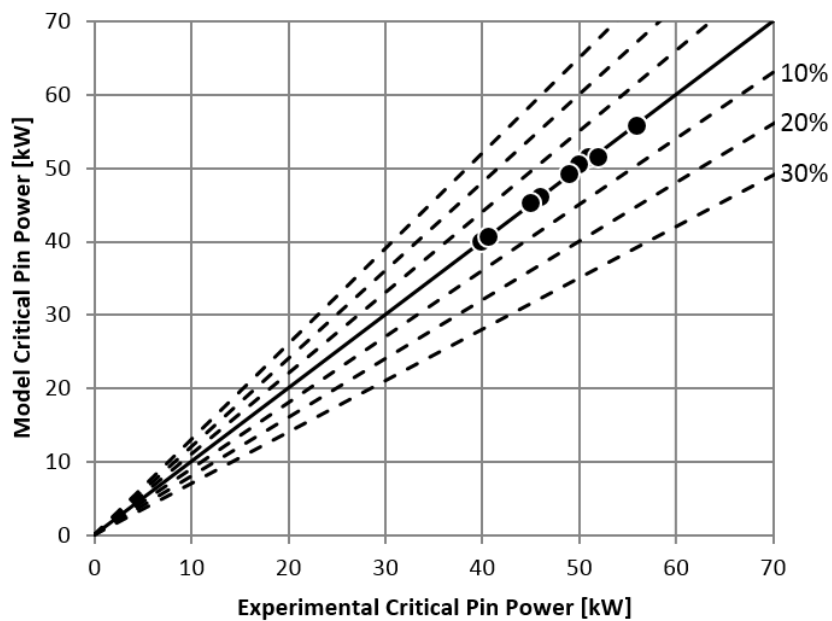


Figure 7.10: CHF model performance against UofW database.

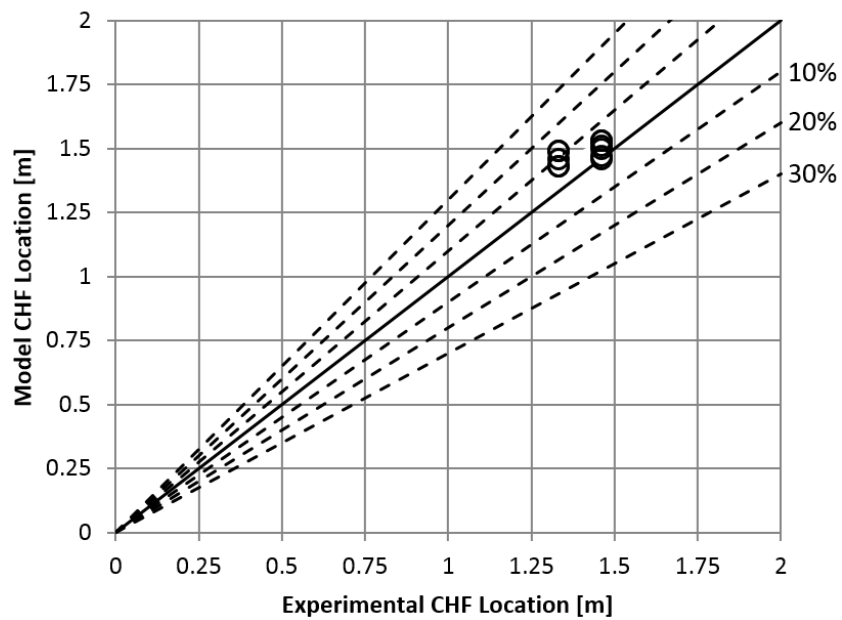


Figure 7.11: Predicted CHF location performance against UofW database.

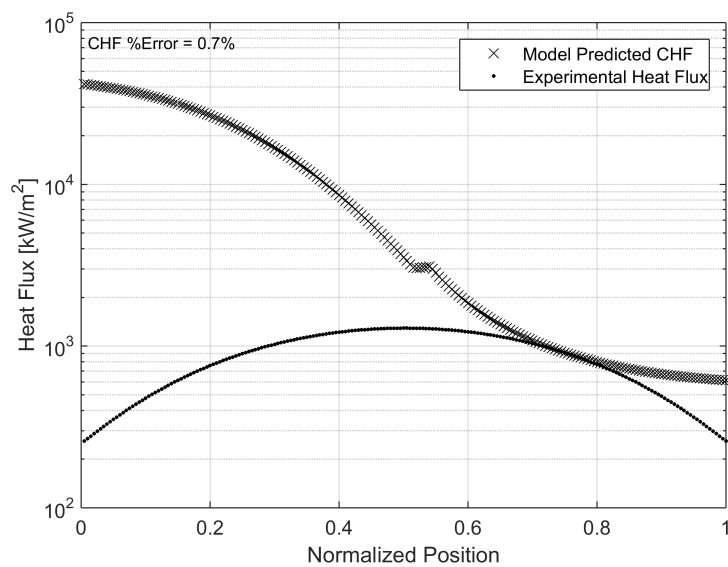


Figure 7.12: CHF versus axial position for UofW run 2 of 11.

7.5 EPRI Database Results

7.5.1 Critical Heat Flux Value for the EPRI Database

Using the calibration function of Equation 7.2 for determining the effective nucleation site size, the algorithm outlined in Figure 6.5, and Equation 6.35, the critical rod power (CRP), the critical heat flux (CHF), and the critical heat flux onset location are determined. A plot of the experimental CHF conditions for all tests and the model determined CHF condition is shown in Figure 7.13 with relative error regions. Reduced performance is observed here at the fringes of the tested domain due to the sparse number of data points available to capture the surface characteristics at those conditions.

Figure 7.14 presents the data that is applicable to the range of development for the model. The distribution of error is presented in Figure 7.15 and as can be seen a normal distribution is obtained with a RMSE of 12.9%.

Individual plots are provided for each test series in Figure 7.16 through Figure 7.36 to assess individual performance more closely. As can be seen excellent agreement has been obtained with the use of the proposed model.

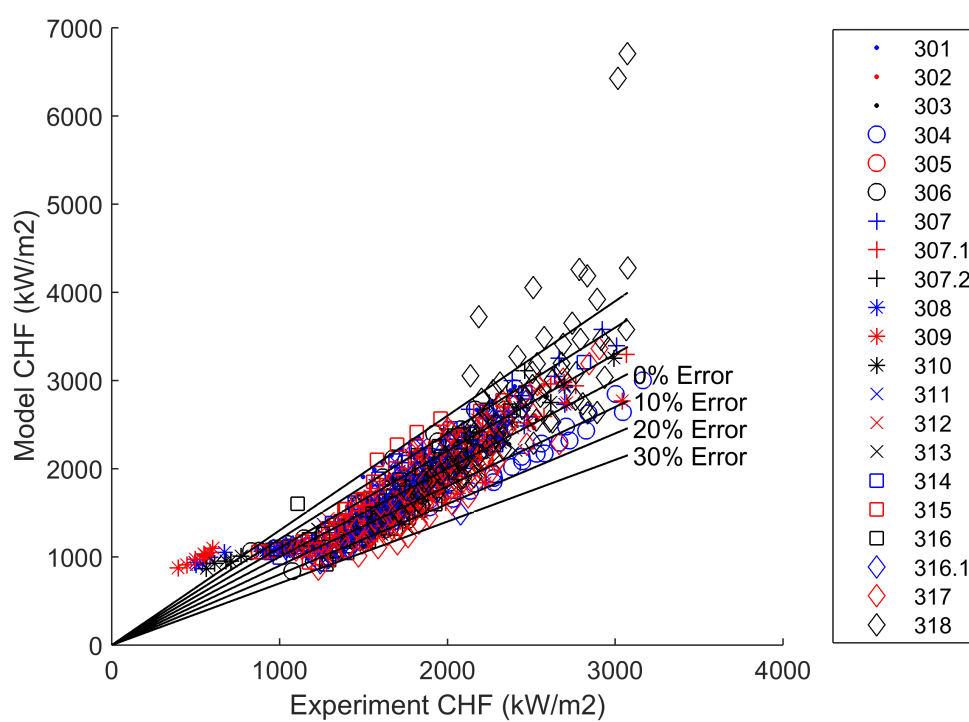


Figure 7.13: Model CHF performance compared to Full EPRI database tests 301-318.

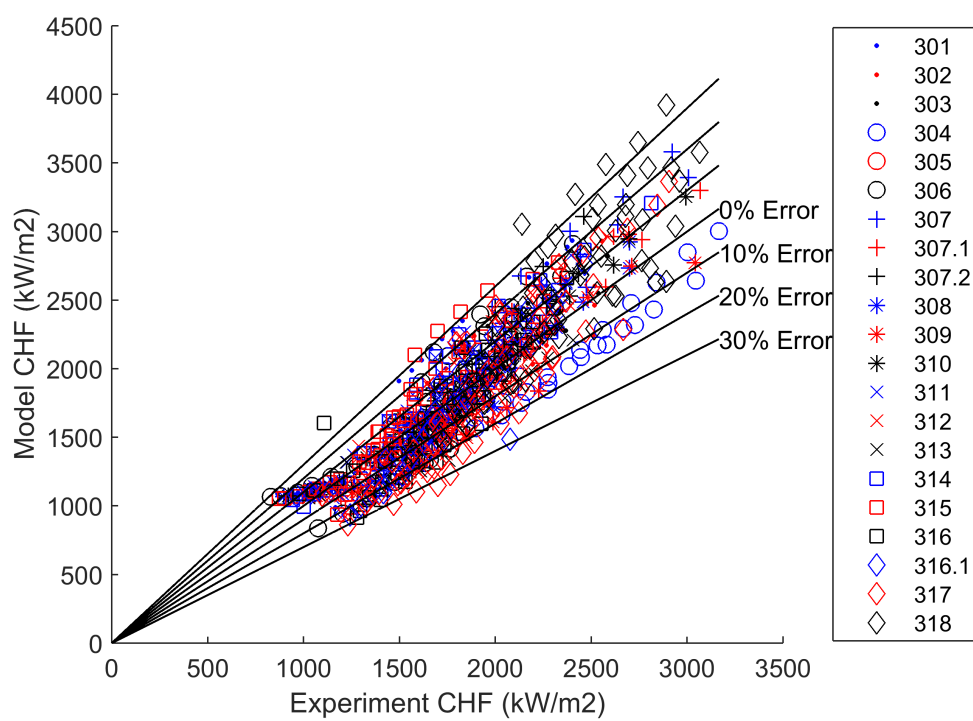


Figure 7.14: Model CHF performance compared to Applicable Range of EPRI database tests 301-318.

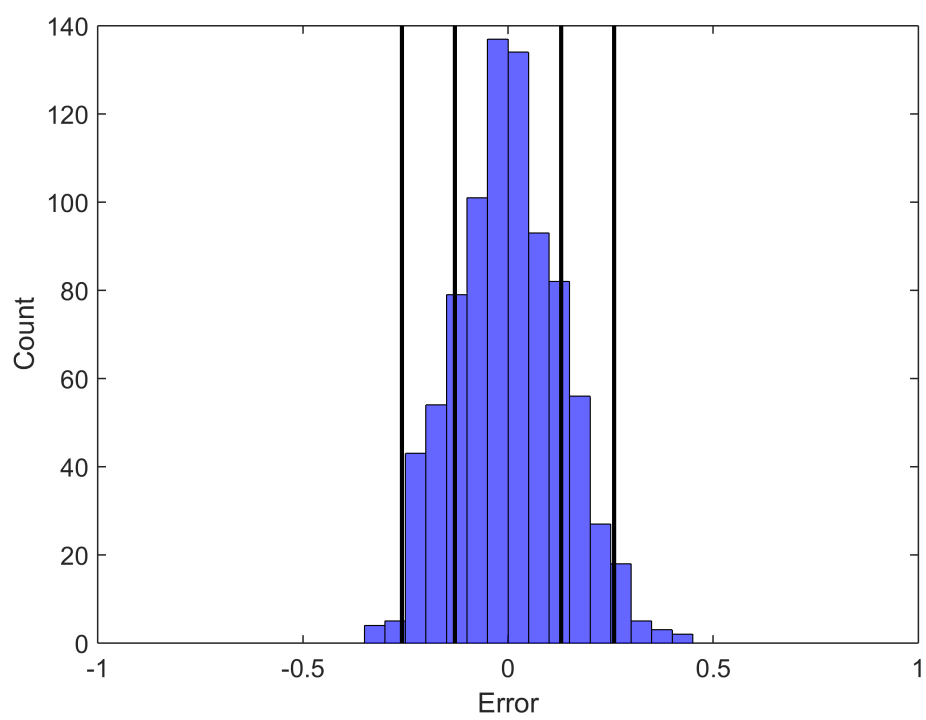


Figure 7.15: CHF error distribution for model compared to EPRI database tests 301-318.

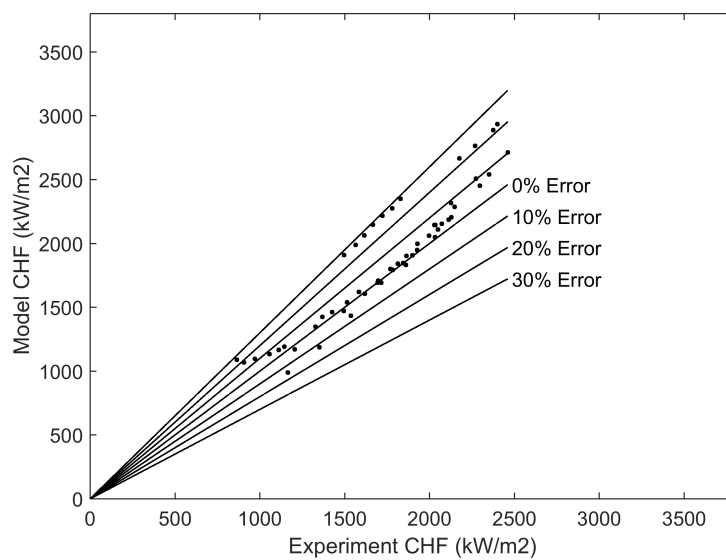


Figure 7.16: CHF model results for EPRI test 301.

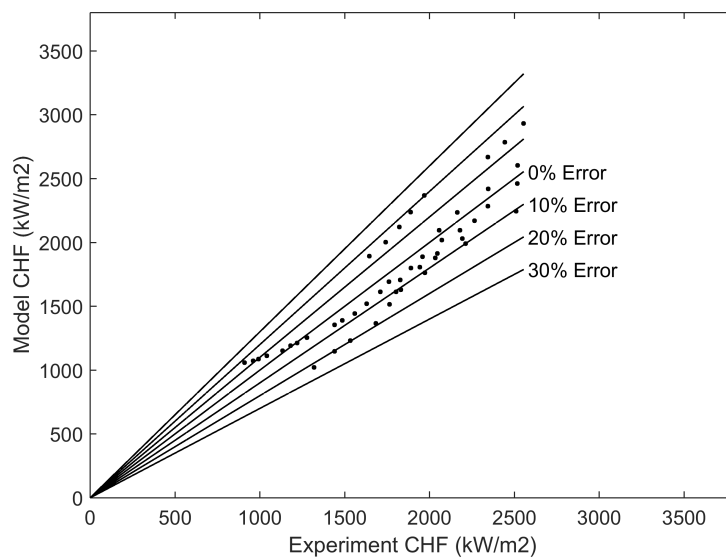


Figure 7.17: CHF model results for EPRI test 302.

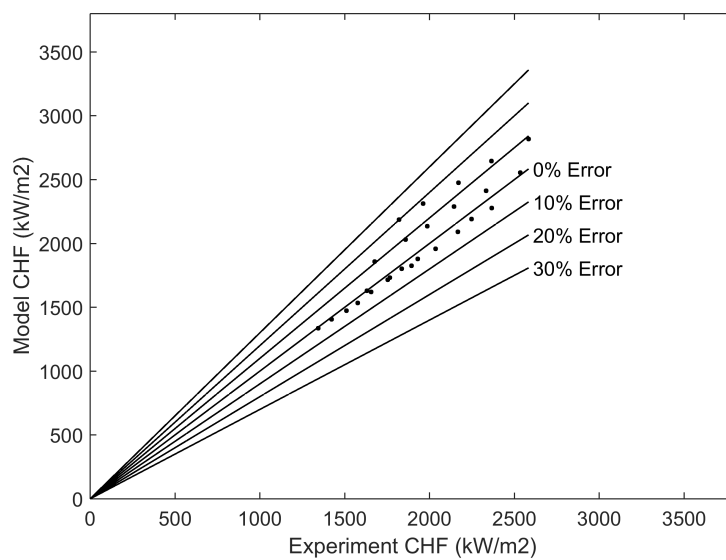


Figure 7.18: CHF model results for EPRI test 303.

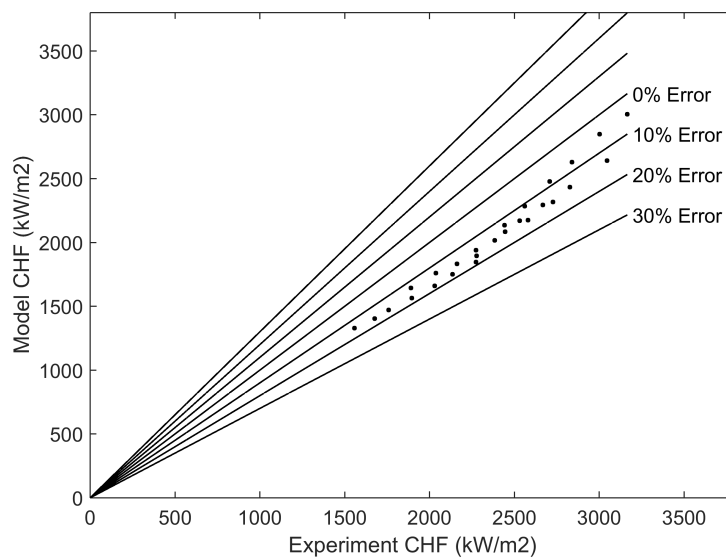


Figure 7.19: CHF model results for EPRI test 304.

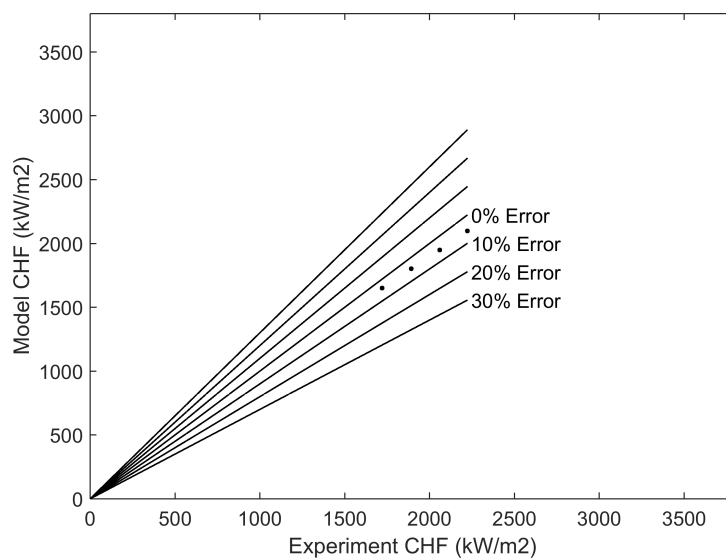


Figure 7.20: CHF model results for EPRI test 305.

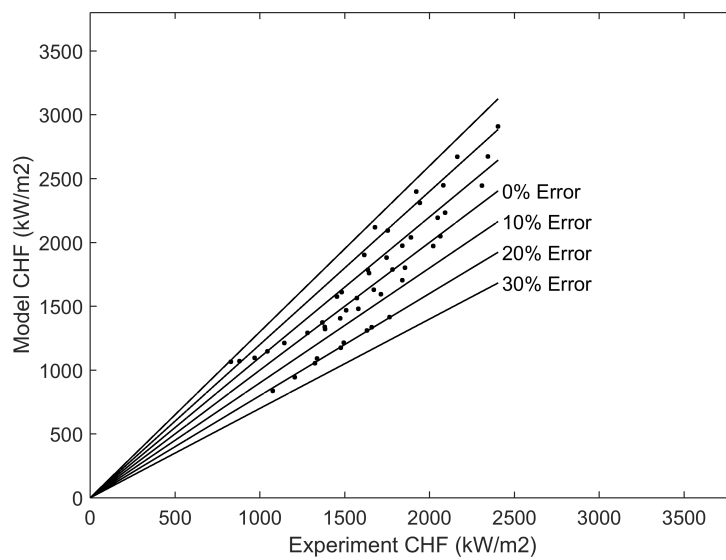


Figure 7.21: CHF model results for EPRI test 306.

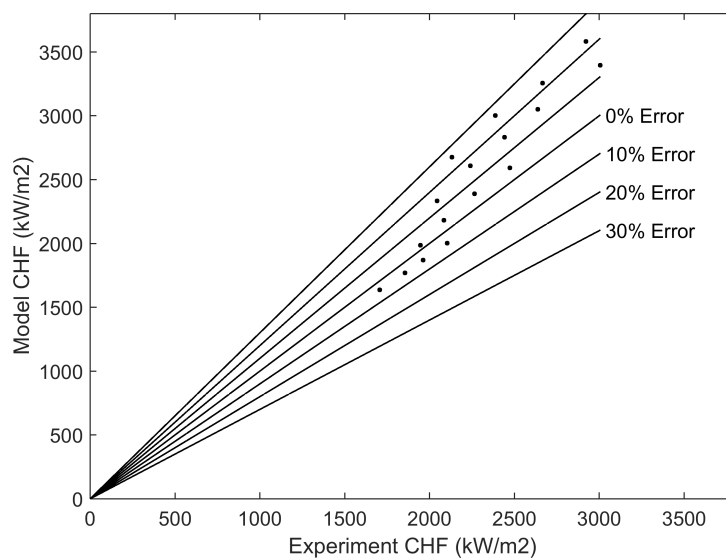


Figure 7.22: CHF model results for EPR test 307.

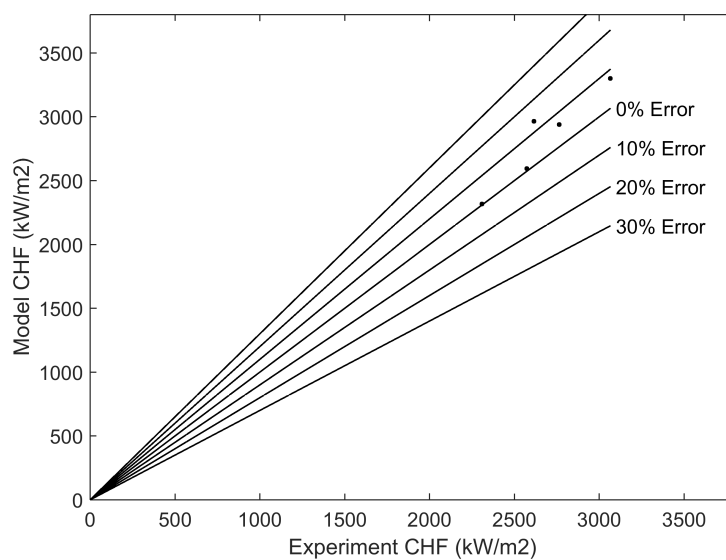


Figure 7.23: CHF model results for EPR test 307.1.

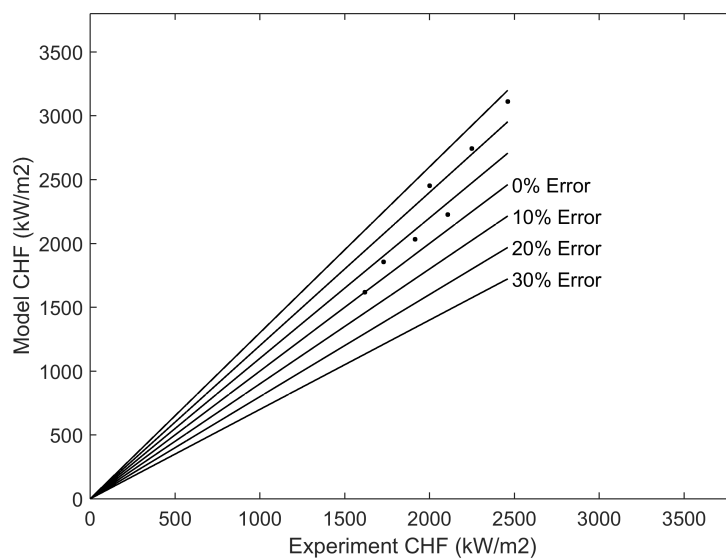


Figure 7.24: CHF model results for EPRI test 307.2.

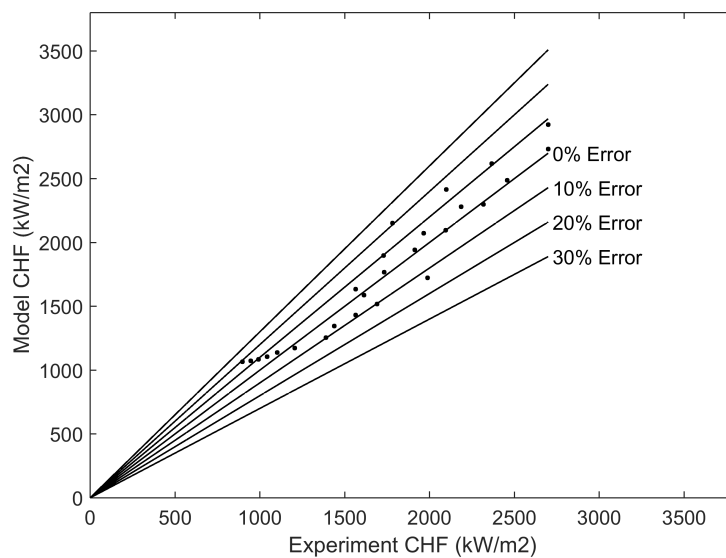


Figure 7.25: CHF model results for EPRI test 308.

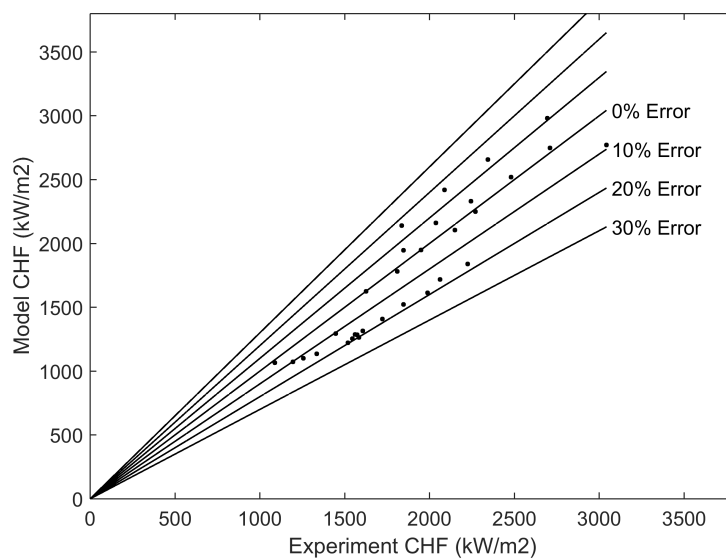


Figure 7.26: CHF model results for EPRI test 309.

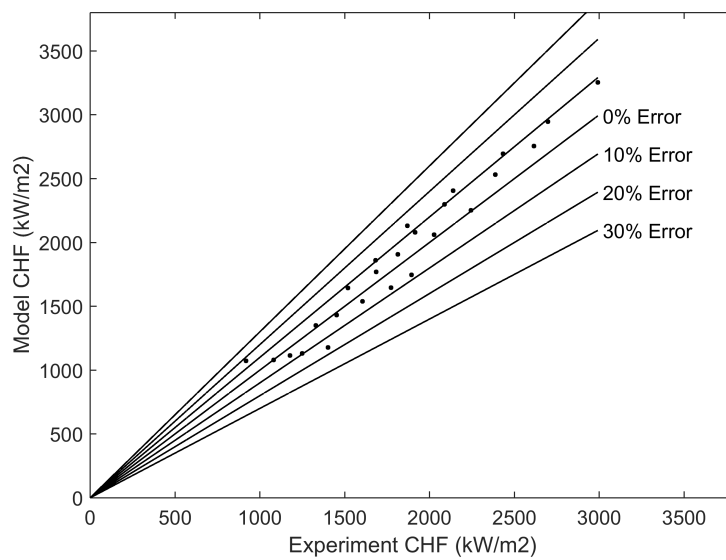


Figure 7.27: CHF model results for EPRI test 310.

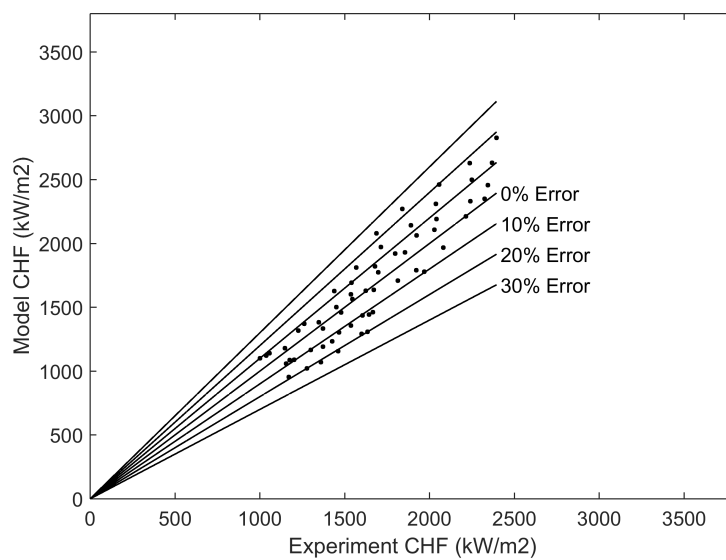


Figure 7.28: CHF model results for EPRI test 311.

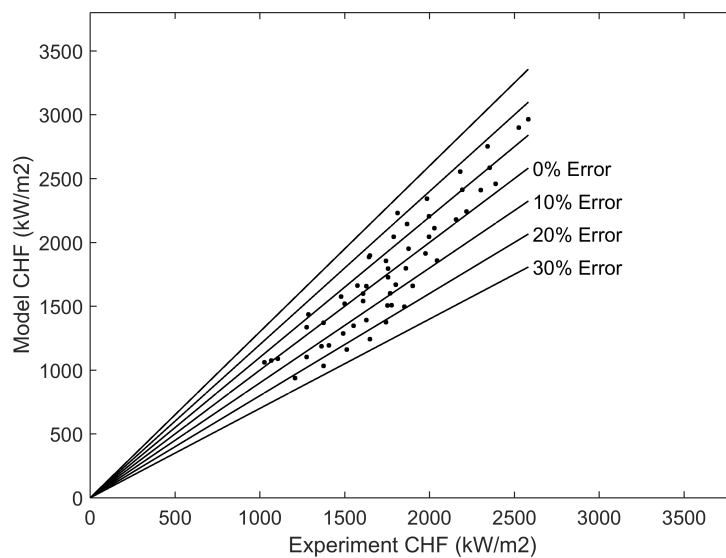


Figure 7.29: CHF model results for EPRI test 312.

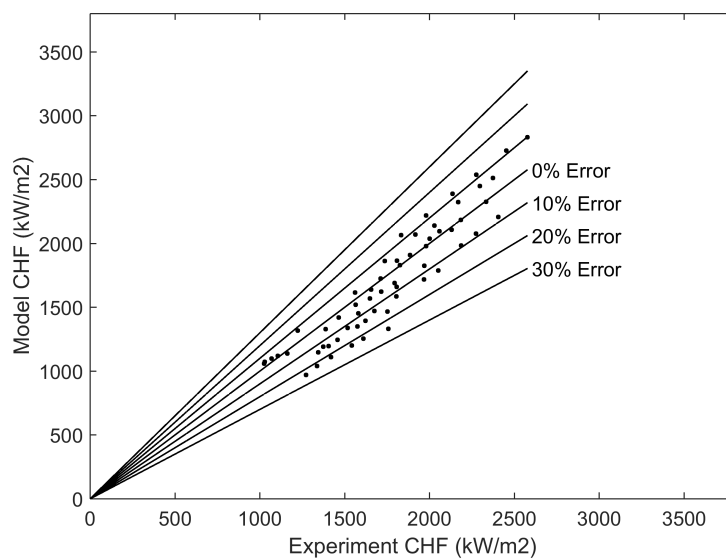


Figure 7.30: CHF model results for EPRI test 313.

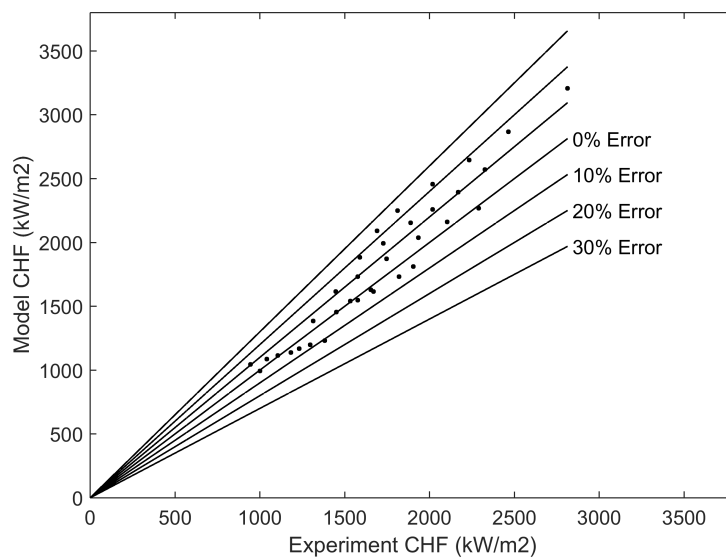


Figure 7.31: CHF model results for EPRI test 314.

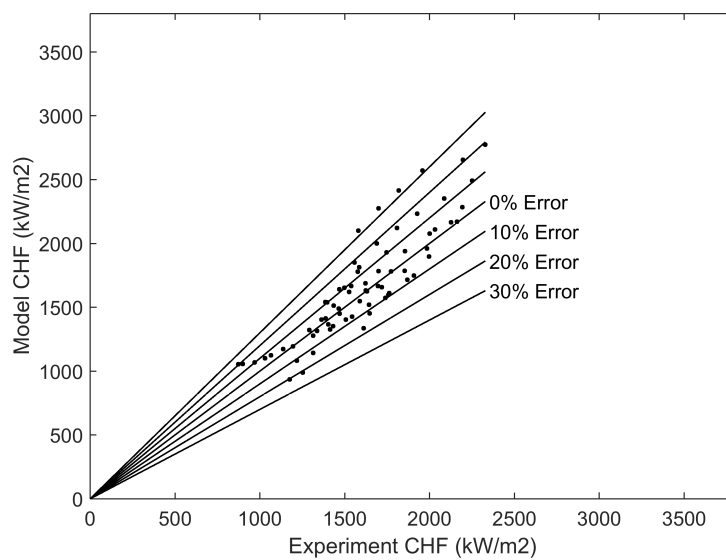


Figure 7.32: CHF model results for EPRI test 315.

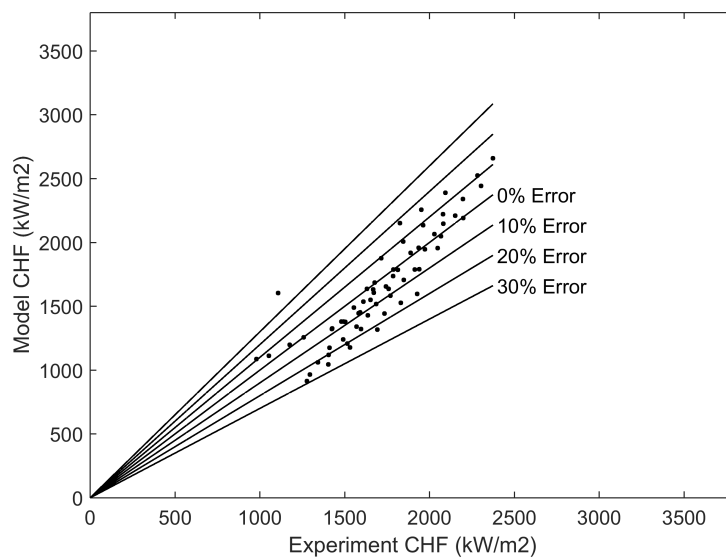


Figure 7.33: CHF model results for EPRI test 316.

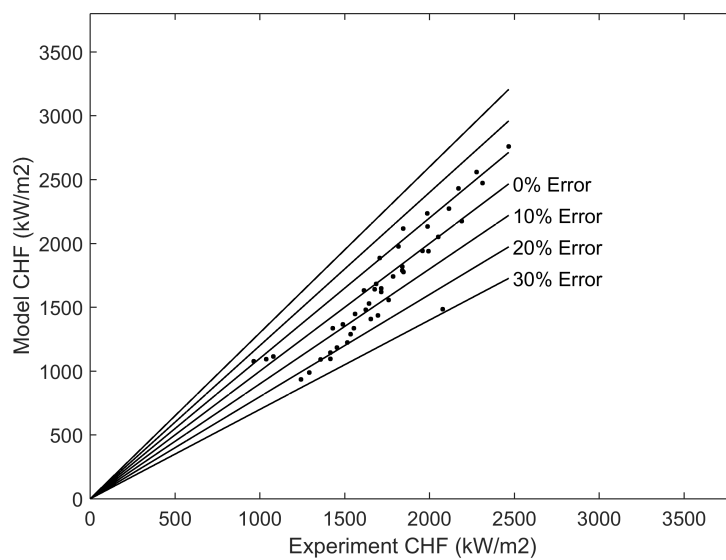


Figure 7.34: CHF model results for EPRI test 316.1.

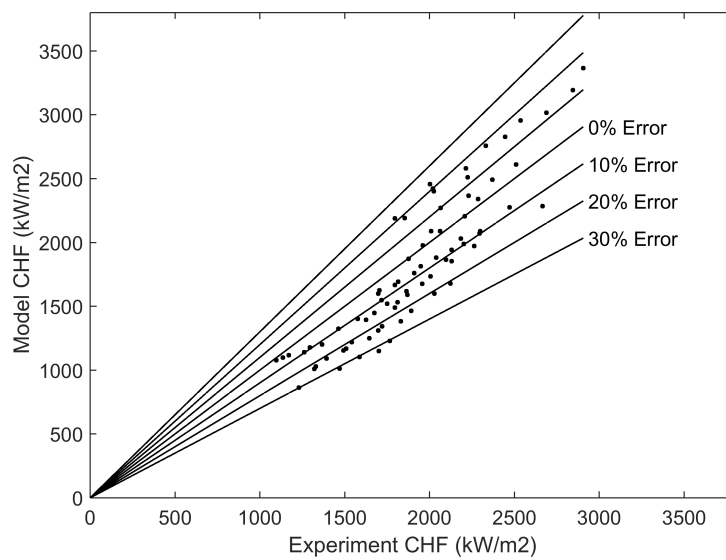


Figure 7.35: CHF model results for EPRI test 317.

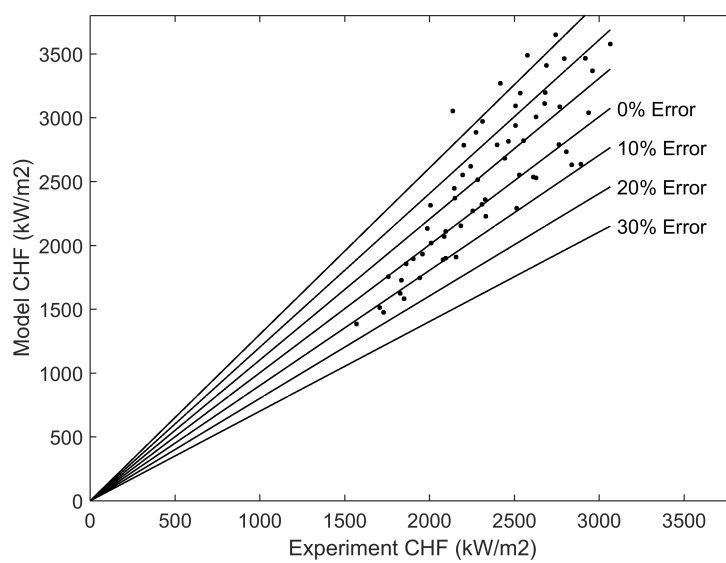


Figure 7.36: CHF model results for EPR test 318.

7.5.2 Critical Heat Flux Location

The results of the critical heat flux are presented here graphically more so to provide the dependence of the CHF value along an axial channel for the uniform heat flux case. A typical curve of the critical heat flux value versus location is provided in Figure 7.37 and Figure 7.38. In this case the CHF value is over-predicted by 2.0% and 14.1% respectively.

An increase in the axial position along a channel will result in a continuous decrease in the CHF limit due to the increased enthalpy of the fluid along the channel. For the uniform case the CHF location will occur at the exit of the channel. However, for the non-uniform (cosine shaped) heat flux profile the CHF location will occur in the upper half of the channel but not necessarily at the exit due to the meeting of the tangency requirement of the CHF curve and the actual heat flux curve (Figure 7.12).

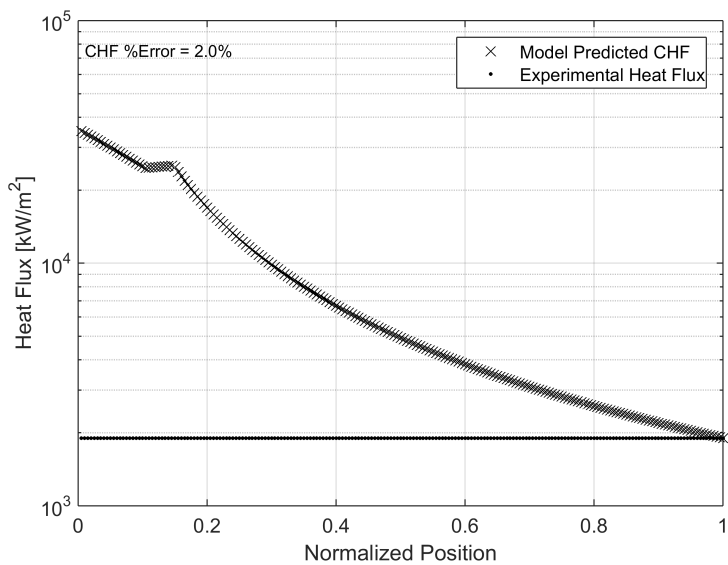


Figure 7.37: CHF versus axial position for EPRI test 301 run 17.

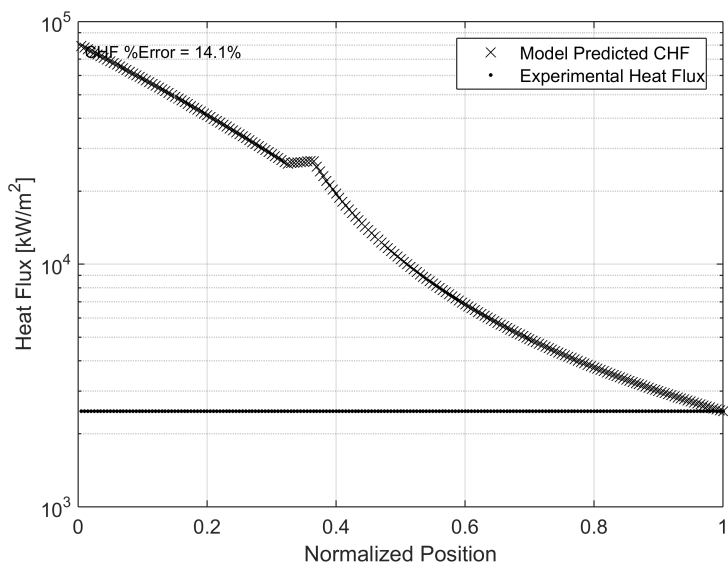


Figure 7.38: CHF versus axial position for EPRI test 303 run 24.

7.5.3 Correlation Bias

The correlation bias is investigated by comparing the calculated error of the results to various model parameters. Here bias is defined by distinct upward/positive or downward/negative shift in the error as a function of the magnitude of the observed parameter. This is done to ensure there are no large dependencies/drift in correlation results due to model parameters. It is desired that error be a result of the models random statistical error such as presented in Figure 7.15. These parameters include:

- inlet mass flux (Figure 7.39)
- system pressure (Figure 7.40)
- inlet temperature (Figure 7.41)
- inlet quality (Figure 7.42)
- critical quality (Figure 7.43)

As observed by the results no large bias exists in the results as function of a given parameter. A dip is observed for pressures towards 120 bar. Overall these plots demonstrate that the relative importance of each parameter has been correctly captured.

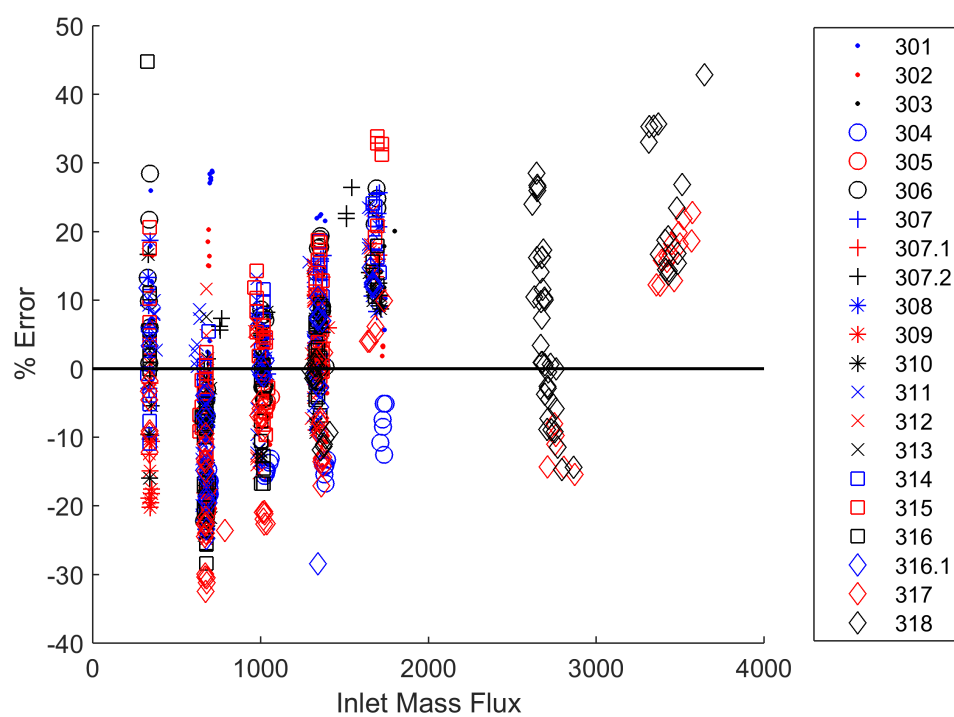


Figure 7.39: Correlation bias on mass flux for EPR database tests 301-318.

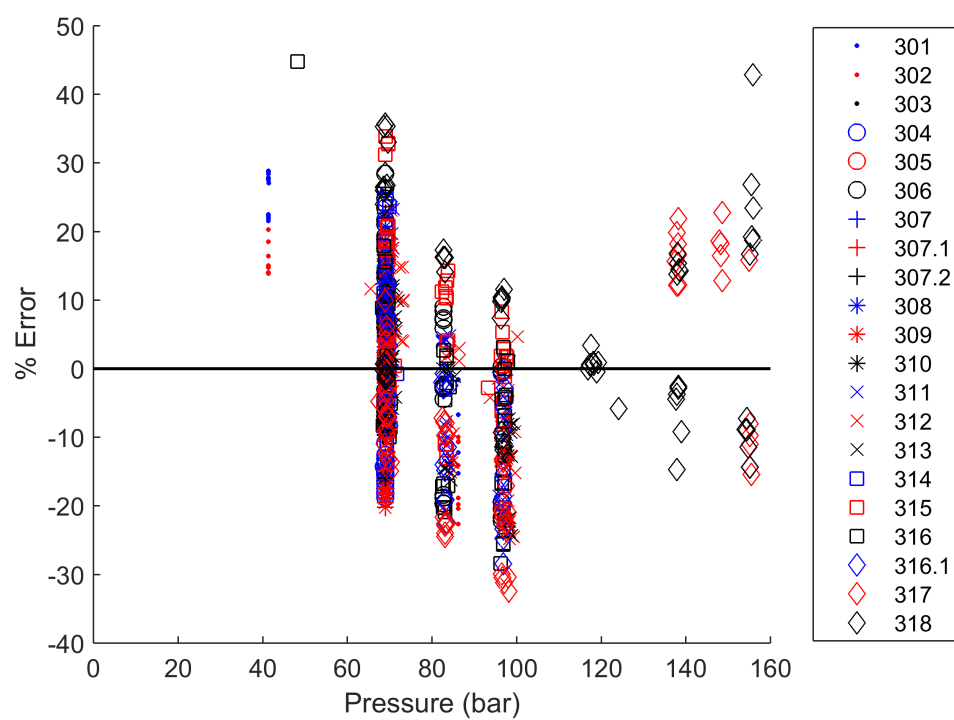


Figure 7.40: Correlation bias on system pressure for EPR database tests 301-318.

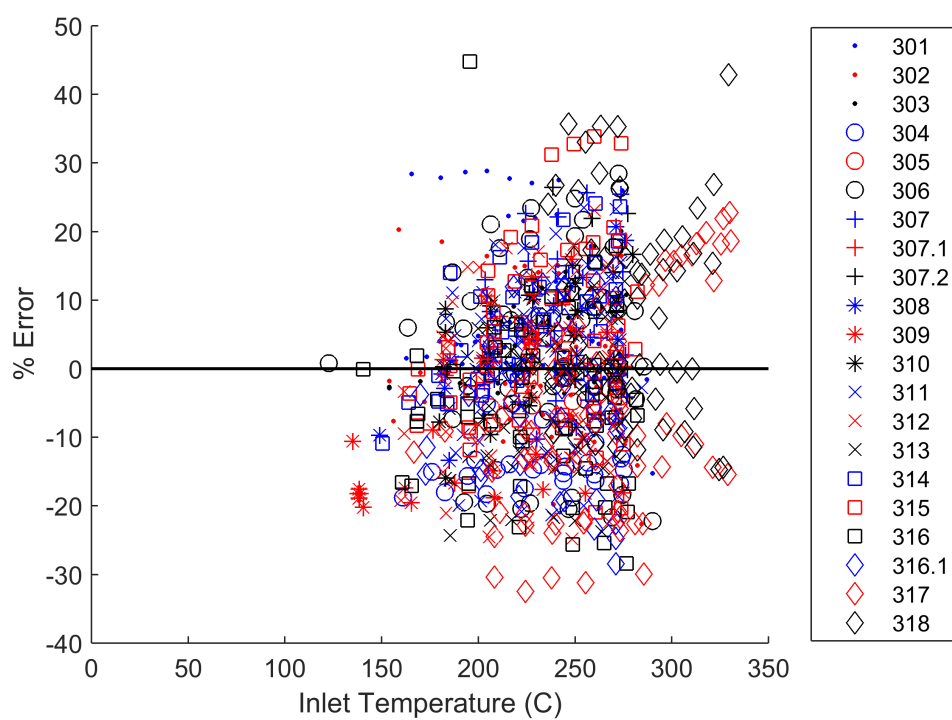


Figure 7.41: Correlation bias on inlet temperature for EPRI database tests 301-318.

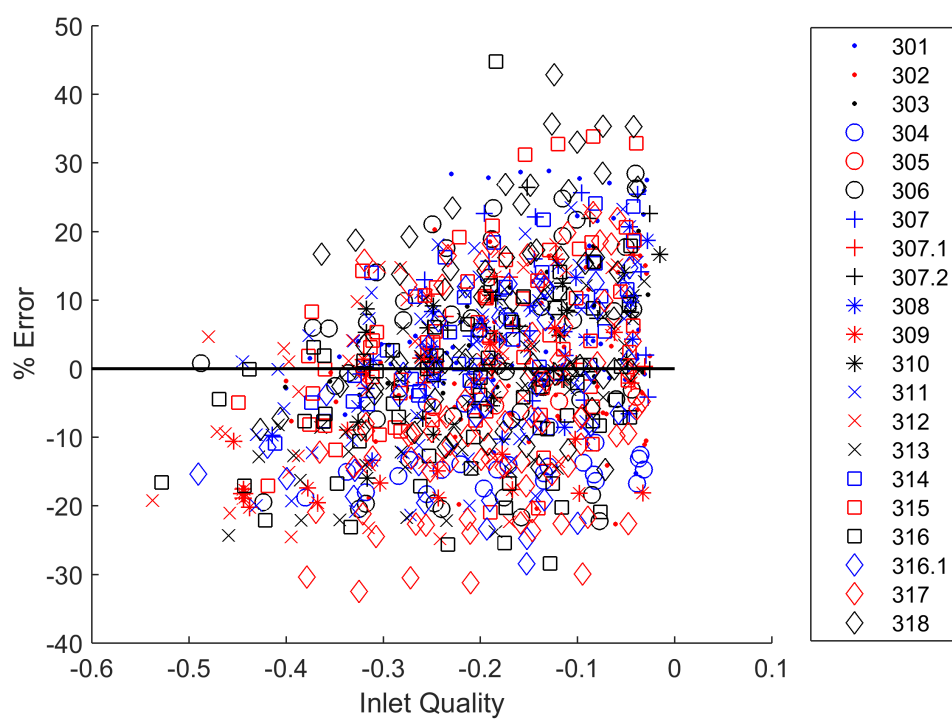


Figure 7.42: Correlation bias on inlet quality for EPRI database tests 301-318.

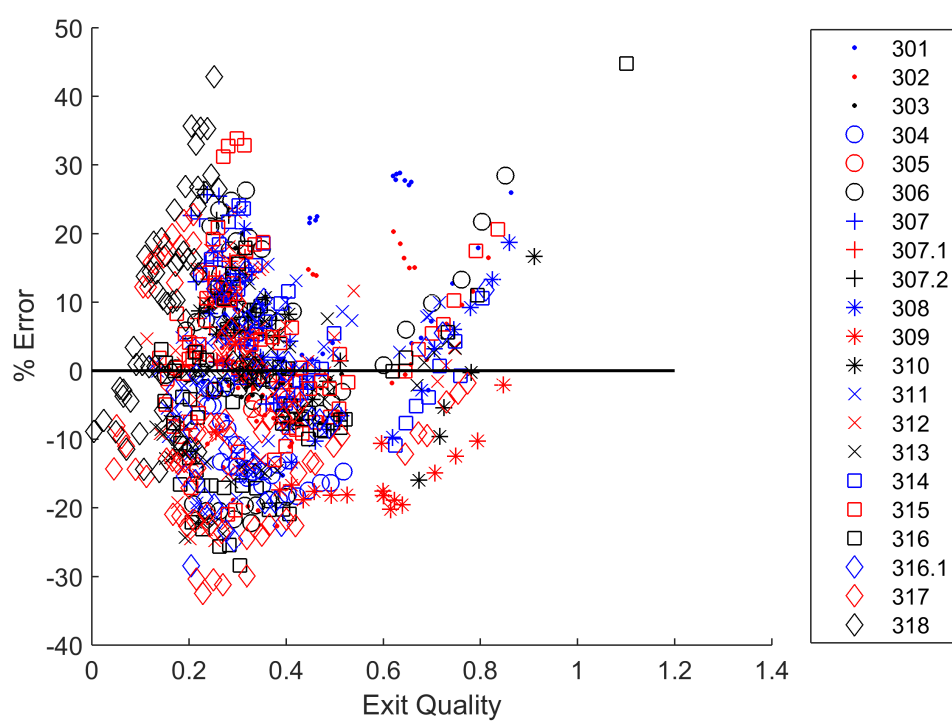


Figure 7.43: Correlation bias on critical quality for EPRI database tests 301-318.

Chapter 8: Conclusions

A mechanistic CHF correlation (Equation 6.35) has been developed for parameter ranges of inlet mass fluxes between 200 to 4000 $kg/(m^2 - s)$, pressures between 4.0 to 15.6 MPa , and critical qualities between -0.03 to 1.0. The root mean square error of the CHF value against the tested data base of over 800 points was determined to be 12.9%. The proposed model also allows for determination of the CHF location and critical rod power.

It is noted that this model is mechanistic based but like all mechanistic based correlations, empirical closure relations are required to obtain a final solution. With the proposed model little dependence on the specific closure chosen was observed in regards to the magnitude of the input from the relation as long as the general trends are captured by the constitutive relation. This is due to the use of a single calibration factor that accounts for surface and geometric configuration of the test/facility in the proposed CHF model. Further investigation into the hypothesized mechanisms for closure relations is encouraged. The method allows for swapping out specific models and closures if need is demonstrated for a specific application.

A specific area of focus for added development that is recommend is the nucleation site size distribution. Within this work a constant effective size has been used for all conditions which may be far from reality but lack of explicit modeling here has been captured by the calibration process. Better agreement may be possible by accounting for the size distribution. It is generally accepted that the cavity and bubble size distribution either follows a normal or Poisson distribution within the given possible nucleation site sizes as depicted by Figure 2.5. Orientation effects could also be added to the model requiring other forces to also be considered (e.g. buoyancy).

The model proposed attempts to define a unified approach to predict the onset of CHF for

a wide range of conditions independent of the flow regime. This has been demonstrated here; however, it is recognized that work is yet needed to understand the site distribution characteristics (in a statistical sense) to provide a more informed closure approach. The result will be a distribution of the possible CHF values related to the stochastic features of the surface.

Bibliography

- [1] S. Kutateladze, "On the transition to film boiling under natural convection," *Kotlo-turbostroenie*, vol. 3, 1948.
- [2] Y. Katto, "Generalized correlations for critical heat flux of natural convection boiling in confined channels," *Transactions of The Japan Society of Mechanical Engineers (in Japanese)*, vol. 44, no. 387, pp. 3908–3911, 1978.
- [3] J. T. Rogers, M. Salcudean, and A. E. Tahir, "Flow boiling critical heat fluxes for water in a vertical annulus at low pressure and velocities," *Proceedings of the 7th International Heat Transfer Conference*, vol. 4, pp. 339–344, 1982.
- [4] M. Monde, H. Kusuda, and H. Uehara, "Critical heat-flux during natural convective boiling in vertical rectangular channels submerged in saturated liquid," *Journal of Heat Transfer-Transactions of the Asme*, vol. 104, no. 2, pp. 300–303, 1982.
- [5] J. Weisman and B. S. Pei, "Prediction of critical heat flux in flow boiling at low qualities," *International Journal of Heat and Mass Transfer*, vol. 26, no. 10, pp. 1463–1477, 1983.
- [6] J. Weisman and S. H. Ying, "A theoretically based critical heat-flux prediction for rod bundles at pwr conditions," *Nuclear Engineering and Design*, vol. 85, no. 2, pp. 239–250, 1985.
- [7] C. Lee and I. Mudawwar, "A mechanistic critical heat flux model for subcooled flow boiling based on local bulk flow conditions," *International Journal of Multi-phase Flow*, vol. 14, no. 6, pp. 711–728, 1988.
- [8] W. Liu, H. Nariai, and F. Inasaka, "Prediction of critical heat flux for subcooled flow boiling," *International Journal of Heat and Mass Transfer*, vol. 43, no. 18, pp. 3371–3390, 2000.
- [9] M. Kureta and H. Akimoto, "Critical heat flux correlation for subcooled boiling flow in narrow channels," *International Journal of Heat and Mass Transfer*, vol. 45, no. 20, pp. 4107–4115, 2002.

- [10] M. Corradini and M. Greenwood, "Critical heat flux phenomenon at high pressure and low mass fluxes, neup final report part i: Experiments," tech. rep., Department of Engineering Physics, University of Wisconsin, 2014.
- [11] V. H. D. Valle and K. D.B.R., "Subcooled flow boiling at high heat flux," *International Journal of Heat and Mass Transfer*, vol. 28, pp. 1907–1920, 1985.
- [12] N. Basu, G. R. Warrier, and V. K. Dhir, "Onset of nucleate boiling and active nucleation site density during subcooled flow boiling," *Journal of Heat Transfer*, vol. 124, no. 4, pp. 717–728, 2002.
- [13] Y.-Y. Hsu and R. W. Graham, "Transport processes in boiling and two-phase systems, including near-critical fluids," no. Book, Whole, 1976.
- [14] S.-P. Liaw and V. K. Dhir, "Effect of surface wettability on transition boiling heat transfer from a vertical surface," *8th International Heat Transfer Conference*, vol. 4, pp. 2031–2036, 1986.
- [15] S. G. Kandlikar and M. E. Steinke, "Contact angles and interface behavior during rapid evaporation of liquid on a heated surface," *International Journal of Heat and Mass Transfer*, vol. 45, no. 18, pp. 3771–3780, 2002.
- [16] V. K. Dhir, H. S. Abarajith, and D. Li, "Bubble dynamics and heat transfer during pool and flow boiling," *Heat Transfer Engineering*, vol. 28, no. 7, pp. 608–624, 2007.
- [17] M. Misale, P. Ruffino, and M. Frogheri, "The influence of the wall thermal capacity and axial conduction over a single-phase natural circulation loop: 2-d numerical study," *Heat and Mass Transfer*, vol. 36, no. 6, pp. 533–539, 2000.
- [18] L. S. Tong and Y. S. Tang, "Boiling heat transfer and two-phase flow," no. Book, Whole, 1997.
- [19] D. D. Hall and I. Mudawar, "Critical heat flux (chf) for water flow in tubes - i. compilation and assessment of world chf data," *International Journal of Heat and Mass Transfer*, vol. 43, no. 14, pp. 2573–2604, 2000.
- [20] D. D. Hall and I. Mudawar, "Critical heat flux (chf) for water flow in tubes - ii. subcooled chf correlations," *International Journal of Heat and Mass Transfer*, vol. 43, no. 14, pp. 2605–2640, 2000.

- [21] Y. Hsu, "On the size range of active nucleation cavities on a heating surface," *Journal of Heat Transfer*, vol. 84, no. 3, pp. 207–213, 1962.
- [22] N. Zuber, "Hydrodynamic aspects of boiling heat transfer," *Ph.D Thesis*, 1959.
- [23] R. F. Gaertner and J. W. Westwater, "Population of active sites in nucleate boiling heat transfer," *Chemical Engineering Progress Symposium Series*, vol. 56, pp. 39–48, 1960.
- [24] B. Mikic and W. M. Rohsenow, "A new correlation of pool boiling data including the effect of heating surface characteristics," *ASME Journal of Heat Transfer*, vol. 91, pp. 245–250, 1969.
- [25] K. Cornwell and R. D. Brown, "Boiling surface topography," *Proceedings of 6th International Heat Transfer Conference, Toronto*, vol. 1, pp. 157–161, 1978.
- [26] G. Kocamustafaogullari, I. Chen, and M. Ishii, "Correlation for nucleation site density and its effects on interfacial area," no. NUREG/CR-2778; ANL-82-32, 1982.
- [27] C. H. Wang and V. K. Dhir, "Effect of surface wettability on active nucleation site density during pool boiling of water on a vertical surface," *Journal of Heat Transfer*, vol. 115, no. 3, pp. 659–669, 1993.
- [28] M. Ishii and T. Hibiki, "Thermo-fluid dynamics of two-phase flow second edition," 2011.
- [29] S. R. Yang and R. H. Kim, "A mathematical model of pool boiling nucleation site density in terms of surface characteristics," *Int. J. Heat and Mass Transfer*, vol. 31, pp. 1127–1135, 1988.
- [30] M. Jakob, "Heat transfer: v. 1," 1949.
- [31] C. Han and P. Griffith, "Technical report 19: The mechanism of heat transfer in nucleate pool boiling, part i, bubble initiation, growth and departure," no. 7673-19, 1962.
- [32] A. P. Hatton and I. S. Hall, "Photographic study of boiling on prepared surfaces," *Chemical Engineering Progress*, vol. 62, no. 8, 1966.
- [33] P. Griffith, "Bubble growth rates in boiling," *Transactions ASME Journal of Heat and Mass Transfer*, vol. 80, pp. 721–727, 1958.

- [34] M. Ellion, "Study of the mechanisms of boiling heat transfer," no. JPL-Memo-20-88, 1954.
- [35] N. Zuber, "The dynamics of vapor bubbles in non-uniform temperature fields," *Int. J. Heat and Mass Transfer*, vol. 2, pp. 83–105, 1961.
- [36] Nishikawa, H. K. Kusuda, and K. Yamasaki, "Growth and collapse of bubbles in nucleate boiling," *Transactions of the Japan Society of Mechanical Engineers*, vol. 30, no. 216, pp. 989–994, 1964.
- [37] Y. Hsu and R. Graham, "An analytical and experimental study of the thermal boundary layer and ebullition cycle in nucleate boiling," no. Book, Whole, 1961.
- [38] W. Fritz, "Maximum volume of vapor bubbles," *Physik Zeitschr*, vol. 36, pp. 379–384, 1935.
- [39] B. Staniszewski, "Technical report 16: Nucleate boiling bubble growth and departure," 1959.
- [40] R. Cole and H. Shulman, "Bubble departure diameters at subatmospheric pressures," *Chemical Engineering Progress Symposium Series 62*, vol. 64, pp. 6–16, 1966.
- [41] R. Semeria, "Quelques resultats sur le mecanisme de l'ebullition," *Journal de l'Hydraulic de la Societe Hydrotechnique de France*, vol. 7, 1962.
- [42] K. Nishikawa and K. Urakawa, "An experiment of nucleate boiling under reduced pressure," *Transactions of the Japan Society of Mechanical Engineers*, vol. 23, no. 136, pp. 935–939, 1957.
- [43] F. Peebles and H. Garber, "Studies on the motion of gas bubbles in liquids," *Chem. Engr. Progress*, vol. 49, no. 2, p. 88, 1953.
- [44] M. Jakob and W. Linke, "Heat transfer from a horizontal plate," *Forsch Gebiete Ingenieurw*, vol. 80, no. 2, pp. 75–81, 1933.
- [45] R. Graham and R. Hendricks, "Assessment of convection, conduction and evaporation in nucleate boiling," *NASA-TN D-3943*, 1967.
- [46] H. Forster and G. R., "Heat transfer to boiling liquids, mechanisms and correlations," *Transactions ASME Journal of Heat and Mass Transfer*, vol. 81, pp. 43–53, 1959.

- [47] M. Cooper, M. Judd, and R. Pike, "Shape and departure of single bubble growing at a wall," 1978.
- [48] J. C. Chen, "Correlation for boiling heat transfer to saturated fluids in convective flow," *Industrial and Engineering Chemistry Process Design and Development*, vol. 5, no. 3, pp. 322–329, 1966.
- [49] H. Forster and N. Zuber, "Dynamics of vapor bubbles and boiling heat transfer," *The American Institute of Chemical Engineers*, vol. 1, no. 4, pp. 531–535, 1955.
- [50] "Westinghouse ap1000 design control document rev. 19," 2011.
- [51] "Nuscale plant design overview," 2013.
- [52] C. Fighetti and D. Reddy, "Parametric study of chf data, volume 1: Compilation of rod bundle chf data available at the columbia university heat transfer research facility," 1982.
- [53] C. Fighetti and D. Reddy, "Parametric study of chf data, volume 2: A generalized chf correlation," 1982.
- [54] C. Fighetti and D. Reddy, "Parametric study of chf data, volume 3 part 1: Critical heat flux data," 1982.
- [55] C. Fighetti and D. Reddy, "Parametric study of chf data, volume 3 part 2: Critical heat flux data," 1982.
- [56] L. S. Tong, H. Currin, and A. Thorp, "An evaluation of the departure from nucleate boiling in bundles of reactor fuel rods," *Nuclear Science and Engineering*, vol. 33, no. 1, pp. 7–15, 1968.
- [57] D. C. Groeneveld, S. C. Cheng, and T. Doan, "1986 aecl-uo critical heat flux look-up table," *Heat Transfer Engineering*, vol. 7, no. 1-2, pp. 46–62, 1986.
- [58] D. C. Groeneveld, L. K. H. Leung, P. L. Kirillov, V. P. Bobkov, I. P. Smogalev, V. N. Vinogradov, X. C. Huang, and E. Royer, "The 1995 look-up table for critical heat flux in tubes," *Nuclear Engineering and Design*, vol. 163, no. 1–2, pp. 1–23, 1996.
- [59] D. C. Groeneveld, J. Q. Shan, A. Z. Vasić, L. K. H. Leung, A. Durmayaz, J. Yang, S. C. Cheng, and A. Tanase, "The 2006 chf look-up table," *Nuclear Engineering and Design*, vol. 237, no. 15-17, pp. 1909–1922, 2007.

- [60] Y. Katto, "Critical heat flux," *International Journal of Multiphase Flow*, vol. 20, pp. 53–94, 1994.
- [61] N. Zuber, "On stability of boiling heat transfer," *Transactions ASME Journal of Heat and Mass Transfer*, vol. 80, pp. 711–720, 1958.
- [62] Lamb, "Hydrodynamics," 1945.
- [63] P. Weber and K. Johannsen, "Convective transition boiling of water at medium pressure," *Proceedings of the 9th International Heat Transfer Conference*, vol. 6, pp. 63–68, 1990.
- [64] P. Weber and K. Johannsen, "Study of the critical heat flux condition at convective boiling of water: temperature and power controlled experiments," *Proc. 9th Int. Heat Transfer Conf*, vol. 2, pp. 63–68, 1990.
- [65] Y. Katto, "A prediction model of subcooled water flow boiling chf for pressure in the range 0.1–20 mpa," *International Journal of Heat and Mass Transfer*, vol. 35, no. 5, pp. 1115–1123, 1992.
- [66] X. C. Huang, P. Weber, and G. Bartsch, "Comparison of transient and steady-state boiling curves for forced upflow of water in a circular tube at medium pressure," *International Communications in Heat and Mass Transfer*, vol. 20, no. 3, pp. 383–392, 1993.
- [67] C. H. Oh and S. B. Englert, "Critical heat-flux for low flow boiling in vertical uniformly heated thin rectangular channels," *International Journal of Heat and Mass Transfer*, vol. 36, no. 2, pp. 325–335, 1993.
- [68] H. S. Kwon, D. H. Hwang, H. Y. Kim, and Y. C. Kim, "A theoretical model of critical heat flux in flow boiling at low qualities," *Ksme International Journal*, vol. 15, no. 7, pp. 921–930, 2001.
- [69] H. J. Chung and H. C. No, "A nucleate boiling limitation model for the prediction of pool boiling chf," *International Journal of Heat and Mass Transfer*, vol. 50, no. 15-16, pp. 2944–2951, 2007.
- [70] C. T. Wright, J. E. O'Brien, and R. E. Spall, "A new critical heat flux correlation for vertical water flow through multiple thin rectangular channels," *International Journal of Heat and Mass Transfer*, vol. 51, no. 5-6, pp. 1071–1084, 2008.

- [71] Y. Katto and Y. Kosho, "Critical heat flux of saturated natural convection boiling in a space bounded by two horizontal coaxial disks and heated from below," *International Journal of Multiphase Flow*, vol. 4, pp. 219–224, 1979.
- [72] S. Kutateladze, "Heat transfer in condensation and boiling," Original 1952 (Russian), Republished 1959 (English).
- [73] G. E. Thorncroft, J. F. Klausner, and R. Mei, "An experimental investigation of bubble growth and detachment in vertical upflow and downflow boiling," *International Journal of Heat and Mass Transfer*, vol. 41, no. 23, pp. 3857–3871, 1998.
- [74] G. E. Thorncroft, "Bubble forces and detachment models," *Multiphase Science and Technology*, vol. 13, no. 3, pp. 35–76, 2001.
- [75] S. G. Kandlikar, "A theoretical model to predict pool boiling chf incorporating effects of contact angle and orientation," *Journal of Heat Transfer*, vol. 123, no. 6, p. 1071, 2001.
- [76] J. F. Klausner, R. Mei, D. M. Bernhard, and L. Z. Zeng, "Vapor bubble departure in forced-convection boiling," *International Journal of Heat and Mass Transfer*, vol. 36, no. 3, pp. 651–662, 1993.

APPENDICES

Appendix A: Clausius-Clapeyron Derivation

Throughout literature different simplifying assumptions are used to derive the Clausius-Clapeyron equations. Derived here are some of the different variations of the Clausius-Clapeyron relation.

All derivations begin in the following matter. Beginning with the definition of entropy,

$$ds = \frac{\partial s}{\partial v}dv + \frac{\partial s}{\partial T}dT \quad (\text{A.1})$$

Since during phase change temperature is constant simplifying the above to

$$ds = \frac{\partial s}{\partial v}dv \quad (\text{A.2})$$

Using the general Maxwell relation which is represented in the following form:

$$\frac{\partial}{\partial x_i} \left(\frac{\partial \Phi}{\partial x_j} \right)_{x_i} = \frac{\partial}{\partial x_j} \left(\frac{\partial \Phi}{\partial x_i} \right)_{x_j} \quad (\text{A.3})$$

where Φ represents a thermodynamic potential such enthalpy or internal energy. Using specific enthalpy as the thermodynamic potential and taking the partials with respect to pressure and entropy,

$$\frac{\partial}{\partial P} \left(\frac{\partial h}{\partial s} \right)_P = \frac{\partial}{\partial s} \left(\frac{\partial h}{\partial P} \right)_s \quad (\text{A.4})$$

Using the definition of specific enthalpy

$$dh = Tds + vdP \quad (\text{A.5})$$

or written in terms of partials,

$$dh = \frac{\partial h}{\partial s} ds + \frac{\partial h}{\partial P} dP \quad (\text{A.6})$$

while noting that

$$T = \frac{\partial h}{\partial s} \quad \text{and} \quad v = \frac{\partial h}{\partial P} \quad (\text{A.7})$$

After substituting Equation A.7 into Equation A.6 the desired relationship is obtained,

$$\frac{\partial T}{\partial P} = \frac{\partial v}{\partial s} \quad (\text{A.8})$$

Substitute Equation A.8 into Equation A.2 to obtain

$$ds = \frac{\partial P}{\partial T} dv \quad (\text{A.9})$$

Since pressure and temperature are constant during phase transition the partial derivative is not a function of the total differentials and thus,

$$\frac{\partial P}{\partial T} = \frac{s_v - s_l}{v_v - v_l} = \frac{\Delta s}{\Delta v} \quad (\text{A.10})$$

Using another definition of specific enthalpy and again noting that temperature is constant during the phase change process,

$$dh = T ds \quad (\text{A.11})$$

$$\Delta s = \frac{\Delta h_{fg}}{T} \quad (\text{A.12})$$

Substituting this into Equation A.9,

$$\frac{\partial P}{\partial T} = \frac{\Delta h_{fg}}{\Delta v T} \quad (\text{A.13})$$

From this point are where different assumptions can be made in evaluating the differential of Equation A.13. These are described here.

A.1 Clausius-Clapeyron Solution in Finite Difference Form

Representing Equation 2.2 in finite difference form the pressure drop can be related as such:

$$P_v - P_l = (T_v - T_{sat}) \frac{\Delta h_{fg}}{(\nu_v - \nu_l) T_{sat}}. \quad (\text{A.14})$$

A.2 Clausius-Clapeyron Solution with Ideal Gas Law

The ideal gas law can be used to relate density changes with pressure. It is first assumed that $\nu_f \ll \nu_g$ such that $\Delta \nu \approx \nu_g$.

The ideal gas law,

$$\nu = \frac{RT}{P} \quad (\text{A.15})$$

is then inserted into Equation A.13.

$$\frac{\partial P}{\partial T} = \frac{\Delta h_{fg} P}{RT^2} \quad (\text{A.16})$$

Integration is then performed assuming that Δh_{fg} does not change greatly with pressure to yield:

$$\int_{P_f}^{P_g} \frac{1}{P} \partial P = \int_{T_{sat}}^{T_v} \frac{\Delta h_{fg}}{RT^2} \partial T \quad (\text{A.17})$$

$$\ln\left(\frac{P_g}{P_f}\right) = \frac{\Delta h_{fg}}{R} \left(\frac{1}{T_v} - \frac{1}{T_{sat}}\right) \quad (\text{A.18})$$

Note that from Equation 2.1 that critical radius can be related to the bubble interior pressure, thus

$$\ln\left(\frac{P_f + 2\sigma/r_c}{P_f}\right) = \frac{\Delta h_{fg}}{R} \left(\frac{1}{T_v} - \frac{1}{T_{sat}}\right) \quad (\text{A.19})$$

Solving for the critical radius,

$$r_c = \frac{2\sigma}{P_f} \left[e^{\frac{\Delta h_{fg}}{R} \left(\frac{1}{T_v} - \frac{1}{T_{sat}}\right)} - 1 \right]^{-1} \quad (\text{A.20})$$

Appendix B: MATLAB Script for Test Call Function

```

1 %-----
2 % Wrapper for determine CHF location and value for comparing model
3 % to experimental data.
4 %-----
5 clc,clear
6 tic;
7 SAVELOC = ['Results\EPRI\']
8 %load([SAVELOC, 'TEST.mat'])
9 diary([SAVELOC, 'TestScreen.txt'])
10 run('Functions\PlotSettings.m');
11 HBM=1;
12 maxcount = 50;
13 %% TESTS-----
14 J = [24];
15 if ~exist('Data')
16     Data(1:J(end)) = struct('Geometry', [], 'Input', [], 'Results', [], 'NodalResults', []);
17 end
18 %% MODEL CONSTANTS-----
19 beta_deg = 45;
20 I=200;
21 tolerance = 0.0005;
22 %% CONVERSION CONSTANTS-----
23 PSIA_2_BAR=0.0689475729;
24 PA_2_BAR=1E-5;
25 MLBM_FT2HR_2_KG_M2S=0.0013562309*1E6;
26 MBTU_FT2HR_2_W_M2=3.154594*1E6/1000;
27 BTU_LBM_2_KJ_KG=2326.000292/1000;
28 %-----
29 for k=1:length(J)
30     run('Units.m')
31     %% SOLUTION-----
32     for i=1:length(G)
33         x = G(i);
34         y = P_sys(i,1);

```

```

35     if j == 23 % for UofW HP tests
36         a = 2.151;
37         b = -0.09458;
38         c = 0.0;
39         d = -0.005594;
40     elseif j == 24 % for UofW LP tests
41         % Dont have CHF value so error(i,1) will be meaningless
42         % Error determined by CRP manually
43         % NOT USED - PLACEHOLDER
44         a = 12.04;
45         b = 0.4747;
46         c = 0.0;
47         d = -30.25;
48         %
49     else % For EPRI tests 301-318
50         a = 26.55;
51         b = -0.5631;
52         c = 0.0;
53         d = -0.001472;
54     end
55     rc(i,1) = (a*x^b + c + d*y)*1E-6;
56
57     [qtot(:,i),qflux_exp(:,i),qCHF(i,1),Lc(i,1),f(:,i),Na(:,i),vbi(:,i),dTW(:,i),quality(:,i),Re(:,i),rb(i,1),drho(i,1),minRowIdx(i,1),
58     =CHF(qpin_exp(i,1),G(i,1),Tin(i,1),P_sys(i,1),heatflux_dist,rc(i,1),Geometry,I,beta_deg,tolerance,i);
59
60     % For HBM force tangency of CHF curve and hypothetical heat flux
61     % curve and then compare CHF curve to the actual heat flux curve
62     if HBM == 1
63         qpin_new(i,1) = qpin_exp(i,1);
64         qpin_old = qpin_new(i,1);
65         tan_error= 1.0;
66         qpin_high = 1000;
67         qpin_low = 0.0;
68         count = 0;

```

```

69 while abs(tan_error) > tolerance && count <= maxcount
70
71     [qtot(:,i),qCHF(:,i),qCHF(i,1),Lc(i,1),f(:,i),Na(:,i),vbi(:,i),dTW(:,i),quality(:,i),Re(:,i),rb(i,1),drho(i,1),minRowIdx
72     =CHF(qpin_new(i,1),G(i,1),Tin(i,1),P_sys(i,1),heatflux_dist,rc(i,1),Geometry,I,beta_deg,tolerance,i);
73
74     xloc=minRowIdx(i,1); % forces tangency convergence
75     tan_error=(qflux(xloc,i)-qtot(xloc,i))...
76     /qflux(xloc,i);
77
78     if tan_error >= 0 && abs(tan_error) > tolerance % for positive error q"exp > q"model
79         qpin_new(i,1)=(qpin_new(i,1)*1/2 + qpin_low*1/2);
80         qpin_high=qpin_old;
81     elseif tan_error < 0 && abs(tan_error) > tolerance % for negative error q"exp < q"model
82         qpin_new(i,1)=(qpin_new(i,1)*1/2 + qpin_high*1/2);
83         qpin_low=qpin_old;
84     end
85     qpin_old = qpin_new(i,1);
86     count=count+1;
87 end
88
89 error(i,1) = (qCHF(i,1)-Input(i,5,1))/Input(i,5,1);
90 fprintf('Set: %d; run: %d/%d; Experimental CRP= %0.2f kW; Error= %0.2f percent; rc= %0.5f micron; Gin= %0.1f kg/m-s2; Psys= %0.1f
91
92 %% SAVE PLOT OF CONVERGED SOLUTION-----
93 l(:,1) = 1/I:1/I:1; % nodal spacing
94
95 figure('Visible','off')
96 h1=semilogy(l(:,1), qtot(:,i), 'xk', l(:,1), qflux(:,i), '.k' );
97 legebd_h=legend('Model Predicted CHF', 'Experimental CHF', 'Experimental Heat Flux', 'Location', 'northeast');
98 ylabel('Heat Flux [kW/m^2]')
99 xlabel('Normalized Position')
100 axis([min(xlim) max(xlim) min(ylim) min(max(ylim), 100*max(qflux(:,i)))])
101 grid on
102

```

```

103 callout1 = ['CHF %Error = ', sprintf('%1f', error(i,1)*100), '%'];
104 callout = {callout1};
105 text(0.01, 0.75*(max(ylim)-min(ylim))-min(ylim), callout, 'FontSize', 10)
106 savelabel=[SAVELOC, 'TestPlots\DataSet_', num2str(j), '_Run_', num2str(i), 'of', num2str(length(G))];
107 print(gcf, '-dpng', resolution, savelabel);
108
109 end
110
111 Results(:,1) = qpin_new;
112 Results(:,2) = qCHF;
113 Results(:,3) = Lc;
114 Results(:,4) = rc;
115 Results(:,5) = error;
116 Results(:,6) = minRowIdx;
117 Results(:,7) = count;
118 Results(:,8) = drho;
119 Results(:,9) = rb;
120
121 NodalResults(:,1) = qtot;
122 NodalResults(:,2) = qflux;
123 NodalResults(:,3) = f;
124 NodalResults(:,4) = Na;
125 NodalResults(:,5) = vbi;
126 NodalResults(:,6) = dTW;
127 NodalResults(:,7) = quality;
128 NodalResults(:,8) = Re;
129 NodalResults(:,9) = Re;
130
131 Data(j).Results = Results;
132 Data(j).NodalResults = NodalResults;
133
134 cclear Input Geometry HeatFlux_dist Results NodalResults
135 cclear qpin_new qCHF Lc rc error minRowIdx count drho rb
136 cclear qtot qflux f Na vbi dTW quality Re

```

```
137 end
138 save([SAVELOC, 'TEST.mat'], 'Data')
139 toc
140 diary off
```

Appendix C: MATLAB Script for Calibration Call Function

```

1 %-----
2 %-----
3 % This function is used to as calibration function for effectice cavity size.
4 % Works for both uniform and non-uniform cases.
5 %-----
6 %-----
7 clc,clear
8 tic;
9 %% AVAILABLE TEST DATA-----
10 J = [24]; % test database range applied
11 LoadData=1; % loads current populated database
12 SAVELOC = ['Results\UofWLP\'J
13 diary([SAVELOC, 'CalibrationScreen.txt'])
14 if LoadData == 1;
15 load([SAVELOC, 'Calibration.mat'])
16 else
17 Data(1:J(end))=struct('Geometry',[], 'Input',[], 'HeatFluxDist',[], 'Results',[], 'NodalResults',[]);
18 end
19 %-----
20 %
21 %% MODEL CONSTANTS-----
22 beta_deg = 45; % bubble-surface contact angle [deg]
23 I=500; % number of axial nodes in flow channel
24 tolerance = 0.000001; % convergence tolerance
25 %% CONVERSION CONSTANTS-----
26 PSIA_2_BAR=0.0689475729; % psia to bar
27 PA_2_BAR=1E-5; % Pa to bar
28 MLBM_FT2HR_2_KG_M2S=0.0013562309*1E6; % MLbm/(ft2-hr) to kg/(m2-s)
29 MBTU_FT2HR_2_W_M2=3.154594*1E6/1000; % MBtu/(ft2-hr) to kW/m2
30 BTU_LBM_2_KJ_KG=2326.000292/1000; % Btu/lbm to kJ/kg
31 %-----
32 %
33 %% INPUT SETUP-----
34 for k=1:1:length(J)

```

```

35 run('Units.m')
36 %% SOLUTION-----
37 for i=1:length(G)
38     count(i,1)=0;
39     maxcount = 200;
40     error(i,1)=1;
41     rc_high=1*10^(-3);
42     rc_low=1*10^(-8);
43     rc_new=0.6978*10^(-6)*P_sys(i,1).^(-0.962);
44     rc_old=rc_new;
45
46     fprintf('Set: %d; run: %d/%d; Experimental CPR = %0.2f kW;', j, i, length(G), qpin_exp(i))
47
48     while abs(error(i,1)) > tolerance && count(i,1) < maxcount+1
49
50         [qtot(:,i),qCHF(:,i),qCHF(i,1),Lc(i,1),f(:,i),Na(:,i),vbi(:,i),dTW(:,i),quality(:,i),Re(:,i),rb(i,1),drho(i,1),minRowIdx(i,1)]...
51         =CHF(qpin_exp(i,1),G(i,1),Tin(i,1),P_sys(i,1),heatflux_dist,rc_new,Geometry,I,beta_deg,tolerance,i);
52
53         if ~isnan(qCHF(i,1))
54             xloc=minRowIdx(i,1);
55             error(i,1)=(qflux(xloc,i)-qtot(xloc,i))...
56             /qflux(xloc,i);
57         end
58
59         if error(i,1) >= 0
60             rc_new=(rc_new*1/2 + rc_low*1/2);
61             rc_high=rc_old;
62         elseif error(i,1) < 0
63             rc_new=(rc_new*1/2 + rc_high*1/2);
64             rc_low=rc_old;
65         else
66             rc_new=rc_new + 1*10^-5;
67         end
68

```

```

69     rc_old = rc_new;
70     count(i,1)=count(i,1)+1;
71     end
72
73     if count(i,1) > maxcount           % solution divergent
74         rc(i,1) = NaN;
75         qCHF(i,1) = NaN;
76         fprintf(' qCHF = divergent; max iterations reached')
77     else
78         rc(i,1) = rc_new;           % final converged cavity size [m]
79     end
80
81     fprintf(' count = %d, Error= %0.2f percent; rc= %0.5f micron; Gin= %0.1f kg/m-s2; Psys= %0.1f bar; Tin= %0.1f C; Xexit= %0.2f; Lc/L= %0.
82     count(i,1), error(i,1)*100, rc(i,1)*10^6, G(i,1), P_sys(i,1), Tin(i,1), quality(I,i), Lc(i)/Geometry(11,2))
83
84     % SAVE PLOT OF CONVERGED SOLUTION-----
85     Lstar(i,1) = Lc(i,1)/Data(j).Geometry(11,2);           % CHF location from model [normalized]
86     l(:,1) = 1/I:1/I:1;
87     qCHF(i,1) = qtot(xloc,i);           % nodal spacing
88                                         % CHF value from model [kW/m2]
89
90     figure('Visible','off')
91     semilogy(l(:,1), qtot(:,i), 'xk', l(:,1), qflux(:,i), 'k')
92     legebd_h=legend('Model Predicted CHF', 'Experimental Heat Flux');
93     ylabel('Heat Flux [kW/m^2]')
94     xlabel('Normalized Position')
95     axis([min(xlim) max(xlim) min(ylim) min(max(ylim), 100*max(qflux(:,i)))])
96     grid on
97     line([Lstar(i,1) Lstar(i,1)], [min(ylim) qCHF(i,1)], 'Color', [0 0 0]); %Mark CHF value
98     line([min(xlim) Lstar(i,1)], [qCHF(i,1) qCHF(i,1)], 'Color', [0 0 0]); %Mark CHF location
99     callout1 = ['CHF = ', sprintf('%1f', qCHF(i,1)), ' kW/m^2'];
100    callout2 = ['CRP = ', sprintf('%1f', qpin_exp(i,1)), ' kW'];
101    callout3 = ['L* = ', sprintf('%3f', Lstar(i,1))];
102    callout = {callout1; callout2; callout3};
103    text(0.01, 0.65*(max(ylim)-min(ylim))+min(ylim), callout, 'FontSize', 10)

```

```

103
104 saveLabel=[SAVELOC, 'CalibrationPlots\DataSet_', num2str(j), '_Run_', num2str(i), 'of', num2str(length(G))];
105 saveas(gcf, saveLabel, 'png');
106 end
107 %-----
108 %
109 %% POST PROCESSING-----
110 Results(:,1) = qpin_exp;
111 Results(:,2) = qCHF;
112 Results(:,3) = Lc;
113 Results(:,4) = rc;
114 Results(:,5) = error;
115 Results(:,6) = minRowIdx;
116 Results(:,7) = count;
117 Results(:,8) = drho;
118 Results(:,9) = rb;
119
120 NodalResults(:,1) = qtot;
121 NodalResults(:,2) = qlux;
122 NodalResults(:,3) = f;
123 NodalResults(:,4) = Na;
124 NodalResults(:,5) = vbi;
125 NodalResults(:,6) = dTW;
126 NodalResults(:,7) = quality;
127 NodalResults(:,8) = Re;
128 NodalResults(:,9) = vbi;
129
130 Data(j).Results = Results;
131 Data(j).NodalResults = NodalResults;
132
133 clear Input Geometry Heatflux_dist Results NodalResults
134 clear qpin_CHF qpin_exp qCHF Lc rc error minRowIdx count drho rb
135 clear qtot qlux f Na vbi dTW quality Re vbi rbavg
136 save([SAVELOC, 'Calibration.mat'], 'Data')

```

```

137 end
138 %-----
139 %
140 %% PLOTS-----
141 figure(1)
142 for i=1:length(J)
143     j=J(i);
144     semiilogy( Data(j).Input(:,2), Data(j).Results(:,4)*1.0E6, '.', 'MarkerSize',10)
145     hold on
146 end
147 xlabel('Pressure (bar)')
148 ylabel('Minimum Cavity Radius (microns)')
149 legend show
150 %-----
151 figure(2)
152 for i=1:length(J)
153     j=J(i);
154     plot( Data(j).Input(:,5), Data(j).Results(:,2), '.', 'MarkerSize',10)
155     hold on
156 end
157 xlabel('Experiment CHF (kW/m2)')
158 ylabel('Model CHF (kW/m2)')
159 axis([0 3000 0 3000])
160 line([0 3000], [0 3000])
161 legend show
162 %-----
163 figure(93)
164 for i=1:length(J)
165     j=J(i);
166     plot( mean(Data(j).ModalResults(:,4)), Data(j).Results(:,5)*100, '.', 'MarkerSize',10)
167     hold on
168 end
169 xlabel('Mean Nucleation Site Density (sites/m2)')
170 ylabel('Error % ')

```

171 *Legend show*

172 %------

173 **toc;**

174 %------

175 %------

Appendix D: MATLAB Script for CHF Function

```

1 function [qtot,qFlux,qCHF,Lc,f,Na,vbi,dTw,quality,Re,rb,drho,minRowIdx]...
2 = CHF(qpin,G,Tin,P_sys,heatflux_dist,rc,Geometry,I,beta_deg,tolerance,test)
3 %-----
4 %-----
5 % This function is used to find the CHF value with the DSM or HBM or
6 % used as calibration function for determining effective cavity size.
7 %-----
8 %-----
9 %
10 %% INPUTS-----
11 Af=Geometry(7,2); % flow area [m2]
12 Ah=Geometry(8,2); % total heated area [m2]
13 Pw=Geometry(10,2); % wetted perimeter [m]
14 Ph=Geometry(9,2); % heated perimeter [m]
15 L=Geometry(11,2); % heated length [m]
16 D_heated=4*Af/Ph; % heated hydraulic diameter [m]
17 D_wetted=4*Af/Pw; % wetted hydraulic diameter [m]
18 mdot=G*Af; % mass flowrate [kg/s]
19 % CONSTANTS-----
20 g=9.81; % gravitational constant [m/s2]
21 % MODEL INPUTS-----
22 beta=beta_deg*pi/180; % bubble static contact angle [rad]
23 Cvm=11/16; % virtual mass coefficient
24 Cvm=0.0; % virtual mass coefficient (remove Fvm)
25 rb=rc/sin(beta); % bubble size
26 % NODALIZATION INPUTS-----
27 dLength = L/(I-1); % length of each axial nod [m]
28 Ahi=dLength*Ph; % node heated area [m2]
29 l(:,1)=0:dLength:L; % initialize axial nodal cell lengths
30 hin(1:I,1)=XSteam('h_pt',P_sys,Tin); % channel inlet enthalpy [kJ/kg]
31 % BULK SATURATED FLUID PROPERTIES-----
32 hf= XSteam('hL_p', P_sys); % liquid enthalpy [kJ/kg]
33 hg= XSteam('hV_p', P_sys); % liquid enthalpy [kJ/kg]
34 hfg = hg - hf; % vaporization enthalpy [kJ/kg]

```

```

35 Tsat = XSteam('Tsat_p', P_sys); % saturation temperature [C]
36 rhov_sat=XSteam('rhoV_p', P_sys); % saturated vapor density [kg/m3]
37 rhol_sat=XSteam('rhoL_p', P_sys); % saturated liquid density[kg/m3]
38 drho = (rhov_sat-rhov_sat)/rhol_sat; % buoyancy modulus
39 % HEAT FLUX DISTRIBUTION INPUT-----
40 qflux(:,1)=heatflux_dist(:,1)*qpin;
41 %-----
42 %
43 %% NODAL MIXTURE FLUID PROPERTIES-----
44 for i=1:I
45     ho(i,1) = qflux(i,1)*Ahi/mdot + hin(i,1); % nodal exit enthalpy [kJ/kg]
46     h(i,1) = (hin(i,1) + ho(i,1))/2; % nodal average enthalpy [kJ/kg]
47     quality(i,1) = (h(i,1) - hf)/hfg; % nodal quality
48
49     if i~=I
50         hin(i+1,1) = ho(i,1); % set channel exit enthalpy equal to
51         end % previous node exit enthalpy
52
53     Tm(i,1)=XSteam('T_ph', P_sys, h(i,1)); % mixture temperature [C]
54
55     if Tm(i,1) > Tsat; % limit bulk temp. to sat temp.
56         Tm(i,1) = XSteam('Tsat_p', P_sys);
57     end
58
59     rhom(i,1)=XSteam('rho_ph', P_sys, h(i,1)); % mixture density [kg/m3]
60     viscositym(i,1)=XSteam('my_pT',P_sys, Tm(i,1)-1); % mixture viscosity [Pa-s]
61     viscosity_l(i,1)=XSteam('my_ph',P_sys, hf); % liquid viscosity [Pa-s]
62     viscosity_v(i,1)=XSteam('my_ph',P_sys, hg); % vapor viscosity [Pa-s]
63     sigmam(i,1)=XSteam('st_T', Tm(i,1)); % mixture surface tension [N/m]
64     cplm(i,1)=XSteam('CpL_T',Tm(i,1)-1)*1000; % mixture specific heat [J/(kg-C)]
65     klm(i,1)=XSteam('tcl_T',Tm(i,1)-1); % mixture thermal conductivity [W/m-C]
66     Prandlt(i,1)=viscositym(i,1)*cplm(i,1)/klm(i,1); % mixture Prandtl number
67     %% CHEN BOILING MODEL-----
68     Xtt(i,1) = (((1-quality(i,1))/quality(i,1))^0.9)... % Martinelli parameter

```

```

69      *(rhov_sat/rhol_sat)^0.5...
70      *(viscosity_l(i,1)/viscosity_v(i,1))^0.1;
71
72      if 1/Xtt(i,1) <= 0.1
73          F(i,1) = 1;
74      else
75          F(i,1) = 2.35*(1/Xtt(i,1)+0.213)^0.736;
76      end
77
78      if quality(i,1) >= 0.0 && quality(i,1) <= 1.0
79          qualtemp = quality(i,1);
80      elseif quality(i,1) < 0.0 || ~isreal(quality(i,1)) || isnan(quality(i,1))
81          qualtemp = 0.0;
82      elseif quality(i,1) > 1.0
83          qualtemp = 1.0;
84      end
85      Re_TP(i,1) = (G*(1-qualtemp)*D_wetted)...
86      /(viscosity_m(i,1)*F(i,1)^1.25;
87      S(i,1) = (1+1.4*10^4-5*Re_TP(i,1))^1;
88      %-----
89      end
90      %-----
91      %
92      %% WALL FLUID PROPERTIES-----
93      for i=1:I
94          Pb(i,1) = P_sys+2*sigmam(i,1)./rb/(10^5);
95
96          if Pb(i,1) > 219
97              Pb(i,1) = 219;
98          end
99
100         H_bubble(i,1) = rb*(1 + cos(beta));
101         Ai(1,1) = 2*pi*H_bubble(1,1)*rb;
102
103         % internal bubble pressure [bar]
104         % limit to below critical pressure
105         % bubble height [m]
106         % bubble interfacial area [m2]

```

```

103 %T_w(i,1)=XSteam('Tsat_p',Pb(i,1));
104 T_w(i,1) = (Tsat+273.15)*(1+2*sigmam(i,1)...
105 /((rc*rhov_sat*hfg*1e3))-273.15;
106 dTw(i,1) = T_w(i,1) - Tsat;
107 dTw(i,1) = dTw(i,1)*S(i,1);
108 T_w(i,1) = dTw(i,1) + Tsat;
109
110 if T_w(i,1) > 370
111     T_w(i,1) = 370;
112 end
113
114 rhoL_w(i,1)=XSteam('rhoL_T', T_w(i,1));
115 rhov_w(i,1)=XSteam('rhoV_T', T_w(i,1));
116 viscosity_w(i,1)=XSteam('my_pT',Pb(i,1),T_w(i,1)-2);
117 hf_w(i,1)=XSteam('hL_T', T_w(i,1))*1000;
118 hg_w(i,1)=XSteam('hV_T', T_w(i,1))*1000;
119 hfg_w(i,1)=(hg_w(i,1)-hf_w(i,1));
120 sigma_w(i,1)=XSteam('st_T', T_w(i,1));
121 end
122 %-----
123 %
124 %% FRICTION COEFFICIENT-----
125 for i=1:I
126     uf(i,1)=G/rhom(i,1);
127     Re(i,1)=G*D_wetted/viscositym(i,1);
128     Nu(i,1) = 0.023*Re(i,1)^0.8*Prandlt(i,1)^0.4;
129     hconv(i,1) = Nu(i,1)*kIm(i,1)/D_wetted;
130
131     if Re(i,1) <= 2320
132         lambda(i,1) = 64/(Re(i,1));
133     elseif 2320 > Re(i,1) <= 10^5
134         lambda(i,1) = 0.3164*(Re(i,1)^(-0.25));
135     else
136         lambda(i,1) = 0.0032+0.221*(Re(i,1)^(-0.237));

```

```

% wall temp based sat temp at Pb [C]
% wall temp.- Clausius-Claperyeon [C]
% wall superheat [C]
% effective wall superheat [C]
% effective wall temp. [C]

```

```

% limit wall temperature to
% critical wall temperature

```

```

% sat. liquid density [kg/m3]
% sat. vapor density kg/m3]
% viscosity [m2/s]
% sat. liquid enthalpy [J/kg]
% sat. vapor enthalpy [J/kg]
% heat of vaporization [J/kg]
% surface tension [N/m]

```

```

% bulk velocity [m/s]
% bulk Reynolds number
% Nusselt number
% convective heat xfr cffnt [W/m2-K]
% laminar flow
% turbulent flow

```

```

137 end
138
139 Cf(i,1) = Lambda(i,1)/4;
140 tau_w(i,1) = Cf(i,1)/2.*rhoL_w(i,1).*uf(i,1)^2;
141 uf_y(i,1)=H_bubble/2*tau_w(i,1)/viscosity_w(i,1);
142 Re_b(i,1)=rhoL_w(i,1)*uf_y(i,1)*rb...
143 /viscosity_w(i,1);
144 Gs(i,1)=1;
145 CL(i,1)=3.877*Gs(i,1)^0.5...
146 *((Re_b(i,1)^(-2))+0.014*Gs(i,1)^2)^0.25;
147 end
148 %-----
149 %
150 %% FORCES ACTING ON BUBBLE-----
151 for i=1:I
152 F_sigma(i,1)=2*pi*rc*sigma_w(i,1)*sin(beta);
153 F_lift(i,1)=0.5*CL(i,1)*rhoL_w(i,1) ...
154 *pi*rb^2*uf_y(i,1)^2;
155 F_i(i,1)=Ai/(rhoV_w(i,1)*hfg_w(i,1)^2);
156 end
157 %-----
158 %
159 %% CRITICAL HEAT FLUX-----
160 for i=1:I
161 qevap(i,1) = ((F_sigma(i,1) - F_lift(i,1))...
162 ./F_i(i,1)).^0.5*(1/1000);
163
164 if imag(qevap(i,1))~=0 || isnan(qevap(i,1))
165 qevap(i,1)=0;
166 end
167
168 vbi(i,1) = 2*qevap(i,1)/(rhoV_w(i,1)*hfg_w(i,1)/1000);
169 end
170 % NUCLEATION SITE DENSITY (BASU)-----

```

```

% skin friction coefficient
% shear stress [Pa]
% bubble center velocity [m/s]
% bubble Reynolds number
% shear lift Coefficient

```

```

% surface tension force component
% bubble lift force component
% bubble vapor inertial force component

```

```

% evaporative heat flux [kW/m2]
% remove imaginary+NaN components
% means no bubble can be generated

```

```

% bubble vel. normal to surface [m/s]

```

```

171 for i=1:I
172     if dTw(i,1) >= 15
173         Na(i,1) = 0.34*(1-cos(beta))*dTw(i,1)^5.3;
174     else
175         Na(i,1) = 0.34*(1-cos(beta))*dTw(i,1)^2*100^2;
176     end
177
178     ravg = (0.5)*2.54/100;
179
180     f(i,1) = Na(i,1)*pi*ravg^2;
181
182     if f(i,1) > 1
183         f(i,1) = 1;
184         Na(i,1)=1/(pi*ravg^2);
185     end
186 end
187 % HEAT FLUX PARTITIONING-----
188 for i=1:I
189     qevapf(i,1) = qevap(i,1). *f(i,1);
190     Nu(i,1) = 0.023*Re(i,1)^0.8*Prandlt(i,1)^0.4;
191     hconv(i,1) = Nu(i,1)*kIm(i,1)/D_wetted;
192     qconv(i,1)= hconv(i,1)*dTw(i,1)*(1-f(i,1))/1000;
193     qtot(i,1) = qconv(i,1)+qevapf(i,1);
194 end
195 CHFR(:,1)= qtot(:,1)./qflux(:,1);
196 qdif(:,1) = qtot(:,1) - qflux(:,1);
197 [minColVal, minRowIndex] = min(qdif);
198 Lc = l(minRowIndex,1);
199 qCHF = qtot(minRowIndex,1);
200 % -----
201 end %function end

```

% site density based on dTw [sites/m2]

% Constant average cavity size

% surface boiling fraction

% limit boiling fraction 1.0

% fractioned evap. heat flux [kW/m2]
% Nussult number
% convective heat xfr cffnt [W/m2-K]
% fractioned conv. heat flux [kW/m2]
% total effective heat flux [kW/m2]

% local CHFR ratio
% local margin (abs) to CHF [kW/m2]
% location and value of qdif
% CHF location [m]
% critical heat flux value [kW/m2]

Appendix E: MATLAB Script for Heat Flux Distribution Function

```

1 %-----
2 % Determines heat flux distribution based on experiment
3 %-----
4 function [heatflux_dist] = qfluxdist(Ah, L, N, I, i)
5
6     dLength = L/(I-1);      % length of each axial nod [m]
7     l(:,1)=0:dLength:L;    % initialize axial nodal cell lengths
8
9     if i == 23
10        theta_0 = 0.8187458177;
11        theta_1 = 0.6812541823;
12        theta_2 = 2.436354311;
13        heatflux_dist(:,1)=(theta_0+theta_1*cos(2*theta_2*((l(:,1)/L-1/2))))*(1/Ah);
14
15    elseif i==24
16        heatflux_dist(:,1)=1.1626*cos(4.926*l(:,1)+5.3447)*(1/Ah);
17    else
18        heatflux_dist(1:I,1) = (1/Ah);
19    end

```

Appendix F: MATLAB Script for Units Conversion Function

```

1 %-----
2 % Sets up units for problem based on input type.
3 %-----
4 j=J(k);
5 Input(:,1)=xlsread('Data.xls',j+1);
6 Geometry(:,1) = xlsread('Geometry.xlsx',j+1);
7 Heatflux_dist(:,1) = qfluxdist(Geometry(8,2), Geometry(11,2), Geometry(2,2), I, j);
8
9 if Geometry(1,2) == 0
10     Input(:,2,1)=Input(:,2,1)*PSIA_2_BAR;
11     Input(:,3,1)=(Input(:,3,1)-32.0)/1.8;
12     Input(:,4,1)=Input(:,4,1)*MLBM_FT2HR_2_KG_M2S;
13     Input(:,5,1)=Input(:,5,1)...
14         *MBTU_FT2HR_2_W_M2.*Input(:,7);
15     Input(:,6,1)=Input(:,5,1)*Geometry(8,2);
16
17 elseif Geometry(1,2) == 1
18     Input(:,2,1)=Input(:,2,1)*PSIA_2_BAR;
19     Input(:,4,1)=Input(:,4,1)*MLBM_FT2HR_2_KG_M2S;
20     Input(:,5,1)=Input(:,5,1)...
21         *MBTU_FT2HR_2_W_M2.*Geometry(6,2);
22     Input(:,6,1)=Input(:,5,1)*Geometry(8,2);
23
24     for i=1:length(Input(:,4,1))
25         Input(i,3,1)=Input(i,3,1)*BTU_LBM_2_KJ_KG;
26         Input(i,3,1)=...
27             XSteam('T_ph',Input(i,2,1),Input(i,3,1));
28     end
29
30 elseif Geometry(1,2) == 2
31     Input(:,2,1) = Input(:,2,1)*1E-5;
32     Input(:,5,1) = Input(:,5,1).*Input(:,7);
33 end
34 %STORE INPUTS-----

```

```
35
36 Data(j).Geometry = Geometry;
37 Data(j).Input = Input;
38 Data(j).HeatFluxDist = HeatFlux_dist;
39 %TEMP PARAMETERS FOR FUNCTION PASSING-----
40 P_sys = Data(j).Input(:,2);
41 Tin = Data(j).Input(:,3);
42 G = Data(j).Input(:,4);
43 qpin_exp = Data(j).Input(:,6);
44 heatflux_dist = Data(j).HeatFluxDist(:,1);
45 Geometry = Data(j).Geometry;
46 %-----
```

Appendix G: EPRI Data for Tests 301-318

Table G.1: General Electric test data 301 from EPRI CHF database.

#	P_{out} (<i>psia</i>)	T_{in} (<i>F</i>)	G (<i>Mlbm/hr - ft²</i>)	q_{CHF} (<i>Mbtu/hr - ft²</i>)	CHF <i>Pin</i>	Pin <i>Peak</i>
1	1000.0	528.0	0.758	0.516	4	0.9950
2	1001.0	506.0	0.761	0.540	4	0.9950
3	999.0	482.0	0.764	0.568	4	0.9950
4	1000.0	452.0	0.763	0.605	4	0.9950
5	1000.0	418.0	0.767	0.644	7	1.0000
6	1000.0	389.0	0.759	0.657	7	1.0000
7	1000.0	371.0	0.749	0.675	7	1.0000
8	1000.0	416.0	0.768	0.633	7	1.0000
9	1001.0	524.0	0.517	0.421	7	1.0000
10	990.0	498.0	0.514	0.436	4	0.9950
11	1000.0	472.0	0.505	0.452	7	1.0000
12	1000.0	442.0	0.507	0.480	7	1.0000
13	1000.0	412.0	0.510	0.501	10	1.0020
14	1000.0	377.0	0.510	0.537	10	1.0020
15	1000.0	344.0	0.512	0.560	10	1.0020

Continued on next page...

#	P_{out} (psia)	T_{in} (F)	G (Mlbm/hr - ft ²)	q_{CHF} (Mbtu/hr - ft ²)	CHF Pin	Pin Peak
16	1000.0	325.0	0.508	0.575	7	1.0000
17	1000.0	524.0	1.028	0.591	8	1.0000
18	1000.0	504.0	1.019	0.610	10	1.0020
19	1000.0	478.0	1.025	0.645	7	1.0000
20	1001.0	452.0	1.027	0.681	7	1.0000
21	1000.0	421.0	1.024	0.728	7	1.0000
22	1000.0	404.0	1.019	0.745	7	1.0000
23	1000.0	525.0	1.282	0.642	10	1.0020
24	1000.0	500.0	1.287	0.673	10	1.0020
25	1000.0	472.0	1.285	0.721	7	1.0000
26	1000.0	441.0	1.280	0.780	7	1.0000
27	990.0	526.0	0.255	0.274	7	1.0000
28	1001.0	497.0	0.254	0.287	7	1.0000
29	1001.0	464.0	0.259	0.308	7	1.0000
30	1001.0	433.0	0.265	0.335	7	1.0000
31	1000.0	392.0	0.259	0.349	1	1.0100
32	1001.0	356.0	0.254	0.363	7	1.0000
33	1000.0	309.0	0.225	0.382	7	1.0000
34	1002.0	509.0	0.772	0.544	7	1.0000
35	1000.0	471.0	0.773	0.585	7	1.0000

Continued on next page...

#	P_{out} (psia)	T_{in} (F)	G (Mlbm/hr – ft ²)	q_{CHF} (Mbtu/hr – ft ²)	CHF Pin	Pin Peak
36	1000.0	435.0	0.747	0.611	7	1.0000
37	1001.0	402.0	0.765	0.650	7	1.0000
38	1000.0	376.0	0.749	0.670	7	1.0000
39	600.0	465.0	1.002	0.690	7	1.0000
40	600.0	445.0	0.985	0.719	7	1.0000
41	600.0	420.0	0.997	0.761	7	1.0000
42	600.0	434.0	1.021	0.753	7	1.0000
43	600.0	467.0	0.519	0.477	4	0.9950
44	601.0	442.0	0.515	0.496	7	1.0000
45	599.0	421.0	0.518	0.512	7	1.0000
46	600.0	400.0	0.524	0.528	7	1.0000
47	600.0	380.0	0.526	0.546	7	1.0000
48	600.0	357.0	0.519	0.564	7	1.0000
49	600.0	330.0	0.515	0.580	7	1.0000
50	1250.0	554.0	0.517	0.366	1	1.0100
51	1250.0	481.0	0.518	0.424	1	1.0100
52	1250.0	397.0	0.525	0.487	7	1.0000
53	1250.0	549.0	1.013	0.469	1	1.0100
54	1250.0	481.0	0.998	0.590	7	1.0000

Table G.2: General Electric test data 302 from EPRI CHF database.

	P_{out}	T_{in}	G	q_{CHF}	CHF	Pin
#	($psia$)	(F)	($Mlbm/hr - ft^2$)	($Mbtu/hr - ft^2$)	Pin	$Peak$
1	1000.0	528.0	0.779	0.577	7	1.0060
2	1000.0	507.0	0.775	0.576	7	1.0060
3	1000.0	479.0	0.767	0.612	7	1.0060
4	1000.0	451.0	0.764	0.645	7	1.0060
5	1000.0	421.0	0.763	0.691	7	1.0060
6	1000.0	390.0	0.771	0.714	7	1.0060
7	1000.0	524.0	0.522	0.450	10	1.0150
8	1000.0	505.0	0.512	0.464	10	1.0150
9	1000.0	480.0	0.506	0.487	10	1.0150
10	1000.0	452.0	0.511	0.509	10	1.0150
11	1000.0	417.0	0.514	0.540	4	1.0040
12	1000.0	382.0	0.508	0.556	4	1.0040
13	1000.0	342.0	0.509	0.597	4	1.0040
14	1000.0	525.0	0.261	0.287	4	1.0040
15	1000.0	496.5	0.258	0.300	10	1.0150
16	1000.0	469.0	0.254	0.310	10	1.0150
17	1000.0	441.0	0.255	0.325	10	1.0150
18	1000.0	401.0	0.257	0.354	10	1.0150

Continued on next page...

#	P_{out} (psia)	T_{in} (F)	G (Mlbm/hr - ft ²)	q_{CHF} (Mbtu/hr - ft ²)	CHF Pin	Pin Peak
19	1000.0	370.0	0.261	0.369	10	1.0150
20	1000.0	338.0	0.255	0.381	10	1.0150
21	1000.0	309.0	0.259	0.399	10	1.0150
22	1000.0	529.0	0.768	0.568	7	1.0060
23	1000.0	527.0	1.030	0.617	7	1.0060
24	1000.0	502.0	1.027	0.653	7	1.0060
25	1000.0	478.0	0.986	0.688	4	1.0040
26	1000.0	450.0	1.017	0.732	10	1.0150
27	1000.0	417.0	1.015	0.786	10	1.0150
28	1000.0	531.0	1.272	0.655	6	0.9950
29	1000.0	510.0	1.273	0.682	7	1.0060
30	1000.0	483.0	1.276	0.739	7	1.0060
31	1000.0	456.0	1.275	0.794	7	1.0060
32	600.0	467.0	1.014	0.732	10	1.0150
33	600.0	448.0	1.011	0.763	10	1.0150
34	600.0	426.0	1.017	0.805	7	1.0060
35	600.0	466.0	0.508	0.514	10	1.0150
36	600.0	435.0	0.511	0.544	10	1.0150
37	600.0	400.0	0.512	0.569	10	1.0150
38	600.0	358.0	0.506	0.590	10	1.0150

Continued on next page...

	P_{out}	T_{in}	G	q_{CHF}	CHF	Pin
#	(psia)	(F)	(Mlbm/hr – ft ²)	(Mbtu/hr – ft ²)	Pin	Peak
39	600.0	318.0	0.509	0.615	10	1.0150
40	1000.0	313.0	0.510	0.635	10	1.0150
41	1250.0	544.0	0.522	0.412	10	1.0150
42	1250.0	504.0	0.536	0.450	10	1.0150
43	1250.0	462.0	0.513	0.479	10	1.0150
44	1250.0	411.0	0.511	0.526	10	1.0150
45	1250.0	540.0	1.008	0.556	7	1.0060
46	1250.0	500.0	1.028	0.616	10	1.0150
47	1250.0	460.0	1.028	0.691	10	1.0150
48	1250.0	415.0	1.019	0.784	10	1.0150

Table G.3: General Electric test data 303 from EPRI CHF database.

	P_{out}	T_{in}	G	q_{CHF}	CHF	Pin
#	($psia$)	(F)	($Mlbm/hr - ft^2$)	($Mbtu/hr - ft^2$)	Pin	$Peak$
1	1000.0	527.0	0.513	0.425	1	1.0020
2	1000.0	500.0	0.515	0.450	1	1.0020
3	1000.0	470.0	0.509	0.478	1	1.0020
4	1000.0	443.0	0.506	0.499	1	1.0020
5	1000.0	410.0	0.508	0.524	1	1.0020
6	1000.0	375.0	0.511	0.555	1	1.0020
7	1000.0	338.0	0.506	0.581	1	1.0020
8	1000.0	309.0	0.506	0.611	1	1.0020
9	1000.0	525.0	0.769	0.509	10	1.0160
10	1000.0	500.0	0.772	0.551	10	1.0160
11	1000.0	472.0	0.760	0.591	10	1.0160
12	1000.0	440.0	0.765	0.635	10	1.0160
13	1000.0	410.0	0.772	0.683	7	1.0060
14	1000.0	380.0	0.760	0.708	7	1.0060
15	1000.0	357.0	0.756	0.746	7	1.0060
16	1000.0	530.0	1.015	0.523	10	1.0160
17	1000.0	500.0	1.029	0.580	10	1.0160
18	1000.0	476.0	1.010	0.620	10	1.0160

Continued on next page...

	P_{out}	T_{in}	G	q_{CHF}	CHF	Pin
#	(psia)	(F)	(Mlbm/hr – ft ²)	(Mbtu/hr – ft ²)	Pin	Peak
19	1000.0	452.0	1.027	0.669	10	1.0160
20	1000.0	426.0	1.015	0.728	10	1.0160
21	1000.0	399.0	1.011	0.791	10	1.0160
22	1000.0	525.0	1.326	0.568	10	1.0160
23	1000.0	500.0	1.281	0.612	10	1.0160
24	1000.0	473.0	1.266	0.677	10	1.0160
25	1000.0	451.0	1.280	0.738	10	1.0160
26	1000.0	425.0	1.273	0.806	10	1.0160

Table G.4: General Electric test data 304 from EPRI CHF database.

#	P_{out} (<i>psia</i>)	T_{in} (<i>F</i>)	G (<i>Mlbm/hr - ft²</i>)	q_{CHF} (<i>Mbtu/hr - ft²</i>)	CHF <i>Pin</i>	Pin <i>Peak</i>
1	1000.0	527.5	0.507	0.391	15	1.2626
2	1000.0	501.0	0.514	0.421	15	1.2626
3	1000.0	471.0	0.510	0.442	13	1.2620
4	1000.0	435.0	0.512	0.476	16	1.2626
5	1000.0	399.5	0.514	0.510	16	1.2626
6	1000.0	361.0	0.509	0.536	15	1.2626
7	1000.0	322.0	0.507	0.571	15	1.2626
8	1000.0	525.0	0.782	0.475	13	1.2620
9	1000.0	494.0	0.776	0.512	13	1.2620
10	1000.0	471.0	0.762	0.543	13	1.2620
11	1000.0	443.0	0.760	0.571	13	1.2620
12	1000.0	409.0	0.766	0.614	15	1.2626
13	1000.0	382.0	0.756	0.648	13	1.2620
14	1000.0	349.0	0.760	0.685	13	1.2620
15	1000.0	524.0	1.023	0.572	13	1.2620
16	1000.0	500.0	1.017	0.599	13	1.2620
17	995.0	473.0	1.019	0.636	13	1.2620
18	1000.0	450.0	1.023	0.670	13	1.2620

Continued on next page...

	P_{out}	T_{in}	G	q_{CHF}	CHF	Pin
#	(psia)	(F)	(Mlbm/hr – ft ²)	(Mbtu/hr – ft ²)	Pin	Peak
19	1001.0	421.0	1.011	0.710	13	1.2620
20	1001.0	389.0	1.030	0.765	13	1.2620
21	1000.0	526.0	1.281	0.613	15	1.2626
22	1000.0	501.0	1.263	0.643	15	1.2626
23	1000.0	474.5	1.276	0.680	15	1.2626
24	1000.0	452.0	1.273	0.713	15	1.2626
25	1000.0	423.5	1.287	0.754	13	1.2620
26	1000.0	400.0	1.279	0.795	13	1.2620

Table G.5: General Electric test data 305 from EPRI CHF database.

	P_{out}	T_{in}	G	q_{CHF}	CHF	Pin
#	($psia$)	(F)	($Mlbm/hr - ft^2$)	($Mbtu/hr - ft^2$)	Pin	$Peak$
1	1000	523.5	0.783	0.432	15	1.2630
2	1000	480.0	0.766	0.475	13	1.2630
3	1000	442.0	0.764	0.517	16	1.2630
4	1000	403.5	0.761	0.558	16	1.2630

Table G.6: General Electric test data 306 from EPRI CHF database.

#	P_{out} (<i>psia</i>)	T_{in} (<i>F</i>)	G (<i>Mlbm/hr - ft²</i>)	q_{CHF} (<i>Mbtu/hr - ft²</i>)	<i>CHF</i> <i>Pin</i>	<i>Pin</i> <i>Peak</i>
1	1000.000	521.0	0.503	0.438	1	1.0000
2	1000.000	492.0	0.500	0.467	4	1.0000
3	1000.000	457.0	0.494	0.501	4	1.0000
4	1000.000	416.0	0.501	0.543	4	1.0000
5	1000.000	368.0	0.496	0.583	13	1.0000
6	1000.000	522.0	0.741	0.470	4	1.0000
7	1000.000	488.0	0.758	0.521	4	1.0000
8	1000.000	449.0	0.738	0.554	13	1.0000
9	1000.000	415.0	0.754	0.599	13	1.0000
10	1000.000	362.0	0.744	0.663	13	1.0000
11	1001.000	518.0	0.999	0.512	13	1.0000
12	1000.000	482.0	1.001	0.556	13	1.0000
13	1000.000	440.0	0.998	0.616	13	1.0000
14	1000.000	412.0	0.990	0.660	13	1.0000
15	1000.000	368.0	0.983	0.743	13	1.0000
16	1000.000	523.5	1.247	0.532	13	1.0000
17	1000.000	482.0	1.251	0.609	13	1.0000
18	1000.000	441.0	1.250	0.686	13	1.0000

Continued on next page...

#	P_{out} (psia)	T_{in} (F)	G (Mlbm/hr - ft ²)	q_{CHF} (Mbtu/hr - ft ²)	CHF Pin	Pin Peak
19	1000.000	403.5	1.238	0.762	13	1.0000
20	1000.000	522.5	0.251	0.263	4	1.0000
21	1000.000	489.5	0.249	0.279	4	1.0000
22	1000.000	437.5	0.242	0.307	4	1.0000
23	1000.000	385.0	0.246	0.331	4	1.0000
24	1000.000	326.5	0.250	0.363	4	1.0000
25	1000.000	253.0	0.249	0.406	4	1.0000
26	1200.000	499.5	1.008	0.519	13	1.0000
27	1200.000	461.0	0.991	0.583	14	1.0000
28	1200.000	422.0	0.990	0.649	14	1.0000
29	1200.000	378.0	0.990	0.732	13	1.0000
30	1200.000	526.0	0.501	0.424	1	1.0000
31	1200.000	479.0	0.502	0.474	4	1.0000
32	1200.000	440.0	0.499	0.517	13	1.0000
33	1200.000	400.0	0.499	0.559	13	1.0000
34	1200.000	538.5	0.752	0.439	13	1.0000
35	1200.000	500.0	0.745	0.478	13	1.0000
36	1200.000	462.0	0.751	0.530	13	1.0000
37	1200.000	420.0	0.750	0.588	13	1.0000
38	1200.000	382.0	0.755	0.641	13	1.0000

Continued on next page...

#	P_{out} (psia)	T_{in} (F)	G (Mlbm/hr - ft ²)	q_{CHF} (Mbtu/hr - ft ²)	CHF Pin	Pin Peak
39	1200.000	537.5	1.008	0.461	13	1.0000
40	1400.000	546.0	1.022	0.434	13	1.0000
41	1400.000	509.0	1.000	0.498	13	1.0000
42	1400.000	472.0	1.005	0.565	13	1.0000
43	1400.000	426.0	0.996	0.654	13	1.0000
44	1400.000	554.0	0.490	0.341	4	1.0000
45	1400.000	516.5	0.497	0.382	4	1.0000
46	1400.000	476.0	0.497	0.420	4	1.0000
47	1400.000	432.0	0.496	0.468	13	1.0000
48	1400.000	379.0	0.502	0.526	4	1.0000

Table G.7: General Electric test data 307 from EPRI CHF database.

#	P_{out} (<i>psia</i>)	T_{in} (<i>F</i>)	G (<i>Mlbm/hr - ft²</i>)	q_{CHF} (<i>Mbtu/hr - ft²</i>)	CHF <i>Pin</i>	Pin <i>Peak</i>
1	1000	529.9	0.501	0.541	10	1.0000
2	1000	494.3	0.502	0.588	10	1.0000
3	1000	464.2	0.496	0.622	14	1.0000
4	1000	429.6	0.497	0.667	14	1.0000
5	1000	526.2	0.987	0.648	14	1.0000
6	1000	495.6	1.013	0.710	14	1.0000
7	1000	465.4	1.001	0.774	14	1.0000
8	1000	438.4	1.001	0.836	7	1.0000
9	1000	528.8	0.738	0.617	14	1.0000
10	1000	495.9	0.744	0.661	14	1.0000
11	1000	462.6	0.752	0.718	14	1.0000
12	1000	427.5	0.748	0.784	14	1.0000
13	1000	524.4	1.247	0.676	14	1.0000
14	1000	493.0	1.258	0.757	14	1.0000
15	1000	466.2	1.246	0.845	14	1.0000
16	1000	435.8	1.253	0.926	14	1.0000
17	1000	398.4	1.005	0.953	16	1.0000

Table G.8: General Electric test data 307.1 from EPRI CHF database.

	P_{out}	T_{in}	G	q_{CHF}	CHF	Pin
#	($psia$)	(F)	($Mlbm/hr - ft^2$)	($Mbtu/hr - ft^2$)	Pin	$Peak$
1	1000	528.3	0.988	0.732	1	1.0000
2	1000	490.0	0.976	0.816	14	1.0000
3	1000	450.7	1.008	0.829	9	1.0000
4	1000	452.7	1.004	0.876	14	1.0000
5	1000	411.8	1.013	0.972	7	1.0000

Table G.9: General Electric test data 307.2 from EPRI CHF database.

	P_{out}	T_{in}	G	q_{CHF}	CHF	Pin
#	($psia$)	(F)	($Mlbm/hr - ft^2$)	($Mbtu/hr - ft^2$)	Pin	$Peak$
1	1000	530.7	0.491	0.513	1	1.0000
2	1000	502.1	0.568	0.548	1	1.0000
3	1000	456.5	0.559	0.607	1	1.0000
4	1000	413.0	0.561	0.668	1	1.0000
5	1000	530.9	1.114	0.634	7	1.0000
6	1000	497.7	1.114	0.713	7	1.0000
7	1000	461.2	1.137	0.780	6	1.0000

Table G.10: General Electric test data 308 from EPRI CHF database.

#	P_{out} (psia)	T_{in} (F)	G (Mlbm/hr - ft ²)	q_{CHF} (Mbtu/hr - ft ²)	CHF Pin	Pin Peak
1	1000	519.5	0.505	0.377	1.000	1.2100
2	1000	483.0	0.503	0.410	1.000	1.2100
3	1000	446.0	0.500	0.443	1.000	1.2100
4	1000	407.0	0.486	0.465	12.000	1.1000
5	1000	365.0	0.501	0.521	1.000	1.2100
6	1000	520.5	1.005	0.453	1.000	1.2100
7	1000	483.0	0.989	0.515	1.000	1.2100
8	1000	444.5	0.993	0.573	1.000	1.2100
9	1000	406.0	0.994	0.644	1.000	1.2100
10	1000	366.0	1.008	0.707	1.000	1.2100
11	1000	521.5	0.760	0.410	1.000	1.2100
12	1000	483.5	0.750	0.454	1.000	1.2100
13	1000	442.0	0.760	0.501	1.000	1.2100
14	1000	401.5	0.756	0.549	1.000	1.2100
15	1000	358.0	0.769	0.607	1.000	1.2100
16	1000	529.0	0.252	0.235	1.000	1.2100
17	1000	489.0	0.243	0.248	1.000	1.2100
18	1000	462.0	0.245	0.260	1.000	1.2100

Continued on next page...

	P_{out}	T_{in}	G	q_{CHF}	CHF	Pin
#	(psia)	(F)	(Mlbm/hr - ft ²)	(Mbtu/hr - ft ²)	Pin	Peak
19	1000	434.0	0.246	0.273	1.000	1.2100
20	1000	402.0	0.250	0.289	1.000	1.2100
21	1000	361.0	0.247	0.316	1.000	1.2100
22	1000	300.0	0.255	0.364	1.000	1.2100
23	1000	521.5	0.109	0.130	1.000	1.2100
24	1000	475.0	0.098	0.132	1.000	1.2100
25	1000	435.0	0.095	0.142	1.000	1.2100
26	1000	378.0	0.099	0.154	1.000	1.2100
27	1000	293.0	0.098	0.176	1.000	1.2100
28	1000	520.0	1.257	0.467	1.000	1.2100
29	1000	479.5	1.252	0.550	1.000	1.2100
30	1000	444.0	1.227	0.620	1.000	1.2100
31	1000	403.5	1.247	0.707	1.000	1.2100

Table G.11: General Electric test data 309 from EPRI CHF database.

#	P_{out} (psia)	T_{in} (F)	G (Mlbm/hr – ft ²)	q_{CHF} (Mbtu/hr – ft ²)	CHF Pin	Pin Peak
1	1000	527.0	0.495	0.421	13	1.2100
2	1000	491.5	0.501	0.451	13	1.2100
3	1000	452.0	0.512	0.484	13	1.2100
4	1000	407.0	0.500	0.521	13	1.2100
5	1000	370.0	0.505	0.540	13	1.2100
6	1000	323.5	0.505	0.583	13	1.2100
7	1000	511.5	1.008	0.484	13	1.2100
8	1000	477.5	1.036	0.534	13	1.2100
9	1000	439.0	1.009	0.588	13	1.2100
10	1000	396.0	0.982	0.650	13	1.2100
11	1000	359.5	0.997	0.710	13	1.2100
12	1000	349.5	0.982	0.797	13	1.2100
13	1000	522.0	0.755	0.426	13	1.2100
14	1000	481.5	0.755	0.474	13	1.2100
15	1000	440.0	0.759	0.511	13	1.2100
16	1000	398.0	0.753	0.563	13	1.2100
17	1000	361.5	0.751	0.595	13	1.2100
18	1000	522.0	1.257	0.481	13	1.2100

Continued on next page...

#	P_{out} (psia)	T_{in} (F)	G (Mlbm/hr - ft ²)	q_{CHF} (Mbtu/hr - ft ²)	CHF Pin	Pin Peak
19	1000	478.5	1.250	0.547	13	1.2100
20	1000	441.5	1.242	0.614	13	1.2100
21	1000	400.0	1.266	0.706	13	1.2100
22	1000	329.5	0.255	0.398	13	1.2100
23	1000	285.0	0.252	0.415	13	1.2100
24	1000	406.0	0.251	0.350	13	1.2100
25	1000	520.0	0.251	0.285	13	1.2100
26	1000	488.5	0.251	0.313	13	1.2100
27	1000	445.5	0.249	0.329	13	1.2100
28	1000	524.0	0.099	0.133	1	0.9400
29	1000	481.0	0.099	0.151	1	0.9400
30	1000	422.0	0.101	0.168	1	0.9400
31	1000	335.0	0.100	0.186	1	0.9400
32	1000	355.0	0.098	0.192	1	0.9400
33	1000	356.0	0.100	0.188	1	0.9400
34	1000	279.0	0.097	0.198	1	0.9400
35	1000	280.0	0.103	0.203	1	0.9400
36	1000	281.0	0.247	0.405	13	1.2100
37	1000	280.0	0.258	0.412	13	1.2100
38	1000	282.0	0.259	0.412	13	1.2100

Continued on next page...

	P_{out}	T_{in}	G	q_{CHF}	CHF	Pin
#	($psia$)	(F)	($Mlbm/hr - ft^2$)	($Mbtu/hr - ft^2$)	Pin	$Peak$
39	1000	281.0	0.259	0.409	13	1.2100
40	1000	275.0	0.259	0.379	13	1.2100

Table G.12: General Electric test data 310 from EPRI CHF database.

#	P_{out} (<i>psia</i>)	T_{in} (<i>F</i>)	G (<i>Mlbm/hr - ft²</i>)	q_{CHF} (<i>Mbtu/hr - ft²</i>)	CHF <i>Pin</i>	Pin <i>Peak</i>
1	1000	518.0	0.506	0.262	1	1.6100
2	1000	482.5	0.501	0.286	1	1.6100
3	1000	441.0	0.505	0.316	1	1.6100
4	1000	397.0	0.503	0.349	1	1.6100
5	1000	356.0	0.502	0.373	1	1.6100
6	1000	522.0	0.978	0.331	1	1.6100
7	1000	484.5	1.000	0.377	1	1.6100
8	1000	442.5	0.999	0.411	1	1.6100
9	1000	400.5	1.002	0.470	1	1.6100
10	1000	361.5	1.007	0.515	1	1.6100
11	1000	520.5	0.766	0.299	1	1.6100
12	1000	480.5	0.742	0.332	1	1.6100
13	1000	441.5	0.736	0.357	1	1.6100
14	1000	403.0	0.739	0.399	1	1.6100
15	1000	360.0	0.750	0.442	1	1.6100
16	1000	517.0	1.215	0.368	1	1.6100
17	1000	482.0	1.257	0.421	1	1.6100
18	1000	439.5	1.258	0.479	1	1.6100

Continued on next page...

	P_{out}	T_{in}	G	q_{CHF}	CHF	Pin
#	(psia)	(F)	(Mlbm/hr – ft ²)	(Mbtu/hr – ft ²)	Pin	Peak
19	1000	404.0	1.261	0.531	1	1.6100
20	1000	361.5	1.265	0.589	1	1.6100
21	1000	535.5	0.243	0.181	1	1.6100
22	1000	476.0	0.250	0.213	1	1.6100
23	1000	439.0	0.256	0.232	1	1.6100
24	1000	403.5	0.246	0.246	1	1.6100
25	1000	361.5	0.250	0.276	1	1.6100
26	1000	529.0	0.098	0.111	1	1.6100
27	1000	472.0	0.100	0.121	1	1.6100
28	1000	440.0	0.100	0.134	1	1.6100
29	1000	404.0	0.096	0.140	1	1.6100
30	1000	348.0	0.098	0.152	1	1.6100

Table G.13: General Electric test data 311 from EPRI CHF database.

#	P_{out} (<i>psia</i>)	T_{in} (<i>F</i>)	G (<i>Mlbm/hr – ft²</i>)	q_{CHF} (<i>Mbtu/hr – ft²</i>)	CHF <i>Pin</i>	Pin <i>Peak</i>
1	995	516.0	0.470	0.389	1	1.0000
2	995	492.0	0.470	0.400	1	1.0000
3	1010	464.0	0.450	0.427	1	1.0000
4	993	427.3	0.460	0.460	1	1.0000
5	1000	396.0	0.460	0.490	1	1.0000
6	1010	362.0	0.460	0.515	10	1.0000
7	990	515.0	0.720	0.456	1	1.0000
8	1000	493.0	0.720	0.488	1	1.0000
9	990	462.0	0.720	0.532	1	1.0000
10	995	433.0	0.720	0.570	1	1.0000
11	995	395.0	0.720	0.610	1	1.0000
12	995	362.0	0.720	0.647	10	1.0000
13	1005	525.0	0.950	0.497	1	1.0000
14	1210	524.0	0.970	0.487	1	1.0000
15	1389	525.0	0.980	0.469	1	1.0000
16	1402	544.0	0.970	0.435	1	1.0000
17	1017	494.0	0.970	0.543	10	1.0000
18	1200	493.0	0.970	0.538	10	1.0000

Continued on next page...

#	P_{out} (psia)	T_{in} (F)	G (Mlbm/hr - ft ²)	q_{CHF} (Mbtu/hr - ft ²)	CHF Pin	Pin Peak
19	1395	493.0	0.980	0.530	4	1.0000
20	995	466.0	0.970	0.599	10	1.0000
21	1200	464.0	0.970	0.588	10	1.0000
22	1400	463.0	0.970	0.609	1	1.0000
23	1000	432.0	0.970	0.646	1	1.0000
24	1195	432.0	0.970	0.643	1	1.0000
25	1405	432.0	0.970	0.660	1	1.0000
26	1000	396.0	0.970	0.713	1	1.0000
27	1195	392.0	0.970	0.710	1	1.0000
28	1415	390.0	0.970	0.702	1	1.0000
29	1015	368.0	0.970	0.751	1	1.0000
30	1220	370.0	0.980	0.743	1	1.0000
31	1405	368.0	0.970	0.737	1	1.0000
32	1005	468.0	0.270	0.317	1	1.0000
33	1005	446.0	0.270	0.329	1	1.0000
34	1001	434.0	0.270	0.335	1	1.0000
35	1011	402.0	0.280	0.364	1	1.0000
36	1205	525.0	0.500	0.381	1	1.0000
37	1207	522.0	0.470	0.366	1	1.0000
38	1210	524.0	0.500	0.373	1	1.0000

Continued on next page...

#	P_{out} (psia)	T_{in} (F)	G (Mlbm/hr - ft ²)	q_{CHF} (Mbtu/hr - ft ²)	CHF Pin	Pin Peak
39	1389	522.0	0.510	0.371	1	1.0000
40	1217	490.0	0.500	0.412	1	1.0000
41	1397	490.0	0.500	0.405	1	1.0000
42	1230	464.0	0.480	0.435	1	1.0000
43	1402	460.0	0.480	0.431	1	1.0000
44	1212	433.0	0.490	0.465	1	1.0000
45	1412	432.0	0.490	0.463	1	1.0000
46	1203	392.0	0.500	0.509	1	1.0000
47	1397	394.0	0.500	0.507	1	1.0000
48	1215	371.0	0.480	0.521	1	1.0000
49	1395	374.0	0.480	0.518	1	1.0000
50	1028	520.0	1.220	0.535	1	1.0000
51	1021	490.0	1.210	0.583	10	1.0000
52	1024	464.0	1.230	0.652	10	1.0000
53	1026	434.0	1.210	0.709	1	1.0000
54	1005	408.0	1.210	0.759	1	1.0000
55	1403	512.0	0.730	0.452	1	1.0000
56	1405	482.0	0.730	0.487	10	1.0000
57	1395	455.0	0.720	0.528	1	1.0000
58	1418	394.0	0.720	0.575	10	1.0000

Continued on next page...

	P_{out}	T_{in}	G	q_{CHF}	CHF	Pin
#	(psia)	(F)	(Mlbm/hr - ft ²)	(Mbtu/hr - ft ²)	Pin	Peak
59	1415	378.0	0.720	0.624	1	1.0000

Table G.14: General Electric test data 312 from EPRI CHF database.

#	P_{out} (psia)	T_{in} (F)	G (Mlbm/hr – ft ²)	q_{CHF} (Mbtu/hr – ft ²)	CHF Pin	Pin Peak
1	1000	513.0	0.970	0.411	1	1.2710
2	1212	513.0	0.970	0.406	1	1.2710
3	1360	512.0	0.970	0.401	1	1.2710
4	1000	484.2	0.970	0.446	1	1.2710
5	1227	482.4	0.960	0.438	1	1.2710
6	1425	479.3	0.960	0.449	1	1.2710
7	1040	443.0	0.970	0.498	1	1.2710
8	1220	440.0	0.970	0.498	1	1.2710
9	1420	440.0	0.970	0.493	1	1.2710
10	1062	399.0	0.970	0.547	1	1.2710
11	1254	400.0	0.970	0.553	1	1.2710
12	1425	398.0	0.980	0.538	1	1.2710
13	1060	368.0	0.970	0.587	1	1.2710
14	1254	362.0	0.970	0.596	1	1.2710
15	1453	359.0	0.980	0.574	1	1.2710
16	1445	515.0	0.730	0.351	1	1.2710
17	1028	515.0	0.720	0.369	1	1.2710
18	1037	485.0	0.710	0.393	1	1.2710

Continued on next page...

#	P_{out} (psia)	T_{in} (F)	G (Mlbm/hr – ft ²)	q_{CHF} (Mbtu/hr – ft ²)	CHF Pin	Pin Peak
19	1417	479.0	0.720	0.387	1	1.2710
20	1420	441.0	0.720	0.437	1	1.2710
21	1029	439.0	0.720	0.435	1	1.2710
22	1061	404.0	0.720	0.468	1	1.2710
23	1430	404.0	0.720	0.474	1	1.2710
24	1055	364.0	0.720	0.506	1	1.2710
25	1444	362.0	0.730	0.510	1	1.2710
26	1019	500.0 ¹	1.230	0.452	1	1.2710
27	1019	481.0	1.220	0.495	1	1.2710
28	1024	448.0	1.220	0.544	1	1.2710
29	1027	418.0	1.220	0.584	1	1.2710
30	1049	393.0	1.220	0.630	1	1.2710
31	1060	382.0	1.220	0.644	1	1.2710
32	1425	514.0	0.500	0.301	1	1.2710
33	1225	512.0	0.500	0.318	1	1.2710
34	950	508.0	0.500	0.321	1	1.2710
35	1025	487.0	0.490	0.343	1	1.2710
36	1230	477.7	0.500	0.340	1	1.2710
37	1425	479.0	0.500	0.343	1	1.2710

Continued on next page...

¹This was originally recorded as 50.0 in [55]. This is believed to be in error based on trends of increasing to decreasing temperature sets in the test order and is corrected to be 500.0 here.

#	P_{out} (psia)	T_{in} (F)	G (Mlbm/hr – ft ²)	q_{CHF} (Mbtu/hr – ft ²)	CHF Pin	Pin Peak
38	1405	438.0	0.500	0.377	1	1.2710
39	1230	439.5	0.500	0.372	1	1.2710
40	1015	437.3	0.500	0.374	1	1.2710
41	1020	402.5	0.500	0.401	1	1.2710
42	1225	402.0	0.500	0.406	1	1.2710
43	1440	402.0	0.500	0.411	1	1.2710
44	1410	362.0	0.500	0.435	1	1.2710
45	1225	359.0	0.500	0.443	1	1.2710
46	1005	360.0	0.500	0.438	1	1.2710
47	1025	323.0	0.500	0.464	1	1.2710
48	1235	323.0	0.500	0.441 ²	1	1.2710
49	1420	320.0	0.500	0.462	1	1.2710
50	1013	461.0	0.970	0.466	1	1.2710
51	1013	512.0	0.970	0.410	1	1.2710
52	1015	512.0	0.500	0.318	1	1.2710
53	1015	465.0	0.250	0.256	1	1.2710
54	1015	448.0	0.250	0.266	1	1.2710
55	1015	431.0	0.250	0.276	1	1.2710

²This was originally recorded as 0.241 in [55]. This is believed to be in error based on this block of data being performed in the 0.4 kg/(m² – s) mass flux range and is corrected to be 0.441 here.

Table G.15: General Electric test data 313 from EPRI CHF database.

#	P_{out} (<i>psia</i>)	T_{in} (<i>F</i>)	G (<i>Mlbm/hr - ft²</i>)	q_{CHF} (<i>Mbtu/hr - ft²</i>)	CHF <i>Pin</i>	Pin <i>Peak</i>
1	1035	510.0	0.500	0.386	8	1.0050
2	1035	510.0	0.510	0.445	1	0.9880
3	1000	486.0	0.500	0.470	1	0.9880
4	1000	458.0	0.520	0.502	1	0.9880
5	1000	425.0	0.500	0.529	1	0.9880
6	1003	402.0	0.500	0.550	7	0.9890
7	1025	365.0	0.500	0.575	7	0.9890
8	1201	508.0	0.510	0.431	1	0.9880
9	1425	507.0	0.510	0.408	1	0.9880
10	1215	485.0	0.510	0.451	1	0.9880
11	1423	482.0	0.510	0.429	1	0.9880
12	1427	462.0	0.520	0.455	7	0.9890
13	1208	463.0	0.500	0.467	7	0.9890
14	1206	424.0	0.500	0.505	7	0.9890
15	1409	423.0	0.500	0.494	7	0.9890
16	1415	403.0	0.500	0.516	7	0.9890
17	1218	403.0	0.500	0.520	7	0.9890
18	1226	366.0	0.490	0.562	1	0.9880

Continued on next page...

#	P_{out} (psia)	T_{in} (F)	G (Mlbm/hr - ft ²)	q_{CHF} (Mbtu/hr - ft ²)	CHF Pin	Pin Peak
19	1433	366.0	0.490	0.564	1	0.9880
20	1001	522.0	0.980	0.557	1	0.9880
21	1215	518.0	0.980	0.531	1	0.9880
22	1440	520.0	0.980	0.507	1	0.9880
23	1420	486.0	0.980	0.579	7	0.9890
24	1221	484.0	0.990	0.586	1	0.9880
25	1008	484.0	1.000	0.615	1	0.9880
26	1027	461.0	0.980	0.651	1	0.9880
27	1208	459.0	0.990	0.635	1	0.9880
28	1423	460.0	0.990	0.632	1	0.9880
29	1431	430.0	0.980	0.683	4	1.0150
30	1239	429.0	0.980	0.683	7	0.9890
31	1023	427.0	0.980	0.695	7	0.9890
32	1007	410.0	0.990	0.736	7	0.9890
33	1197	420.9	0.980	0.700	7	0.9890
34	1422	415.0	0.980	0.710	4	1.0150
35	1430	393.0	0.980	0.751	4	1.0150
36	1218	393.0	0.980	0.748	7	0.9890
37	1037	392.0	0.990	0.761	7	0.9890
38	1007	518.0	0.740	0.501	1	0.9880

Continued on next page...

#	P_{out} (psia)	T_{in} (F)	G (Mlbm/hr - ft ²)	q_{CHF} (Mbtu/hr - ft ²)	CHF Pin	Pin Peak
39	1409	524.0	0.740	0.441	1	0.9880
40	1402	487.0	0.730	0.487	1	0.9880
41	1009	488.0	0.740	0.549	1	0.9880
42	995	460.0	0.750	0.580	1	0.9880
43	1415	457.0	0.740	0.537	7	0.9890
44	1420	430.0	0.740	0.579	1	0.9880
45	1023	431.0	0.730	0.604	7	0.9890
46	1028	401.0	0.740	0.641	7	0.9890
47	1421	400.0	0.740	0.631	1	0.9880
48	1433	383.0	0.740	0.658	1	0.9880
49	1025	382.0	0.730	0.660	7	0.9890
50	1000	528.0	1.220	0.588	1	0.9880
51	1029	500.0	1.230	0.635	1	0.9880
52	1018	476.0	1.230	0.685	1	0.9880
53	1027	452.0	1.230	0.730	1	0.9880
54	1015	426.0	1.230	0.787	1	0.9880
55	1044	406.0	1.230	0.826	7	0.9890
56	1015	467.0	0.250	0.329	1	0.9880
57	1015	450.0	0.250	0.330	1	0.9880
58	1015	422.0	0.250	0.343	1	0.9880

Continued on next page...

	P_{out}	T_{in}	G	q_{CHF}	CHF	Pin
#	(<i>psia</i>)	(<i>F</i>)	(<i>Mlbm/hr – ft²</i>)	(<i>Mbtu/hr – ft²</i>)	<i>Pin</i>	<i>Peak</i>
59	1015	399.0	0.250	0.355	1	0.9880
60	1015	380.0	0.250	0.373	1	0.9880

Table G.16: General Electric test data 314 from EPRI CHF database.

#	P_{out} (<i>psia</i>)	T_{in} (<i>F</i>)	G (<i>Mlbm/hr - ft²</i>)	q_{CHF} (<i>Mbtu/hr - ft²</i>)	CHF <i>Pin</i>	Pin <i>Peak</i>
1	1000	506.0	0.510	0.324	1	1.2850
2	1005	469.0	0.500	0.358	1	1.2850
3	1010	428.0	0.500	0.389	1	1.2850
4	1005	396.0	0.490	0.412	1	1.2850
5	1010	355.0	0.500	0.449	1	1.2850
6	1005	327.0	0.500	0.470	1	1.2850
7	1010	520.0	0.750	0.357	1	1.2850
8	1000	493.0	0.750	0.389	1	1.2850
9	1010	453.0	0.750	0.431	1	1.2850
10	1000	414.0	0.750	0.477	1	1.2850
11	1007	376.0	0.740	0.519	1	1.2850
12	1005	355.0	0.750	0.565	1	1.2850
13	1000	522.0	1.000	0.392	1	1.2850
14	1000	501.0	1.000	0.426	1	1.2850
15	1000	470.0	1.000	0.466	1	1.2850
16	1005	449.0	1.000	0.498	1	1.2850
17	1005	424.0	1.000	0.535	1	1.2850
18	1007	394.0	1.010	0.574	1	1.2850

Continued on next page...

	P_{out}	T_{in}	G	q_{CHF}	CHF	Pin
#	(<i>psia</i>)	(<i>F</i>)	(<i>Mlbm/hr – ft²</i>)	(<i>Mbtu/hr – ft²</i>)	<i>Pin</i>	<i>Peak</i>
19	1015	524.0	1.240	0.417	1	1.2850
20	1000	501.0	1.230	0.447	1	1.2850
21	1000	471.0	1.240	0.498	1	1.2850
22	1005	442.0	1.240	0.551	1	1.2850
23	1005	412.0	1.250	0.608	1	1.2850
24	1005	366.0	1.260	0.694	1	1.2850
25	1005	391.0	0.490	0.408	1	1.2850
26	1000	430.0	0.490	0.378	1	1.2850
27	1010	505.0	0.250	0.233	1	1.2850
28	1040	484.0	0.240	0.247	1	1.2850
29	1005	453.0	0.250	0.257	1	1.2850
30	1005	420.0	0.250	0.273	1	1.2850
31	1005	395.0	0.250	0.292	1	1.2850
32	1005	363.0	0.250	0.304	1	1.2850
33	1005	335.0	0.250	0.320	1	1.2850
34	1005	303.0	0.250	0.341	1	1.2850

Table G.17: General Electric test data 315 from EPRI CHF database.

#	P_{out}	T_{in}	G	q_{CHF}	CHF	Pin
	(<i>psia</i>)	(<i>F</i>)	(<i>Mlbm/hr – ft²</i>)	(<i>Mbtu/hr – ft²</i>)	<i>Pin</i>	<i>Peak</i>
1	1001	519.0	0.480	0.427	1	0.9920
2	1005	500.0	0.480	0.446	4	1.0180
3	1007	470.0	0.470	0.469	4	1.0180
4	1001	430.0	0.480	0.512	4	1.0180
5	1018	383.0	0.480	0.549	4	1.0180
6	1001	335.0	0.480	0.594	4	1.0180
7	1000	522.0	0.750	0.475	4	1.0180
8	1013	500.0	0.750	0.505	4	1.0180
9	1010	476.0	0.750	0.536	13	1.0050
10	1009	440.0	0.760	0.585	13	1.0050
11	1000	400.0	0.760	0.633	4	1.0180
12	1032	366.0	0.740	0.673	4	1.0180
13	1010	524.0	0.990	0.498	1	0.9920
14	1001	499.0	1.000	0.540	1	0.9920
15	1005	475.0	1.000	0.578	1	0.9920
16	1010	450.0	0.990	0.616	1	0.9920
17	1005	426.0	0.980	0.656	7	1.0080
18	1012	401.0	0.990	0.701	4	1.0180

Continued on next page...

#	P_{out} (psia)	T_{in} (F)	G (Mlbm/hr - ft ²)	q_{CHF} (Mbtu/hr - ft ²)	CHF Pin	Pin Peak
19	1010	525.0	1.250	0.505	1	0.9920
20	1002	500.0	1.250	0.543	1	0.9920
21	1010	481.0	1.270	0.581	1	0.9920
22	1000	460.0	1.270	0.626	1	0.9920
23	1010	442.0	1.250	0.684	4	1.0180
24	1010	422.0	1.240	0.725	4	1.0180
25	1407	538.0	1.010	0.429	7	1.0080
26	1195	540.0	0.980	0.443	1	0.9920
27	1417	520.0	1.000	0.468	1	0.9920
28	1207	519.0	0.990	0.471	7	1.0080
29	1407	500.0	1.010	0.513	7	1.0080
30	1211	499.0	1.010	0.504	1	0.9920
31	1405	474.0	1.010	0.566	14	0.9930
32	1209	470.0	1.000	0.558	1	0.9920
33	1410	441.0	1.000	0.618	4	1.0180
34	1210	441.0	0.990	0.623	4	1.0180
35	1415	407.0	1.000	0.662	4	1.0180
36	1215	407.0	1.000	0.683	4	1.0180
37	1353	521.0	0.770	0.420	1	0.9920
38	1400	499.0	0.760	0.452	1	0.9920

Continued on next page...

#	P_{out} (<i>psia</i>)	T_{in} (<i>F</i>)	G (<i>Mlbm/hr - ft²</i>)	q_{CHF} (<i>Mbtu/hr - ft²</i>)	CHF <i>Pin</i>	Pin <i>Peak</i>
39	1405	472.0	0.750	0.493	1	0.9920
40	1400	443.0	0.760	0.542	4	1.0180
41	1407	406.0	0.750	0.582	4	1.0180
42	1405	366.0	0.750	0.622	4	1.0180
43	1400	525.0	0.510	0.366	4	1.0180
44	1205	527.0	0.500	0.379	4	1.0180
45	1400	501.0	0.500	0.390	4	1.0180
46	1210	502.0	0.500	0.409	4	1.0180
47	1397	470.0	0.730	0.432	4	1.0180
48	1210	471.0	0.720	0.439	7	1.0080
49	1402	442.0	0.720	0.447	4	1.0180
50	1206	442.0	0.710	0.457	4	1.0180
51	1400	406.0	0.720	0.479	4	1.0180
52	1216	401.0	0.720	0.494	4	1.0180
53	1000	400.0	0.500	0.506	4	1.0180
54	1408	383.0	0.510	0.502	4	1.0180
55	1210	384.0	0.500	0.513	4	1.0180
56	1003	384.0	0.500	0.528	4	1.0180
57	1010	385.0	0.470	0.547	4	1.0180
58	1010	385.0	0.500	0.535	4	1.0180

Continued on next page...

	P_{out}	T_{in}	G	q_{CHF}	CHF	Pin
#	(<i>psia</i>)	(<i>F</i>)	(<i>Mlbm/hr – ft²</i>)	(<i>Mbtu/hr – ft²</i>)	<i>Pin</i>	<i>Peak</i>
59	1010	521.0	0.500	0.402	4	1.0180
60	1015	500.0	0.500	0.437	4	1.0180
61	1007	470.0	0.500	0.458	4	1.0180
62	1003	432.0	0.500	0.495	4	1.0180
63	1005	328.0	0.490	0.577	4	1.0180
64	1005	518.0	0.250	0.272	4	1.0180
65	1007	492.0	0.250	0.280	4	1.0180
66	1012	460.0	0.250	0.302	4	1.0180
67	1007	432.0	0.250	0.321	4	1.0180
68	1007	406.0	0.250	0.332	4	1.0180
69	1002	364.0	0.250	0.354	4	1.0180
70	1007	336.0	0.250	0.372	4	1.0180

Table G.18: General Electric test data 316 from EPRI CHF database.

#	P_{out}	T_{in}	G	q_{CHF}	CHF	Pin
	(<i>psia</i>)	(<i>F</i>)	(<i>Mlbm/hr – ft²</i>)	(<i>Mbtu/hr – ft²</i>)	<i>Pin</i>	<i>Peak</i>
1	1010	516.0	0.490	0.450	7	1.0030
2	1005	500.0	0.500	0.472	7	1.0030
3	1010	470.0	0.500	0.500	7	1.0030
4	1005	430.0	0.500	0.522	7	1.0030
5	1018	382.0	0.500	0.551	7	1.0030
6	1005	336.0	0.500	0.596	4	1.0180
7	1005	516.0	0.750	0.521	14	0.9930
8	1015	500.0	0.750	0.535	14	0.9930
9	1010	472.0	0.740	0.572	13	1.0050
10	1000	433.0	0.740	0.622	13	1.0050
11	1005	405.0	0.740	0.652	13	1.0050
12	1005	369.0	0.740	0.695	7	1.0030
13	1010	521.0	1.000	0.543	15	1.0010
14	1002	500.0	1.010	0.584	15	1.0010
15	990	476.0	1.000	0.619	13	1.0050
16	1000	452.0	0.980	0.656	13	1.0050
17	1010	427.0	0.980	0.693	13	1.0050
18	1013	407.0	0.980	0.728	7	1.0030

Continued on next page...

#	P_{out} (psia)	T_{in} (F)	G (Mlbm/hr - ft ²)	q_{CHF} (Mbtu/hr - ft ²)	CHF Pin	Pin Peak
19	995	520.0	1.250	0.578	15	1.0010
20	1000	500.0	1.230	0.618	15	1.0010
21	997	480.0	1.230	0.663	15	1.0010
22	1005	460.0	1.240	0.711	4	1.0180
23	1010	441.0	1.250	0.739	4	1.0180
24	1410	540.0	1.000	0.468	7	1.0030
25	1205	539.0	0.980	0.509	8	1.0030
26	1210	520.0	0.980	0.527	8	1.0030
27	1410	519.0	0.990	0.491	7	1.0030
28	1220	501.0	0.990	0.564	8	1.0030
29	1415	498.0	0.990	0.528	7	1.0030
30	1210	472.0	1.000	0.597	7	1.0030
31	1410	470.0	1.000	0.565	7	1.0030
32	1210	443.0	0.990	0.641	7	1.0030
33	1420	438.0	0.990	0.612	7	1.0030
34	1200	416.0	0.980	0.680	7	1.0030
35	1405	408.0	0.990	0.658	7	1.0030
36	1400	532.0	0.750	0.446	7	1.0030
37	1410	512.0	0.740	0.471	7	1.0030
38	1405	492.0	0.750	0.496	7	1.0030

Continued on next page...

#	P_{out} (psia)	T_{in} (F)	G (Mlbm/hr - ft ²)	q_{CHF} (Mbtu/hr - ft ²)	CHF Pin	Pin Peak
39	1410	471.0	0.750	0.517	7	1.0030
40	1405	433.0	0.740	0.559	7	1.0030
41	1410	404.0	0.740	0.584	7	1.0030
42	1400	354.0	0.750	0.647	7	1.0030
43	1395	530.0	0.500	0.398	4	1.0180
44	1205	531.0	0.490	0.424	8	1.0030
45	1000	520.0	0.490	0.451	8	1.0030
46	1405	509.0	0.500	0.403	4	1.0180
47	1198	510.0	0.490	0.444	8	1.0030
48	993	502.0	0.490	0.475	8	1.0030
49	1200	480.0	0.500	0.472	4	1.0180
50	1405	480.0	0.500	0.437	4	1.0180
51	1000	473.0	0.500	0.504	15	1.0010
52	1415	430.0	0.500	0.477	4	1.0180
53	1196	431.0	0.490	0.497	4	1.0180
54	1015	431.0	0.490	0.525	4	1.0180
55	1410	382.0	0.500	0.527	4	1.0180
56	1200	383.0	0.490	0.540	4	1.0180
57	1000	382.0	0.480	0.548	4	1.0180
58	1400	321.0	0.510	0.570	4	1.0180

Continued on next page...

	P_{out}	T_{in}	G	q_{CHF}	CHF	Pin
#	(<i>psia</i>)	(<i>F</i>)	(<i>Mlbm/hr – ft²</i>)	(<i>Mbtu/hr – ft²</i>)	<i>Pin</i>	<i>Peak</i>
59	1215	330.0	0.500	0.600	4	1.0180
60	1005	335.0	0.500	0.604	4	1.0180
61	995	479.0	0.250	0.305	4	1.0180
62	1000	432.0	0.250	0.328	4	1.0180
63	700	384.0	0.240	0.345	4	1.0180
64	1005	335.0	0.250	0.366	4	1.0180
65	1000	285.0	0.250	0.392	4	1.0180

Table G.19: General Electric test data 316.1 from EPRI CHF database.

#	P_{out}	T_{in}	G	q_{CHF}	CHF	Pin
	(<i>psia</i>)	(<i>F</i>)	(<i>Mlbm/hr – ft²</i>)	(<i>Mbtu/hr – ft²</i>)	<i>Pin</i>	<i>Peak</i>
1	1010	515.0	0.500	0.445	4	1.0180
2	1015	500.0	0.500	0.464	4	1.0180
3	1010	469.0	0.500	0.486	4	1.0180
4	1005	431.0	0.490	0.512	4	1.0180
5	1005	383.0	0.490	0.534	4	1.0180
6	1010	338.0	0.500	0.575	4	1.0180
7	1005	520.0	0.760	0.515	14	0.9930
8	1000	499.0	0.730	0.538	14	0.9930
9	1000	470.0	0.750	0.587	14	0.9930
10	1010	431.0	0.740	0.625	14	0.9930
11	1010	407.0	0.750	0.655	14	0.9930
12	999	520.0	0.990	0.545	14	0.9930
13	1000	502.0	0.990	0.580	14	0.9930
14	1000	472.0	0.990	0.635	14	0.9930
15	1000	445.0	0.990	0.675	14	0.9930
16	1015	410.0	1.010	0.738	14	0.9930
17	1000	520.0	1.220	0.589	14	0.9930
18	1005	502.0	1.230	0.634	14	0.9930

Continued on next page...

#	P_{out} (psia)	T_{in} (F)	G (Mlbm/hr - ft ²)	q_{CHF} (Mbtu/hr - ft ²)	CHF Pin	Pin Peak
19	1005	472.0	1.230	0.693	14	0.9930
20	1010	452.0	1.230	0.727	14	0.9930
21	1005	425.0	1.240	0.768	4	1.0180
22	1405	521.0	0.990	0.506	4	1.0180
23	1195	521.0	0.980	0.535	14	0.9930
24	1405	499.0	1.000	0.534	4	1.0180
25	1220	500.0	0.990	0.570	14	0.9930
26	1410	470.0	1.000	0.587	14	0.9930
27	1200	470.0	1.000	0.621	4	1.0180
28	1405	520.0	0.990	0.664	1	0.9920
29	1200	422.0	0.980	0.682	4	1.0180
30	1405	520.0	0.500	0.387	4	1.0180
31	1210	520.0	0.500	0.452	14	0.9930
32	1405	500.0	0.500	0.402	4	1.0180
33	1207	502.0	0.500	0.452	14	0.9930
34	1405	468.0	0.510	0.423	4	1.0180
35	1205	472.0	0.500	0.472	4	1.0180
36	1405	430.0	0.500	0.453	4	1.0180
37	1200	431.0	0.500	0.484	4	1.0180
38	1405	393.0	0.500	0.478	4	1.0180

Continued on next page...

	P_{out}	T_{in}	G	q_{CHF}	CHF	Pin
#	(<i>psia</i>)	(<i>F</i>)	(<i>Mlbm/hr – ft²</i>)	(<i>Mbtu/hr – ft²</i>)	<i>Pin</i>	<i>Peak</i>
39	1205	394.5	0.490	0.515	4	1.0180
40	1405	343.0	0.500	0.528	4	1.0180
41	1215	344.0	0.500	0.548	4	1.0180
42	1000	472.0	0.240	0.300	4	1.0180
43	1010	434.0	0.250	0.323	4	1.0180
44	1015	403.0	0.250	0.336	4	1.0180

Table G.20: General Electric test data 317 from EPRI CHF database.

#	P_{out} (<i>psia</i>)	T_{in} (<i>F</i>)	G (<i>Mlbm/hr - ft²</i>)	q_{CHF} (<i>Mbtu/hr - ft²</i>)	CHF <i>Pin</i>	Pin <i>Peak</i>
1	2145	627.0	2.631	0.533	1	1.2040
2	2155	626.0	2.635	0.527	1	1.2040
3	2005	620.0	2.596	0.473	1	1.2040
4	1002	522.0	1.208	0.529	1	1.2040
5	1000	506.0	1.281	0.544	1	1.2040
6	1005	484.0	1.242	0.587	1	1.2040
7	1005	465.0	1.241	0.624	1	1.2040
8	1000	443.0	1.217	0.661	1	1.2040
9	1405	540.0	1.011	0.428	1	1.2040
10	1210	540.0	1.003	0.452	1	1.2040
11	1415	521.0	1.004	0.473	1	1.2040
12	1196	520.0	1.000	0.473	1	1.2040
13	1007	520.0	0.987	0.494	1	1.2040
14	1402	501.0	1.007	0.491	1	1.2040
15	1207	501.0	0.999	0.503	1	1.2040
16	1000	502.0	0.991	0.516	1	1.2040
17	1403	481.0	1.005	0.528	1	1.2040
18	1201	480.0	1.000	0.537	1	1.2040

Continued on next page...

#	P_{out} (<i>psia</i>)	T_{in} (<i>F</i>)	G (<i>Mlbm/hr – ft²</i>)	q_{CHF} (<i>Mbtu/hr – ft²</i>)	CHF <i>Pin</i>	Pin <i>Peak</i>
19	1002	480.0	0.991	0.543	1	1.2040
20	1405	461.0	1.006	0.561	1	1.2040
21	1205	460.0	0.999	0.580	1	1.2040
22	997	463.0	1.007	0.581	1	1.2040
23	1415	442.0	1.012	0.596	1	1.2040
24	1215	441.0	1.000	0.605	1	1.2040
25	1000	440.0	1.018	0.602	1	1.2040
26	1400	546.0	0.494	0.324	1	1.2040
27	1205	545.0	0.492	0.350	1	1.2040
28	1415	524.0 ¹	0.581	0.348	1	1.2040
29	1200	524.0	0.497	0.367	1	1.2040
30	1007	520.0	0.496	0.385	1	1.2040
31	1407	492.0	0.501	0.387	1	1.2040
32	1213	490.0	0.499	0.397	1	1.2040
33	997	492.0	0.495	0.415	1	1.2040
34	1402	460.0	0.501	0.418	1	1.2040

Continued on next page...

⁰The CHF location was originally reported by [55] to occur on pins 6 and 7 of the assembly. Pins 6 and 7 are on the edge of the channel (Figure 5.2) with peaking factors of 0.911 and 0.908 respectively (Table 5.26). Pine 1 is also an edge pin with a peaking of 1.204. Large errors were observed using the reported peaking factors versus 1.204. It is believed that a peaking of 1.204 is correct and physical and is used here.

¹This was originally recorded as 324.0 in [55]. This is believed to be in error based on this block of data being performed in the 500F temperature range and is corrected to be 524.0F here.

#	P_{out} (<i>psia</i>)	T_{in} (<i>F</i>)	G (<i>Mlbm/hr - ft²</i>)	q_{CHF} (<i>Mbtu/hr - ft²</i>)	CHF <i>Pin</i>	Pin <i>Peak</i>
35	1205	461.0	0.498	0.433	1	1.2040
36	1020	461.0	0.495	0.441	1	1.2040
37	1423	436.0	0.496	0.448	1	1.2040
38	1205	436.0	0.495	0.447	1	1.2040
39	1010	435.0	0.493	0.461	1	1.2040
40	1420	407.0	0.494	0.465	1	1.2040
41	1205	407.0	0.493	0.482	1	1.2040
42	1017	405.0	0.496	0.492	1	1.2040
43	1415	538.0	0.766	0.393	1	1.2040
44	980	524.0	0.735	0.449	1	1.2040
45	1000	524.0	0.737	0.447	1	1.2040
46	1400	522.0	0.753	0.406	1	1.2040
47	1005	494.0	0.727	0.478	1	1.2040
48	1410	491.0	0.751	0.453	1	1.2040
49	1410	464.0	0.753	0.498	1	1.2040
50	1010	465.0	0.741	0.513	1	1.2040
51	1005	436.0	0.748	0.561	1	1.2040
52	1405	435.0	0.756	0.534	1	1.2040
53	1420	412.0	0.747	0.559	1	1.2040
54	1005	413.0	0.747	0.575	1	1.2040

Continued on next page...

#	P_{out} (<i>psia</i>)	T_{in} (<i>F</i>)	G (<i>Mlbm/hr - ft²</i>)	q_{CHF} (<i>Mbtu/hr - ft²</i>)	CHF <i>Pin</i>	Pin <i>Peak</i>
55	2003	618.0	2.579	0.488	1	1.2040
56	2155	611.0	2.555	0.586	1	1.2040
57	2000	604.0	2.575	0.532	1	1.2040
58	2150	595.0	2.544	0.614	1	1.2040
59	2003	591.0	2.540	0.583	1	1.2040
60	2150	581.0	2.524	0.668	1	1.2040
61	1995	574.0	2.523	0.644	1	1.2040
62	2247	566.0	2.500	0.765	1	1.2040
63	2000	560.0	2.494	0.708	1	1.2040
64	2005	548.0	2.477	0.749	1	1.2040
65	2255	624.0	2.117	0.477	1	1.2040
66	2250	610.0	2.069	0.515	1	1.2040
67	2250	594.0	2.032	0.552	1	1.2040
68	2250	581.0	2.035	0.604	1	1.2040
69	2250	567.0	2.028	0.651	1	1.2040
70	2250	563.0	1.998	0.702	1	1.2040
71	1000	423.0	0.248	0.308	1	1.2040
72	1000	444.0	0.247	0.299	1	1.2040
73	1002	472.0	0.250	0.289	1	1.2040
74	1005	391.0	0.250	0.332	1	1.2040

Continued on next page...

	P_{out}	T_{in}	G	q_{CHF}	CHF	Pin
#	(<i>psia</i>)	(<i>F</i>)	(<i>Mlbm/hr – ft²</i>)	(<i>Mbtu/hr – ft²</i>)	<i>Pin</i>	<i>Peak</i>
75	1000	361.0	0.250	0.341	1	1.2040
76	1005	332.0	0.250	0.360	1	1.2040

Table G.21: General Electric test data 318 from EPRI CHF database.

#	P_{out} (<i>psia</i>)	T_{in} (<i>F</i>)	G (<i>Mlbm/hr – ft²</i>)	q_{CHF} (<i>Mbtu/hr – ft²</i>)	CHF <i>Pin</i>	Pin <i>Peak</i>
1	2000	616.0	2.062	0.445	13	1.2320
2	2250	620.0	2.112	0.476	13	1.2320
3	2245	592.0	2.043	0.555	13	1.2320
4	2015	584.0	2.029	0.535	13	1.2320
5	2240	564.0	2.015	0.647	13	1.2320
6	1997	557.0	2.005	0.600	13	1.2320
7	2240	536.0	2.001	0.730	13	1.2320
8	2005	535.0	1.999	0.672	13	1.2320
9	2235	528.0	1.997	0.744	13	1.2320
10	2005	521.0	1.998	0.722	13	1.2320
11	995	524.0	1.955	0.580	14	1.2040
12	1000	505.0	1.950	0.609	14	1.2040
13	995	485.0	1.953	0.652	13	1.2320
14	1005	464.0	1.954	0.692	13	1.2320
15	995	457.0	1.931	0.719	13	1.2320
16	995	521.6	2.445	0.622	13	1.2320
17	1005	506.0	2.465	0.663	13	1.2320
18	1009	492.0	2.443	0.706	13	1.2320

Continued on next page...

#	P_{out} (psia)	T_{in} (F)	G (Mlbm/hr - ft ²)	q_{CHF} (Mbtu/hr - ft ²)	CHF Pin	Pin Peak
19	1000	476.0	2.485	0.744	13	1.2320
20	2260	625.0	2.687	0.550	13	1.2320
21	2255	611.0	2.590	0.585	13	1.2320
22	2003	610.0	2.571	0.516	13	1.2320
23	2261	596.0	2.567	0.645	13	1.2320
24	2002	592.0	2.569	0.577	13	1.2320
25	2257	582.0	2.528	0.691	15	1.2300
26	2010	577.0	2.532	0.634	13	1.2320
27	2260	565.0	2.515	0.752	15	1.2300
28	2007	564.0	2.518	0.677	15	1.2300
29	2250	552.0	2.486	0.790	15	1.2300
30	2001	544.0	2.529	0.763	15	1.2300
31	2253	625.0	3.169	0.598	15	1.2300
32	2250	615.0	3.086	0.630	15	1.2300
33	1998	612.0	3.099	0.563	13	1.2320
34	2254	602.0	3.054	0.697	15	1.2300
35	2015	594.0	3.068	0.646	13	1.2320
36	2250	586.0	3.005	0.776	13	1.2320
37	2013	579.0	3.048	0.718	15	1.2300
38	2245	582.0	3.026	0.792	15	1.2300

Continued on next page...

#	P_{out} (psia)	T_{in} (F)	G (Mlbm/hr – ft ²)	q_{CHF} (Mbtu/hr – ft ²)	CHF Pin	Pin Peak
39	1995	572.0	3.015	0.729	13	1.2320
40	2001	561.0	2.973	0.791	13	1.2320
41	995	520.0	0.957	0.479	13	1.2320
42	1005	506.0	0.975	0.504	13	1.2320
43	1000	492.0	0.982	0.517	13	1.2320
44	1003	478.0	0.970	0.537	13	1.2320
45	1000	462.0	0.968	0.562	13	1.2320
46	995	443.0	0.976	0.580	13	1.2320
47	1005	425.0	0.981	0.599	13	1.2320
48	1800	593.0	2.034	0.472	13	1.2320
49	1695	591.0	2.036	0.452	13	1.2320
50	1725	577.0	2.002	0.490	13	1.2320
51	1715	561.0	2.011	0.539	13	1.2320
52	1702	542.0	1.986	0.594	13	1.2320
53	1713	523.0	1.974	0.651	13	1.2320
54	1730	505.0	1.972	0.711	13	1.2320
55	1705	485.0	1.969	0.756	13	1.2320
56	1395	560.0	1.973	0.511	13	1.2320
57	1400	540.0	1.984	0.553	13	1.2320
58	1205	540.0	1.968	0.552	13	1.2320

Continued on next page...

	P_{out}	T_{in}	G	q_{CHF}	CHF	Pin
#	(psia)	(F)	(Mlbm/hr – ft ²)	(Mbtu/hr – ft ²)	Pin	Peak
59	1205	529.0	1.952	0.565	13	1.2320
60	1400	528.0	1.987	0.588	13	1.2320
61	1397	512.0	1.970	0.629	13	1.2320
62	1200	510.0	1.974	0.617	13	1.2320
63	1200	497.0	1.979	0.645	13	1.2320
64	1400	497.0	1.940	0.657	13	1.2320
65	1407	479.0	1.976	0.712	13	1.2320
66	1203	481.0	1.973	0.689	13	1.2320
67	2000	534.0	1.987	0.677	15	1.2300
68	1405	540.0	1.001	0.404	13	1.2320
69	1405	520.0	1.014	0.439	13	1.2320
70	1407	501.0	1.016	0.470	13	1.2320
71	1403	483.0	1.025	0.500	13	1.2320
72	1400	462.0	1.041	0.539	13	1.2320

